

**WL-TR-97-2094**

ADVANCED LASER DIAGNOSTICS OF  
COMPRESSIBLE FLOWS



C. D. CARTER

SYSTEMS RESEARCH LABORATORIES  
*CALSPAN SRL CORPORATION*  
2800 INDIAN RIPPLE ROAD  
DAYTON, OH 45440-3696

MAY 1997

FINAL REPORT FOR 01/17/92 - 12/31/96

**DTIC QUALITY INSPECTED 8**

APPROVED FOR PUBLIC RELEASE; DISTRIBUTION UNLIMITED.

AERO PROPULSION AND POWER DIRECTORATE  
WRIGHT LABORATORY  
AIR FORCE MATERIEL COMMAND  
WRIGHT-PATTERSON AIR FORCE BASE, OH 45433-7251

19971223 120

## NOTICE

WHEN GOVERNMENT DRAWINGS, SPECIFICATIONS, OR OTHER DATA ARE USED FOR ANY PURPOSE OTHER THAN IN CONNECTION WITH A DEFINITELY GOVERNMENT-RELATED PROCUREMENT, THE UNITED STATES GOVERNMENT INCURS NO RESPONSIBILITY OR ANY OBLIGATION WHATSOEVER. THE FACT THAT THE GOVERNMENT MAY HAVE FORMULATED OR IN ANY WAY SUPPLIED THE SAID DRAWINGS, SPECIFICATIONS, OR OTHER DATA, IS NOT TO BE REGARDED BY IMPLICATION, OR OTHERWISE IN ANY MANNER CONSTRUED, AS LICENSING THE HOLDER, OR ANY OTHER PERSON OR CORPORATION; OR AS CONVEYING ANY RIGHTS OR PERMISSION TO MANUFACTURE, USE, OR SELL ANY PATENTED INVENTION THAT MAY IN ANY WAY BE RELATED THERETO.

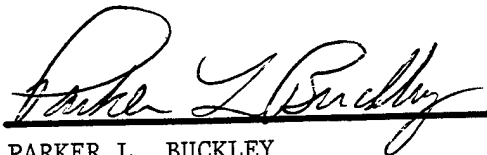
THE TECHNICAL REPORT HAS BEEN REVIEWED AND IS APPROVED FOR PUBLICATION.



DIANA D. GLAWE, PhD  
Aerospace Engineer (WL/POPT)  
Advanced Propulsion Division



MARK R. GRUBER, PhD  
Acting Branch Chief (WL/POPT)  
Advanced Propulsion Division



PARKER L. BUCKLEY  
Acting Chief  
Advanced Propulsion Division  
Aero Propulsion & Power Directorate

IF YOUR ADDRESS HAS CHANGED, IF YOU WISH TO BE REMOVED FROM OUR MAILING LIST, OR IF THE ADDRESSEE IS NO LONGER EMPLOYED BY YOUR ORGANIZATION PLEASE NOTIFY, WL/POP, BLDG 18A, WPAFB OH 45433-7 251 TO HELP MAINTAIN A CURRENT MAILING LIST.

Copies of this report should not be returned unless return is required by Security Consideration, contractual obligations, or notice on a specific document.

# REPORT DOCUMENTATION PAGE

*Form Approved*  
OMB No. 0704-0188

Public reporting burden for this collection of information is estimated to average 1 hour per response, including the time for reviewing instructions, searching existing data sources, gathering and maintaining the data needed, and completing and reviewing the collection of information. Send comments regarding this burden estimate or any other aspect of this collection of information, including suggestions for reducing this burden, to Washington Headquarters Services, Directorate for Information Operations and Reports, 1215 Jefferson Davis Highway, Suite 1204, Arlington, VA 22202-4302, and to the Office of Management and Budget, Paperwork Reduction Project (0704-0188), Washington, DC 20503.

1. AGENCY USE ONLY (Leave Blank)	2. REPORT DATE May 1997	3. REPORT TYPE AND DATES COVERED FINAL 01/17/92 - 12/31/96	
4. TITLE AND SUBTITLE  ADVANCED LASER DIAGNOSTICS OF COMPRESSIBLE FLOWS		5. FUNDING NUMBERS  C F33615-92-C-2022 PE 61102 PR 2308 TA S1 WU 00	
6. AUTHOR(S)  C. D. Carter		8. PERFORMING ORGANIZATION REPORT NUMBER  5596 Final	
7. PERFORMING ORGANIZATION NAME(S) AND ADDRESS(ES) Systems Research Laboratories Calspan SRL Corporation 2800 Indian Ripple Road Dayton, OH 45440-3696		10. SPONSORING/MONITORING AGENCY REPORT NUMBER  WL-TR-97-2094	
9. SPONSORING/MONITORING AGENCY NAME(S) AND ADDRESS(ES) Wright Laboratory Aero Propulsion and Power Directorate Air Force Materiel Command Wright-Patterson Air Force Base, OH 45433-7251 POC: DIANA D. GLAWE, WL/POPT (937) 255-1234		11. SUPPLEMENTARY NOTES	
12a. DISTRIBUTION/AVAILABILITY STATEMENT  Approved for public release; distribution unlimited		12b. DISTRIBUTION CODE	
13. ABSTRACT (Maximum 200 words)  We report the results of experimental and numerical investigations of fluid mechanics in reacting and high-speed nonreacting flows. For these experiments, the primary focus was on the development and application of advanced laser-based diagnostics for quantitative measurements of 1) temperature (coherent anti-Stokes Raman spectroscopy of N <sub>2</sub> and molecular filtered Rayleigh scattering) in reacting subsonic flows, 2) species concentration (OH, CH, NO, CO, and acetone laser-induced fluorescence) also in reacting subsonic flows, and 3) velocity (particle-imaging velocimetry and filtered Rayleigh scattering) in both subsonic and supersonic flows.			
14. SUBJECT TERMS Laser Diagnostics, Combustion, High-Speed Flows, Coherent Anti-Stokes Raman Spectroscopy (CARS), Laser- Induced Fluorescence (LIF), Filtered Rayleigh Scattering (FRS)		15. NUMBER OF PAGES 152	
17. SECURITY CLASSIFICATION OF REPORT UNCLASSIFIED		18. SECURITY CLASSIFICATION OF THIS PAGE UNCLASSIFIED	
19. SECURITY CLASSIFICATION OF ABSTRACT UNCLASSIFIED		20. LIMITATION OF ABSTRACT  SAR	

## TABLE OF CONTENTS

SECTION	PAGE
1. INTRODUCTION .....	1
2. OVERVIEW OF DIAGNOSTIC DEVELOPMENT AND APPLICATION .....	2
2.1 Laser-Based Rayleigh- and Mie-Scattering Methods .....	2
2.2 Development and Application of a 50-Hz CARS System for Thermometry in a High-Swirl Combustor .....	2
2.3 Application of Raman\Rayleigh Scattering and OH and NO LIF to the Study of Jet Diffusion Flames .....	19
2.4 Injection of Supercritical Ethylene into Nitrogen .....	21
2.5 Application of OH and Acetone PLIF to the Study of a Bluff-Body-Stabilized Nonpremixed Combustor .....	21
2.6 Development and Application of PIV and CH-PLIF .....	22
2.7 Development of FRS Thermometry .....	33
2.8 Development and Application of FRS Velocimetry .....	34
2.9 Application of Laser Diagnostics and Thin-Filament Pyrometry to the Study of an Unsteady Laminar H <sub>2</sub> -N <sub>2</sub> /Air Flame .....	40
3. REFERENCES .....	43
4. APPENDIX: Presentations and Publications .....	45

## LIST OF FIGURES

FIGURE		PAGE
1	Theoretical N <sub>2</sub> CARS Spectra (3.4 cm <sup>-1</sup> Slit Function) from 300 to 2300 K in 200-K Increments . . . . .	8
2	Recorded N <sub>2</sub> Spectrum from a H <sub>2</sub> -Air Hencken Flame. The best-fit temperature is 1775 K, while the adiabatic flame temperature is 1784 K . . . . .	9
3	2-D Mean and rms Maps of Temperature for an Overall Equivalence Ratio of 0.45 . . . . .	14
4	Mean and rms Temperature Plots for an Overall Equivalence Ratio of 0.45 and a Downstream Location of z/R = 0.167 . . . . .	15
5	Plots of the Probability Density Function (PDF) for an Overall Equivalence Ratio of 0.45 and a Downstream Location of z/R = 0.167 . . . . .	16
6	Mean and rms Temperature Plots for an Overall Equivalence Ratio of 0.45 and a Downstream Location of z/R = 1 . . . . .	17
7	Plots of the Probability Density Function (PDF) for an Overall Equivalence Ratio of 0.45 and a Downstream Location of z/R = 1 . . . . .	18
8	LIF Spectrum of CH Subsequent to Excitation to the B <sup>2</sup> Σ (v=0) State. The spectrum reflects fluorescence contributions from the A-X(0,0) and A-X(1,1) bands, both having Q-branch peaks at 431 nm, and the B-X(0,1) band, having its Q-branch peak at ~ 432.5 nm . . . . .	24

## LIST OF FIGURES (Continued)

FIGURE		PAGE
9	High- and Low-Power Laser Excitation Spectra of the B-X(0,0) Band . . . . .	25
10	Relative CH LIF Profiles Across a Laminar CH <sub>4</sub> -N <sub>2</sub> /O <sub>2</sub> Flame Using High and Low Laser Powers. Note that the low-power profile was recorded over only one-half of the flame . . . . .	27
11	Average Flamefront Thickness ( $\delta$ ) as a Function of Axial Distance ( $z$ ), Relative to the Stoichiometric Flame Length ( $L_f$ ), for Four Flames with Jet Exit $Re = 1700 - 18600$ . . . . .	28
12	Four Instantaneous 45-deg Images [i.e., the Laser Sheet and Camera Were Oriented 45 deg Relative to the (Typical) Vertical Plane] of the Flamefront Location (i.e., CH LIF) in the $Re = 18600$ Flame. Here, the downstream location is approximately one-third the stoichiometric flame length, and the field of view of each image is $\sim 30$ mm x 45 mm . . . . .	29
13	Instantaneous Overlaid Images of the Flamefront Location (i.e., CH LIF) and Velocity Field (via PIV) in the $Re = 18600$ Flame; the Downstream Location is the Time-Averaged Stoichiometric Flame Length, and the Field of View is 23 mm (Vertical) x 35 mm (Horizontal). Here, three-fourths of the centerline velocity has been subtracted from all vectors to reveal the local structure . . . . .	32

LIST OF FIGURES (Continued)

FIGURE	PAGE
14	Schematic of the Interaction Between the Incident Radiation and a Particle with Velocity Vector $\bar{u}$ in the Plane of Observation (Plane of the Page) . . . . .
	35
15	Iodine Absorption Spectrum Within the Frequency Tuning Range of the Nd:YAG (Second Harmonic) Laser [From Ref. 15] . . . . .
	37
16	Schematic of the Optical Setup for FRS Velocimetry Measurements [From Ref. 15] . . . . .
	39
17	Axial and Spanwise 2-D Velocity Distribution of a Jet in a Mach-2 Cross Flow . . . . .
	41

TABLES	PAGE
1	Combustor Operating Conditions, with $\Delta\phi$ Representing Precision of Control of Overall Equivalence Ratio and Taking Into Account Both Air and Fuel Control. Calculated adiabatic flame temperature, $T_{ad}$ (assuming fuel of pure propane, $T_{reactants} = 298$ K, and constant pressure of 0.95 atm), and its variation based on $\Delta\phi$ are also shown . . . . .
	12

## PREFACE

This report was prepared by Dr. Campbell D. Carter and covers work performed during the period 17 January 1992 to 31 December 1996 under Air Force Contract F33615-92-C-2202. The contract was administered under the direction of Wright Laboratory, Aero Propulsion and Power Directorate, Wright-Patterson Air Force Base, Ohio, with Dr. A. S. Nejad as Government Project Monitor.

## 1.0 INTRODUCTION

This report describes the results of experimental and numerical investigations of fluid mechanics in reacting and high-speed nonreacting flows. For these experiments the primary focus was on the development and application of advanced laser-based diagnostics for quantitative measurements of temperature [coherent anti-Stokes Raman spectroscopy (CARS) of  $N_2$  and molecular filtered Rayleigh scattering (FRS)], species concentration [OH, CH, NO, CO, and acetone laser-induced fluorescence (LIF)], and velocity [particle-imaging velocimetry (PIV) and FRS].

The research conducted for this program resulted in eight publications and presentations (included in the Appendix to this report); furthermore, four to six publications are in the planning or preparation stage. In addition to these publications and presentations, Dr. Carter was invited by Dr. J.-P. Taran (of ONERA, France), Chairman of the 1995 Gordon Conference on the Chemistry and Physics of Laser Diagnostics in Combustion, to make a presentation on laser-based measurements in practical combustion systems. Dr. Carter prepared a presentation entitled, "CARS Temperature Measurements in Model Gas-Turbine Combustors," based on CARS temperature measurements in the Rolls-Royce combustor.

The research efforts are summarized in Section 2, while the details--in cases where the results have been published in a journal or presented at a conference--of the development and application of advanced laser techniques for high-speed flows and/or reacting flows can be found in the Appendix to this report.

## **2.0 OVERVIEW OF DIAGNOSTIC DEVELOPMENT AND APPLICATION**

### **2.1 Laser-Based Rayleigh- and Mie-Scattering Methods**

At the request by Prof. J. A. Schetz (Virginia Polytechnic Institute), Dr. Carter contributed a section on laser-based Rayleigh- and Mie-scattering methods to the *Handbook of Fluid Mechanics and Fluid Machinery* (published in 1996 by John Wiley and edited by J. A. Schetz and A. E. Fuhs). The purpose of this section was to acquaint fluid-mechanics students and potential users of Rayleigh and Mie scattering with these techniques. The section presented first a review of fundamental aspects of scattering techniques, including relevant equations, and then a description of some of the applications that have appeared in the literature involving 1) species-concentration or mixture-fraction measurements when one gas mixes with another, 2) temperature and density measurements, particularly in reacting flows, and 3) velocity measurements in subsonic and supersonic flows. A copy of this section is included in the Appendix.

### **2.2 Development and Application of a 50-Hz CARS System for Thermometry in a High-Swirl Combustor**

The beneficial effects of high swirl for combustion are well known.<sup>1</sup> A central, toroidal vortex serves as a reservoir of hot combustion products; this well-mixed zone of hot gases and combustion radicals acts as an ignition source for the reactants (located outside of the recirculation zone). For this reason, swirl-stabilized flames have been an integral part of gas-turbine combustors. Nevertheless, combustors employing high-swirl turbulent fluid flow have not been studied extensively with nonintrusive diagnostic techniques. Consequently, Drs. Carter, Goss [of Systems Research Laboratories (SRL)], and Nejad (of Wright Laboratory (WL)], in collaboration with Rolls-Royce Aerospace, have studied the temperature field of a swirl-stabilized combustor employing CARS.

For monochromatic pump and Stokes beams, the CARS signal strength (power) is related to the powers of the pump and Stokes beams by the relation

$$P_{\text{signal}} \propto P_{\text{pump}}^2 P_{\text{Stokes}} |X^{(3)}|^2 \quad (1)$$

$X^{(3)}$  is the third-order susceptibility of the medium and can be represented as a summation of Raman resonant and nonresonant contributions. The resulting coherent laser-beam-like signal has a divergence comparable to that of the pump and Stokes beams and a frequency of  $2\omega_{\text{pump}} - \omega_{\text{Stokes}}$ . All the species within the probe volume contribute to the nonresonant CARS signal which results from remote vibrational resonances and the nonlinear distortion of the electron cloud of the probe species.<sup>2</sup> When the frequency difference between the pump and Stokes beams,  $\omega_{\text{pump}} - \omega_{\text{Stokes}}$ , matches a Raman-allowed transition of a species--for example,  $\omega_{\text{pump}} - \omega_{\text{Stokes}} \approx 2325 \text{ cm}^{-1}$  to match the  $v=1-0$  vibrational transition of  $\text{N}_2$ --the resulting CARS signal is resonantly enhanced. In particular, this signal strength is dependent on the difference in number density of initial and final rotational quantum states. Thus, the temperature of the probed species is encoded in the spectrum of the signal (anti-Stokes) beam. For non-overlapped Doppler-broadened transitions,  $X^{(3)}$  is proportional to the number density and, thus, the signal strength is proportional to the square of the number density; from a practical standpoint this means that for flame thermometry, the signal detector [e.g., linear array, charge-coupled device (CCD), etc.] must have a large dynamic range for recording temperatures from 300 to 2000 K. Traditionally, CARS has been applied for thermometry by 1) using a narrow-band dye laser and scanning the wavelength of this laser through the Raman transitions and 2) employing a broadband dye laser and a spectrometer along with an array detector. The latter approach was employed for this study and allows one to record temperatures in a single laser shot, if the spectral distribution of dye-laser irradiance is taken into account.

For mapping the temperature field of this model gas-turbine combustor, a CARS system was designed and constructed for thermometry (using  $\text{N}_2$  as the probe species) and species-concentration measurements (in future experiments). This system is designed around a Quanta-Ray

GCR-4 50-Hz Nd:YAG laser (delivering up to 350 mJ/pulse at 532 nm) and also includes 1) a broadband dye laser, 2) optics translation stages, 3) a custom-designed 0.75-m spectrometer, and 4) an intensified CCD (ICCD) camera for recording spectra at the 50-Hz pulse repetition frequency of the GCR-4. Furthermore, this facility includes custom software for integrating the positioning of the CARS probe volume--through movement of the transmission and collection optics--into the CCD data-collection software.

Of course, one must provide a means of translating the probe volume relative to the combustor, which was most easily accomplished by translating a subset of the optics rather than the optical table; consequently, we configured two stepper-motor-driven, three-axis translation systems and placed one on either side of the combustor test section. Each three-axis system included three large prisms for beam steering and a focusing/collimating lens. Custom software was written to permit the systems to be translated in concert (over a 300-mm range) and, of course, independently; each stage included a linear encoder to ensure accurate positioning of the individual stages and of one three-axis system relative to the other. The translation system, dye laser, and associated CARS optics were fixed on a 4 x 12 ft optical table having retractable casters to permit table movement; the YAG laser was designed to fit beneath this table but, for convenience, was placed on an optical breadboard adjacent to the main optical table.

The translation-system interfacing software was written to run on a stand-alone personal computer (PC); this computer was then interfaced to a second PC via the RS-232 (serial) port. This second PC controlled the Princeton Instruments ICCD camera; the camera-interfacing software (CSMA) was modified using Princeton Instruments *Spectrum Basic* language to communicate with the translation-system PC. With this software, numerous CARS spectra can be recorded and stored for a single probe location. Subsequent to recording data at one location, the *camera* PC sends a flag to the *translation* PC, initiating the movement of the probe volume; the *translation* PC then sends a flag to the *camera* PC, signaling that the translation is complete; finally, the software initiates the shuttering of the dye laser (i.e., a simple shutter placed in the dye-laser oscilla-

tor), and an average background spectrum is recorded. Using *Spectrum Basic*, we configured the CSMA program to record a temperature profile across the combustor, with 1000 CARS spectra being recorded for each location.

Because of the limited dynamic range of intensified CCD systems and the dynamic range necessary to record CARS signals from 300 to 2000 K, the signal beam was split into three parts, having ~ 1, 10, and 89% of the original signal energy; the channel having 89% of the original signal was employed for the highest temperatures, while the part having 1% was used for the lowest temperatures. These three signals were then routed to the spectrometer using 200- $\mu$ m-core fiber-optic cables. Of course, the resolution of the spectra is limited by the core diameter of the fiber, which acts as the entrance slit of the spectrometer. A concave holographic grating (200-mm diam., 737-mm radius of curvature, and 2000 grooves/mm) manufactured by American Holographic collected the signal beams and focused the dispersed light on the photocathode of the ICCD. The three spectra (from the three-way-split signal beam) lay side-by-side across the 384-pixel axis, and the individual pixel values were binned in the transverse direction; this binning allowed the use of a low-noise pixel-readout rate (50 kpixels/s) with the 50-Hz data collection.

Of course, the binning and readout processes must be completed within the 20-ms interval between laser pulses. Note, that our ICCD includes the short-lifetime P-46 phosphor;<sup>3-4</sup> other phosphors, the P-22 and P-20, for example, have sufficient persistence over this 20-ms time period to bias individual spectra. This problem is particularly acute with CARS because of the large variation in signal strength from room to flame temperatures.<sup>5</sup>

In addition to providing the 532-nm pump beams for CARS signal generation, the GCR-4 Nd:YAG also provided the excitation source for a broad-band dye laser operating at 607 nm. The dye laser was specially designed for high pump-repetition rates; initially, however, we employed simple flow-through oscillator/amplifier dye cells and a longitudinal pump geometry. This approach had been used successfully with previous CARS systems. However, the design proved inadequate with the 50-Hz pump rate; the windows on the dye cells (the inner, dye surface) were consis-

tently damaged because of the low speed of the dye fluid adjacent to the inner window surface and the higher pump frequency, 50 Hz as compared to 10 Hz. Consequently, we designed a broadband dye laser based on a transversely pumped oscillator (in a simple Fabry-Perot geometry) and amplifier. For the oscillator we employed a standard Lumonics (Hyperdye) dye cell; this design employs a knife edge at the pump region to ensure that the dye fluid is replenished between laser pulses. The design proved to be robust, and alignment was easy. To provide some degree of wavelength tuning of the dye laser, we placed a dielectric filter in the oscillator; this resulted in a  $\sim 70\text{-cm}^{-1}$  linewidth (FWHM), as compared to  $\sim 130\text{ cm}^{-1}$  for operation without the filter. Tuning was accomplished by varying the angle of the filter relative to the oscillator optical axis. To improve the symmetry of the dye beam, a Bethune-cell<sup>6</sup> with a 3-mm bore was used in an amplifier; a single dye pump and the dye mixture Exciton KR620 and R640 dissolved in methanol were employed for both oscillator and amplifier, simplifying the system setup. Typically, we recorded a 25% conversion efficiency for the dye laser (oscillator and amplifier). Finally, to both expand the dye beam and control its divergence (and match the focal positions of the pump and Stokes beams), we employed a Galilean telescope after the Bethune-cell amplifier.

For optimum spatial resolution, we employed a folded BOXCARS phase-matching geometry.<sup>7</sup> The beams were focused with a 300-mm focal-length lens (the crossing angle for the pump beams was  $\sim 0.83$  rad.), resulting in a beam waist of  $\sim 40\text{ }\mu\text{m}$  for the 532-nm pump beams and  $\sim 90\text{ }\mu\text{m}$  for the 607-nm Stokes beam. The spatial resolution in the lengthwise direction was evaluated by placing a 160- $\mu\text{m}$ -thick fused-silica cover slip in the probe volume. Of course, the beam irradiances were greatly attenuated (below the damage threshold of the fused silica); with the reduced beam irradiance, a CARS signal was generated in the fused silica but not in the room air. We then translated the CARS probe volume through the cover slip, recording signal strengths. With this approach, we determined that 95% of the CARS signal was generated from a region  $\sim 1$  mm in length. The beam energies were adjusted such that no significant *Stokes pumping*, i.e., production of a hot-band CARS signal through population of the  $v=1$  state,<sup>5</sup> was observed. Typical probe-volume energies for the pump and Stokes beams were 35 mJ (for each pump beam) and 10 mJ, respectively.

Calculated spectra over a range of temperatures (300 to 2300 K) are shown in Fig. 1. An experimental  $N_2$  spectra recorded in a steady, laminar  $H_2$ -air flame--employing a so-called Hencken burner which produces near-adiabatic flame temperatures<sup>8</sup>--is shown in Fig. 2; here, the best-fit temperature is 1775 K. This measurement illustrates the ideal case: 1) no shot-to-shot beam steering or distortion due to turbulence; 2) optimized laser alignment (not possible to maintain during long run times with the high-swirl combustor); and 3) large signals that are below the level of saturation for the ICCD analog-to-digital converter. The recorded CARS spectra were processed subsequent to data collection; temperatures were deduced from the spectra using a nonlinear least-squares fitting routine and a library of spectra (calculated at 10-K increments between 200 and 2600 K). Within the fitting routine, the peak intensity of the library spectra was set by matching integrated theoretical and experimental signals; this match was made on each fit cycle (except the first), and this procedure provided a modest improvement ( $\sim 10\%$ ) in the overall precision of the temperature measurements over that achieved by matching the peak intensities of theoretical and experimental spectra. Additionally, the data-reduction program included a frequency-fitting routine; the frequency fit, however, could be bypassed once we obtained confidence in the starting frequency of the experimental spectra. Bypassing the frequency fit improved the speed of the fitting routine and also produced additional improvement ( $\sim 10\%$ ) in the precision of the temperature measurement. The fitting routine employed 10 cycles for the fit, although usually it converged within five cycles.

At flame temperatures, most of the temperature information resides in the low-intensity portions of the spectrum (e.g., the  $v=1-2$  hot band); that is, the intensities of the hot band are much more sensitive to temperature than those of the cold band ( $v=0-1$  band); thus, a simple reciprocal intensity-weighting scheme was employed (see Ref. 9 for a discussion of weighting schemes). Although this approach has little effect on the derived average temperature, it can have a significant impact on the precision of the measurement. For example, the use of a constant weighting factor in a  $H_2$ -air flame (one of the 400 spectra recorded is shown in Fig. 2) yields mean and root-mean-square (rms) values of 1760

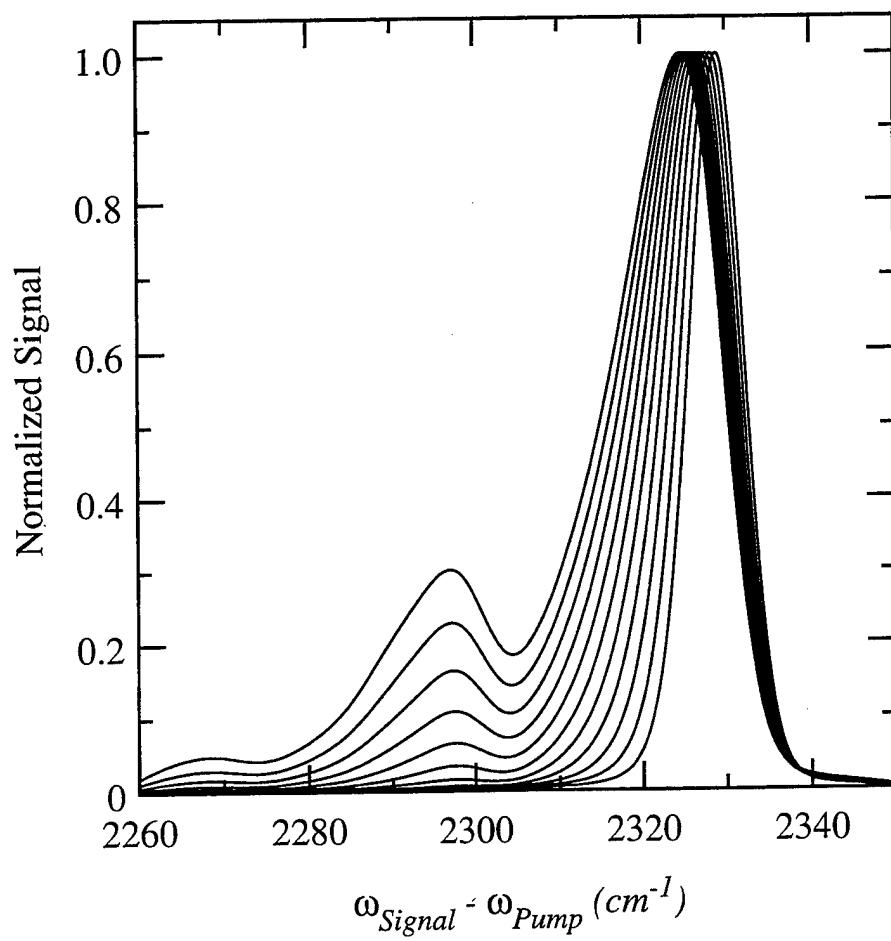


Figure 1. Theoretical N<sub>2</sub> CARS Spectra (3.4 cm<sup>-1</sup> Slit Function) from 300 to 2300 K in 200-K Increments.

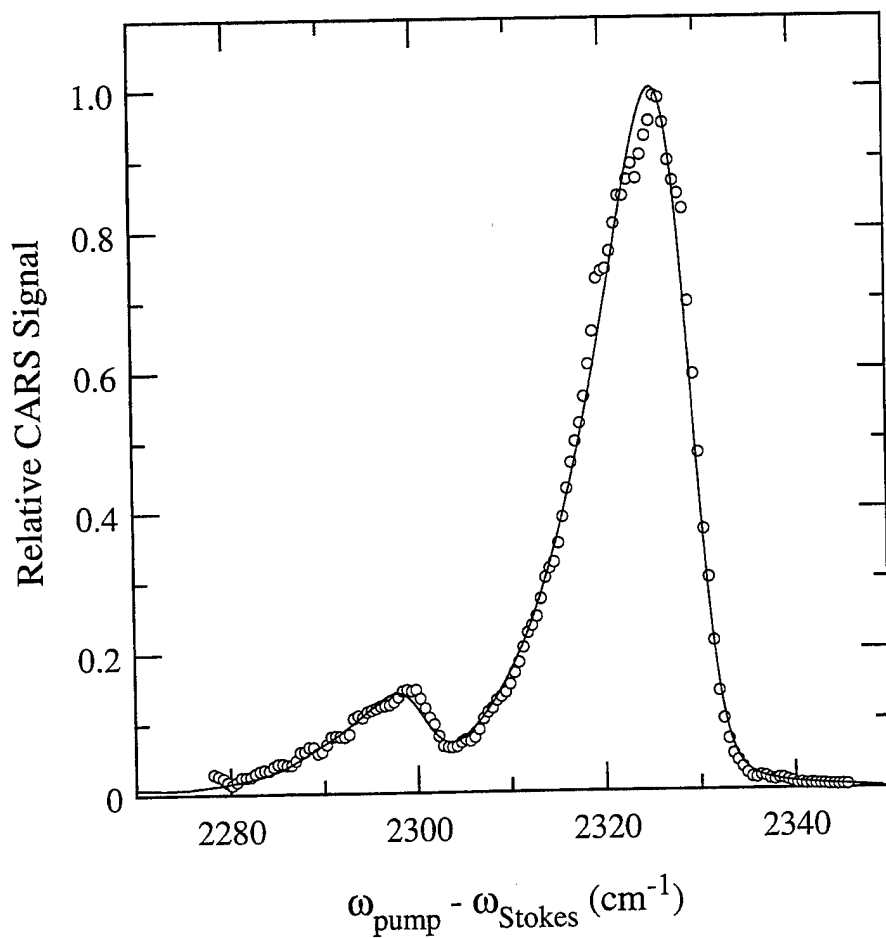


Figure 2. Recorded N<sub>2</sub> Spectrum from a H<sub>2</sub>-Air Hencken Flame. The best-fit temperature is 1775 K, while the adiabatic flame temperature is 1784 K.

and 83 K, respectively; however, the use of inverse intensity weighting yields average and rms values of 1787 and 37 K, respectively.

A significant contributor to the shot-to-shot temperature fluctuations is the shot-to-shot variations in the dye-laser spectrum, which result from the presence of the dye-laser axial cavity modes and the random nature of mode competition.<sup>9</sup> Recent studies have shown improvements in the precision of CARS temperature and species-concentration measurements through the use of so-called *modeless* lasers and a single-longitudinal-mode (injection-seeded) Nd:YAG pump laser.<sup>10</sup>

Finally, we noted significant shifts in the central wavelength of the dye laser--despite the fact that the dye solution was water cooled--which corresponded to variations in the test-cell temperature. With large room-temperature changes (which occurred when the test-cell doors were opened to bring in additional bottles of propane), this shift in the dye-laser wavelength was sufficient to change the derived CARS temperatures by as much as 10% (at ~ 1600 K). To mitigate the effect of test-cell temperature variations on the derived temperatures, we monitored the dye-laser spectrum with a 0.5-m spectrometer and a photodiode array detector. This enabled us to monitor the dye-laser spectrum and, as necessary, adjust the wavelength using the dielectric tuning filter. We tested the efficacy of this approach using the McKenna calibration flame; here, we intentionally detuned and then reset the dye-laser wavelength. We could consistently reset the temperature with a precision of about  $\pm 1\%$ ; however, for the combustor measurements, we estimated that uncertainty contribution from the dye-laser drift was  $\pm 2\%$ . Our approach was similar to that described by Snelling et al.<sup>3</sup>

To calibrate the CARS system, we employed a small, sintered-bronze flat-flame burner (25-cm diam., manufactured by McKenna Products) and a lean mixture of CH<sub>4</sub> and air (each was metered with a Tylan mass-flow controller). The small size of this burner, coupled with its excellent repeatability and 1-D nature permitted easy calibration. At low temperatures, the CARS spectra are sensitive to the instrumental slit function; on the other hand, at flame temperatures they are not. Thus, once the CARS system was calibrated with the McKenna flame, the instrumental slit function could be determined by recording CARS spectra in ambient, room-

temperature air; with the correct slit function ( $\sim 3.4 \text{ cm}^{-1}$  with our fiber-coupled spectrometer), the mean CARS temperature matched the ambient temperature (within about  $\pm 15 \text{ K}$ ). This procedure was then repeated to remove the small dependence of the slit function on the CARS calibration.

**2.2.1 Measurement Conditions.** For this study we chose three conditions corresponding to overall fuel-air equivalence ratios of 0.45, 0.65, and 0.9. For these cases the air flow rate was held constant at  $\sim 0.089 \text{ kg/s}$ , while the fuel flow rate was varied. The composition of the so-called industrial-grade propane was specified to be least 90% propane (by volume of liquid), with no more than 5% propylene and 2.5% butane (or heavier hydrocarbons). The air was delivered from compressors and metered using a calibrated orifice plate. The fuel mass-flow rate was metered with a turbine flow meter. The combustion chamber was typically operating slightly below standard atmospheric pressure at  $\sim 0.95 \text{ atm}$ .

This was, in fact, a second-generation combustor design. Both designs were based on a can-type geometry; however, the first was a simpler design (although having the same bore as the current version) in that it included two flush-mounted windows--one on either side of the combustor. Two-component laser Doppler velocimetry (LDV) was applied in both the cold and reacting flowfields; the nominal combustor conditions (air flow rate of  $\sim 0.090 \text{ kg/s}$  and overall equivalence ratio of 0.45) were the same as Condition A in Table 1. These measurements show the central recirculation region that is characteristic of high-swirl flows; the stagnation point (i.e., farthest downstream location of reversed axial flow) was found to be  $\sim 150 \text{ mm}$  (or 2.5 times the swirler outer diameter downstream of the dome). With combustion, the reversed-flow velocities were higher than in the nonreacting case; also, the maximum mean axial velocities,  $\sim 45 \text{ m/s}$ , were located along the path of the air flow exiting the swirler and along the wall, after the point of the impingement of the swirler air ( $\sim 75 \text{ mm}$  downstream of the dome). This zone of high axial velocity at the combustor periphery extends to a distance of several centimeters. The tangential velocity imparted by the swirler is  $\sim 20 \text{ m/s}$  at  $x = 25 \text{ mm}$  (in both the reacting and nonreacting cases). Farther downstream, combustion

Table 1

Combustor Operating Conditions, with  $\Delta\phi$  Representing Precision of Control of Overall Equivalence Ratio and Taking Into Account Both Air and Fuel Control. Calculated adiabatic flame temperature,  $T_{ad}$  (assuming fuel of pure propane,  $T_{reactants} = 298$  K, and constant pressure of 0.95 atm), and its variation based on  $\Delta\phi$  are also shown.

Condition	$\phi$	$\Delta\phi$	$\dot{m}_{fuel}$ (kg/s)	$T_{ad}$ (K)	$\Delta T_{ad}$ (K)
A	0.45	0.01	$2.56 \times 10^{-3}$	1407	$\pm 21$
B	0.65	0.01	$3.70 \times 10^{-3}$	1792	$\pm 18$
C	0.90	0.01	$5.08 \times 10^{-3}$	2180	$\pm 12$

increases the tangential velocity, particularly in the central region of the flow. For example, at  $x = 300$  mm, the maximum mean tangential velocity is 38 m/s at  $r = 10$  mm; in the nonreacting flow, the maximum mean tangential velocity,  $\sim 25$  m/s, is shifted to  $r = 22$  mm.

The flame was ignited by injecting silane ( $\text{SiH}_4$ ) into the combustor through the fuel line. The fuel line was first purged with  $\text{N}_2$  to remove  $\text{O}_2$ ; the silane gas was then injected along with the propane. During this ignition process, the window ports were purged with air to minimize deposition of  $\text{SiO}_2$  onto the windows. Despite these efforts, a small amount of residual  $\text{SiO}_2$  did reach the windows (and the walls of the combustor). Once ignition was achieved, the silane flow was terminated, and the combustor operating conditions were set.

Transient density gradients--and the concomitant refractive-index gradients--encountered in turbulent flames result in shot-to-shot beam

steering and phase distortions, with the net result being a reduction in signal strength. In this combustor, near the combustor dome where the turbulent mixing is most intense, beam steering and phase distortions were particularly acute; accordingly, the shot-to-shot variations in signal strength were large, even though the variation in temperature was small (less than  $\pm 60$  K). Far downstream, e.g., 200 mm from the dome, the effect of refractive-index gradients was small. To mitigate the effect of transient beam steering, we recorded temperature profiles only in the *near* half of the combustor (on the optics-transmission side). Although this causes the signal beam to traverse a greater distance before exiting the combustor, the pump and Stokes beams travel a lesser distance before intersecting, the net effect being a reduction in the shot-to-shot variations in signal.

**2.2.2 Results and Discussion.** In Fig. 3 we show the mean and rms temperature maps for conditions where the overall equivalence ratio is 0.45. This figure shows that in the central part of the combustor, the temperature is relatively uniform:  $\sim 1600$  K, near the combustor dome, to 1500 K, 300 mm downstream of the dome. For the farthest downstream location,  $z = 304$  mm, the centerline temperature,  $\sim 1510$  K, matches well with the radiation-corrected thermocouple measurement of 1490 K. In addition to the spatial uniformity, the instantaneous measurements show a remarkable shot-to-shot uniformity in the central portion of the combustor; this is illustrated in Figs. 4 - 7 with line graphs and probability-density-function plots. Only at positions very near the dome did we observe temperature fluctuations above approximately  $\pm 60$  K (roughly, the precision of the CARS instrument) within the central region of the combustor. Thus, the central recirculation zone does indeed function as a well-stirred reactor.

Of course, near the mixing regions, the shot-to-shot temperature variations are large; this is also illustrated in Figs. 3 - 7. Although the radial grid for recording the temperatures was relatively coarse (measurements at  $\sim 5$  mm intervals), we did not observe, except on rare occasions, stoichiometric or near-stoichiometric flame temperatures. Very rapid premixing of the reactants (between the dome and the region of flame stabilization) would, of course, account for this result; however, two additional reasons are 1) nonlinear spatial-averaging effects and 2) aero-

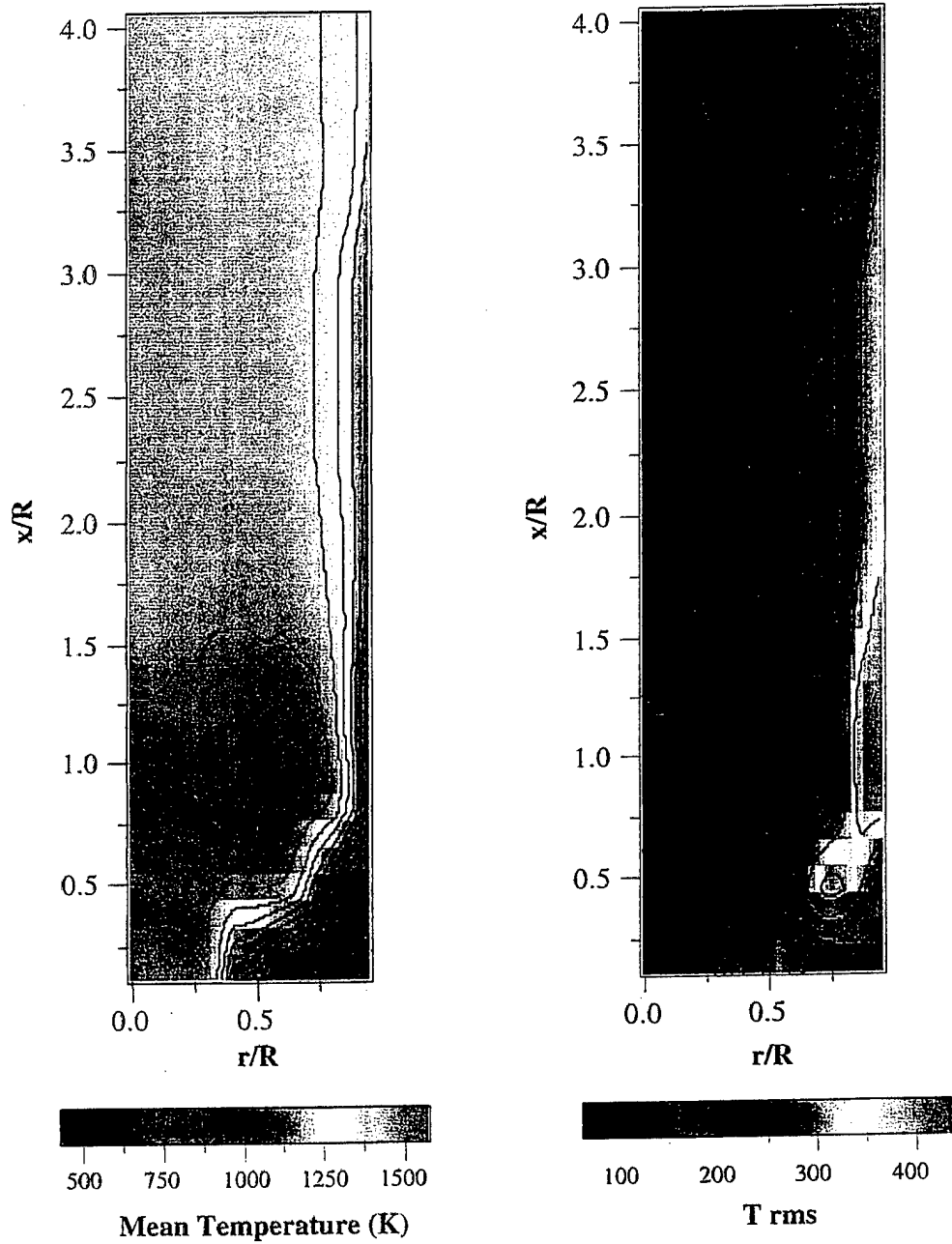


Figure 3. 2-D Mean and rms Maps of Temperature for an Overall Equivalence Ratio of 0.45.

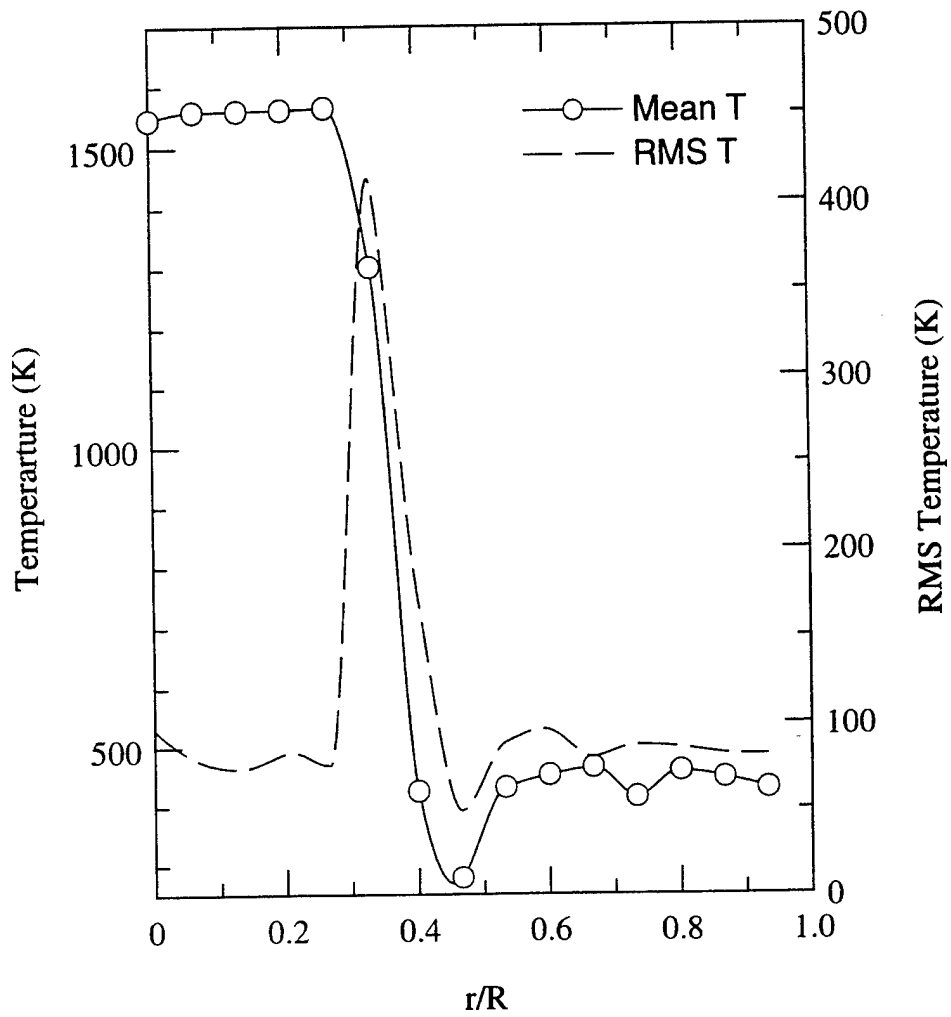


Figure 4. Mean and rms Temperature Plots for an Overall Equivalence Ratio of 0.45 and a Downstream Location of  $z/R = 0.167$

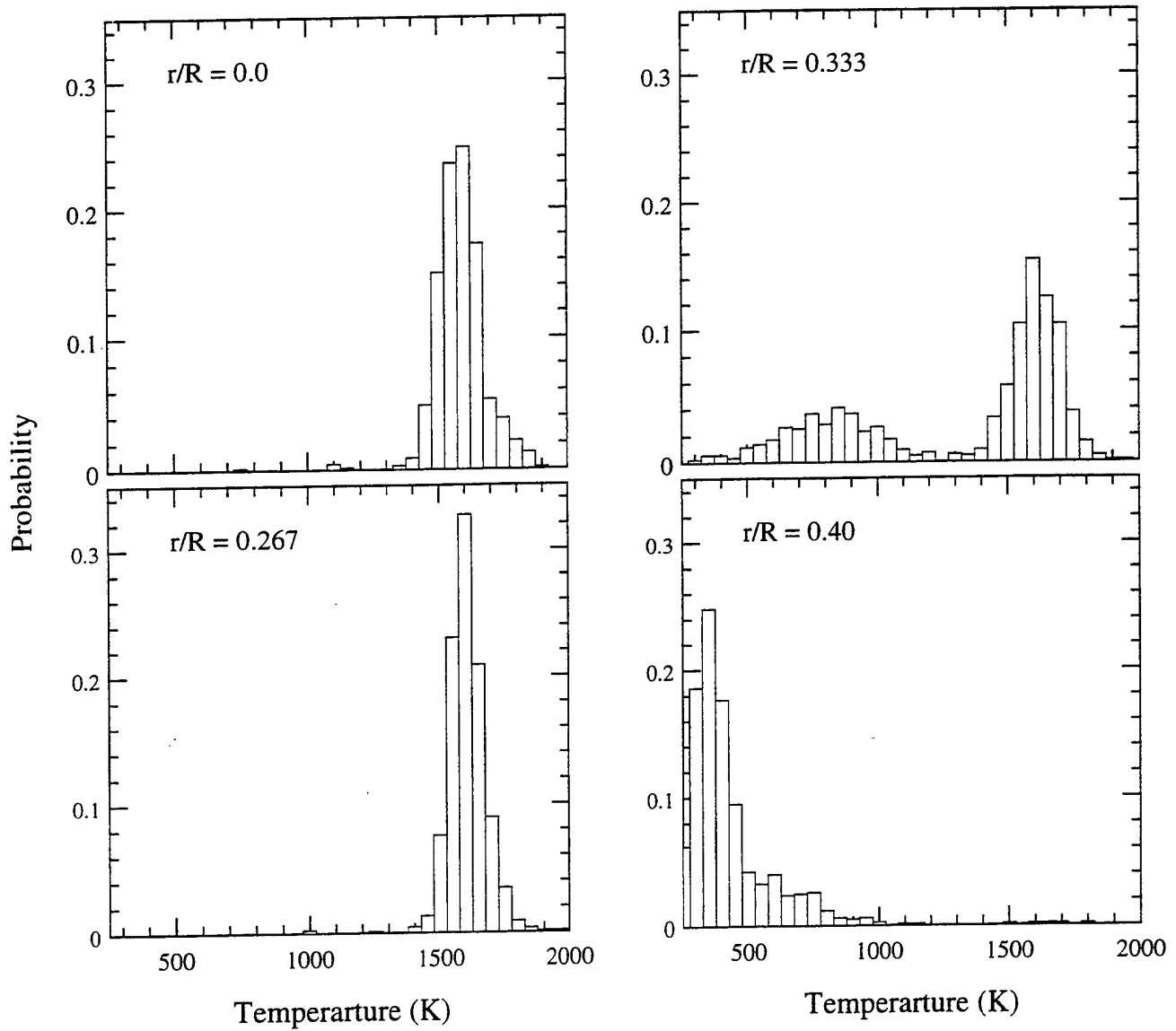


Figure 5. Plots of the Probability Density Function (PDF) for an Overall Equivalence Ratio of 0.45 and a Downstream Location of  $z/R = 0.167$ .

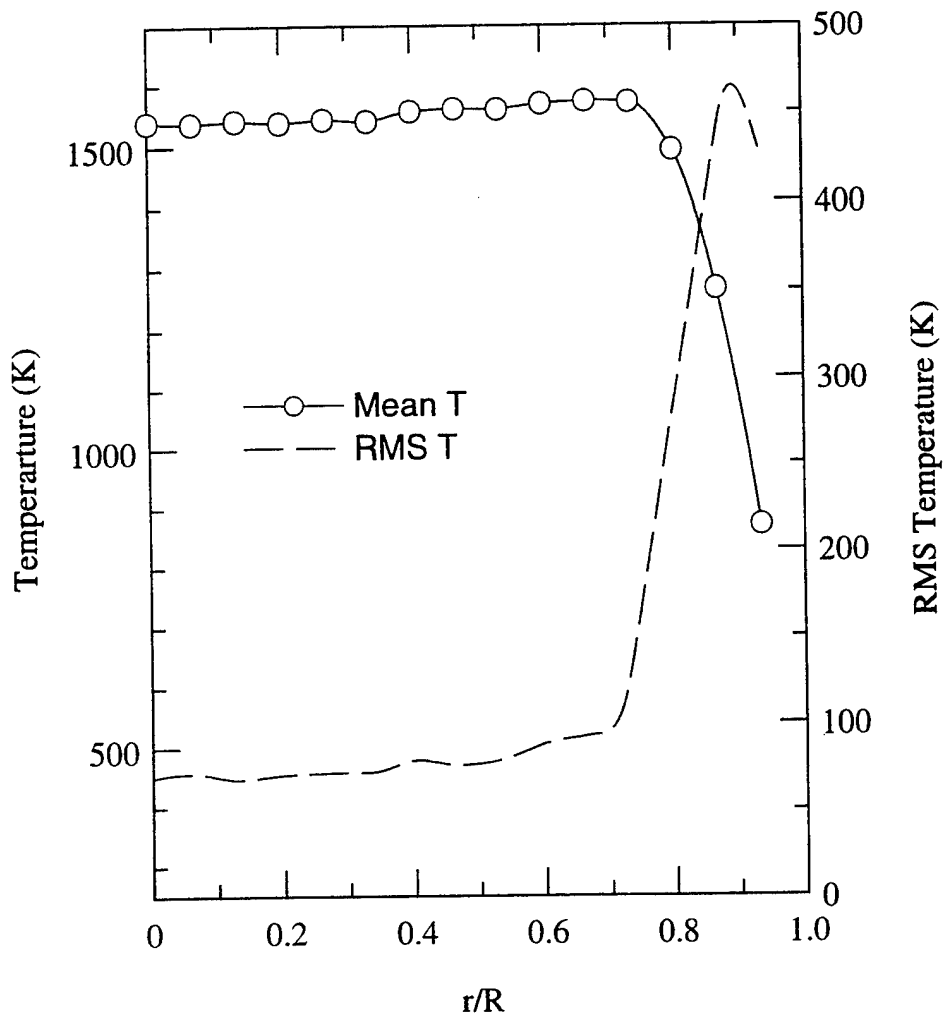


Figure 6. Mean and rms Temperature Plots for an Overall Equivalence Ratio of 0.45 and a Downstream Location of  $z/R = 1$ .

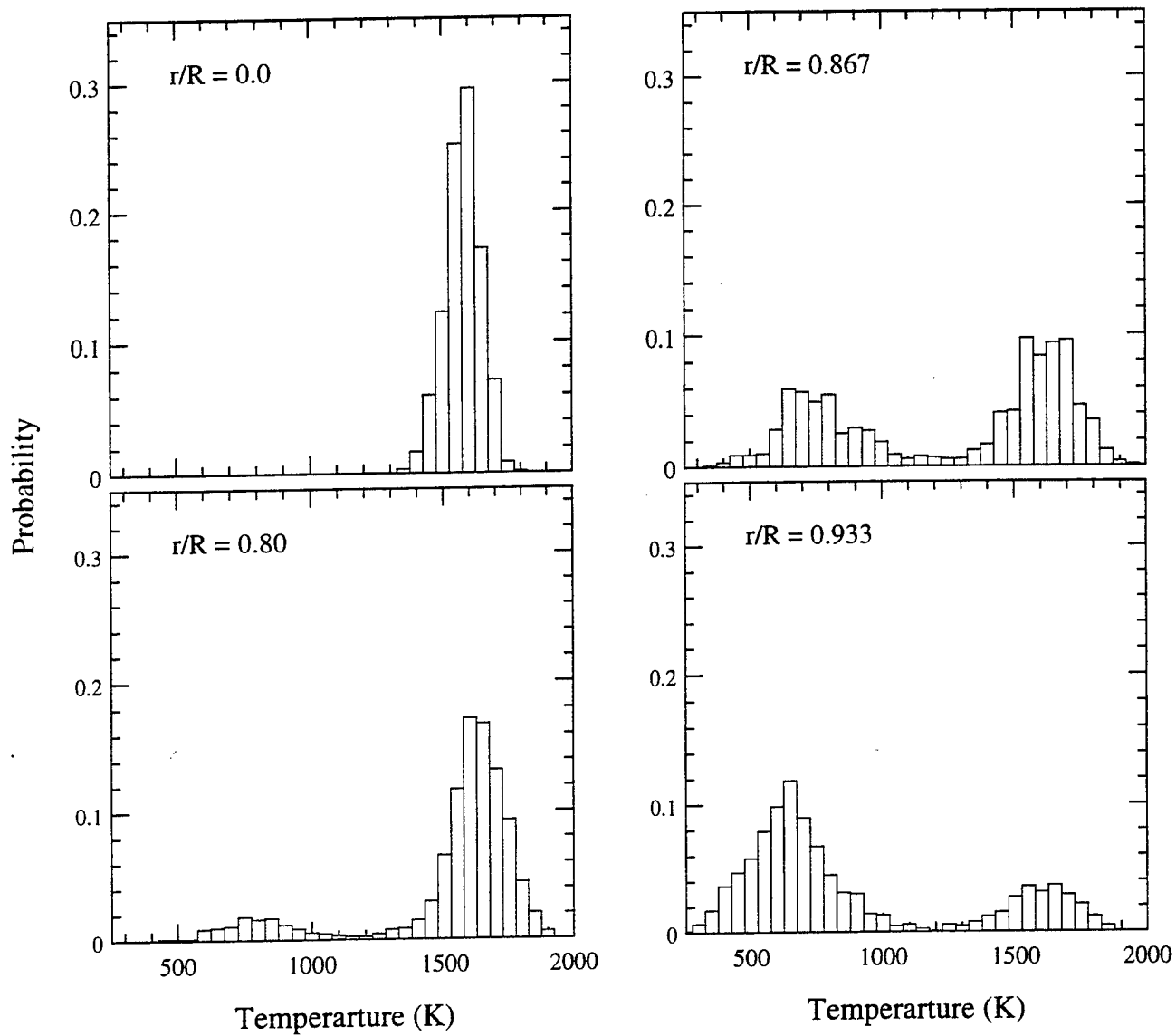


Figure 7. Plots of the Probability Density Function (PDF) for an Overall Equivalence Ratio of 0.45 and a Downstream Location of  $z/R = 1$ .

dynamic strain effects. With CARS measurements, temperatures are always biased toward the lower values when there is a variation within the probe volume; furthermore, adequate definition of the probe volume can be difficult because of the nonlinear dependence of the signal strength on number density. Consequently, resolving temperature gradients along the beam-propagation axis can be difficult. As noted above, however, we configured the CARS optics to yield a small probe size of  $\sim 1$  mm; of course, this was achieved at the expense of signal strength. Note that, in general, the number of spectra retained was greater than 95% of the total recorded (i.e., 950 out of 1000); spectra were rejected on the basis of low signal and/or poor fitting precision.

### **2.3 Application of Raman/Rayleigh Scattering and OH and NO LIF to the Study of Jet Diffusion Flames**

Dr. Carter, at the invitation of Dr. Robert Barlow, visited the Turbulent Diffusion Flame (TDF) Laboratory at Sandia National Laboratories (Livermore, CA) for the purpose of collaborating on a study of jet diffusion flames. Drs. Carter and Barlow conducted a variety of studies on 1) a turbulent jet diffusion flame with CO and H<sub>2</sub> as fuel, 2) a laminar CH<sub>4</sub>-air Bunsen flame, and 3) fluorescence interferences for NO LIF. The first study employed Raman and Rayleigh scattering for detection of major species and temperature, and LIF for OH and NO concentration. The resulting data were recorded at a variety of radial and axial locations within the flame for elucidating the structure of the flame and the interaction of turbulence and flame chemistry--particularly with regard to its role in the formation of the pollutant NO. A publication describing this study is being prepared for submission to *Combustion and Flame*.

The second study, which was also in collaboration with Dr. G. J. Fiechtner (also of Sandia) and Mr. Q. V. Nguyen and Prof. R. W. Dibble (University of California, Berkeley), was motivated by interest in the structure of partially premixed flames. These measurements, employing the TDF laser diagnostics (Raman/Rayleigh scattering and OH and NO LIF), show that the unburned fuel-air mixture undergoes considerable preheating as it travels upward; as a result of this preheating, the maximum centerline temperatures,  $\sim 2000$  K, were relatively insensitive to stoi-

chiometry (at least over the range  $\phi = 1.38 - 1.70$ ). Furthermore, the peak NO concentration decreased from 79 to 63 ppm as the fuel-air equivalence ratio was increased from  $\phi = 1.38$  to 1.70. For verifying the efficacy of the approach for calibrating and reducing the NO LIF signals, NO concentrations from LIF and probe sampling (employing a chemiluminescent NOx analyzer) were compared along the centerline of the flame at  $\phi = 1.38$  and found to differ by only a few percent, demonstrating the reliability of the NO LIF measurements. The results of this study were recently published in an article entitled, "Raman-LIF Measurements of Temperature, Major Species, OH, and NO in a Methane-air Bunsen Flame," by Q. V. Nguyen, R. W. Dibble, C. D. Carter, G. J. Fiechtner, and R. S. Barlow in *Combustion and Flame* [Vol. 105, pp. 499-510 (1996)]. This paper is included in the Appendix.

In the third study, Drs. Carter, Fiechtner, and Barlow initiated an investigation of the O<sub>2</sub> Schuman-Runge band interferences for the  $\gamma(0,0)$  bands of NO ( $A^2\Sigma^+ - X^2\Pi$ ). Previously, Drs. Carter and Barlow (among others) had reported<sup>11</sup> the presence of interfering transitions of O<sub>2</sub> originating from hot bands of the Schuman-Runge system ( $B^3\Sigma^- - X^3\Sigma^-$ ) in the 225-nm region; in addition to interferences from distinct O<sub>2</sub> transitions, these investigators had observed a broadband interference, presumably also due to O<sub>2</sub> since the O<sub>2</sub> transitions are strongly broadened as a result of predissociation. The goal of this effort was to identify NO transitions suitable for NO LIF measurements from room to flame temperatures and having minimal interference. From the initial part of the study, the overlapped Q<sub>1</sub>(12) and Q<sub>2</sub>(20) lines were identified as having reduced O<sub>2</sub> interference (both narrowband and broadband). A paper reporting the results of this study of O<sub>2</sub> interference, which includes excitation scans for a variety of temperatures is being prepared for publication in *Applied Optics*.

In addition to these studies, Drs. Fiechtner, Barlow, and Carter began experiments to determine the efficacy of two-photon LIF measurements of CO. The detection limit with this technique is significantly better than that with spontaneous Raman scattering; however, the nonlinear dependence of two-photon LIF on laser power is a disadvantage in the case of quantitative point measurements. Furthermore, with CO LIF, a third photon pho-

to ionizes the excited CO, which can further complicate the interpretation of the fluorescence signal for quantitative measurements of concentration.

## **2.4 Injection of Supercritical Ethylene in Nitrogen**

Dr. Carter, in collaboration with Dr. P.-K Wu (Taitech, Inc.) studied the injection behavior of a fluid (ethylene) under supercritical conditions. Here, the goal was to elucidate the thermophysical and transport properties near the critical point on jet appearance, shock structure, and choking. Ethylene and nitrogen were used to simulate interactions between fuel and air. Conditions near the thermodynamic critical point of ethylene were considered, along with supercritical temperatures and pressures upstream of the injector and subcritical pressures downstream of the injector. At high injectant temperatures, the ethylene jet was found to have a shock structure similar to that of an underexpanded ideal-gas jet. Mass flow rates were found to be insensitive to the variation of back pressure, indicating that the jet flow was choked. As the critical temperature was approached, the normalized mass flow rate first increased, apparently as a result of the rapid increase in fluid density, and then decreased, possibly as the result of the coexistence of liquid and gas phases at the nozzle exit.

The results of this study were recently published in an article entitled, "Injection of Supercritical Ethylene in Nitrogen," by P.-K. Wu, T. H. Chen, A. S. Nejad, and C. D. Carter in the *Journal of Propulsion and Power* [Vol. 12, pp. 770-777 (1996)]. This paper is included in the Appendix.

## **2.5 Application of OH and Acetone Planar LIF (PLIF) to the Study of a Bluff-Body-Stabilized Nonpremixed Combustor**

Dr. Carter and Mr. J. Donbar (Wright Laboratory, WL/POPT) assisted Prof. R. Gould (on sabbatical from North Carolina State University) in conducting experiments detailing mixing and combustion in a nonpremixed bluff-body combustor. They recorded acetone and OH PLIF employing a Quanta-Ray Nd:YAG/dye-laser system which was placed on a computer-controlled, high-capacity, three-axis traversing table. The dye laser and doubler (Inrad Autotrakker II) were configured to pump the R<sub>1</sub>(8) transi-

tion within the  $A^2\Sigma^+ - X^2\Pi$  (1,0) band of OH. Since acetone also absorbs at this pump wavelength, this single laser system was employed for visualizing acetone and OH LIF. While the acetone fluorescence signal reflects the degree of fuel mixing, the OH marks the flamefront and regions of hot products. Because of the high degree of turbulence within the flowfield, 200 images were recorded at each spanwise location. The images were recorded over an 82 x 55 mm field of view that includes the bluff-body fuel injector and the regions downstream of the injector. This set of averaged acetone images illustrates the mixing behavior of the fuel. The fuel must stay near the bluff-body surface directly after injection if it is to be entrained into the recirculation zone behind the body. If the fuel jet penetrates substantially into the air cross flow, entrainment into the bluff-body recirculation zone will be minimal and no flame holding will occur.

The results of this experiment will be presented in Paper No. FEDSM97-3097 entitled, "Three-Dimensional Mixing Study of Reacting and Isothermal Flow Behind a Bluff Body Flameholder with Normal Fuel Jet Injection," by R. D. Gould, C. D. Carter, J. M. Donbar, and A. S. Nejad (WL) at the Laser Anemometry and Experimental and Numerical Flow Visualization Symposium to be held during the ASME Fluids Engineering Division Summer Meeting, 22-26 June 1997, Vancouver, B.C. A copy of the presentation is included in the Appendix.

## 2.6 Development and Application of PIV and CH PLIF

Dr. Carter and Mr. J. Donbar have recorded measurements of CH PLIF--exciting an isolated CH transition in the  $B^2\Sigma^- - X^2\Pi(0,0)$  band ( $\lambda = 390$  nm) and detecting fluorescence at 420-440 nm--in turbulent nonpremixed  $CH_4-N_2/O_2$  jet flames. The goal was to study the flamefront strain field in laminar and turbulent nonpremixed  $CH_4$ -based jet flames using simultaneous PIV and PLIF of the CH radical (which effectively marks the flame reaction zone). Four flames having cold-jet exit Reynolds numbers  $Re$  from 1700 (laminar) to 18600 (fully turbulent) were investigated. For each flame, Carter and Donbar recorded/evaluated the flamefront thickness (i.e., the width at half the maximum signal of the CH layer), the degree of flamefront wrinkling from the base to the flame tip, and the flame-surface density (i.e., the probability of observing the flame within a

defined area). To circumvent problems with interferences with polycyclic aromatic hydrocarbons (PAHs), they employed a fuel mixture of  $\text{CH}_4$  and  $\text{N}_2$  and a coflow of pure  $\text{O}_2$ . Typical means of reducing PAH interferences, such as simply adding  $\text{H}_2$  or  $\text{N}_2$  to the  $\text{CH}_4$ , while still using air in the coflow were much less effective than substituting  $\text{O}_2$  for air in the coflow. By adjusting the concentration of  $\text{N}_2$  dilution in the fuel while using the  $\text{O}_2$  coflow, one can easily obtain nonsmoking flames (i.e., ones that remain blue from base to tip). In addition, the level of CH fluorescence is increased over that found at the base of nonpremixed  $\text{CH}_4$ -air flames (where sufficient concentrations of PAHs have not yet formed).

Excitation and detection spectra of CH LIF were recorded. This study served two purposes. First, the detection spectra allowed assessment of the degree of interference in the flames used in the study. Fluorescence spectra were recorded in a variety of flames, some having known, strong PAH interferences (nonpremixed  $\text{CH}_4$ -air flames); these measurements were accomplished by attaching the ICCD camera (normally used for CH PLIF measurements) to a 0.5-m Spex spectrometer. With this arrangement, they could observe the 420 - 440 nm region. From this study, they concluded that the flames of interest ( $\text{N}_2$ -diluted  $\text{CH}_4$  fuel and  $\text{O}_2$  coflow) had no observable interfering fluorescence; only the distinctive fluorescence of CH--from the A-X(1,1) and (0,0) bands and from the B-X(0,1) band--could be detected. A sample fluorescence spectrum recorded by averaging 1000 individual spectra (one for each laser shot) is shown in Fig. 8. Note that the A( $v=1$ ) state is populated via fast electronic-energy transfer--i.e., the ratio of electronic-energy transfer to electronic quenching of the B( $v=0$ ) is  $\sim 0.15$ --from the B( $v=0$ ) state); likewise, the A( $v=0$ ) state can be populated via vibrational energy-transfer collisions.

Excitation spectra allowed Carter and Donbar to assess the role of optical saturation of the LIF signal and to search for other unexpected/unknown spectral features (of CH or other molecules). Again, only the expected features of the CH B-X(0,0)-band transitions were observed (Fig. 9). However, when high laser irradiance was employed (the typical situation), strong saturation broadening of the transitions was observed; this is also shown in Fig. 9. With the aid of these excitation scans, it was determined that the  $Q_1(7.5)$  transition was the optimum one in terms of

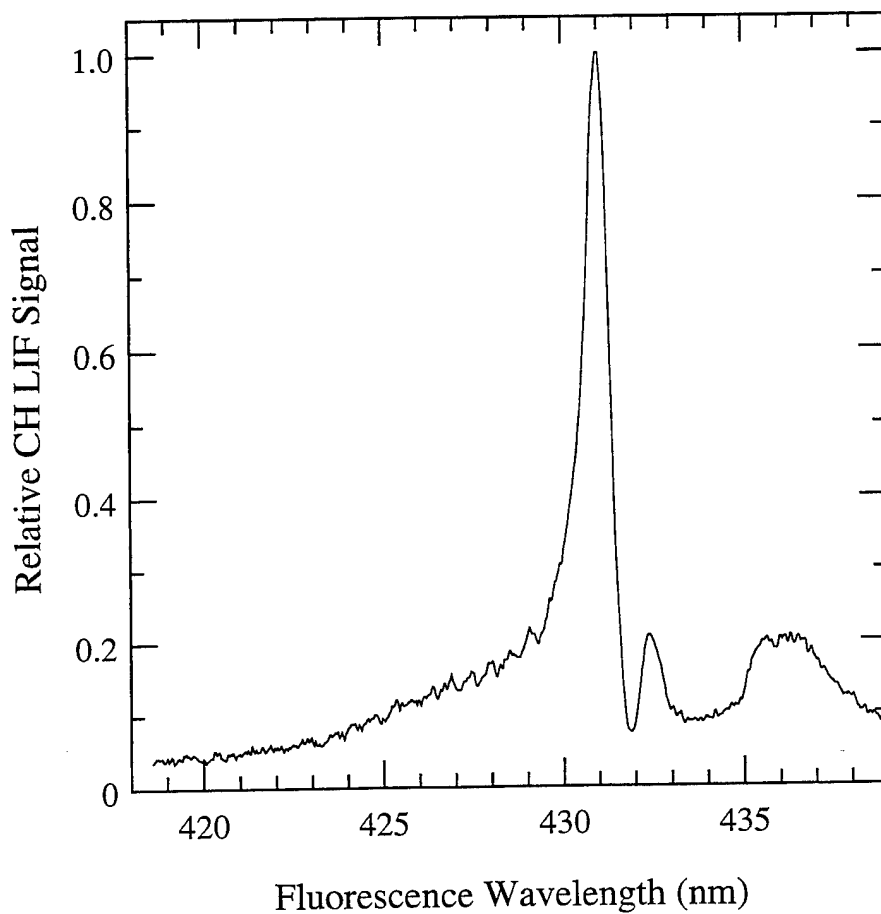


Figure 8. LIF Spectrum of CH Subsequent to Excitation to the  $B^2\Sigma$  ( $v=0$ ) State. The spectrum reflects fluorescence contributions from the A-X(0,0) and A-X(1,1) bands, both having Q-branch peaks at 431 nm, and the B-X(0,1) band, having its Q-branch peak at  $\sim 432.5$  nm.

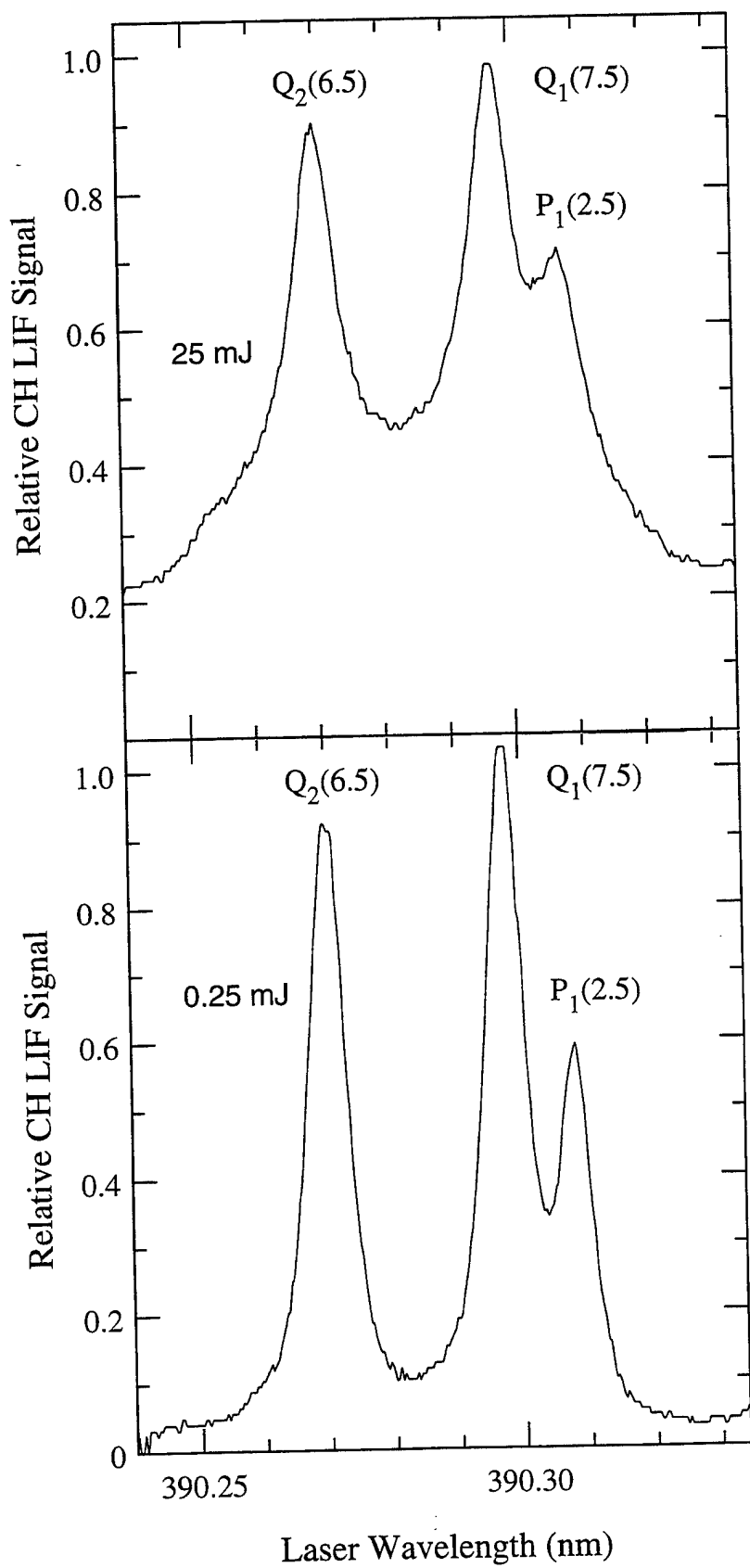


Figure 9. High- and Low-Power Laser Excitation Spectra of the B-X(0,0) Band.

signal strength because the  $Q_1(7.5)$  and  $P_1(2.5)$  lines overlap to some degree, thereby increasing the LIF signal strength. Regarding the effect of high laser irradiance, these investigators also observed some apparent photolytic production of CH fluorescence in the low-speed laminar flame using a PMT and small 0.1-m spectrometer (Fig. 10). With high laser irradiance, a small but finite LIF signal could always be observed in the center of the jet (where CH should not be present); with low irradiance (reduced by about an order of magnitude from the previous measurement), the CH width was slightly less ( $230\ \mu\text{m}$  as compared to  $250\ \mu\text{m}$ ), and no LIF signal was recorded in the central part of the jet. Fortunately, because of optical saturation of the strong B-X(0,0) transitions, reducing the laser irradiance by a factor of eight reduces the fluorescence signal by only  $\sim 50\%$ . Thus, photolytic production of the signal can be reduced without significant loss in the quality of the CH PLIF images.

Carter and Donbar used CH PLIF measurements to determine the average location of the flame tip (corresponding to the so-called stoichiometric flame length) and the average flamefront/CH thickness. Near the flame base in each case, the CH thickness is very small,  $\sim 300\ \mu\text{m}$  (or perhaps smaller). On average, the flamefront thickness increases from the base to the tip, reaching  $\sim 0.9\ \text{mm}$  (on the average) for the flame with  $Re = 18600$ ; this is shown in Fig. 11. Furthermore, they observed that the CH signal increases with jet Reynolds number (note, however, that the adiabatic flame temperatures are higher for the higher-Reynolds-number flames) and that a correlation exists between the high signals and the thin regions. Indeed, strained laminar flame calculations show that CH concentration can be increased by high aerodynamic strain.

In addition to recording PLIF images with a vertically oriented laser sheet, these investigators rotated the laser sheet and ICCD camera  $45^\circ$  with respect to the vertical (and horizontal) planes and recorded the CH signals; this orientation gives a quasi-cross-sectional view of the flame zone. A sample set of four images is shown (in a binary black and white format) in Fig. 12. These images reveal that the flame surface is highly distorted/wrinkled; although the CH signal levels vary along the flame surface (in some cases to such a degree that the level is just barely above the detection limit), the flame does not appear to be broken.

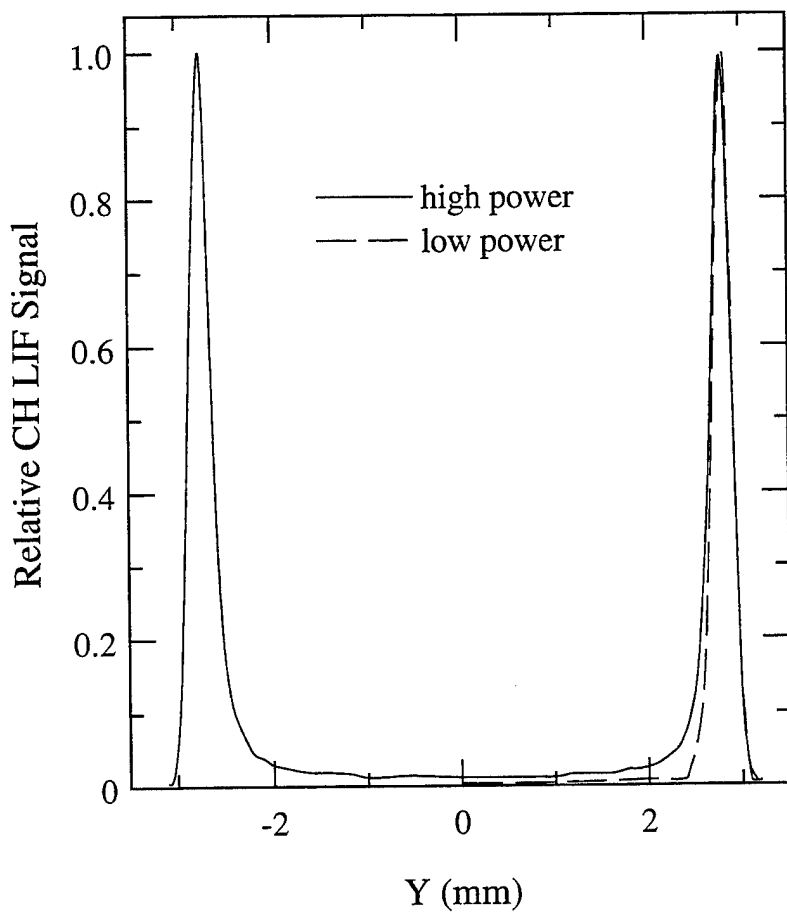


Figure 10. Relative CH LIF Profiles Across a Laminar  $\text{CH}_4\text{-N}_2/\text{O}_2$  Flame Using High and Low Laser Powers. Note that the low-power profile was recorded over only one-half of the flame.

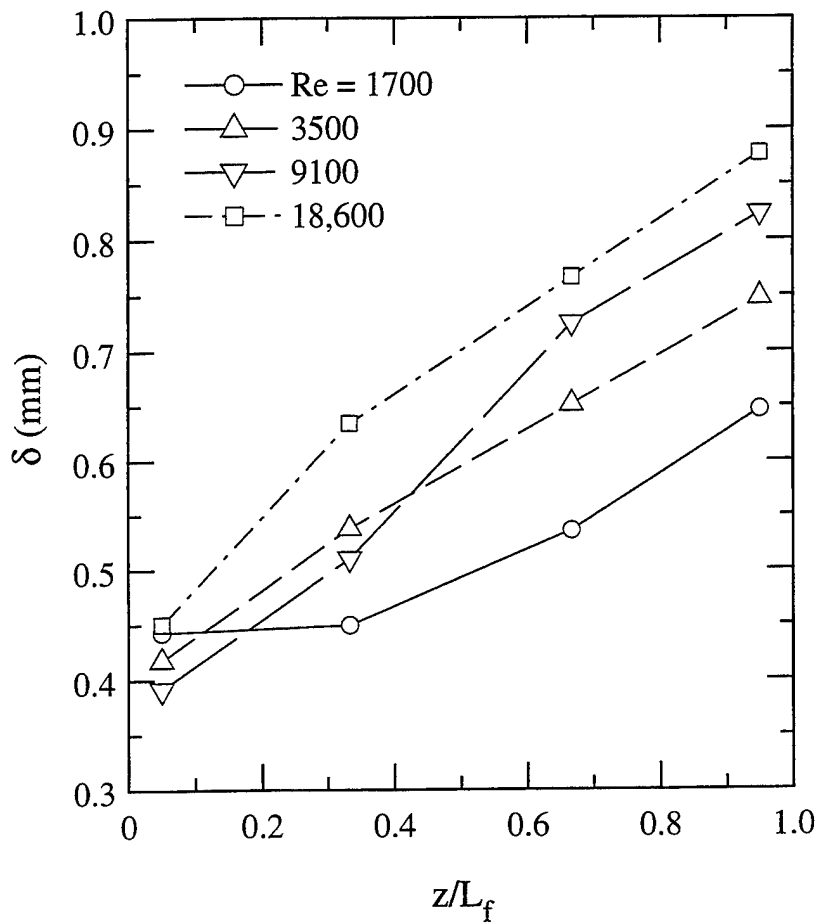


Figure 11. Average Flamefront Thickness ( $\delta$ ) as a Function of Axial Distance ( $z$ ), Relative to the Stoichiometric Flame Length ( $L_f$ ), for Four Flames with Jet Exit  $\text{Re} = 1700 - 18600$ .

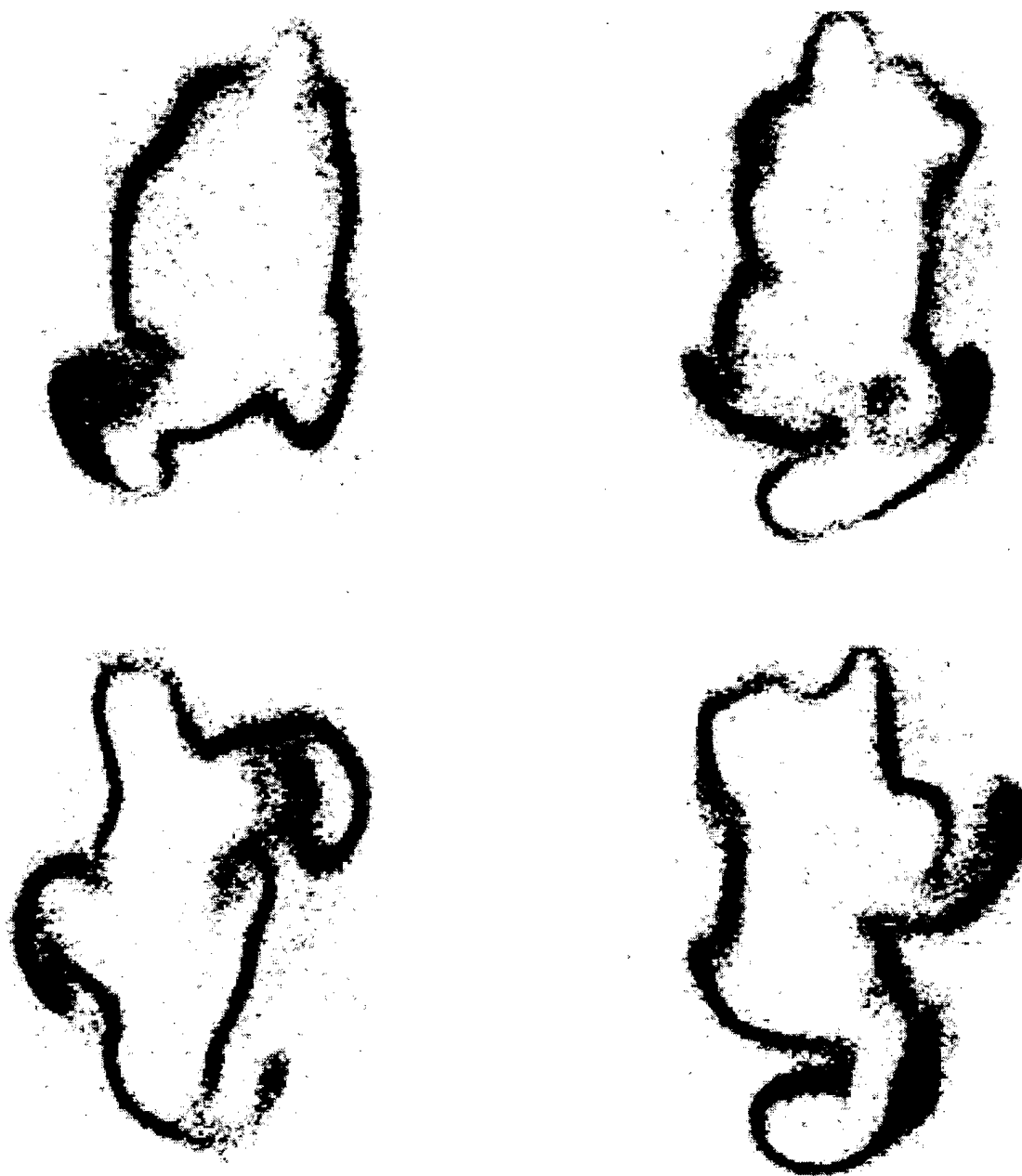


Figure 12. Four Instantaneous 45-deg Images [i.e., the Laser Sheet and Camera Were Oriented 45 deg Relative to the (Typical) Vertical Plane] of the Flamefront Location (i.e., CH LIF) in the  $Re = 18600$  Flame. Here, the downstream location is approximately one-third the stoichiometric flame length, and the field of view of each image is  $\sim 30 \text{ mm} \times 45 \text{ mm}$ .

Of course, the filters used with the PLIF system are critical to the success of this effort to integrate CH PLIF and PIV. In particular, Carter and Donbar found that the KV-418 (one piece) and BG-1 (one 3-mm piece) Schott colored-glass filters provided excellent rejection of particle scattering at  $\lambda = 390$  and 616 nm (note that the 532-nm PIV beam is present in the probe volume at a later time, after the gate for the CH PLIF measurement) and good transmission ( $\sim 65\%$ ) of the 430-nm fluorescence (see Fig. 8). Furthermore, they made additional improvements to the PLIF setup by purchasing and implementing a Princeton Instruments PG-200 Pulser System and a Stanford Research Systems DG535 Delay Generator. The pulser system allows the ICCD camera to be gated for times as short as 25 ns (whereas the old system allowed only a 200-ns minimum gate duration), further reducing the influence of flame emission--which can be quite strong with the addition of particles to the flame--on the CH PLIF images. The SRS delay generator made it easier to set the timing of the laser pulses for the two lasers used in the PIV experiment.

Carter and Donbar experimented with a variety of PIV arrangements to obtain optimum results from flame measurements. Their original setup included the use of a standard 35-mm camera for recording the PIV images. Although film is superior to some digital recording media (e.g., a Kodak large-format color CCD system) in terms of resolution and dynamic range, the turn-around time limits the usefulness of the film for experimentation purposes. Multiple trials with film produced only modest results with respect to the quality of the derived velocity field; furthermore, it was recognized that accurate indexing of the film and the ICCD images was more difficult (e.g., a marker could not be placed in the field to match the respective fields of view of the two cameras). Thus, they replaced the 35-mm camera with an available color CCD camera (2k x 3k pixel format). With this system, they were able to improve greatly the reliability of the seeding process (because with the digital camera, the feedback is almost instantaneous) and, thereby, the quality of the velocity images.

These investigators experimented with a variety of seeding media. Although hollow  $\text{Al}_2\text{O}_3$  microspheres yielded excellent results across the flamefront, the large size of this seed material resulted in interference

with the CH PLIF (and also appeared to alter the flame length).  $ZrO_2$  was also used since its melting temperature is significantly higher than that of  $Al_2O_3$ . Velocity images with this material were comparable to those with  $Al_2O_3$ ; however,  $Al_2O_3$  is more readily available (commercially) since it is frequently used as an abrasive (cutting) material. Thus, they chose 0.5- $\mu m$   $Al_2O_3$  seed particles, which can be easily seeded into the jet and coflow.

The original plan was to use the 390-nm beam (used for CH excitation) and a 532-nm beam from a second Nd:YAG laser for the PIV beams. This approach was satisfactory when the 35-mm camera was used for the PIV measurements (although a bleed of the 390-nm light into the green layer of the film was significant) but was not acceptable with the color CCD camera (since the CCD was not sufficiently sensitive to the 390-nm radiation). Thus, the optical setup was changed to permit the use of the residual 616-nm laser light from the dye laser (the light remaining after the mixing process that generates the 390-nm radiation). One additional advantage of this arrangement is that it allows the energies of the beams and the beam widths to be adjusted independently to achieve optimum results, not only for PIV but also for CH PLIF. The width of the CH beam was maintained at  $\sim 250 \mu m$ ; the width of the two PIV beams was adjusted to be  $\sim 600 - 800 \mu m$  at the probe volume, which corresponds to the attainable PIV resolution. The field of view for both camera systems is  $\sim 22$  mm (high) x 35 mm (wide).

A sample PIV-derived velocity image along with the overlaid CH PLIF image is shown in Fig. 13; here, the field of view of this subsection of the complete imaged region is 9.4 mm (high) x 17.2 mm (wide). This composite image was recorded near the flame tip in the flame having a jet exit  $Re$  of 18600. For convenience of visualizing the local flow structures (i.e., the vortices), 75% of the mean, centerline velocity has been subtracted from all vectors. This figure clearly shows the interaction of an air-side vortex and the flame surface. The flame surface has been pulled several millimeters into the  $O_2$  coflow; and on the inside of the portion of the stretched flame vortex, the flame appears to have been extinguished. However, this is apparently not the case (although, indeed, the CH signals are very weak here), as can be more easily seen in the original 14-bit PLIF image. Note that in this image, the flame surface is thin everywhere.

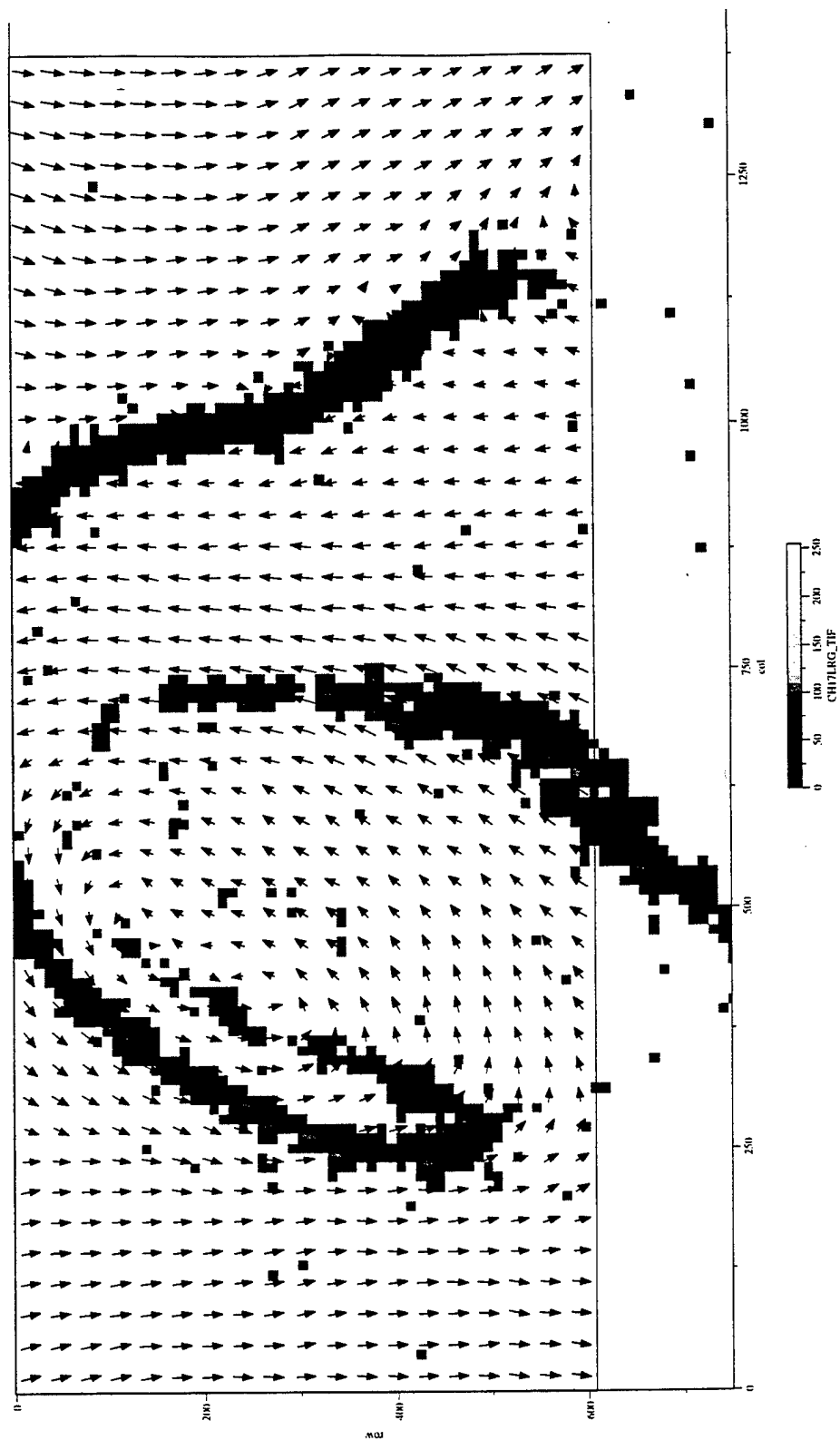


Figure 13. Instantaneous Overlaid Images of the Flamefront Location (i.e., CH LIF) and Velocity Field (via PIV) in the  $Re = 18600$  Flame; the Downstream Location is the Time-Averaged Stoichiometric Flame Length, and the Field of View is 23 mm (Vertical)  $\times$  35 mm (Horizontal). Here, three-fourths of the centerline velocity has been subtracted from all vectors to reveal the local structure.

## 2.7 Development of FRS Thermometry

With FRS techniques, molecular iodine ( $I_2$ )--within a Pyrex cell, placed before the detector--is used as an optical filter or spectrometer to measure the Doppler broadening or Doppler shift of the Rayleigh scattering. If the Doppler broadening is known, one can deduce the gas temperature; by knowing the Doppler shift, one can determine the flow velocity. Of course, these techniques can be implemented in a 2-D region of space. The principal advantage of this technique over standard Rayleigh-scattering thermometry is that measurements can be made in particle-laden flows and near surfaces. Thus, this method is more suitable for practical combustion environments than standard Rayleigh scattering. As noted above, the temperature is deduced from the Doppler broadening of the Rayleigh scattering. At sufficiently low pressures and in the absence of a filter, the scattered irradiance is Doppler broadened because of the Maxwell-Boltzmann velocity distribution of species within the gas:

$$I_s(\nu) \propto \exp\left(\frac{(\nu - \nu_{\text{shift}})^2}{\Delta\nu_D}\right)^2 \quad (2)$$

with

$$\Delta\nu_D = 1.7206 \times 10^{-6} \left(\frac{T}{M}\right) \sin \frac{\theta}{2} \quad (3)$$

where  $T$  is the gas temperature (K) and  $M$  is the atomic/molecular mass (a.m.u). At higher pressures, however, the scattering spectrum is dependent on gas number density through the Brillouin effect (described below).<sup>12,13</sup>

The fraction of Rayleigh scattering that is transmitted is dependent on the Doppler width which, in turn, is dependent on the temperature and the species molecular weight. For this investigation, Drs. Carter and Elliott (Rutgers University) employed laminar  $H_2$ -air and  $CH_4$ -air flames with different burner geometries. First, they compared the derived temperature to the value calculated from the theoretical model. This model includes the effect of Brillouin scattering; but, for simplification purposes, they assumed that  $N_2$  was the only scattering component. This is a reason-

able approximation for premixed flames and for the burnt-gas region of nonpremixed flames.

Two papers describing the use and efficacy of FRS thermometry have been submitted and accepted for presentation and publication. The first paper is entitled, "The Measurement of Two-Dimensional Temperature Field Using Filtered Rayleigh Scattering," by G. S. Elliott, N. Glumac (also of Rutgers University), C. D. Carter, and A. S. Nejad (WL) and will be presented at the Laser Anemometry and Experimental and Numerical Flow Visualization Symposium to be held during the ASME Fluids Engineering Division Summer Meeting, 22-26 June 1997, Vancouver, B.C. The second paper is entitled, "Two-Dimensional Temperature Field Measurements Using a Molecular Filter Based Technique," by G. S. Elliott, N. Glumac, C. D. Carter, and A. S. Nejad and has been accepted for publication in *Combustion Science and Technology*. These papers are included in the Appendix.

## 2.8 Development and Application of FRS Velocimetry

In principle, the FRS technique allows one to record the three components of the velocity vector in the plane of the laser sheet. Because the method relies on Rayleigh (or even Lorentz-Mie) scattering, the addition of seed material is not necessary; in fact, one can use naturally occurring ice fog or condensation as the scattering medium. Consequently, FRS is a potentially powerful laser-diagnostic technique for 2-D time-resolved velocity measurements in high-speed flows. Furthermore, under conditions where particles (of any sort) are absent from the flow, one can scan the probe-laser frequency in time and obtain 2-D time-averaged velocity, temperature, pressure, and density. With FRS, one takes advantage of the spectral coincidence of a tunable narrow-linewidth laser and the absorption lines of gas-phase molecules or atoms within a glass cell. This molecular or atomic filter acts as a high-resolution 2-D spectrometer, allowing one to measure the Doppler shift of the Rayleigh-scattered radiation in a field. One can then deduce the velocity  $\bar{u}$  from the Doppler frequency shift  $v_{shift}$  (see Fig. 14):

$$v_{shift} = \frac{1}{2\pi} (\bar{k}_s - \bar{k}_i) \cdot \bar{u} = v_i \frac{2|\bar{u}|}{c} \sin \frac{\theta}{2} \sin \left( \alpha - \frac{\theta}{2} \right) \quad (4)$$

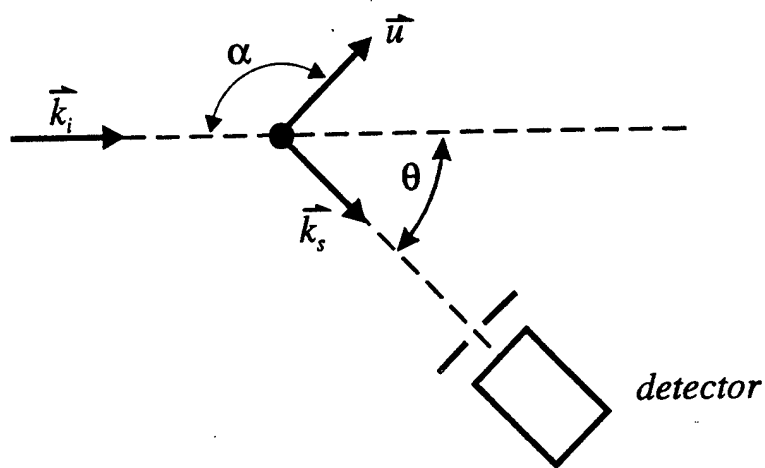


Figure 14. Schematic of the Interaction Between the Incident Radiation and a Particle with Velocity Vector  $\vec{u}$  in the Plane of Observation (Plane of the Page).

where  $\nu_i$  is the frequency of the incident radiation,  $\bar{k}_i$  and  $\bar{k}_s$  are the incident and scattering wave vectors, respectively, and the angles  $\alpha$  and  $\theta$  are defined in Fig. 14. With three detectors (located at different angles, with at least one being out of plane), one can then measure the total velocity vector at each point in the region illuminated by the laser beam. Thus, 2-D images of the velocity field can be obtained by spreading the laser beam into a sheet. Of course, each image must be divided by an unfiltered image to remove the dependence on the local number density of scatterers. Furthermore, one must carefully match the observation fields of the *velocity and number-density cameras*.

The FRS method is, thus, similar to PIV in that one can record 2-D velocity information; however, a significant advantage of the FRS method--particularly for high-speed flows--is that seeding of the flow is not required. Furthermore, with FRS, the spatial resolution is typically limited by either the thickness of the laser sheet or the modulation transfer function (MTF) of the camera/lens system; thus, one can more easily resolve features such as shock boundaries. Finally, with the FRS velocimetry technique, one can measure all three velocity components within the plane of the laser sheet (although this requires three camera systems); with PIV, however, one is limited to measurement of the velocity component in the plane of the laser sheet, and out-of-plane motion decreases the number of particle pairs.

Because the duration of a laser pulse from a Q-switched Nd:YAG laser is  $\sim 10$  ns, the individual scattering images show the flowfield at an instant in time. When the laser is tuned to the edge of an  $I_2$  absorption transition, the scattered light which has not been Doppler shifted is absorbed by the iodine filter that has been placed in front of the detector (see Fig. 15 for a sample  $I_2$  absorption spectrum). However, light that has been frequency shifted is not absorbed or is only partially absorbed by the iodine transitions. One then relates transmission of the scattering through the filter to the local Doppler shift.

The FRS method is most easily applied to high-speed flows since these flows provide sufficient Doppler frequency shift. Because of this, Elliott et al.<sup>14</sup> have estimated the lower limit of detection/resolution to be  $\sim 10$  m/s. Although one can employ molecular scattering for the velocime-

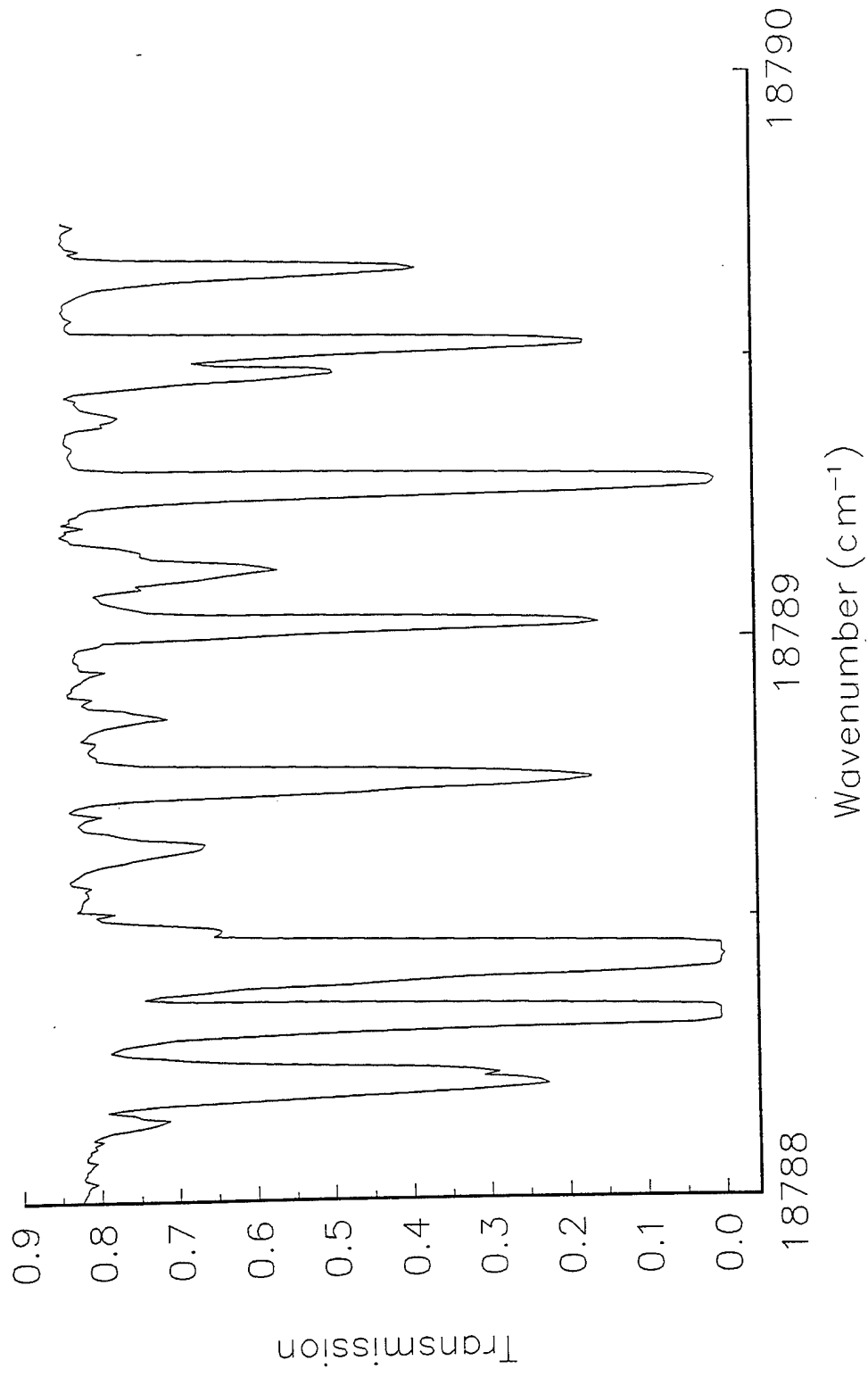


Figure 15. Iodine Absorption Spectrum Within the Frequency Tuning Range of the Nd:YAG (Second Harmonic) Laser [From Ref. 15].

try measurements, using small particles (sufficiently small to be within the Rayleigh scattering limit) is advantageous, not only from the standpoint of increased scattering (i.e., higher signal-to-noise ratios) but also because of the spectrally narrow distribution of scattering from particles. Fortunately, under many conditions in high-speed flows, one finds a significant number density (i.e., sufficiently large to minimize marker shot noise) of ice particles (or clusters) originating from the naturally occurring moisture in the air; this *ice fog* is, thus, used as the scattering medium. To discriminate against surface scattering--for example, within the boundary layer--one need only set the laser frequency such that the non-Doppler shifted scattering is strongly absorbed within the filter; the Doppler-shifted scattering, however, will be transmitted by the filter to the detector.

Prof. Elliott who participated in the Summer Faculty Research Program (now with Rutgers University) teamed with Dr. Carter and Drs. Glawe and Gruber (WL/POPT) in using FRS techniques in a variety of reacting subsonic and nonreacting supersonic flows; these experiments were performed at Wright Laboratory in the WL/POPT Supersonic Facility. Prior to this, Elliott et al.<sup>15</sup> had determined the tuning range ( $\nu = 18788.5 - 18791.0 \text{ cm}^{-1}$  or  $\lambda = 532.240 - 532.170 \text{ nm}$ ) and the optimum  $I_2$  transition within this range ( $\nu = 18789.3 \text{ cm}^{-1}$  or  $\lambda = 532.218 \text{ nm}$ ); this transition was judged to be the optimum one within the tuning range because of its strong line-center absorption and its relative isolation from neighboring  $I_2$  transitions. As a demonstration of FRS, Elliott et al.<sup>15</sup> measured time-resolved velocities in a Mach-2 air flow with transverse injection of  $N_2$ . Rather than rely on ice fog for the scattering medium, they injected silane ( $SiH_4$ ) into the settling chamber of the supersonic facility; the resulting  $SiO_2$  particles, which were sufficiently small to be within the Rayleigh limit, were used as the scattering medium. The laser sheet was positioned at various spanwise locations along the flowfield, from just upstream of the injector to several diameters downstream (Fig. 16). Two intensified CCD camera systems (Princeton Instruments) were employed to record 1) the filtered Doppler-shifted scattering, using the custom designed  $I_2$  cell, and 2) the unfiltered scattering, representing the total particle number density. A schematic of the optical setup is shown in Fig. 16. For these measurements,  $N_2$  is added (the amount depending on the expected range of velocities to be measured) to the  $I_2$  vapor within the Pyrex cell; the

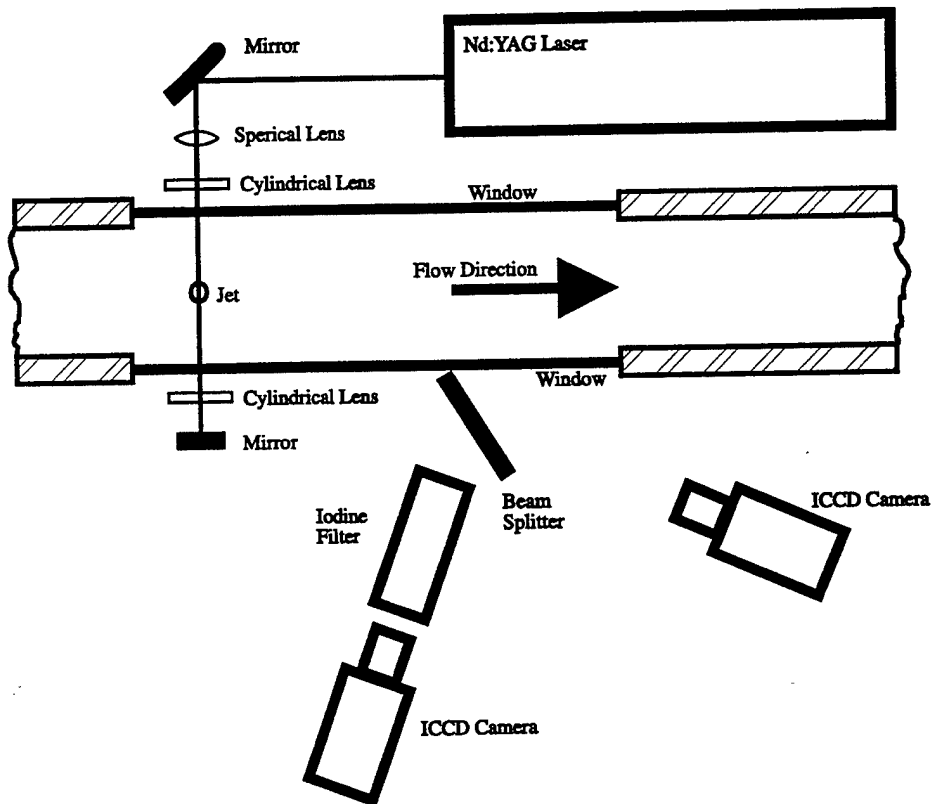


Figure 16. Schematic of the Optical Setup for FRS Velocimetry Measurements [From Ref. 15].

resulting collisions between  $I_2$  and  $N_2$  broaden the  $I_2$  absorption line. Two of the resulting gray-scale 2-D velocity maps (one showing spanwise and the other axial velocities) are presented in Fig. 17; these maps were recorded sequentially, rather than simultaneously, downstream of the transverse jet centerline. The axial velocities were recorded via a novel approach employing retro-reflecting optics to send the beam back along its path through the flow; in this way, the Doppler shift from the spanwise velocity component is largely canceled [see Eq. (4)]. Then, for recording spanwise velocities, the retro-reflecting mirror was simply removed.

The results of this study are being documented in a paper by G. S. Elliott, C. D. Carter, M. Gruber (WL), and A. S. Nejad which will be presented at the 33rd AIAA/ASME/SAE/ASEE Joint Propulsion Conference and Exhibit, 6-9 July 1997, Seattle, WA.

## **2.9 Application of Laser Diagnostics and Thin-Filament Pyrometry to the Study of an Unsteady Laminar $H_2$ - $N_2$ /Air Flame**

Dr. Carter collaborated with Drs. L. P. Goss, K.-Y. Hsu, and V. R. Katta (SRL) and with W. M. Roquemore (WL) in comparing experimental results and model predictions of a laminar, unsteady  $H_2$ - $N_2$ /air flame. Studies of simple, vertically oriented, nonpremixed jet flames have shown that when the coflowing velocity is low, buoyancy-induced periodic toroidal vortices form outside the flame surface. These vortices convect downstream and interact with the flame to produce stretched and compressed flamelets. Direct numerical simulations on nonpremixed unsteady flames suggest that preferential diffusion (i.e., nonunity Lewis number), acting in concert with flame curvature, influences the temperature along the flame surface. To test model predictions for an  $H_2$ -air flame, these investigators recorded in space and time, through phase-locked point measurements, 1) the temperature using Thin-Filament Pyrometry (TFP) and CARS and 2) the concentrations of OH and NO using LIF.

At 50 mm above the jet exit, both measurements and computations show some temporal structure that includes a small broadening and narrowing of the high-temperature and high- $X_{NO}$  ( $X$  denoting mole fraction) zones; accompanying this broadening is a modest increase in the NO concentration. At 85 mm above the jet, the compressed and stretched regions

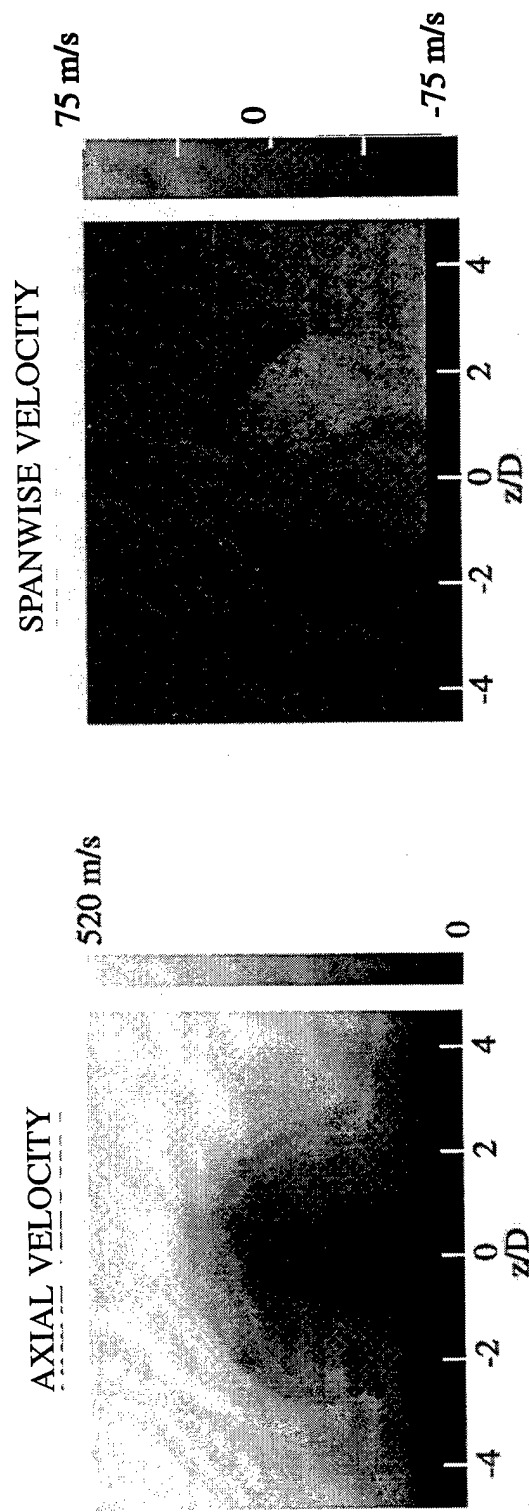


Figure 17. Axial and Spanwise 2-D Velocity Distributions of a Jet in a Mach-2 Cross Flow.

are clearly visible, as are the variations in  $X_{NO}$  and  $X_{OH}$ . Whereas the NO concentrations are at a maximum within the compressed region, the flame-front OH concentrations are at their minimum values. Finally, at 135 mm downstream, the bulge is fully developed. Both measurements and calculations show the  $X_{NO}$  within the bulge to be  $> 450$  ppm; with the stretched regions of the flame, the  $X_{NO}$  is greatly reduced. At each downstream location, the comparison between measurements and computations is good, especially for OH and NO concentrations. Although some discrepancies were present between the measurements and calculations--particularly in the peak temperatures and the inlet coflowing velocity necessary to reproduce the observed development of the structures--these measurements provide a positive test for predictions regarding the roles of flame curvature and nonunity Lewis number in the flame structure.

The results of this study were documented in two papers, both entitled, "The Structure of a Dynamic Nonpremixed H<sub>2</sub>-Air Flame." The first, co-authored by C. D. Carter, L. P. Goss, K. Y. Hsu, V. R. Katta, and D. D. Trump (all of SRL), was presented at the 1995 Joint Technical Meeting of the Western and Central States and Mexican National Sections of the Combustion Institute, 23-26 April 1995, San Antonio, TX. The second paper (WSS/CI 95F-222), co-authored by C. D. Carter, R. D. Gould, L. P. Goss, V. R. Katta, and K.-Y Hsu, was presented at the Meeting of the Western States Section of the Combustion Institute, 30-31 October 1995, Stanford, CA. These papers are included in the Appendix. A paper detailing this study is also in preparation for submission to *Combustion and Flame*.

### 3.0 REFERENCES

1. Beer, J. M., and Chigier, N. A., *Combustion Aerodynamics* (Krieger, Malabar, Florida, 1972).
2. Attal-Tretout, B., Bouchardy, P., Magre, P., Pealat, M., and Taran, J.-P. "CARS in Combustion: Prospects and Problems," *Appl. Phys. B* **51**, 1990, pp. 17-24.
3. Snelling, D. R., Sawchuk, R. A., Smallwood, G. J., "An Improved CARS Spectrometer for Single-Shot Measurements in Turbulent Combustion," *Rev. Sci. Instrum.* **63**, 1992, pp. 5556-5564.
4. Csorba, I. P., *Image Tubes* (Howard W. Sams and Co., Indianapolis, IN, 1985).
5. Snelling, D. R., Smallwood, G. J., Parameswaran, T., "Effect of Detector Nonlinearity and Image Persistence on CARS Derived Temperatures," *Appl. Opt.* **28**, 1989, pp. 3233-3241.
6. Bethune, D. S., "Dye Cell Design for High-Power Low-Divergence Excimer-Pumped Dye Lasers," *Appl. Opt.* **20**, 1981, pp. 1897-1899.
7. Eckbreth, A. C., "BOXCARS: Crossed-Beam Phase-Matched CARS Generation in Nitric Oxide Formation in Turbulent Hydrogen Jet Flames," *Combust. Flame* **97**, 1994, 261-280.
9. Snelling, D. R., Smallwood, G. J., Sawchuk, R. A., and Parameswaran, T., "Precision of Multiplex CARS Temperatures Using Both Single-Mode and Multimode Pump Lasers," *Appl. Opt.* **26**, 1987, pp. 99-110.
10. Snelling, D. R., Sawchuk, R. A., and Parameswaran, T., "Noise in Single-Shot Broadband Coherent Anti-Stokes Raman Spectroscopy That Employs a Modeless Dye Laser," *Appl. Opt.* **33**, 1994, pp. 8295-8301.
11. Carter, C., and Barlow, R., "Simultaneous Measurements of NO, OH, and the Major Species in Turbulent Flames," *Opt. Lett.* **19**, 1994, pp. 299-301.
12. Yip, S., and Nelkin, M., "Application of a Kinetic Model to Time-Dependent Density Correlations in Fluids," *Phys. Rev.* **135**, 1964, pp. A1241-A1247.

13. Fabelinskii, I. L., *Molecular Scattering of Light* (Plenum Press, New York, 1968).
14. Elliott, G. S., Samimy, M., and Arnette, S. A., "A Molecular Filter Based Velocimetry Technique for High Speed Flows." To appear in *Experiments in Fluids*.
15. Elliott, G. S., "Laser Based Diagnostic Techniques for Combustion and Compressible Flows," Final Report for Summer Faculty Research Program, Wright-Patterson Air Force Base, OH, 1996.

## **4.0 APPENDIX: PRESENTATIONS AND PUBLICATIONS**

# **HANDBOOK OF FLUID DYNAMICS AND FLUID MACHINERY**

---

**VOLUME II: EXPERIMENTAL AND COMPUTATIONAL  
FLUID DYNAMICS**

**Edited by**

**Joseph A. Schetz and Allen E. Fuhs**



A WILEY-INTERSCIENCE PUBLICATION

**JOHN WILEY & SONS, INC.**

New York • Chichester • Brisbane • Toronto • Singapore

the *mean or first moment* vorticity distributions are given by Westerweel (1992) in a turbulent flow and Robinson and Rockwell (1993) and Lourenco and Krothapalli (1994) in laminar flows. Additional studies which investigate the spatial character of the instantaneous vorticity field can be found in Reuss *et al.* (1989), Willert and Gharib (1991), Liu *et al.* (1991), Rockwell (1992), and Towfighi and Rockwell (1994), among others, however statistics regarding the vorticity field are either not given or not compared with other methods in these additional studies.

Urushihara *et al.* (1993) employed very high resolution PIV to study the logarithmic layer of fully developed turbulent pipe flow at moderate Reynolds numbers ( $Re_D \approx 50,000$ ). The high resolution was achieved by imaging the flow field onto large format photographic film with a magnification of  $6\times$ . With this, they were able to obtain a measurement volume significantly smaller than that reported with thermal anemometry probes. They compare their r.m.s. azimuthal vorticity results with two turbulent boundary layer studies—Direct Numerical Simulation (DNS) of a low Reynolds number turbulent boundary at  $Re_\theta = 670$  and a moderate Reynolds number turbulent boundary layer at  $Re_\theta \approx 2900$  [Balint *et al.* (1991)] utilizing thermal anemometry. The PIV results are larger in magnitude than both the DNS and the thermal anemometry results for all  $y$  (distance from the wall) locations investigated except for locations close to the wall where the agreement with DNS is fairly good.

Aside from the fact that all three studies employed wall-bounded turbulent shear flows at different Reynolds numbers, the authors point out that the high rms values for the PIV investigation could result from the amplification of noise in the velocity field due to the differentiation inherent in Eq. (15.214).

Comparisons of vorticity measurements from PIV data with those resulting from a DNS of turbulent pipe flow are given by Eggels *et al.* (1993). Excellent agreement is obtained when comparing the r.m.s. value of the fluctuating azimuthal vorticity throughout most of the pipe, except near the wall. This is most probably due to the relatively large velocity gradients that exist near the wall which, result in an increased uncertainty in the velocity measurement.

Westerweel (1993) investigated turbulent pipe flow using PIV and presents the mean azimuthal vorticity profile compared with Reichardt's formula for fully developed turbulent pipe flow. The measurements and the Reichardt formula show good agreement for  $y^+ > 44$  with a maximum deviation of approximately 15% at  $y^+ \approx 66$ . However, for smaller  $y^+$  values the data trend is qualitatively, incorrect since the mean vorticity magnitude is decreasing with decreasing  $y^+$  values.

Lourenco and Krothapalli (1994) calculate the spanwise vorticity distribution in a laminar wall jet experiment and compare the results with those from a numerical simulation of the same flow. The former exhibit variations of order 10% (nondimensional values) with respect to the mean.

## 15.12 LASER-BASED RAYLEIGH AND MIE SCATTERING METHODS

Campbell D. Carter

### 15.12.1 Introduction

Laser-based measurements of gas properties such as temperature, velocity, and species concentration have given researchers new and valuable insight into the chem-

istry and physics of reacting and nonreacting flows. Laser-based techniques have significant advantages over physical probes (e.g., hot wires and thermocouples), because they provide measurements that are spatially and temporally resolved (resolutions of  $<0.1 \text{ mm}^3$  and  $<10 \text{ ns}$ ) and nonintrusive. In addition, instantaneous two- or even three-dimensional measurements are feasible with these methods. Thus, one can obtain instantaneous spatial and temporal correlations. In this section, we focus on Rayleigh and Mie scattering techniques which, because of the modest requirements for equipment (principally, a cw or pulsed laser), are among the simplest of the laser-based methods.

The purpose of this section is to acquaint the reader with the Rayleigh and Mie scattering techniques as applied to the investigation of gaseous flows. First, we review the fundamental aspects of the scattering techniques, presenting the descriptive equations. Second, we describe some (but certainly not all) of the applications that have appeared in the literature. These applications have been divided into those involving the following: 1) species-concentration or mixture-fraction measurements when one gas mixes with another, 2) temperature and density measurements, particularly in reacting flows, and 3) velocity measurements in subsonic and supersonic flows.

### 15.12.2 Background

Both Rayleigh and Mie scattering (sometimes referred to as Lorentz-Mie scattering) processes are *elastic* in nature, i.e., the scattered radiation experiences no change in frequency or energy in the scattering process. Throughout, we use the term *Mie scattering* to refer to scattering from particles too large to be covered by Rayleigh theory, which is appropriate for particles much smaller than the wavelength of the incident radiation. Strictly speaking, however, this terminology is misleading, since Mie theory describes scattering from a spherical, homogeneous particle of *arbitrary* size when illuminated by plane waves [van de Hulst (1957) and Kerker (1969)]. The problem of scattering from a spherical particle is, in fact, one of the few cases where an exact analytical solution of the Maxwell equations has been found; in general, one must use approximate or numerical methods to describe the scattering process. Since generally the particles in question are not spherical (agglomerated soot, for example), an *equivalent sphere* often must be assumed if the scattering is to be quantified [Jones (1979)].

Another scattering technique, not treated in this section but reviewed elsewhere [Long (1977), Lederman (1977), and Eckbreth (1988)], is spontaneous Raman scattering. As with Rayleigh scattering, the scattered radiation is dipole-like. However, the scattering process is inelastic; that is, the scattered photons are shifted in energy by the separation of 1) the vibrational states with vibrational Raman scattering, 2) the rotational states with rotational Raman scattering, and 3) the electronic states with electronic Raman scattering. Since each molecule has a distinct energy spacing, molecular species can be identified by detecting the scattered radiation with a spectrometer or with optical filters (i.e., colored glass or interference filters). A disadvantage of the Raman technique, however, is that the scattering cross sections are small—about three orders of magnitude less than those for Rayleigh scattering [Eckbreth (1988)].

**Rayleigh Scattering.** Rayleigh theory is appropriate for a spherical particle when the following condition is satisfied for the particle size

$$\alpha \equiv \frac{2\pi a}{\lambda_i} \ll 1 \quad (15.215)$$

where  $a$  is the particle radius,  $\lambda_i$  is the wavelength of the incident radiation, and  $\alpha$  is the dimensionless size parameter. Equation (15.215) indicates that the particle should be sufficiently small that the incident electric field is uniform over the extent of the particle. With the Rayleigh process, the scattering may be thought of as emission from radiating dipoles induced by the incident electric field [Born and Wolf (1980), Fabelinskii (1968), and van de Hulst (1957)]. Consequently, the scattered intensity depends on the polarization of the incident beam and the point of observation. In general, the scattered irradiance  $I_s$  ( $\text{W}/\text{cm}^2$ ) from  $N_p$  identical independent particles in a gas can be written as

$$I_s = \frac{I_i}{r^2} N_p \sigma_p \quad (15.216)$$

where  $I_i$  ( $\text{W}/\text{cm}^2$ ) is the incident irradiance and  $r$  is the distance to the point of observation ( $r \gg$  the dimensions of volume  $V$  containing the  $N_p$  particles). The particle scattering *cross section*,  $\sigma_p$  ( $\text{cm}^2$ ), is dependent on the characteristics of the particles and on the angle between the incident-beam polarization and the scattered radiation.

Consider a collimated beam traveling in the  $y$  direction, linearly polarized in the  $z$  (vertical) direction, and impinging on a spherical, homogeneous dielectric particle. The cross section describing the vertically polarized scattering in the  $x$ - $y$  (horizontal) plane is given by [Kerker (1969)]

$$\sigma_{vp} = \frac{\alpha^6 \lambda_i^2}{4\pi^2} \left( \frac{n_p^2 - 1}{n_p^2 + 2} \right)^2 = \frac{9\pi^2 V_p^2}{\lambda_i^4} \left( \frac{n_p^2 - 1}{n_p^2 + 2} \right)^2 \quad (15.217)$$

where  $n_p$  is the index of refraction of the particle and  $V_p$  is the volume of the individual particles. For horizontally polarized incident radiation, the scattering is in the horizontal plane, but the magnitude depends on the observation angle  $\theta$  (see Fig. 15.91),

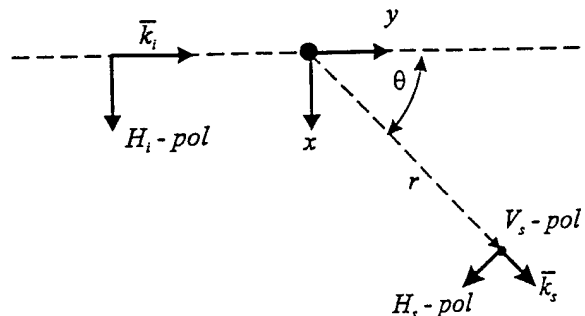


**FIGURE 15.91** Plan-view schematic of scattering from a particle for horizontally polarized incident radiation. H-pol and V-pol denote horizontal and vertical polarization, respectively. Vertical polarization is normal to the plane of the page (the  $z$ -direction).

$$\sigma_{Hp} = \frac{\alpha^6 \lambda_i^2}{4\pi^2} \left( \frac{n_p^2 - 1}{n_p^2 + 2} \right)^2 \cos^2 \theta \quad (15.218)$$

These equations can be generalized for arbitrary polarization by considering the incident beam to be linearly polarized in the  $x$ - $z$  plane, with components  $I_{i,vert} = I_{i,z}$  and  $I_{i,horz} = I_{i,x}$ . If the beam were unpolarized, or if the polarization were at  $45^\circ$  with respect to the  $x$ -axis, then  $I_{i,horz} = I_{i,vert} = I_i/2$ , and the scattering would be proportional to  $(I_i/2)(\cos^2 \theta + 1)$ . Note that these equations are appropriate for a non-absorbing particle. When the particle is not *highly* absorptive or reflective [Kerker (1969)],  $n_p$  can be replaced by the complex refractive index  $m = n_p - ik$ , where the imaginary part describes absorption by the particle.

To determine the scattered power,  $P_s(W)$ , within some solid angle,  $\Delta\Omega$ , (defined by the scattering collection optics), one must integrate over the range of detected angles (see Fig. 15.92),

$$P_s = \int_{\Delta\Omega} I_s r^2 d\Omega \quad (15.219)$$

The collection optics and beam diameter define a *probe* volume  $V = lA_c$ , where  $l$  is the probe length (defined by the detector aperture) and  $A_c$  is the cross-sectional area defined by the beam (Fig. 15.92). The scattered power impinging on a detector is

$$P_s = \epsilon \int_{\Delta\Omega} I_i N V \sigma d\Omega = \epsilon \int_{\Delta\Omega} P_i N l \sigma d\Omega \quad (15.220)$$

where  $N$  ( $\text{cm}^{-3}$ ) is the number density of particles,  $P_i(W)$  is the incident power, and  $\epsilon$  is the efficiency of the collection optics. In the event that the variation in  $\theta$  is small over the collected solid angle, one can use the approximation  $P_s \approx \epsilon I_i N V \sigma \Delta\Omega$ .

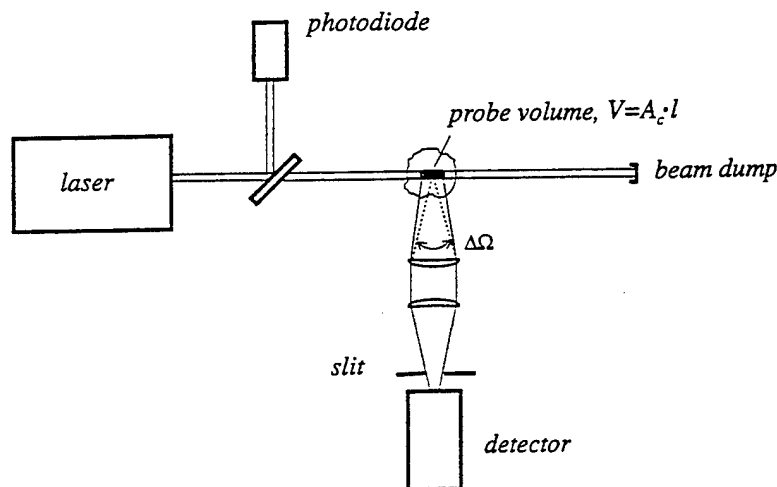


FIGURE 15.92 Plan-view schematic of a point-wise scattering measurement. The photodiode is used to record the beam energy or power.

As written, Eqs. (15.219) and (15.220) are valid whether the medium is considered to be a gas or a group of particles (or even a single particle); however, for a gas, the cross section is normally written as a function of  $n$ , the gas index of refraction. One can relate the refractive index of the gas to that for the individual particles/molecules using the Lorenz-Lorentz formula,

$$\left(\frac{n_p^2 - 1}{n_p^2 + 2}\right) N_p V_p = \left(\frac{n^2 - 1}{n^2 + 2}\right) V \cong \frac{2}{3} (n - 1) V \quad (15.221)$$

where  $V$  is the volume occupied by  $N_p$  particles, the gas number density is  $N = N_p/V$ , and the approximation is valid for  $n \cong 1$  (appropriate for a gas). In addition, this equation leads to the important conclusion that  $(n - 1)/N$  is independent of temperature and pressure.

Although scattering from the ideal spherical, homogeneous particle (and from atoms) is completely polarized (e.g., scattering from a vertically polarized beam will be vertically polarized), scattering from molecules, in general, is not. This *depolarization*,  $\rho_v$ , results from the anisotropy of the scatterer's polarizability and the random orientation of the molecules in a gas; typically  $\rho_v$  is small for gases (Table 15.10). For vertically polarized incident radiation, the vertically polarized scattering cross section for a gas is

$$\sigma_{VV} = \sigma_o = \left[ \frac{4\pi^2 (n_o - 1)^2}{N_o^2 \lambda_i^4} \cdot \left( \frac{3}{3 - 4\rho_v} \right) \right] \quad (15.222)$$

Here  $N_o$  and  $n_o$  are the respective number density and index of refraction at STP ( $N_o = 2.687 \times 10^{19} \text{ cm}^{-3}$  for an ideal gas at  $T = 273 \text{ K}$  and  $P = 760 \text{ Torr}$ ). This equation describes the scattering cross section for a wide range of temperatures and pressures, though not including the neighborhood of the critical point [Fabelinskii (1968)]; implicit in this derivation is that scattered radiation is collected from the complete Doppler-Brillouin structure in addition to any rotational Raman structure [Rowell *et al.* (1971)]. The transverse scattering cross sections resulting from the depolarization  $\sigma_{VH}$  (referring to vertically polarized incident radiation and horizontally polarized scattered radiation) and  $\sigma_{HV}$  (referring to horizontally polarized incident radiation and vertically polarized scattered radiation) have the same magnitude,

$$\sigma_{VH} = \sigma_{HV} = \rho_v \sigma_o \quad (15.223)$$

Of course, the cross section for horizontally polarized incident and scattered radiation is a function of the angle  $\theta$

$$\sigma_{HH} = [(1 - \rho_v) \cos^2 \theta + \rho_v] \sigma_o \quad (15.224)$$

When one is using a vertically polarized laser beam and detecting both polarization states, the total scattering cross section is simply  $\sigma_o(1 + \rho_v)$ , independent of angle in the horizontal plane. Likewise, for a horizontally polarized incident beam, the total scattering cross section (i.e., collecting both polarization states) is  $\sigma_{HH} + \sigma_{HV}$ . Note that the scattering cross section is often described as a *differential* cross section

TABLE 15.10 Refractivity Data

[Values are for STP conditions ( $T = 273$  K, and  $P = 760$  Torr), and the cross sections are given for  $\lambda_i = 488$  nm. The indices of refraction, except for those for Freon 12 and 22, are derived from the data of Gardiner *et al.* (1981), and the cross sections were calculated using Eq. (15.222) and assuming ideal gas behavior (i.e.,  $N_o = 2.687 \times 10^{19}$  cm $^{-3}$ ). The cross sections for Freon 12 and 22 are derived from the data of Shardanand and Rao (1977), and the corresponding  $n_o$  were derived from Eq. (15.222), assuming ideal gas behavior and  $\rho_v = 0$ .]

Species	$n_o - 1$	$100 \cdot \rho_v$	$\sigma_o$ ( $10^{-28}$ cm $^2$ )
Ar	0.000284	0	7.75
CH $_4$	0.000446	0	19.2
CO	0.000339	0.52 <sup>a</sup>	11.1
CO $_2$	0.000450	4.12 <sup>a</sup>	20.6
C $_2$ H $_4$	0.000727	1.27 <sup>a</sup>	51.9
He	0.000035	0	0.118
H $_2$	0.000140	0.95 <sup>b</sup>	1.92
H $_2$ O	0.000255	1.0 <sup>c</sup>	6.33
NO	0.000297	1.54 <sup>d</sup>	8.71
N $_2$	0.000301	1.08 <sup>b</sup>	8.87
O $_2$	0.000273	2.91 <sup>b</sup>	7.50
CHClF $_2$ (Freon 22)	0.000990 <sup>e</sup>	—	94.5
CCl $_2$ F $_2$ (Freon 12)	0.00127 <sup>e</sup>	—	155

<sup>a</sup>Bogaard *et al.* (1978).

<sup>b</sup>Rowell *et al.* (1971).

<sup>c</sup>D'Alessio (1981).

<sup>d</sup> $\lambda_i = 632.8$  nm; Bridge and Buckingham (1966).

<sup>e</sup>Shardanand and Rao (1977).

and typically denoted by  $d\sigma/d\Omega$  (cm $^{-2}$ /steradian); this differential cross section and the one described above have the same magnitude.

For a mixture of gases,  $\sigma_o$  is simply the sum of the mole-fraction-weighted cross sections

$$\sigma_{o,\text{mix}} = \sum_i X_i \sigma_{o,i} \quad (15.225)$$

where  $X_i$  and  $\sigma_{o,i}$  are the mole fraction and cross section of species  $i$ , respectively. The most comprehensive tabulations of the refractive indices of gases are those given by Landolt-Börnstein (1962). Based, in part, on these data, Gardiner *et al.* (1981) compiled refractivity data for a large number of species. In general, the index of refraction and depolarization depend on wavelength [Alms *et al.* (1975)], although this dependence is generally small throughout the visible spectrum [Landolt-Börnstein (1962) and Shardanand and Rao (1977)]. Nonetheless, for each species considered, Gardiner and co-workers have fit the wavelength dependence of the refractive index with the dispersion relation,  $n_o - 1 = a/(b - \lambda_i^{-2})$ . We have used the

data of Gardiner *et al.* (1981) along with published depolarization ratios to calculate the scattering cross sections for  $\lambda_i = 488$  nm shown in Table 15.10.

**Mie Scattering.** In this subsection, we will treat only the basic aspects of Mie scattering theory. For a more in-depth description of the Mie scattering process, the reader is referred to the review article and the chapter by Jones (1979), (1993) and books by Kerker (1969), Bohren and Hüffman (1983), van de Hulst (1957), and Born and Wolf (1980). Whereas we stated above that Rayleigh theory is valid when the particle is much smaller than the incident wavelength, we now modify that criterion by adding that the particle should *also* be much smaller than the wavelength *within* the particle [van de Hulst (1957)], i.e.,  $\alpha|m| \ll 1$ . A more specific guideline was given by Kerker *et al.* (1978) who found that for  $\alpha|m| < 0.2$ , the agreement between the scattering behavior and that predicted by Rayleigh theory was generally within  $\sim 1\%$ . Furthermore, Jones (1979) suggests that the error incurred from using Rayleigh theory to predict the total scattering and/or absorption is within  $\sim 10\%$  for  $\alpha|m| < 0.6$ . As the particle size increases, the departure from the angular dependence observed in Rayleigh scattering increases. The ratio of forward to backward scattering increases, and the angular mode structure becomes increasingly complex; that is, lobed structures (the number of which is on the order of  $\alpha|m|$ ) appear in the polar diagram [Jones (1979)]. In addition, the scattering intensity does not depend on the sixth power of the particle diameter (as is true for a Rayleigh particle). With nonabsorbing dielectric spheres, for example, the scattering efficiency,  $Q_{sca} \equiv \sigma_p / \pi a^2$ , increases monotonically with  $a$  to values of  $Q_{sca} \geq 3$  (depending on the exact value of  $m$ ) until  $\alpha(m-1) \approx 2$  [Kerker (1969)]. With increasing  $\alpha(m-1)$ , the scattering efficiency undergoes a damped oscillation about  $Q_{sca} = 2$  [Kerker (1969)]. Thus, when Mie scattering is used as a diagnostic tool, the collected scattering may depend on 1) the exact angle of detection, 2) the shapes and size distribution of the particles, and 3) the homogeneity of the particles and their surface characteristics. In general, one must use caution in relating the collected scattering to quantitative parameters (mixture fraction, temperature, etc.).

Ideally, scattering by a group of particles in a gas is an extension of scattering by a single particle. This criterion is satisfied under the following conditions [Jones (1979)]: 1) the particles are separated by greater than three particle radii and, thus, no electrical interaction takes place between them [Kerker (1969)]; 2) the *scattered* radiation does not interact with the particles; and 3) the number of particles is sufficiently large that no optical interference occurs between radiation scattered by different particles. The first condition leads to a maximum particle number density; with  $1\text{-}\mu\text{m}$  particles, the maximum seeding density would, therefore, be on the order of  $10^{10}$  particles/cm<sup>3</sup>. The second condition, however, places a greater restriction on the maximum desirable seeding density. Consider the transmission through a nonuniform medium, which is described by a Beer's Law relation,

$$I = I_i \exp \left( - \int_0^L K_{ext} \cdot dx \right) = I_i \exp (-\tau) \quad (15.226)$$

where  $K_{ext}$  is the extinction coefficient,  $L$  is the optical path length, and  $\tau$  is the turbidity. When the particles are identical, the extinction coefficient is the product of the particle number density and the extinction cross section,  $K_{ext} = N\sigma_{ext}$ ; oth-

erwise the extinction coefficient is equal to the integral over the particle size distribution. Kerker (1969) points out that multiple scattering can be important for  $\tau > 0.1$  (a violation of the second condition above). For soot particles with  $a = 0.1 \mu\text{m}$  and an optical path length of 1 m, Jones (1979) reports that the maximum number density consistent with  $\tau = 0.1$  is  $N = 2 \times 10^7 \text{ cm}^{-3}$ . From the standpoint of flow diagnostics, in particular the use of scattering as a measure of the gas density or temperature, high turbidity across the region of interest can lead to two sources of measurement bias. First, with a large  $\tau$ , the laser beam irradiance decreases as the beam traverses the region of interest, and thus the scattering intensity at a particular region depends on the particle number density encountered by the beam *prior* to reaching the measurement point. Second, the scattering can be attenuated as it traverses the particle-laden gas between the measurement region and the detector. This source of measurement bias, referred to as *radiation trapping*, can often be minimized through the choice of viewing position or angle.

In view of the restriction on the number density, a principal limitation of Mie scattering for flow diagnostics is *marker shot noise* or *ambiguity noise*, which results from a finite number of particles within the probe volume [Becker *et al.* (1967)]. That is, even in the absence of gas-number-density variations, the scattering varies from one spatial location to the next (or from one time to the next), depending on the exact number of particles within the probe volume. (A similar problem known as *photon shot noise* is often encountered when the number of collected photons is small.) Thus, reduction of this source of measurement noise requires the use of more small particles rather than fewer large particles. The problem of marker shot noise is exacerbated with a polydisperse group of particles, since scattering is dominated by a few large particles. Because the seeding density is limited, this noise source imposes a bound on the minimum spatial resolution; as the dimensions of the probe volume become smaller, the number of particles decreases and the marker shot noise increases.

Smaller particles also have a higher velocity frequency response, and thus are more capable of tracking turbulent fluctuations of the gas. Becker *et al.* (1967) have calculated the velocity frequency response—the frequency for which the particle velocity amplitude is 10% below the value of the gas—for a range of particle sizes in air near STP. For a particle  $1 \mu\text{m}$  in diameter having a  $1 \text{ gm/cm}^{-3}$  density, the response is  $\sim 22 \text{ kHz}$ ; the frequency response of a  $3\text{-}\mu\text{m}$ -diameter particle, however, is  $\sim 2.7 \text{ kHz}$ . As a *rule of thumb*, the mass fraction of the seed should be limited to 1% to minimize the effect on the gas properties (e.g., density and viscosity). In addition, the influence on the turbulent kinetic energy should be small for a particle mass fraction of 1% or less [Squires and Eaton (1990)]. Of course, the diffusivity of the particles is much lower than that of the gas. Finally, caution must be exercised in interpreting the scattering intensity in reacting flows. Moss (1980), for example, found that as  $\text{TiO}_2$  seed particles passed through the flamefront of a premixed flame, the scattering signal decreased by a factor of 25 rather than 8, as expected from the density variation across the flame. Stepowski (1992) reports that for combustions flows, the more stable  $\text{Al}_2\text{O}_3$  and  $\text{ZrO}_2$  seed is preferable.

*Spectral Distribution of Rayleigh/Mie Scattering.* Scattered radiation can be both *Doppler broadened* by the thermal motion of the scatterers and *Doppler shifted* by the bulk motion of the scatterers. The spectral profile resulting from this thermal

motion is described by a Gaussian function [Fabelinskii (1968)] having a characteristic full width  $\Delta v_D$  (Hz), measured at half the maximum height of the profile, of

$$\Delta v_D = 2v_i \left( \frac{8k_B T \ln 2}{mc^2} \right)^{1/2} \sin \frac{\theta}{2} = 1.4325 \times 10^8 v_i \left( \frac{T}{M} \right)^{1/2} \sin \frac{\theta}{2} \quad (15.227)$$

where  $T$  (K) is the gas temperature,  $m$  (gm) and  $M$  (a.m.u.) refer to the molecular/atomic weight,  $v_i$  (Hz) is the incident frequency,  $k_B$  is the Boltzmann constant,  $c$  is the speed of light, and  $\theta$  is the angle between detection and beam-propagation wave vectors  $\bar{k}_s$  and  $\bar{k}_i$ , respectively (see Fig. 15.93). In addition to this thermal broadening, the scattering can be broadened by the *Brillouin effect*, which is an interaction of the incident radiation and *thermal* acoustic waves [Fabelinskii (1968)]. The relative importance of Brillouin scattering is deduced from the product of the mean free path,  $l$ , between scatterers and the magnitude of the wave vector associated with momentum transfer in the scattering process [Pitz *et al.* (1976) and Miles and Lempert (1990b)]

$$\frac{1}{|\bar{k}_s - \bar{k}_i| l} = \frac{\lambda_i}{4\pi \sin(\theta/2)} \quad (15.228)$$

As before,  $\theta$  is the angle between  $\bar{k}_s$  and  $\bar{k}_i$  (Fig. 15.93). When this ratio is on the order of one or greater, Brillouin scattering is significant, and the spectral profile is not described by a simple Gaussian function [Sandoval and Armstrong (1976)].

With both Rayleigh and Mie scattering, the radiation scattered by a moving particle undergoes a change in frequency. This Doppler frequency shift (Hz) between the incident and scattered radiation, as seen by the stationary observer, is described by the relation [Jones (1993)]

$$\Delta v = \frac{1}{2\pi} (\bar{k}_s - \bar{k}_i) \cdot \bar{u} = v_i \frac{2|\bar{u}|}{c} \sin \frac{\theta}{2} \sin \left( \alpha - \frac{\theta}{2} \right) \quad (15.229)$$

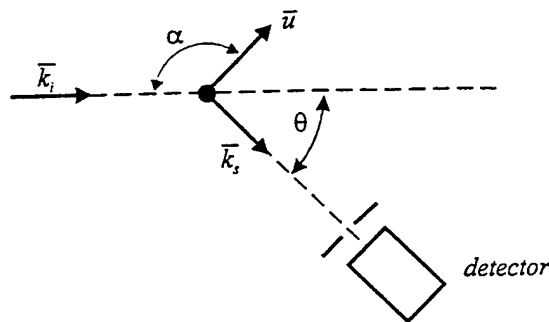


FIGURE 15.93 Plan-view schematic of the interaction between the incident radiation and a particle with velocity vector  $\bar{u}$  in the plane of observation (plane of the page).

where  $\bar{u}$  is the velocity vector within the plane of observation (defined by the vectors  $\bar{k}_s$  and  $\bar{k}_i$ ) and  $\alpha$  is the angle between  $\bar{k}_i$  and  $\bar{u}$  (Fig. 15.93). In reality, of course, the detector will see a range of  $\theta$ .

### 15.12.3 Applications

One requirement for the use of Rayleigh scattering is that the flow be essentially free of particles. Thus, the technique is best suited to laboratory flows, where one can effectively remove particles. Of course, occasional particles do not necessarily compromise an experiment. Because the scattering intensity from the particles is so much greater than that from atoms or molecules, one can often distinguish atomic/molecular scattering from particle scattering, whether point or field measurements are used. Furthermore, Rayleigh and Mie scattering measurements near surfaces can be difficult because of scattering from these surfaces. Optical arrangements for Rayleigh/Mie-scattering (as well as spontaneous-Raman-scattering) measurements often resemble those shown schematically in Figs. 15.92 and 15.94. Vertically polarized laser radiation is directed to the probe volume, and scattering is collected at  $90^\circ$  to the beam-propagation axis. For field (i.e., 2D) measurements, one can use a cylindrical lens or a combination of cylindrical lenses to expand the laser beam into a *sheet*. Two less common methods of forming a laser sheet involve use of a rotating mirror to sweep the laser beam through the region of interest and use of a multi-pass cell, formed by two cylindrical concave mirrors.

Because the scattering intensity is proportional to the laser intensity, monitoring the laser intensity is generally important when relating the strength of the scattering signal to some physical property of the gas (e.g., concentration of fuel). Of course, for field measurements, monitoring the laser intensity is more difficult, since a 1D detector is often necessary (though a linear detector is appropriate only for a collimated laser sheet). Another approach is to infer the irradiance distribution of the laser sheet from the Rayleigh/Mie scattering in a region of flow that is known to be uniform in density. If the sheet irradiance does not vary with time, then one can record the irradiance distribution once and use it to correct subsequent images. Two other factors can affect the quantitative nature of field measurements: 1) the 2D detector may have a nonuniform response (to a uniformly illuminated field), and 2) the solid angle for collection of the scattered light generally varies across the detector

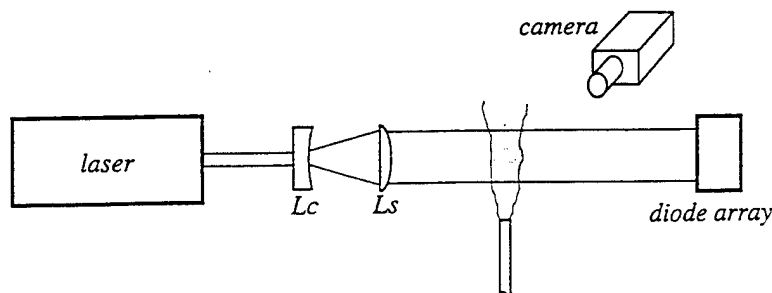


**FIGURE 15.94** Side-view schematic of a typical 2D scattering measurement. Here,  $L_c$ , a plano-concave cylindrical lens, and  $L_s$ , a plano-convex spherical lens, are the sheet-forming optics. The diode array is used to record the beam energy/power in the vertical direction.

(e.g., the edge of the detector will generally subtend a smaller solid angle and, thus, see less scattering).

**Species Concentration.** Perhaps the best application of Rayleigh scattering for a quantitative measurement is in the investigation of the mixing of two fluids at constant temperature and pressure. Dowling and Dimotakis (1990) employed Rayleigh scattering with an argon-ion ( $\text{Ar}^+$ ) laser to study the mixing of a free, turbulent axisymmetric jet with the surrounding quiescent fluid. For one set of measurements with a jet-exit Reynolds number of 5000, they used  $\text{C}_2\text{H}_4$  (ethylene) as the jet fluid and  $\text{N}_2$  as the ambient fluid. Due to the significant difference in scattering cross section (Table 15.10), these two fluids can easily be distinguished, and the scattering signal is linearly related to the jet mole fraction,

$$P_s \propto X_{\text{jet}}(\sigma_{o,\text{jet}} - \sigma_{o,\text{amb}}) + \sigma_{o,\text{amb}} \quad (15.230)$$

With this arrangement, they were able to make point measurements having high signal-to-noise ratios (which, of course, limits the precision of the *mixedness* measurement) at frequencies as high as 100 kHz [Dowling *et al.* (1989)].

In a nonpremixed, turbulent jet flame, Muss *et al.* (1994) applied Rayleigh scattering to the measurement of a fuel mixture fraction (defined as the ratio of the mass originating from the fuel jet to the total value) using a fuel mixture of 80% He and 20%  $\text{H}_2$ . The small  $\sigma_o$  of He—in addition to its large concentration in the jet fluid—ensures that the scattering signal will decrease monotonically as a function of mixture fraction. Thus, they measured the mixture fraction in a field and were able to determine the scalar dissipation.

To investigate the mixing of a turbulent jet into a coflowing stream, Long *et al.* (1979), (1981) measured the concentration of jet fluid in a field using Mie scattering. The fluid was doped with an aerosol of sugar particles (diameter  $\leq 1 \mu\text{m}$ ). The large scattering cross section of the particles enabled them to use a 2.5 W cw  $\text{Ar}^+$  laser. The scattering from a  $2 \times 2 \text{ cm}^2$  area was recorded using a TV camera that was gated on for a period of  $10 \mu\text{s}$ , effectively *freezing* the fluid motion. The images were digitized in a  $100 \times 100$  pixel format, yielding a spatial resolution of  $0.2 \times 0.2 \times 0.15 \text{ mm}$ , with the third dimension (0.15 mm) being set by the thickness of the laser sheet. They investigated the spatial structures and length scales of turbulent flows for different jet-exit Reynolds numbers. In addition, Long and co-workers (1981) demonstrated the feasibility of measuring a 1D scattering image (along the line of the laser beam) as a function of time. They removed the cylindrical lens from the laser focusing optics and added a rotating mirror to the scattering collection optics, which enabled them to sweep the 1D scattering along the second dimension of the camera.

To circumvent the problem of limited spatial resolution with Mie scattering (due to marker shot noise), Escoda and Long (1983) applied molecular Rayleigh scattering to a turbulent jet flow. To increase the scattering signal, they used the second harmonic of a Q-switched Nd:YAG laser ( $\lambda_l = 532 \text{ nm}$ ), delivering 20 mJ per 15 ns pulse (whereas a 2.5-W cw  $\text{Ar}^+$  laser delivers only  $25 \mu\text{J}$  during a  $10 \mu\text{s}$  exposure); in addition, they used Freon 12 as the jet fluid since its scattering cross section is much larger than that of the coflowing  $\text{N}_2$  (see Table 15.10). They were able to resolve fluid structures measuring 100 to  $200 \mu\text{m}$  with an improved spatial resolution of  $\sim 50 \mu\text{m}$ . Furthermore, they investigated the effect of marker diffusivity (or lack

thereof) on the jet-concentration images. The images derived from molecular Rayleigh scattering clearly showed a more diffuse boundary than those derived from Mie scattering because of molecular diffusion.

More recently, Long and co-workers have proved the feasibility of both 2D concentration measurements at high framing rates and 3D concentration measurements. Winter *et al.* (1987) compared three approaches to obtaining 2D high-framing-rate measurements. The highest framing rate reported (10 kHz) was achieved for a system including a rotating mirror and a slow vidicon camera; the drawback of this arrangement was that it allowed only a limited number of exposures. For measuring gas concentrations in 3D, Yip and Long (1986) employed two lasers and two cameras to record molecular Rayleigh scattering in two adjacent planes (separated by 300  $\mu\text{m}$ ) simultaneously within a turbulent jet, again using Freon as the jet fluid. To distinguish the scattering planes, they used different laser wavelengths, 532 nm from a Nd:YAG and 563 nm from an Nd:YAG-pumped dye laser, in conjunction with wavelength filters in front of each camera. They were able to determine the joint probability density function (PDF) of the mixture fraction and the magnitude of the mixture-fraction gradient.

Subsequent to this experiment, Yip *et al.* (1988) used a somewhat different approach to record the scattering from multiple planes *swept* through a turbulent jet flow of Freon. A pulsed laser is required to obtain sufficient scattering signal; however the pulse must be of sufficient duration to be swept through the gas jet. Consequently, they employed a flashlamp-pumped dye laser having a pulse duration of  $\sim 1 \mu\text{s}$  and a pulse energy of 550 mJ. An electronic framing camera recorded as many as twelve 10 ns exposures, each separated by 50 ns. The sweep rate of the laser sheet coupled with the 50 ns delay between exposures resulted in consecutive images being separated by 250  $\mu\text{m}$ . They were able to record surfaces of constant jet-fuel concentration (equivalent to mixture fraction in this case). Unfortunately, the signal-to-noise ratio (where the noise component was probably photon shot noise) was poor; to solve this problem they used laser-induced fluorescence of biacetyl, which was mixed with jet fluid.

To study turbulent mixing, Roquemore *et al.* (1986) seeded  $\text{TiCl}_4$  vapor into the fuel side of a bluff-body combustor. Upon mixing with a moist gas, the  $\text{TiCl}_4$  quickly forms micron-sized  $\text{TiO}_2$  particles through a reaction with  $\text{H}_2\text{O}$ ; as a consequence, the *mixed* fluid can be visualized with the Mie-scattering technique. Through photographs and high-speed movies of the scattering from a laser sheet from an  $\text{Ar}^+$  laser, Roquemore and co-workers were able to characterize regimes for the operation of the bluff-body combustor.

Smith *et al.* (1989) employed an argon-fluoride excimer laser ( $\lambda_i = 193 \text{ nm}$ ) to obtain 2D molecular Rayleigh scattering images within a Mach-2.5 air boundary layer. Use of a deep UV wavelength has two significant advantages: 1) the scattering cross section is much larger than in the visible region (for example, they report that for air,  $\sigma_o$  at  $\lambda_i = 193 \text{ nm}$  is 80 times higher than at  $\lambda_i = 532 \text{ nm}$ ) as a result of the explicit  $\lambda^{-4}$  dependence and the smaller wavelength dependence of the index of refraction, and 2) scattering from surfaces and particles is suppressed due to stronger absorption by most materials in the UV. The latter point is particularly important for measurements near surfaces. They determined the density PDFs, where the density decreases in the boundary layer as a result of frictional heating. Note that the flow was effectively frozen, even at the high velocities, with the 10 ns pulse.

Several investigators have made use of the so-called *vapor-screen technique*

[McGregor (1961)] to study supersonic flows. Vapor, either naturally occurring (usually water) or added (for example, ethanol), condenses in a homogeneous nucleation process to form small ice clusters. Clemens and Mungal (1991), (1992) used this approach to study a supersonic mixing layer. In one experiment, they seeded the ethanol vapor in the subsonic stream; mixing with the supersonic stream resulted in the formation of the ethanol ice particles that effectively scattered the incident radiation. Unfortunately, as Clemens and Mungal (1991) point out, the condensed vapor is not a conserved marker, since sources and sinks for the markers exist throughout the flowfield. Furthermore, assuming that the particles are sufficiently small to be Rayleigh scatterers [for example, Clemens and Mungal (1991) estimated that  $a = 0.02 \mu\text{m}$  under their conditions], the scattering signal scales as the volume squared; consequently, as the ice particles coagulate, the signal can increase significantly without an increase in the total mass of particles. Others have used the vapor-screen method in conjunction with an  $\text{I}_2$  filter, either to record images near surfaces [Forkey *et al.* (1994)] or to collect 2D images of velocity [Miles and Lempert (1990a), (1990b), Miles *et al.* (1991), and Elliott *et al.* (1994)]. The use of an atomic/molecular filter, referred to as the *Filtered Rayleigh-Mie Scattering technique*, is described in more detail below in connection with temperature and velocity measurements.

**Temperature/Density Measurements.** In constant pressure flows where the gas index of refraction is constant (e.g., a heated stream of air flowing into air) or can be determined, one can easily relate the variation in signal to temperature, mass density, or number density; the temperature is proportional to  $\sigma_{o,\text{mix}}/P_s$ , and the mass density is proportional to  $M_{\text{mix}}P_s/\sigma_{o,\text{mix}}$ , where  $M_{\text{mix}}$  is the molecular weight of the mixture. Of course, when  $\sigma_o$  varies throughout the flowfield (due to mixing of gases or chemical reactions), deriving the temperature or mass density from the scattering signal can be difficult. In flames with premixed fuel and air, the problem is ameliorated by the large concentration of  $\text{N}_2$  in the reactants and products. Nevertheless, Namer and Schafer (1985) found that the variation in the net scattering cross section could be large, leading to a large error in the inferred temperature, especially in rich flames because of the large concentrations of  $\text{H}_2$  and  $\text{CO}$ . Interpretation of the signal in terms of mass density was somewhat better, since the variation in  $\sigma_{o,\text{mix}}/M_{\text{mix}}$  was less than that in  $\sigma_{o,\text{mix}}$  alone. They concluded that for premixed  $\text{H}_2$  flames and lean premixed  $\text{CH}_4$  and  $\text{C}_2\text{H}_4$  flames, the errors may be within acceptable limits (<10% error in the inferred temperature).

In the special cases where the species concentrations can be measured, calculated, or estimated, this error can be reduced or eliminated, insofar as the scattering cross sections are known. Inbody (1992) measured temperatures in premixed  $\text{C}_2\text{H}_4/\text{O}_2/\text{N}_2$  laminar flames using an iterative approach. Knowledge of the species concentrations across the flame, which he calculated from an estimated temperature profile, enabled him to obtain a more accurate temperature; this, in turn, was used to calculate more accurate species concentrations. Barat *et al.* (1991) used a similar approach to derive temperatures from Rayleigh scattering employing the second harmonic of a Q-switched Nd:YAG within a premixed, jet-stirred combustor. The  $\sigma_{o,\text{mix}}$  was calculated based on the assumption that the combustion was adiabatic and that the mixture composition consisted of reactants and/or products (no intermediate species). The temperature indicated the relative concentrations of products and reactants

and, thus, the scattering cross section. Because the collected scattering consisted of both the Rayleigh signal and a large background interference (caused by scattering from surfaces within the combustor), they developed a background-subtraction scheme that included splitting and recording both the horizontally polarized scattering component (consisting of background scattering and the small Rayleigh depolarization) and the vertically polarized component (consisting of Rayleigh scattering plus background scattering). In a variety of nonpremixed flames, Dibble *et al.* (1987) have used a combination of Rayleigh and vibrational Raman scattering for determining the temperature and the concentration of the major species; thus,  $\sigma_{o,mix}$  is easily calculated from Eq. (15.225).

In general, the variation in the scattering cross section can be much larger across a nonpremixed flame than across a premixed one (e.g., consider the variation in  $\sigma_{o,mix}$  across  $H_2$ /air and  $CH_4$ /air nonpremixed flames), which makes the measurement of temperatures more difficult. Dibble and Hollenbach (1981) circumvented this problem by choosing a fuel composition of  $H_2$  and  $CH_4$  having the same  $\sigma_{o,mix}$  as that of air. They assumed, of course, that the scattering from the intermediate species was not substantially different from that of the fuel and air. Using an  $Ar^+$  laser, they were able to record temperatures at a data rate of 5 kHz. In a later experiment employing this fuel mixture, Long *et al.* (1985) recorded time-resolved 2D images of temperature (along with 2D images of fuel concentration using vibrational Raman scattering) in a turbulent jet flame.

A different approach was taken by Pitz *et al.* (1976) who inferred the temperature from the measured Doppler width of the scattered radiation. Using a single-mode  $Ar^+$  laser and a Fabry-Perot interferometer for measuring the spectral width of the scattered light, they measured the temperature in an  $H_2$ -air flame and found good agreement with the calculated adiabatic flame temperature ( $T \cong 2300$  K). Under their conditions, Brillouin scattering had only a minor effect on the shape of the spectral profile; however even in cases where Brillouin scattering is significant (e.g., with  $N_2$  near STP) [Sandoval and Armstrong (1976)], one can still deduce the temperature from the spectral profile. For example, Shimizu *et al.* (1986) and Voss *et al.* (1994) have proposed the use of Rayleigh scattering in conjunction with an atomic filter (using Cs or Pb vapor, for instance) for making atmospheric temperature measurements. When the laser wavelength is tuned to the center of the atomic filter transition, the atmospheric aerosol scattering is strongly absorbed by the filter. The fraction of Rayleigh scattering that is transmitted by the filter depends on the spectral width of the scattering (relative to the spectral width of the filter) and, therefore, on the gas temperature.

**Velocity Measurements.** The most familiar velocimetry technique employing Mie scattering is, of course, Laser Doppler Velocimetry (LDV); because of the maturity of LDV and the wealth of available books and review articles, we will not discuss this technique here. Like LDV, Particle Imaging Velocimetry (PIV; see Sec. 15.4.5 for a more detailed discussion of the PIV technique) can be applied to a wide range of flow velocities. Unlike the LDV method, however, the PIV technique can be applied to the measurement of the time-resolved velocity field; consequently, one can obtain velocity gradients and vorticity at an instant in time. Seed particles are illuminated by two collinear laser pulses which are temporally separated; the resulting Mie scattering from both laser pulses is recorded by a photographic or CCD

(charge-coupled device) camera. The velocity field within the laser sheet is then deduced from the known time delay between the two pulses and from a measurement of the displacement of the particles from the first to the second laser pulse.

If the flow velocity is sufficiently large, one can determine the velocity of the gas in the probe volume by measuring the frequency (or Doppler) shift. One simple approach to determining the Doppler shift involves combining the scattered radiation with a portion of the laser beam. When the frequency shift is less than the bandwidth of the detection system, one can illuminate the photodetector with the combined beams; the frequency shift is then given by the beat frequency and is detectable with a spectrum analyzer [Yeh and Cummins (1964)]. When measuring velocities in high-speed flows, where the  $\Delta\nu$  is beyond the bandwidth of the detector, a Fabry-Perot interferometer can be employed [Self (1974)]. Unfortunately, these techniques are difficult to extend to time-resolved, 2D velocity measurements. However, the Filtered Rayleigh-Mie Scattering approach does allow measurements of velocity in the plane of a laser sheet. Here, one takes advantage of the spectral coincidence of a tunable narrow-linewidth laser and the absorption lines of gas-phase molecules or atoms. In supersonic flows with ice particles for scatterers, Miles *et al.* (1991) and Elliott *et al.* (1994) have employed the second harmonic of an injection-seeded (where seeding results in a narrow linewidth) *Q*-switched Nd:YAG laser and iodine vapor for the molecular filter. When the laser is tuned to the edge of an  $I_2$  absorption transition, the scattered light which has not been Doppler shifted is absorbed by the iodine filter that has been placed in front of the detector. However, light that has been frequency shifted is not absorbed or is only partially absorbed by the iodine transition and can thus be detected. Of course, the Filtered Rayleigh-Mie Scattering approach is not limited to supersonic flows. Komine *et al.* (1991) compared results using an  $Ar^+$  laser ( $\lambda_i = 514$  nm) and an injection seeded Nd:YAG laser (for time-resolved measurements) with an aerosol of oil droplets in a small table-top wind tunnel. Rather than setting the laser wavelength so that the static scattering was strong, Komine and co-workers chose  $\lambda_i$  such that the transmission on the unshifted light was  $\sim 50\%$ , thus they were able to record both positive and negative  $\Delta\nu$ . By using three detection systems—where each system was composed of a *Doppler-image* camera (i.e., a camera in conjunction with an  $I_2$  cell), a reference camera, and electronics for analog division of the Doppler image by the reference image—they were able to record the three velocity components. Using a similar approach, Lee *et al.* (1993) [also see Meyers and Cavone (1991)] have recorded velocities in a plane above the wing of an F/A-18 aircraft using propylene-glycol seed particles and an  $Ar^+$  laser.

By controlling the gas mix (using  $N_2$  along with the  $I_2$ , for example), the temperature, and the pressure within the filter, one can control the dependence of attenuation (through absorption) on frequency shift. Note that the desired characteristics of a filter used for temperature measurements are somewhat different from those used for velocity measurements; for recording temperatures the spectral width for absorption should be less than that for scattering, while for velocity measurements the linewidth for scattering should be much smaller than that for absorption. This criterion for velocity measurements is more easily met when the scatterers are ice clusters (or even larger particles) since the particle thermal velocity (due to the mass) and number density (due to the restriction on turbidity) are small. Of course, the frequency-shifted scattering will still depend on the local number density and laser irradiance, consequently for a valid measurement of velocity, one must normalize

frequency-shifted scattering with a second *unfiltered* reference scattering measurement (i.e., one that is independent of the Doppler shift).

#### 15.12.4 Summary

In this section, we have reviewed Rayleigh and Mie scattering theory and diagnostic applications. Although the intensity from Mie scattering is much larger than that from Rayleigh scattering (and thus is more easily detected), the application of Mie scattering for quantitative measurements is somewhat more difficult, since one must use seed material to visualize the flow. In general, the seed mass density should be limited to  $\sim 1\%$  (to avoid altering the turbulent kinetic energy of the flow or the bulk properties of the fluid), and the seed number density should be limited such that the scattered radiation is not scattered (which generally requires that the beam extinction be  $< 10\%$ ). In addition, when applying Mie scattering for concentration measurements, one should use more small particles to reduce the marker shot noise. Nonetheless, because of their relative simplicity and modest requirements for equipment, Rayleigh and Mie scattering are attractive optical diagnostic techniques; as with other optical methods, they offer excellent spatial and temporal resolution and, when used properly, do not perturb the flow. Despite their simplicity, the laser-based Rayleigh and Mie scattering methods are powerful tools for the investigation of the physics and chemistry of gaseous flows, since they allow the measurement of gas properties such as species concentration, temperature, and velocity at a point, along a line, in a plane, or even in a volume.

### 15.13 LASER RAMAN GAS DIAGNOSTICS

Lawrence A. Kennedy

Experimental techniques based upon laser spectroscopy offer the potential for remote, *in-situ*, nonperturbing point flow measurements [Lederman (1977) and Eckbreth (1988)]. In principle, they have the capability of simultaneously achieving high spatial ( $< 10^{-3} \text{ cm}^3$ ) and temporal ( $10^{-8}$ – $10^{-6}$  sec) resolution [Lapp and Penny (1979) and Long (1977)].

These techniques [Bloembergen (1965)] arise from interactions between the  $E$  field of an electromagnetic light wave and the electric polarization,  $P$ . The latter can be expressed as a power series of  $E(\omega_1)$  which is characterized by the linear and nonlinear susceptibilities of the medium. Raman scattering arises due to the oscillating polarization induced through the linear susceptibility. The higher order polarizations are weaker, and the ratio of succeeding polarizations is small unless very large laser intensities are employed. Due to inversion symmetry in isotropic media such as gases, there are no second-order effects. Thus, in a gas, the lowest order nonlinearities arise through the third order nonlinear susceptibility. Examples of third-order processes are Coherent Anti Stokes Scattering (CARS) and stimulated Raman gain/loss spectroscopy.

#### 15.13.1 Spontaneous Raman Scattering

Raman scattering arises due to the inelastic collision processes between photons and the molecules of the medium [see Long (1977) for a detailed discussion]. The ap-

## References

- Alms, G. R., Burnham, A. K., and Flygare, W. H. (1975). "Measurement of the Dispersion in Polarizability Anisotropies." *J. Chem. Phys.* **63**, 3321-3326.
- Barat, R. B., Longwell, J. P., Sarofim, A. F., Smith, S. P., and Bar-Ziv, E. (1991). "Laser Rayleigh Scattering for Flame Thermometry in a Toroidal Jet Stirred Combustor." *Appl. Opt.* **30**, 3003-3010.
- Becker, H. A., Hottel, H. C., and Williams, G. C. (1967). "On the Light-Scatter Technique for the Study of Turbulence and Mixing." *J. Fluid Mech.* **30**, 259-284.
- Bogaard, M. P., Buckingham, A. D., Pierens, R. K., and White, A. H. (1978). "Rayleigh Scattering Depolarization Ratio and Molecular Polarizability Anisotropy for Gases." *J. Chem. Soc. Faraday Trans. I* **74**, 3008-3015.
- Bohren, C. F. and Huffman, D. R. (1983). *Absorption and Scattering of Light by Small Particles*. John Wiley & Sons, New York.
- Born, M. and Wolf, E. (1980). *Principles of Optics*, Sixth Edition. Pergamon Press, Oxford, 647-664.
- Bridge, N. J. and Buckingham, A. D. (1966). "The Polarization of Laser Light Scattered by Gases." *Proc. Roy. Soc. Lond. A.* **295**, 334-349.
- Clemens, N. T. and Mungal, M. G. (1991). "A Planar Mie Scattering Technique for Visualizing Supersonic Mixing Flows." *Exp. Fluids* **11**, 175-185.
- Clemens, N. T. and Mungal, M. G. (1992). "Two- and Three-Dimensional Effects in the Supersonic Mixing Layer." *AIAA J.* **30**, 973-981.
- D'Alessio, A. (1981). "Laser Light Scattering and Fluorescence Diagnostics of Rich Flames Produced by Gaseous and Liquid Fuels." In *Particulate Carbon Formation During Combustion* (ed., D. C. Siegla and G. W. Smith). Plenum Press, New York, 207-259.
- Dibble, R. W. and Hollenbach, R. E. (1981). "Laser Rayleigh Thermometry in Turbulent Flames." *Eighteenth Symposium (International) on Combustion*, The Combustion Institute, Pittsburgh, PA, 1489-1499.
- Dibble, R. W., Masri, A. R., and Bilger, R. W. (1987). "The Spontaneous Raman Scattering Technique Applied to Nonpremixed Flames of Methane." *Combust. Flame* **67**, 189-206.
- Dowling, D. R. and Dimotakis, P. E. (1990). "Similarity of the Concentration Field of Gas-Phase Turbulent Jets." *J. Fluid Mech.* **218**, 109-141.
- Dowling, D. R., Lang, D. B., and Dimotakis, P. E. (1989). "An Improved Laser-Rayleigh Scattering Photodetection System." *Exp. Fluids* **7**, 435-440.

Eckbreth, A. C. (1988). *Laser Diagnostics for Combustion Temperature and Species*. Abacus Press, Cambridge, MA.

Elliott, G. S., Samimy, M., and Arnette, S. A. (1994). "Details of a Molecular Filter-Based Velocimetry Technique." AIAA Paper 94-0490, Presented at the 32nd Aerospace Sciences Meeting and Exhibit, Reno, NV, 10-13 January.

Escoda, M. C. and Long, M. B. (1983). "Rayleigh Scattering Measurements of the Gas Concentration Field in Turbulent Jets." *AIAA J.* **21**, 81-84.

Fabelinskii, I. L. (1968). *Molecular Scattering of Light*. Plenum Press. New York.

Forkey, J. N., Lempert, W. R., Bogdonoff, S. M., Miles, R. B., and Russell, G. R. (1994). "Volumetric Imaging of Supersonic Boundary Layers Using Filtered Rayleigh Scattering Background Suppression." AIAA Paper 94-0491, Presented at the 32nd Aerospace Sciences Meeting and Exhibit, Reno, NV, 10-13 January.

Gardiner, W. C., Jr., Hidaka, Y., and Tanzawa, T. (1981). "Refractivity of Combustion Gases." *Combust. Flame*, **40**, 213-219.

Inbody, M. A. (1992). *Measurements of Soot Formation and Hydroxyl Concentration in Near-Critical Equivalence Ratio Premixed Ethylene Flames*. Ph.D. Dissertation. School of Mechanical Engineering, Purdue University, West Lafayette, IN.

Jones, A. R. (1979). "Scattering of Electromagnetic Radiation in Particulate Laden Fluids." *Prog. Energy Combust. Sci.* **5**, 73-96.

Jones, A. R. (1993). "Light Scattering for Particle Characterization." In *Instrumentation for Flows with Combustion* (ed., A. M. K. P. Taylor). Academic Press, London, 323-404.

Kerker, M. (1969). *The Scattering of Light and Other Electromagnetic Radiation*. Academic Press, New York.

Kerker, M., Scheiner, P., and Cooke, D. D. (1978). "The Range of Validity of the Rayleigh and Thomson Limits for Lorenz-Mie Scattering." *J. Opt. Soc. Am.* **68**, 135-137.

Komine, H., Brosnan, S. J., Litton, A. B., and Stappaerts, E. A. (1991). "Real Time, Doppler Global Velocimetry." AIAA Paper 91-0337, Presented at the 29th Aerospace Sciences Meeting and Exhibit, Reno, NV, January.

Landolt-Börnstein Tabellen, Vol. II, *Eigenschaften der Materie in ihren Aggregatzuständen, Part 8, Optische Konstanten* (1962). Springer-Verlag, Berlin. Sect. 286, 871-888.

Lederman, S. (1977). "The Use of Laser Raman Diagnostics in Flow Fields and Combustion." *Prog. Energy Combust. Sci.* **3**, 1-34.

Lee, J. W., Meyers, J. F., and Cavone, A. A. (1993). "Doppler Global Velocimetry Measurements of the Vortical Flow Above an F/A-18." AIAA Paper 93-0414, Presented at the 31st Aerospace Sciences Meeting and Exhibit, Reno, NV, 11-14 January.

- Long, D. A. (1977). *Raman Spectroscopy*. McGraw Hill, New York.
- Long, M. B., Webber, B. F., and Chang, R. K. (1979). "Instantaneous Two-Dimensional Concentration Measurements in a Flow by Mie Scattering." *Appl. Phys. Lett.* **34**, 22-24.
- Long, M. B., Chu, B. T., and Chang, R. K. (1981). "Instantaneous Two-Dimensional Gas Concentration Measurements by Light Scattering." *AIAA J.* **19**, 1151-1157.
- Long, M. B., Levin, P. S., and Fourquette, D. C. (1985). "Simultaneous Two-Dimensional Mapping of Species Concentration and Temperature in Turbulent Flames." *Opt. Lett.* **10**, 267-269.
- McGregor, I. (1961). "The Vapour-Screen Method of Flow Visualization." *J. Fluid Mech.* **11**, 418-511.
- Meyers, J. F. and Cavone, A. A. (1991). "Signal Processing Schemes for Doppler Global Velocimetry." Presented at the 14th International Congress on Instrumentation in Aerospace Simulation Facilities, Rockville, Maryland, 27-31 October.
- Miles, R. B. and Lempert, W. R. (1990a). "Flow Diagnostics in Unseeded Air." AIAA Paper 90-0624, Presented at the 28th Aerospace Sciences Meeting and Exhibit, Reno, NV, 8-11 January.
- Miles, R. B. and Lempert, W. R. (1990b). "Two-Dimensional Measurement of Density, Velocity, and Temperature in Turbulent High-Speed Air Flows by UV Rayleigh Scattering." *Appl. Phys. B* **51**, 1-7.
- Miles, R. B., Lempert, W. R., and Forkey, J. (1991). "Instantaneous Velocity Fields and Background Suppression by Filtered Rayleigh Scattering." AIAA Paper 91-0357, Presented at the 29th Aerospace Sciences Meeting and Exhibit, Reno, NV, 7-10 January.
- Moss, J. B. (1980). "Simultaneous Measurements of Concentration and Velocity in an Open Premixed Turbulent Flame." *Combust. Sci. Technol.* **22**, 119-129.
- Muss, J. A., Dibble, R. W., and Talbot, L. (1994). "A Helium-Hydrogen Mixture for the Measurement of Mixture Fraction and Scalar Gradient in Non-premixed Reacting Flows." AIAA Paper 94-0612, Presented at the 32nd Aerospace Sciences Meeting and Exhibit, Reno, NV, 10-13 January.
- Namer, I. and Schefer, R. W. (1985). "Error Estimates for Rayleigh Scattering Density and Temperature Measurements in Premixed Flames." *Exp. Fluids* **3**, 1-9.
- Pitz, R. W., Cattolica, R., Robben, F., and Talbot, L. (1976). "Temperature and Density in a Hydrogen-Air Flame from Rayleigh Scattering." *Combust. Flame* **27**, 313-320.
- Roquemore, W. M., Tankin, R. S., Chiu, H. H., and Lottes, S. A. (1986). "A Study of a Bluff-Body Combustor Using Laser Sheet Lighting." *Exp. Fluids* **4**, 205-213.

- Rowell, R. L. and Aval, G. M. (1971). "Rayleigh-Raman Depolarization of Laser Light Scattered by Gases." *J. Chem. Phys.* **54**, 1960-1964.
- Rudder, R. R. and Bach, D. R. (1968). "Rayleigh Scattering of Ruby-Laser Light by Neutral Gases." *J. Opt. Soc. Am.*, **58**, 1260-1266.
- Sandoval, R. P. and Armstrong, R. L. (1976). "Rayleigh-Brillouin Spectra in Molecular Nitrogen." *Phys. Rev. A* **13**, 752-757.
- Self, S. A. (1974). "Laser-Doppler anemometer for Boundary Layer Measurements in High Velocity, High Temperature MHD Channel Flows,." In *Proceedings of the Second International workshop on Laser Velocimetry*, Purdue University, Vol. II, 44-67.
- Shardanand and Prasad Rao, A. D. (1986). Absolute Rayleigh Scattering Cross Sections of Gases and Freons of Stratospheric Interest in the Visible and Ultraviolet Regions. NASA Technical Note, TN D-8442.
- Shimizu, H., Noguchi, K., and She, C.-Y. (1986). "Atmospheric Temperature Measurements by a High-Spectral-Resolution Lidar." *Appl. Opt.* **25**, 1460-1466.
- Smith, M., Smits, A., and Miles, R. B. (1989). "Compressible Boundary-Layer Density Cross Sections by UV Rayleigh Scattering." *Opt. Lett.* **14**, 916-918.
- Squires, K. and Eaton, J. (1990). "Particle Response and Turbulence Modification in Isotropic Turbulence." *Phys. Fluids A* **2**, 1191-1203.
- Stepowski, D. (1992). "Laser Measurements of Scalars in Turbulent Diffusion Flames." *Prog. Energy Combust. Sci.* **18**, 463-491.
- van de Hulst, H. C. (1957). *Light Scattering by Small Particles*. John Wiley & Sons, New York. Reprinted in 1981 by Dover Publications, New York.
- Voss, E., Weitkamp, C., and Michaelis, W. (1994). "Lead-Vapor Filters for High-Spectral-Resolution Temperature Lidar." *Appl. Opt.* **33**, 3250-3260.
- Winter, M. Lam, J. K., and Long, M. B. (1987). "Techniques for High-Speed Digital Imaging of Gas Concentrations in Turbulent Flows." *Exp. Fluids* **5**, 177-183.
- Yeh, Y. and Cummins, H. Z. (1964). "Localized Fluid Flow Measurements with an He-Ne Laser Spectrometer." *Appl. Phys. Lett.* **4**, 176-178.
- Yip, B. and Long, M. B. (1986). "Instantaneous Planar Measurements of the Complete Three-Dimensional Scalar Gradient in a Turbulent Jet." *Opt. Lett.* **11**, 64-66.
- Yip, B., Schmitt, R. L., and Long, M. B. (1988). "Instantaneous Three-Dimensional Concentration Measurements in Turbulent Jets and Flames." *Opt. Lett.* **13**, 96-98.

# Raman-LIF Measurements of Temperature, Major Species, OH, and NO in a Methane-Air Bunsen Flame

Q. V. NGUYEN\* and R. W. DIBBLE

*Department of Mechanical Engineering, University of California, Berkeley, CA 94720*

C. D. CARTER

*Systems Research Laboratories, Inc., 2800 Indian Ripple Road, Dayton, OH 45440-3696*

G. J. FIECHTNER and R. S. BARLOW

*Combustion Research Facility, Sandia National Laboratories, Department 8351, MS 9051, Livermore, CA 94551*

Nonintrusive measurements of temperature, the major species ( $N_2$ ,  $O_2$ ,  $H_2$ ,  $H_2O$ ,  $CO_2$ ,  $CO$ ,  $CH_4$ ), OH, and NO in an atmospheric pressure, laminar methane-air Bunsen flame were obtained using a combination of Raman-Rayleigh scattering and laser-induced fluorescence. Radial profiles were measured at three axial locations for an equivalence ratio of 1.38. Measurements along the centerline of the flame, for equivalence ratios of 1.38, 1.52, and 1.70, were also obtained. The measurements indicate that the inner unburned fuel-air mixture experiences significant preheating as it travels up into the conical flame zone surrounding it. Consequently, the centerline axial temperatures were typically 100–150 K higher than predicted by adiabatic equilibrium for reactants at an initial temperature of 300 K. Because the amount of preheating increases with the equivalence ratio (due to the increased inner flame height), the maximum temperatures (2000 K) in a Bunsen flame were rather insensitive to the stoichiometry. We observed a 20% reduction of the maximum NO concentrations (80 ppm) in a Bunsen flame by increasing the equivalence ratio from 1.38 to 1.70. We also find that using a one-dimensional premixed laminar flame model incorporating finite-rate chemistry, satisfactorily predicts properties such as the temperature, CO, OH, and NO concentrations at the inner flame.

## INTRODUCTION

Natural gas, predominantly composed of methane, is an abundant and relatively clean-burning fossil fuel. Its increasing use as the fuel of choice for power generation, industrial process heating, and residential use has been prompted by recently imposed, low-pollutant emissions standards [1]. A large portion of the natural gas consumed in the United States is burned in atmospheric pressure Bunsen flames, characterized by an inner rich premixed flame, followed by an outer zone of nonpremixed combustion. The Bunsen flame, invented in 1855, is referred to as an "atmospheric shot burner" by the gas appliance industry and is used in a predominant number of burner designs for its inherent stability and passively reliable operation, important considerations for residential and commercial gas appliances.

The goal of developing cleaner and more efficient burners is most effectively realized with the aid of a numerical model of the combustion process, allowing manufacturers of natural gas burners to answer exploratory "what if?" questions on a computer. This approach reduces the reliance of the cut-and-try technique, which is becoming increasingly expensive and time consuming. The development of accurate numerical models of combustion, however, require a high-degree of understanding of the interaction between the complex, finite-rate chemistry and multidimensional fluid dynamics. The extent of this understanding is best verified through a direct comparison of the model results with experimental measurements of properties such as temperature and species concentrations. A recent example of this type of comparison was reported by Norton et al. [2] for a rectangular non-premixed methane-air flame. A goal of this paper is to provide an accurate database for comparisons with comprehensive numerical models of laminar premixed methane-air Bunsen flames.

\*Corresponding author. Current address: Quang-Viet Nguyen, Combustion Research Facility, Sandia National Laboratories, Dept. 8351, MS 9051, Livermore, CA 94551.

Measurements using traditional techniques such as thermocouples and gas sampling probes, while useful for certain applications, are limited by their intrusiveness when used in flames. Besides perturbing the flow field, thermocouples, require radiative corrections which can introduce a large source of uncertainty in the temperature measurement. Species measurements using gas sampling probes cannot measure the highly reactive combustion intermediates such as the hydroxyl radical (OH), a participant in the reaction



This is one of the most important reactions in the oxidation mechanism of hydrocarbon fuels [3, 4]. In lean-premixed natural gas based flames, sampling probes can also introduce errors to the measurement of carbon monoxide (CO), as previously shown by Nguyen et al. [5].

In addition to the measurement of CO and OH, the accurate measurement of nitric oxide (NO) is of interest due to its toxicity and role in air pollutant formation [6]. The production of NO in combustion processes arises from several different mechanisms (see Refs. 7-10 for a discussion of these mechanisms). The measurement of NO in premixed hydrocarbon fuel flames has been investigated by Bachmeier et al. [11] using probe-sampling techniques. More recent nonintrusive studies of NO in flames include the work of Thorne et al. [12], who examined HC-NO interactions, Drake et al. [10], who examined high-pressure lean premixed flames, Heard et al. [13], who examined the role of radicals in the formation of prompt-NO, and Reisel and Laurendeau [14], who examined the NO production in high-pressure  $\text{C}_2\text{H}_6\text{-N}_2\text{-O}_2$  flames. Nonintrusive and quantitative measurements of NO in atmospheric pressure fuel-rich Bunsen flames, to our knowledge, however, have not been reported.

#### EXPERIMENTAL APPROACH AND APPARATUS

Nonintrusive, optical measurements of temperature and concentration were obtained using laser Raman and Rayleigh scattering, and laser-induced fluorescence (LIF). Raman and

Rayleigh scattering have been previously applied with success to spatially and temporally resolved measurements of temperature and mixture fraction in turbulent non-premixed methane-air flames [15]. LIF is a sensitive technique for detecting trace species such as OH and NO in the parts per million (ppm) range. Recently, Barlow and Carter [16] have demonstrated simultaneous measurements of OH and NO in turbulent nonpremixed hydrogen-air jet flames. The recent success of LIF as a quantitative technique, can be largely attributed to the efforts of Crosley [17], Heard et al. [18], Thoman et al. [19], Drake and Ratcliffe [20], and Paul et al. [21] in measuring the cross-sections for the electronic quenching of OH and NO by numerous colliders. Although a recently demonstrated technique allows a direct mapping of the two-dimensional collisional quenching of OH in low-pressure (0.5 atm) Bunsen flames [22], application of this technique for atmospheric pressure flames is made more difficult by the shorter fluorescence decay times. We have applied the technique used by Carter and Barlow [23], for the measurement of the temperature, and concentrations of the major species, OH, and NO, in a laminar, premixed, methane-air, Bunsen flame.

In particular, we have measured the temperature and concentrations of  $\text{N}_2$ ,  $\text{O}_2$ ,  $\text{H}_2\text{O}$ ,  $\text{CO}_2$ , CO,  $\text{H}_2$ , and  $\text{CH}_4$  using a combination of Raman and Rayleigh scattering. The Rayleigh scattering cross-section is typically about three orders of magnitude greater than Raman scattering cross-section, and thus Rayleigh scattering provides greater precision in the measurement of the number density. However, Raman scattering measurements are needed to provide an overall Rayleigh scattering cross-section, required for determining the total number density of the gases in the probe volume. The temperature is then calculated through the perfect gas law. The measurements of the major species and temperature also serve a second purpose: they provide the necessary information for the determination of an overall collisional electronic quench rate, which is required for determining the quantitative concentrations of OH and NO from measurements of their respective LIF signals.

The experiments were performed using the Raman-LIF apparatus in the Turbulent Diffusion Flame laboratory within the Combustion Research Facility at Sandia National Laboratory. The details of this apparatus are described by Dibble et al. [15], Barlow and Carter [16], and Barlow et al. [24]. Modifications and improvements to this apparatus, however, are described in this paper.

### Burner and Flow Conditions

Figure 1 shows a schematic of the Bunsen burner used in the experiment and the axial locations of the measurements. The burner is similar to the one described by Nguyen et al. [25] and consists of an 82-cm-long, 17-mm-diameter stainless-steel tube surrounded by a 70-mm-diameter honeycomb coflow matrix, which stabilizes the flame from the effects of buoyancy. The long length of the tube assures a condition of fully developed laminar pipe flow at the exit, defining the velocity field for numerical simulations. Pressure regulators control the flows of fuel (bottled  $\text{CH}_4$ ) and dry-air through calibrated orifice plate meters, which are fitted with precision digital manometers. A static mixer then homogenizes the fuel and air flows, providing a steady premixed fuel-to-air ratio. Table 1 shows the operating conditions of the burner for the present study.

### Raman and Rayleigh Diagnostics

Figure 2 shows a schematic of the Raman-LIF apparatus. The Bunsen burner is mounted in a vertical wind tunnel, providing filtered air to minimize laser light scattered by dust particles. Stepper motors translate the wind tunnel for spatial profile measurements. For the Raman and Rayleigh scattering measurements, light

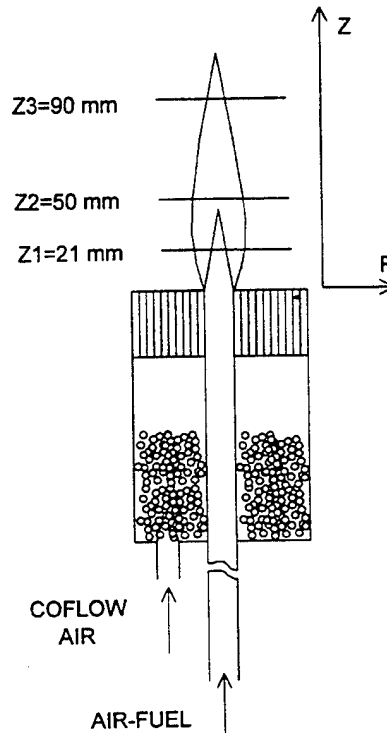


Fig. 1. Schematic of the Bunsen burner used in this study. The coflow air is homogenized by glass beads prior to entering the honeycomb flow straightener. The measurement planes for the radial traverses of flame A are shown.

from a frequency-doubled Nd:YAG laser (532-nm, 10-ns, 700-mJ) was temporally "stretched" to a series of lower energy pulses with an approximate overall width of 100 ns. The longer pulse width reduces the peak laser power, eliminating the breakdown of the gases in the measurement probe volume. The pulse stretcher consists of ten mirrors and two beam-splitter-combiners. The beamsplitters divert fractions of the laser pulse to an optical delay line and subsequently recombine the multiple delayed pulses to a single, longer pulse. Using a 2-m focal length spherical lens, the light

TABLE I  
Premixed Methane-Air Bunsen Flame Operating Conditions

Flame	Traverse	Equivalence Ratio	$\text{CH}_4$ (slm)	Air (slm)	Coflow (slm)	Inner Flame Height (mm)
A	Radial, Axial	1.38	0.97	6.69	82	42
B	Axial	1.52	1.05	6.63	82	55
C	Axial	1.70	1.17	6.57	82	78

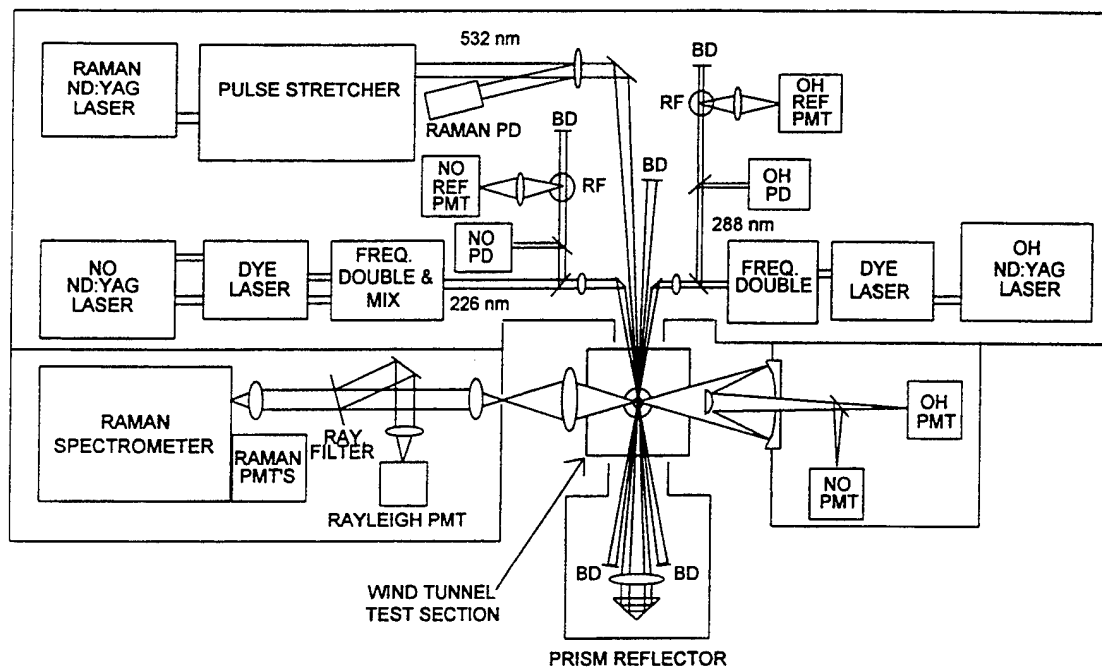


Fig. 2. Schematic of the Raman-Rayleigh-LIF apparatus. Light-tight sheet metal enclosures reduce the background scattered radiation and isolate the laser systems from the collection systems. Legends: BD = beam dump, RF = reference flame, PD = photodiode, PMT = photomultiplier tube.

emerging from the pulse stretcher is focused to a  $750\text{-}\mu\text{m}$  beam waist at the probe volume. A small fraction of light reflected from antireflection coating of this lens is directed to a photodiode detector for an energy measurement. The beam, after passing through the probe volume, is then reflected back into the probe volume using a collimating lens and a right-angle prism; this effectively doubles the laser energy in the probe volume. The probe volume dimensions ( $750\ \mu\text{m}$  in diameter  $\times$   $750\ \mu\text{m}$  long) were defined by the beam waist diameter and the field-stop slit widths of the collection optics.

The Raman and Rayleigh light scattered from the probe volume is collected with a specially designed low  $f$ -number achromatic lens [15] and is then collimated with a camera lens. After collimation, a holographic Raman edge filter reflects the Rayleigh scattered light, while transmitting the Raman scattered light. The Rayleigh scattered portion of the beam is then focused onto a slit placed before a photomultiplier tube (PMT) for detection. An achromatic lens ( $f$ -number matched to the spec-

trometer) focuses the collimated Raman beam onto the entrance slit of a  $3/4\text{-m}$  spectrometer fitted with an 1800 line/mm holographic grating. An achromatic  $1/2\text{-}\lambda$  waveplate mounted behind the slits of the spectrometer rotates the vertically polarized Raman beam to a horizontal plane, which is the optimum orientation for the grating. Small mirrors direct the specific vibrational Raman bands of the major species ( $\text{N}_2$ ,  $\text{O}_2$ ,  $\text{H}_2$ ,  $\text{H}_2\text{O}$ ,  $\text{CO}_2$ ,  $\text{CO}$ , and  $\text{CH}_4$ ) onto seven PMTs mounted at the exit plane of the spectrometer. A 16-channel gated charge integrator measures and digitizes, with 12-bit resolution, the photocurrents from the PMTs and photodiode.

The possible Raman interferences arising from laser-induced fluorescence were monitored using three additional PMTs positioned at approximately the 590-, 615-, and 640-nm exit plane positions. These spectral regions have laser-induced fluorescence effects from the 532-nm excitation; in particular, fluorescence emissions from the  $\text{C}_2$  Swan bands [26] onto the CO channel can give anomalously high CO measurements at fuel-rich conditions.

Properly accounting this effect is especially important for the inner-cone flame front of a Bunsen flame, which is known to have high levels of  $C_2$ , as is evident from the observable  $C_2$  chemiluminescence [27].

### Laser-Induced Fluorescence Diagnostics

Figure 2 also shows the two frequency-doubled, Nd:YAG-pumped dye laser systems used to generate the ultraviolet (UV) wavelengths required for OH and NO excitation. The UV beams were overlapped onto the Raman probe volume at a small crossing angle. The measurement probe volume was defined by a kinematically removable, 800- $\mu\text{m}$  pinhole located at the waist of the Raman-Rayleigh probe volume. By adjusting the 532-nm Raman and UV laser beams through the pinhole prior to each experiment, the proper alignment of the probe volumes with respect to the collection optics was consistently obtained. Telescopes were used to adjust the beam waists such that about 90% of the UV energy passed through the 800- $\mu\text{m}$  pinhole; this approach maximizes the linear fluorescence range for the desired spatial resolution ( $\sim 750\text{-}\mu\text{m}$ ).

Digital delay pulse generators time the firing sequence of the three lasers. The Raman and LIF lasers are each fired 150 ns apart, eliminating the interference between the Raman and two LIF channels. Time-resolved data on the order of a fraction of a microsecond were collected at the laser pulse repetition frequency of 10 Hz; however, the steady-state laminar nature of the Bunsen flame permitted averaging the single-shot data over a period of 20 s or 200 shots, thereby increasing the signal-to-noise ratio (SNR).

For the OH excitation, we tuned the frequency-doubled dye laser output to the  $O_{12}(8)$  transition of the  $A^2\Sigma^+ \leftarrow X^2\Pi(1,0)$  band of OH ( $\lambda = 287.9$  nm). Use of this satellite transition reduces the absorption of the laser beam propagating through the flame, since its line-strength is substantially weaker than those of the main branch transitions. The OH and NO transitions were easily saturated with the available laser energies; consequently, to remain in the linear regime, we attenuated the UV beam for the OH excitation to approximately 40

$\mu\text{J}/\text{pulse}$  using neutral density filters. For the NO excitation, we tuned the second dye-laser to the  $Q_1(18)$  transition of the  $A^2\Sigma^+ \leftarrow X^2\Pi(0,0)$  band of NO ( $\lambda = 225.9$  nm). This wavelength was generated by frequency doubling the output of the second dye laser ( $\lambda = 286.8$  nm) and mixing it with the residual 1064-nm radiation from the Nd:YAG pump laser. This transition was selected because it is well populated at flame temperatures (as well as ambient temperatures) and avoids a significant amount of interference from the nearby vibrationally hot oxygen transitions in the  $B^3\Sigma^+ \leftarrow X^3\Sigma^- (2,4)$  and  $(5,5)$  bands. To ensure a linear-fluorescence regime, the laser energy used for the NO excitation was attenuated to approximately 10  $\mu\text{J}/\text{pulse}$ .

The LIF signal from the probe volume was collected using a specially designed low  $f$ -number Cassegrain mirror-lens system. The reflective design eliminates the chromatic aberration present in transmissive lenses, permitting easy alignment and focusing of the different fluorescence wavelengths. A dichroic mirror separates the OH and NO fluorescence components, which are subsequently imaged onto the slits of two different PMTs fitted with color glass filters. For the detection of the OH fluorescence, we used Schott WG-295 and Hoya U-340 color glass filters, which reject the scattered radiation, and transmit the fluorescence from the dominant  $(1,1)$  and  $(0,0)$  bands ( $295 < \lambda < 340$  nm). The fluorescence from the  $(0,0)$  band results from the vibrational energy transfer (VET) from the  $v' = 1$  to  $v' = 0$  states [28]. For NO detection, we used Schott UG-5 color glass filters and a PMT with a solarblind photocathode; this combination effectively reduces scattered background radiation and permits broad band detection of the fluorescence from the NO,  $v' = 0$ , and  $v'' = 1-5$  bands ( $230 < \lambda < 300$  nm). Again, the slits in front of the PMTs defined the probe volume dimensions along the beam propagation axis and were adjusted to match those of the Raman-Rayleigh system.

Beamsplitters direct portions of the OH and NO laser beams to photodiodes for energy measurements. These secondary beams were also used in recording the LIF from two reference flames burning near-stoichiometric mix-

tures of CH<sub>4</sub> and air. The fluorescence signals from the reference flames permit the wavelength monitoring of the dye lasers throughout the experiment to ensure that they remain constant.

### Raman Signal Calibration

In principle, Raman scattering provides a signal proportional to the number density of all the species being probed; however, the signals are also slightly modified by the following: increases in the temperature, which result in a broadening and shift of the vibrational bands; and the "crosstalk" between various vibrational and rotational bands of the different species. The most notable case is that of N<sub>2</sub> and O<sub>2</sub> which partially overlap with CO and CO<sub>2</sub>, respectively. The temperature and crosstalk effects were accounted for through the calibration procedure. This involved recording the Raman signals over a wide range of known temperatures, gas compositions, and concentrations.

The calibrations include measurements in cold gases, lean and rich mixtures of H<sub>2</sub>-air, H<sub>2</sub>-CO-air, and CH<sub>4</sub>-air flames burned above a non-premixed calibration burner. The non-premixed calibration burner (a so-called Hencken burner) was constructed from a bundle of small-diameter stainless-steel air and fuel tubes arranged in an alternating matrix; the separate fuel and air flows then burn as an array of small nonpremixed flames. This burner design prevents flashback problems associated with premixed H<sub>2</sub>-air flames [15], and at locations sufficiently far downstream, most of the species (NO is an exception) are in local thermodynamic equilibrium. Thus, this burner provides a means of calculating the species concentration and temperature from the fuel-air flow rates [24].

### Fluorescence Signal Calibration

For the OH and NO LIF measurements, the temperature and species concentrations measured by the Raman and Rayleigh scattering provide the necessary information for calculating the electronic quenching corrections. We employ the methodology described by Carter

and Barlow [23] for calculating the temperature and mixture dependent quenching corrections for OH and NO, using the quenching cross-sections provided by Paul [29] and Paul et al. [21]. The conversion of fluorescence signal to number densities, in general, requires: (1) the cross sections describing electronic quenching for all excited vibrational levels with specific colliders, and (2) the cross sections for the VET between the different excited vibrational levels. Currently, however, insufficient data exists for completely describing both the electronic quenching of the  $v' = 1$  excited state and the VET between the  $v' = 1$  and  $v' = 0$  states of OH. Thus, for the OH quenching corrections, we approximate the temperature dependence of the net collisional de-excitation rate using the quenching rates for the  $v' = 0$  state [29].

For the linear-fluorescence regime, the number density  $N$  (cm<sup>-3</sup>) of NO and OH is related to the fluorescence signal  $S_f$  through the relation

$$N = \left[ \frac{N}{S_f} \right]_{\text{CAL}} \left( \frac{[F_B]_{\text{CAL}}}{F_B} \right) \left( \frac{[E_L/Q]_{\text{CAL}}}{[E_L/Q]} \right) \times \left\{ \frac{[g(\nu_0)]_{\text{CAL}}}{g(\nu_0)} \right\} S_f, \quad (2)$$

where  $F_B$  is the Boltzmann fractional population,  $E_L$  is the laser energy,  $Q$  is the overall collisional quench rate (s<sup>-1</sup>),  $\nu_0$  is the transition frequency,  $g(\nu_0)$  is the spectral overlap between the laser and the transition, and the subscript CAL refers to the calibration values [23]. The spectral overlap  $g(\nu_0)$  was modeled using a Gaussian profile for the laser and a Voigt profile for absorption lineshape. The variation of the spectral overlap with temperature, however, was found to be minimal in these measurements.

The OH LIF calibration factor  $[N/S_f]_{\text{CAL}}$ , was obtained in a fuel-lean CH<sub>4</sub>-air flame ( $\phi = 0.94$ ) using the calibration burner in a premixed mode. The equilibrium OH number density was calculated using the Raman-Rayleigh measured temperature, which was typically only 10 to 30 K less than the adiabatic equilibrium value. For the NO calibrations, equilibrium calculations could not be used

since NO is typically far below equilibrium at reasonable distances above the burner. Additionally, the concentrations encountered in the calibration flame were too small for measurement using absorption. Consequently, we obtained the calibration factor  $[N/S_f]_{CAL}$  using two fuel-lean ( $\phi = 0.72$ )  $CH_4-O_2-N_2$  flames stabilized above a watercooled, sintered-bronze, flat-flame McKenna burner: one flame contains a known amount of NO that is substituted for a portion of the total  $N_2$ . The two flames are otherwise identical; the Raman-Rayleigh measurements in the flames showed that the temperatures and concentrations differ by less than a percent between the two flames. By dividing the doped-NO number density by the difference of the two signals, a background-free calibration factor,  $[N_{doped}/(S_{f-doped} - S_{f-undoped})]_{CAL}$  was obtained.

We verified the NO calibration procedure by measuring the LIF signal from an NO-doped room-temperature air flow; this doped-NO number density (deduced from the known air and NO flow rates) was then compared to the value resulting from Eq. 2 using the flame calibration factor  $[N_{doped}/(S_{f-doped} - S_{f-undoped})]_{CAL}$  described above. The known and calculated number densities differed by only 7%. This difference is within the range of uncertainty for the quenching corrections (10%). Furthermore, we performed a one-dimensional flame calculation of the NO-doping procedure using a well established flame code [30, 31], in conjunction with the mechanism of Glarborg et al. [32] as modified by

Drake and Blint [33]. The results of the model showed that none of the doped-NO was destroyed by the flame front.

## RESULTS

A series of  $CH_4$ -air flames in the calibration burner operating with equivalence ratios ranging from 0.80 to 1.38 were used to check the measurement accuracy of the Raman-Rayleigh and OH LIF calibrations. Figure 3 shows the experimentally measured and calculated equilibrium (at the measured Raman-Rayleigh temperature) values of the  $N_2$ ,  $O_2$ ,  $H_2$ ,  $H_2O$ ,  $CO_2$ ,  $CO$ , and  $OH$  concentrations. The Hencken calibration burner produced close-to-adiabatic flames (the Raman-Rayleigh measured temperature was typically 15–25 K lower than predicted by adiabatic equilibrium). For single-shot Raman measurements, photon shot noise is the dominant source of uncertainty [15]. By time averaging over 200 shots, however, the precision and detection limits are increased. Based on the Rayleigh scattering signal RMS variance of about 1%, we estimate the precision of the single-shot temperature measurements to be  $\pm 20$  K at a temperature of 2000 K. The absolute temperature uncertainty however, is  $\pm 36$  K at a temperature of 2000 K—due mainly to the uncertainty in the calibration of the effective Rayleigh cross-section. As shown in Fig. 3, the measured major species concentrations agree well with the calculated (equilibrium) values. We estimate the

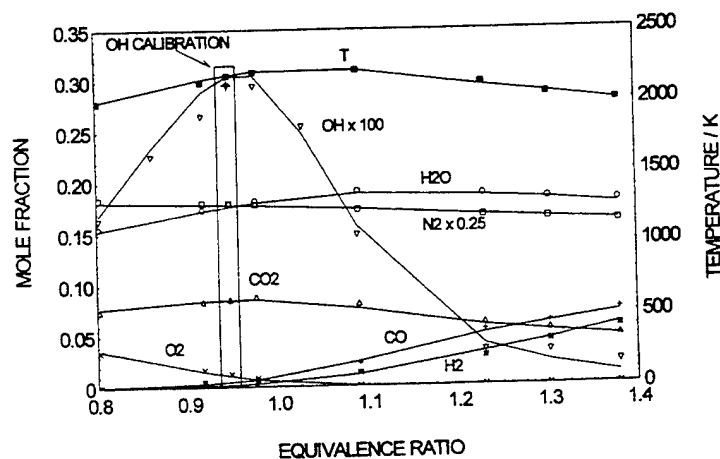


Fig. 3. Comparison of Raman-Rayleigh-LIF measurements (data points) with calculated equilibrium (lines) at the measured Raman-Rayleigh temperature for a series of premixed methane-air calibration flames. Note that the OH scale is magnified, and the  $N_2$  scale is reduced.

time-averaged uncertainty of the major species measurements to be  $\pm 3\%$  of full-scale for the different species (e.g.,  $\pm 0.024$  mole fraction for  $N_2$  in air). The uncertainty in the concentration measurements result mainly from uncertainties in the calibration procedure. For the OH calibration, we used the measured temperature ( $T_{MEAS} = 2180$  K, whereas  $T_{ADIA} = 2187$  K) to calculate the equilibrium OH value. With this single-point calibration, the measured OH at the other equivalence ratios differ with the equilibrium values by no more than 7% (for  $\phi < 1.25$ ). This agreement is excellent considering the simplified treatment of the overall quenching corrections.

Figures 4–6 show the radial profiles of the Bunsen flame at different axial locations for flame A,  $\phi = 1.38$  (see Table 1). Figure 4 details the radial profile across the “double-cone” Bunsen flame at the  $Z_1$  axial location (Fig. 1). Figure 4 shows that the temperature rapidly rises from the cool unburned core to approximately 1980 K, where it plateaus between the inner and outer flame zones. As expected, the temperature reaches a maximum at the outer, stoichiometric flame zone (2077 K). The CO concentration (magnified by 10) peaks at the inner flame zone, coinciding with

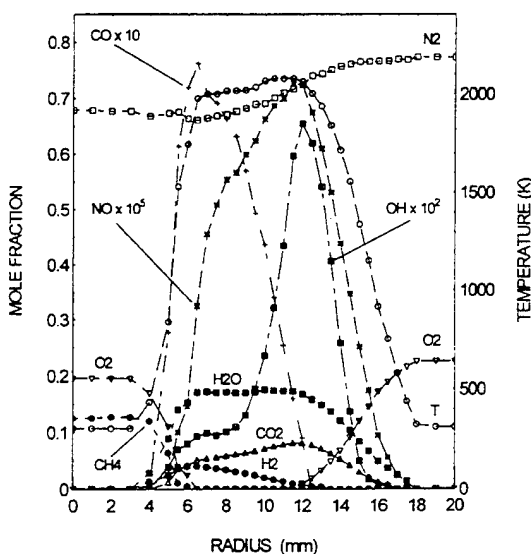


Fig. 4. Radial profiles for flame A ( $\phi = 1.38$ ) at the  $Z_1$  axial location (see Fig. 1). The CO, OH and NO scales are magnified for clarity. For reference, a mole fraction of 1.0 on the left axis corresponds to a NO concentration of 100 ppm.

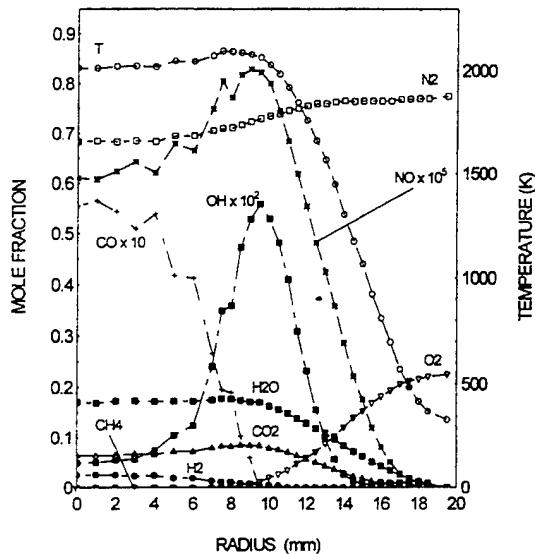


Fig. 5. Radial profiles for flame A at the  $Z_2$  axial location, approximately 10 mm above the inner flame cone tip. Note that the small oscillations in the concentrations are due to disturbances to the flame from air currents in the laboratory.

the oxidation of  $CH_4$  and appearance of  $H_2$ . At this axial location, the measured inner-cone flame temperature is a little lower than predicted by the adiabatic equilibrium calculations ( $T = 1996$  K) due to some radiative losses, but the measured CO concentration ( $X_{CO} = 0.075$ )

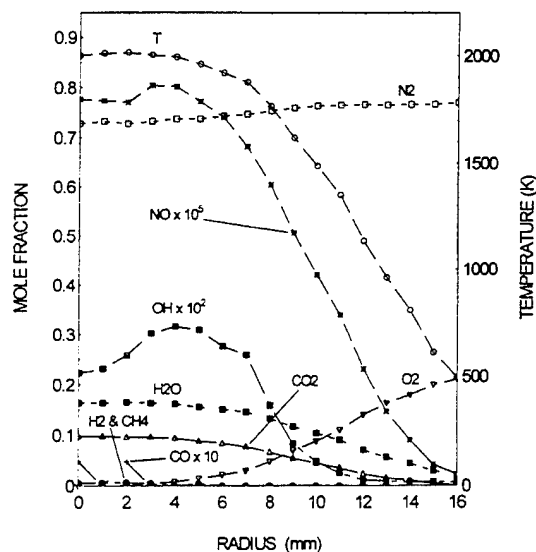


Fig. 6. Radial profiles for flame A at the  $Z_3$  axial location, approximately 20 mm below the outer visible flame tip. At this axial location, the methane is completely consumed and the CO is barely detectable.

is slightly higher than that predicted by equilibrium ( $X_{\text{CO}} = 0.071$ ). The OH (magnified by 100) peaks near the stoichiometric contour defined by the intersection of the  $\text{H}_2$  and the  $\text{O}_2$  concentration profiles.

Figure 4 also shows the radial NO profiles for flame A. The maximum NO concentration (72 ppm) at this axial position coincides with the location of maximum temperature. This results from the thermal NO mechanism which is important at temperatures above 2000 K [13]. The NO forms almost immediately beyond the inner flame zone (hence the term *prompt* NO), and increases linearly with radius.

Although the Bunsen flame is a two-dimensional flame, a rough estimate of the *peak* OH and CO concentrations and temperature at the inner flame front was obtained from the results of a one-dimensional flame model. We calculated profiles of the species of interest using an adiabatic premixed one-dimensional free methane-air flame model [30, 31, 34] incorporating the Miller and Bowman [9] reaction mechanism as modified by Frenklach et al. (49 species with 265 reactions) [35]. For the model inputs, we used a 300 K initial reactant temperature and the methane-air mixture specified in Table 1, flame A. Williams and Fleming [36] have successfully used this modeling approach for the prediction of radicals in NO-doped  $\text{CH}_4\text{-O}_2\text{-N}_2\text{-Ar}$  low-pressure burner-stabilized flat-flames. For flame A, this model agrees well with the measured temperature and CO and OH concentration at the inner flame zone ( $T$  within 2%, OH within 5%). Of particular interest is the agreement of the superequilibrium CO peak discussed earlier: the model agrees within 1% with our measured values of  $X_{\text{CO}} = 0.075$ . Our one-dimensional model also shows that at the inner flame zone, there is a peak of superequilibrium O-atom concentration and CH radicals, located just upstream of the maximum temperature.

Our one-dimensional flame model, however, over-predicts the NO at the inner flame zone by about 15 ppm. Drake and Blint [33] reported that the predicted amount of NO is very sensitive to the rate constant of the reaction



considered the rate controlling step in the prompt NO pathway [9]. The uncertainty in this rate constant, together with the differences in the CH concentration and temperature between the one-dimensional model and the Bunsen flame may be the cause of this discrepancy. The measurements and numerical predictions reported by Reisel et al. [37] for laminar one-dimensional flat  $\text{C}_2\text{H}_6\text{-O}_2\text{-N}_2$  flames, also show a tendency to overpredict the NO in fuel-rich flames.

Figure 5 shows the radial profile for flame A at the  $Z_2$  axial location. This location is approximately 8 mm above the tip of the inner flame cone. The levels of NO are generally increasing, and reach a maximum value of about 82 ppm with a local minimum at the centerline. The temperature is relatively constant in the central portion of the flame and decreases rapidly past the outer flame zone defined by the peak OH location. Also note that the maximum value of the temperature is almost the same as at the  $Z_1$  axial location. The CO peaks at the flame centerline and decreases monotonically with radius. We can also see that most of the  $\text{H}_2$  and essentially all of the  $\text{CH}_4$  has been consumed at this location.

Figure 6 shows the radial profile for flame A at the  $Z_3$  axial location, which is approximately 20 mm below the visible tip of the outer flame cone. Here, the peak temperature has decreased slightly to about 2000 K. The centerline NO value has increased from 60 ppm to about 80 ppm. Note that the centerline OH values have also steadily increased with increasing axial distance. CO at this location was barely detectable using Raman scattering.

Figures 7-9 show the axial profiles along the centerline of the flames A, B, and C (equivalence ratios of 1.38, 1.52, and 1.70, respectively). Figure 7 shows the data for flame A and reveals in detail the trends observed in Figs. 5 and 6. We find that the temperature peaks just beyond the inner-cone flame tip at 2050 K and stays relatively constant at about 2000 K all the way to the visible outer cone flame tip (located at approximately 110 mm). Throughout this region, NO is steadily formed via the thermal mechanism and reaches a peak value of approximately 80 ppm at the outer

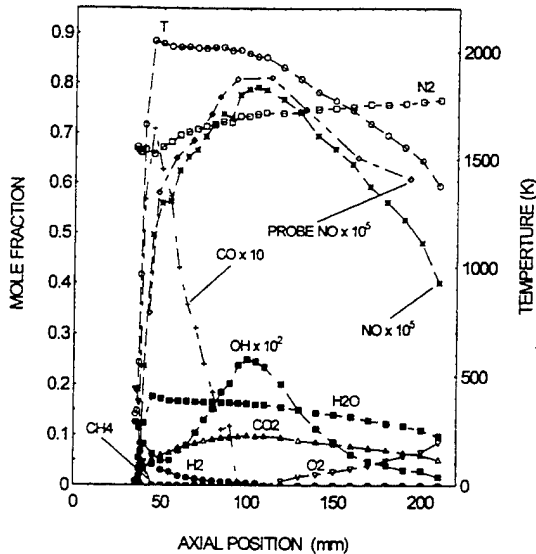


Fig. 7. Axial profiles along the centerline of flame A ( $\phi = 1.38$ ). NO measurements using a quartz suction probe and chemiluminescent  $\text{NO}_x$  analyzer are also shown for comparison.

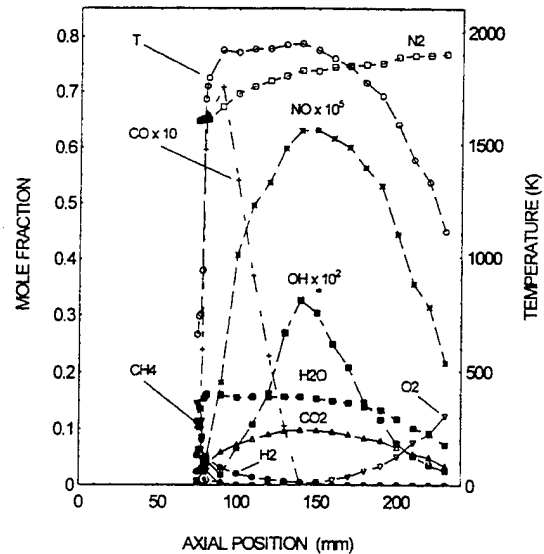


Fig. 9. Axial profiles along the centerline of flame C ( $\phi = 1.70$ ).

cone flame tip where it starts to decrease due to dilution.

We also measured the axial NO concentration for flame A using an uncooled quartz microprobe (3-mm diameter tapered to a 0.5-mm orifice diameter) and chemiluminescent

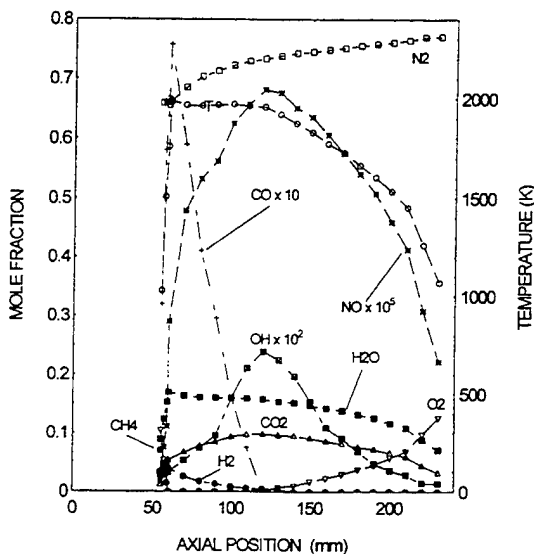


Fig. 8. Axial profiles along the centerline of flame B ( $\phi = 1.52$ ).

$\text{NO}_x$  analyzer; the probe measurements were of dry NO (a water trap was used), and thus we corrected the plotted NO concentration for water content using the Raman measurements. The water trap does not affect the probe sampling measurements of NO, as shown by Kramlich and Malte [38]. Figure 7 shows that the NO probe measurements (adjusted for water content) agree well with the LIF measurements. The good agreement between the two techniques reflects the accuracy of the quenching cross-sections and the calibration procedure. Although the high SNR of the NO measurements provide a single shot precision of 2% for the 80 ppm range, the uncertainty of the quenching corrections and the calibration limit the absolute uncertainty of the time-averaged NO values to  $\pm 10\%$  or about 8 ppm.

We were able to use a suction probe for comparison in this instance due to the slow reactivity of NO with other combustion products [39]. Moreover, at this location, the intrusive effects of the probe on the flame properties are minimal because of the 1-dimensional nature of the flame at the centerline. The probe, however, could not be used for sampling the radial profiles shown in Figs. 4–6, since the flame zones were visually perturbed

by the probe tip due to the steep scalar gradients found in these 2-dimensional flame regions. Access to the chemiluminescent  $\text{NO}_x$  analyzer required performing the probe measurements with the burner mounted outside of the wind tunnel. This necessitated the use of a 300-mm-long, 70-mm-diameter quartz duct to isolate the flame from air currents in the laboratory. Consequently, the last few probe values diverge from the NO fluorescence data points due to the different entrainment and dilution effects existing at far-downstream axial locations.

Figure 8 shows the axial profiles for flame B ( $\phi = 1.52$ ). The maximum NO concentration has decreased to about 68 ppm, at least in part, due to the slightly lower temperature. The peak temperature for this equivalence ratio is about 1990 K, which is 100 K higher than that predicted by adiabatic equilibrium. The superadiabatic temperature is the result of the preheating (through conduction and radiation) of the unburned air-fuel mixture by the coaxial outer flame zone. As the equivalence ratio increases, the height of the inner flame cone also increases, and the unburned air-fuel mixture has more time for preheating. Adiabatic equilibrium calculations that include the observed preheating of the initial reactants, result in temperatures similar to the peak measured temperatures. Thus the peak temperature in a Bunsen flame is relatively independent of the equivalence ratio and remains at about 2000 K.

Figure 9 shows the axial profile of flame C ( $\phi = 1.70$ ). The temperature peaks at about 1900 K; this is about 140 K hotter than predicted by adiabatic equilibrium. At this highly fuel-rich condition, the distinction between the inner and outer flame zones was not as visually apparent, and this is reflected in the smoother temperature profile at the inner flame zone. The peak NO value has decreased to 63 ppm. The decrease in prompt NO with increasing equivalence ratio (for  $\phi > 1.4$ ) is likely the result of the reduced CH concentration (see Eq. (3)). This is also evident from our one-dimensional flame calculations that show that the maximum CH-radical concentrations change from 3.7 ppm at  $\phi = 1.38$ , to only 0.11 ppm at  $\phi = 1.70$ .

## CONCLUSIONS

Using a combination of Raman-Rayleigh scattering and LIF in a methane-air Bunsen flame, we have simultaneously measured the temperature, OH, NO, and the major species ( $\text{N}_2$ ,  $\text{O}_2$ ,  $\text{H}_2$ ,  $\text{H}_2\text{O}$ ,  $\text{CO}_2$ ,  $\text{CO}$ ,  $\text{CH}_4$ ). We obtained both radial and axial profiles for three equivalence ratios (1.38, 1.52, and 1.70). In addition to obtaining an accurate and detailed mapping of temperature and species concentrations in a Bunsen flame, we found that as the equivalence ratio was increased from 1.38 to 1.70, the peak NO value decreased from 79 ppm to 63 ppm. We also found that using a one-dimensional premixed laminar flame model incorporating finite rate chemistry, satisfactorily predicts properties such as the temperature, and CO and OH concentrations at the inner flame zone.

Our measurements show that the axial flame temperatures are typically 100–150 K higher than that predicted by adiabatic equilibrium for reactants with an initial temperature of 300 K. We attribute this to the preheating of the unburned fuel-air mixture as it travels upwards into the conical flame zone surrounding it. The height of the inner-flame cone increases with increasing stoichiometry; hence, the amount of preheating also increases with stoichiometry, offsetting the effect stoichiometry on flame temperature. Consequently, the maximum centerline temperatures in a Bunsen flame (about 2000 K) were insensitive to the stoichiometry.

*The authors would like to thank the following people for their contributions: Mr. Tom Prast for his help with the Raman-LIF apparatus; Mr. Bradley Edgar for his expertise and assistance with the suction probe measurements of NO; Mr. Marc Rumminger for his calculations of the one-dimensional premixed flame used in comparison with the inner Bunsen flame zone; and Prof. John Reisel for his calculations of the one-dimensional NO-doped flames used in the LIF calibrations. Q.V.N. and R.W.D. were supported in part by the California Institute for Energy Efficiency; C.D.C. was supported by the Wright Laboratory, Aero Propulsion and Power Directorate under Contract F33615-92-2202; G.J.F. and R.S.B. were supported by the U.S. Department of Energy,*

Office of Basic Energy Sciences, Division of  
Chemical Sciences.

## REFERENCES

- Correa, S. M., *J. Prop. Power* 8:1144-1151 (1992).
- Norton, T. S., Smyth, K. C., Miller, J. H., and Smooke, M. D., *Combust. Sci. Technol.* 90:1-34 (1993).
- Baulch, D. L., and Drysdale, D. D., *Combust. Flame* 23:215-225 (1974).
- Westbrook, C. K., and Dryer, F. L., *Prog. Ener. Combust. Sci.* 10:1-57 (1984).
- Nguyen, Q. V., Edgar, B. L., Dibble, R. W., and Gulati, A., *Combust. Flame* 100:395-406 (1995).
- Bowman, C. T., *Twenty-Fourth Symposium (International) on Combustion*, The Combustion Institute, Pittsburgh, 1992, pp. 859-878.
- Zeldovich, Ya. B., *Acta Physicochem. USSR* 21:557 (1946).
- Fenimore, C. P., *Combust. Flame* 19:289 (1972).
- Miller, J. A., and Bowman, C. T., *Prog. Ener. Combust. Sci.* 15:287-338 (1989).
- Drake, M. C., Ratcliffe, J. W., Blint, R. J., Carter, C. D., and Laurendeau, N. M., *Twenty-Third Symposium (International) on Combustion*, The Combustion Institute, Pittsburgh, 1990, p. 387.
- Bachmeier, F., Eberius, K. H., and Just, Th., *Combust. Sci. Technol.* 7:77 (1973).
- Thorne, L. R., Branch, M. C., Chandler, D. W., Kee, R. J., and Miller, J. A., *Twenty-First Symposium (International) on Combustion*, The Combustion Institute, Pittsburgh, 1986, pp. 965-977.
- Heard, D. E., Jeffries, J. B., Smith, G. P., and Crosley, D. R., *Combust. Flame* 88:137-148 (1992).
- Reisel, J. R., and Laurendeau, N. M., *Combust. Sci. Technol.* 98:137-160 (1994).
- Dibble, R. W., Masri, A. R., and Bilger, R. W., *Combust. Flame* 67:189-206 (1987).
- Barlow, R. S., and Carter, C. D., *Combust. Flame* 97:261-280 (1994).
- Crosley, D. R., *J. Chem. Phys.* 93:6273 (1989).
- Heard, D. E., Jeffries, and Crosley, D. R., *Chem. Phys. Lett.* 178:533-537 (1991).
- Thoman Jr., J. W., Gray, J. A., Durant Jr., J. L., and Paul, P. H., *J. Chem. Phys.* 97:8156-8163 (1992).
- Drake, M. C., and Ratcliffe, J. W., *J. Chem. Phys.* 98:3850-3865 (1993).
- Paul, P. H., Gray, J. A., Durant Jr., J. L., and Thoman Jr., J. W., *AIAA J.* 32:1670-1675 (1994).
- Hirano, A., Ricoul, F., and Tsujishita, M., *Jpn. J. Appl. Phys.* 32:3300-3307 (1993).
- Carter, C. D., and Barlow, R. S., *Opt. Lett.* 19:299-301 (1994).
- Barlow, R. S., Dibble, R. W., Chen, J. Y., and Lucht, R. P., *Combust. Flame* 82:235 (1990).
- Nguyen, Q. V., Dibble, R. W., Hoffman, D., and Kampmann, S., *Ber. Bunsenges. Phys. Chem.* 97:1634-1642 (1993).
- Faust, W. L., Goldberg, L. S., Craig, B. B., and Weiss, R. G., *Chem. Phys. Lett.* 83:265 (1981).
- Glassman, I., *Combustion*, Academic, Orlando, FL, 1987, p. 331.
- Smith, G. P., and Crosley, D. R., *Appl. Opt.* 22:1428 (1983).
- Paul, P. H., *J. Quant. Spectrosc. Radiat. Transf.* 51:511-524 (1994).
- Kee, R. J., Grcar, J. F., Smooke, M. D., and Miller, J. A., Sandia Report SAND85-8240, Sandia National Laboratories, Livermore, CA, 1985.
- Kee, R. J., Rupley, F. M., and Miller, J. A., Sandia Report SAND89-8009B, Sandia National Laboratories, Livermore, CA, 1989.
- Glarborg, P., Miller, J. A., and Kee, R. J., *Combust. Flame* 65:177-202 (1986).
- Drake, M. C., and Blint, R. J., *Combust. Sci. Technol.* 75:261 (1991).
- Kee, R. J., Dixon-Lewis, G., Warnatz, J., Coltrin, M. E., and Miller, J. A., Sandia Report SAND86-8246, Sandia National Laboratories, Livermore, CA, 1986.
- Frenklach, M., Wang, H., Bowman, C. T., Hanson, R. K., Smith, G. P., Golden, D. M., Gardiner, W. C., and Lisianski, V., 1994, *Twenty-Fifth Symposium (International) on Combustion*, The Combustion Institute, Work in Progress Poster No. 26, Session 3.
- Williams, B. A., and Fleming, J. W., *Combust. Flame* 98:93-106 (1994).
- Reisel, J. R., Carter, C. D., and Laurendeau, N. M., submitted to: Eighth International Symposium on Transport Phenomena in Combustion, 1994.
- Kramlich, J. C., and Malte, P. C., *Combust. Sci. Technol.* 18:94-104 (1978).
- Bowman, C. T., and Seery, D. V., *Emissions from Continuous Combustion Systems*, Plenum, New York, 1972, p. 123.

Received 21 March 1995; revised 3 October 1995

# Injection of Supercritical Ethylene in Nitrogen

Pei-Kuan Wu\* and Tzong H. Chen†  
Taitech, Inc., Beaver Creek, Ohio 45440  
Abdollah S. Nejad‡

U.S. Air Force Wright Laboratory, Wright–Patterson AFB, Ohio 45433  
and  
Campbell D. Carter§  
Systems Research Laboratories, Inc., Dayton, Ohio 45440

The injection of supercritical fuel into a quiescent gas environment was experimentally studied to elucidate the effects of thermophysical and transport properties near the critical point on jet appearance, shock structures, and choking. Ethylene and nitrogen were used to simulate interactions between fuel and air. Conditions near the thermodynamic critical point of ethylene are considered, with supercritical temperatures and pressures upstream of the injector and subcritical pressures downstream of the injector. Flow visualization showed an opaque region resulting from fuel condensation when fuel was injected at near room temperature. At higher injectant temperatures, the ethylene jet was found to have a shock structure similar to that of an underexpanded ideal-gas jet. Mass flow rates were found to be insensitive to the variation of back pressure, indicating that the jet flow is choked. Mass flow rates were normalized by those values calculated for ideal-gas jets under the same conditions. The normalized mass flow rate first increases as injection conditions approach the critical temperature, apparently because of the rapid increase in fluid density, and then decreases, possibly as a result of the coexistence of liquid and gas phases at the nozzle exit.

## Nomenclature

$A$	= cross-sectional area
$a$	= speed of sound
$d$	= nozzle exit diameter
$h$	= fluid enthalpy
$M$	= Mach number
$M$	= gas molecular weight
$\dot{m}$	= fuel mass flow rate
$P$	= pressure
$R$	= universal gas constant
$Re$	= Reynolds number based on nozzle diameter, $\rho d u / \mu$
$T$	= temperature
$u$	= fluid velocity
$\gamma$	= gas specific heat ratio, $C_p/C_v$
$\mu$	= fluid viscosity
$\rho$	= fluid density

## Subscripts

chm	= gas property in injection chamber
$e$	= nozzle exit condition
ideal	= calculated property based on ideal-gas, isentropic-flow assumption
inj	= injectant property before reaching nozzle passage
$r$	= reduced property, normalized by its critical value

## Superscript

*	= choked condition
---	--------------------

## Introduction

FOR hypersonic flight, e.g., flight Mach numbers greater than 8, thermal management of the airframe and of on-board electronic components is an engineering challenge.<sup>1</sup> Conventional cooling techniques using ambient air are not feasible at hypersonic speeds because the stagnation temperature of the air is higher than the high-temperature limit of current aerospace materials. One solution to this problem would be regenerative fuel cooling of the airframe and the combustor components. Endothermic fuels are being investigated as candidates for this type of application.<sup>1</sup> An endothermic fuel is one that can undergo an endothermic thermal cracking (pyrolysis) reaction with a very large reaction heat. It has been shown that the thermal cracking reaction of endothermic fuels occurs at very high temperatures; *n*-dodecane, for example, is stable to 1100 K, before thermal cracking becomes significant. These reaction temperatures are generally much higher than the critical temperature of hydrocarbon fuels, e.g., the critical temperature for *n*-dodecane is 659 K, and the heat management of future aircraft is expected to require the use of supercritical fuels.<sup>1</sup>

The combustor operating conditions are vastly different for the missile's startup, boost, cruise, and final approach phases, and since fuel is used to absorb heat from the combustor for all phases, broad ranges of fuel operating temperatures and pressures are encountered. Thus, the regenerative fuel cooling approach increases the complexity of the fuel system and strongly affects injection and mixing mechanisms. Fuel may be injected as liquid under subcritical conditions or as gas under supercritical conditions, depending on the extent of heating and the fuel's thermodynamic states at the nozzle exit. Furthermore, supercritical fuels exhibit unusual thermophysical and transport properties near their critical point: liquid-like density, zero latent heat, zero surface tension, and low compressibility. These fuels also exhibit large variations in specific heats and speeds of sound, and enhanced values of thermal conductivity, viscosity, and mass diffusivity.<sup>2–4</sup>

An ethylene phase diagram of fluid density as a function of pressure is shown in Fig. 1; the diagram is based on the ther-

Received June 14, 1995; revision received Dec. 18, 1995; accepted for publication Jan. 4, 1996. Copyright © 1996 by the authors. Published by the American Institute of Aeronautics and Astronautics, Inc., with permission.

\*Research Scientist, 3675 Harming Drive. Member AIAA.

†Chief Scientist. Senior Member AIAA.

‡Senior Research Scientist, Aero Propulsion and Power Directorate.

§Research Scientist, 2800 Indian Ripple Road. Member AIAA.

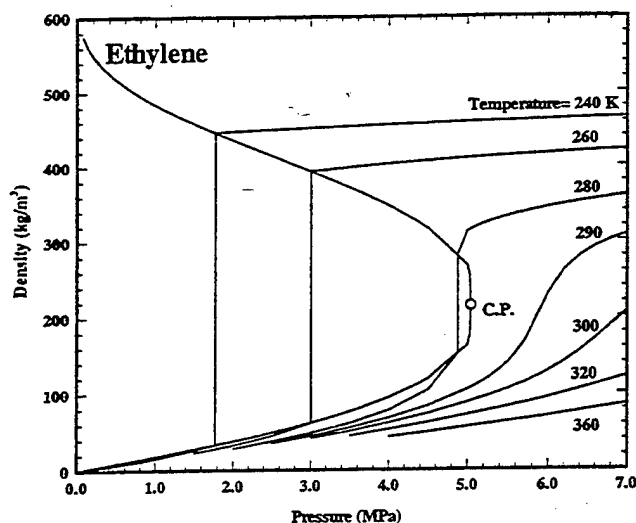


Fig. 1  $\rho$ - $P$ - $T$  diagram for ethylene.

mododynamic properties reported by Younglove.<sup>4</sup> Selected isotherms are plotted to illustrate the density variation; C.P. denotes the thermodynamic critical point. Note that the gradient of fluid density with respect to temperature and pressure is extremely large near the critical point. Thus, for an isothermal process starting at the critical point, a 10% decrease in fluid pressure results in a decrease in fluid density of more than 50%. This is a clear illustration of how the injection characteristics of a fuel under conditions near its critical point can be dramatically different from those of liquids<sup>5,6</sup> or ideal gases.<sup>7,8</sup>

Previous studies of supercritical fuel injection and atomization processes have been limited in scope and have focused primarily on processes at temperatures lower than the critical temperature of the fuel.<sup>9,10</sup> Chen<sup>9</sup> studied the atomization processes of sulfur hexafluoride ( $\text{SF}_6$ ) injected at near critical temperatures into quiescent gaseous environments and found that spray penetration decreases as fuel temperature increases. This decrease is related to the decrease of the density of the fuel as it enters the supercritical state. Hermanson et al.<sup>10</sup> studied the injection of cryogenic nitrogen near the critical temperature into a supersonic crossflow. They found a reduction in penetration height, compared to that observed for the injection of subcritical ethanol, which they attributed to a larger degree of superheat. Yang et al.<sup>11</sup> studied liquid-fuel droplet combustion in both subcritical and supercritical environments and suggested that the combustion mechanism changed considerably at the critical pressure, mainly as a result of reduced mass diffusivity and latent heat of vaporization with increased pressure. These studies indicate that the atomization, mixing, and burning processes of supercritical fluids are significantly different from those observed under subcritical conditions. However, no study has been conducted on the injection of supercritical fluids under conditions near and above the thermodynamic critical point.

The objective of the present investigation was to study the injection of a supercritical fuel at injection temperatures slightly greater than the fuel's critical temperature, with back pressures lower than the critical pressure. Therefore, the injection of ethylene starts the injection process under supercritical conditions and is superheated by the end of the process. Test conditions were designed to simulate injection of an endothermic fuel at temperatures between the critical temperature and the point where thermal cracking becomes significant. For *n*-dodecane, one of the endothermic fuels currently being tested, this temperature range comprises a range of reduced temperatures  $T_r$ , defined as temperature normalized by its critical value, of 1.0–1.67.<sup>1</sup> Therefore, in this study ethylene is

injected with  $T_r$  from 1.04 to 1.29, into quiescent nitrogen. For ideal gases with large enough variations of pressure, an underexpanded jet is obtained; this process has been well characterized.<sup>7,8</sup> The experimental results of the present study were compared with those from ideal-gas studies to illustrate the effects of near-critical-point thermophysical and transport properties on jet appearance and near-field shock structures. This article begins with a description of the experimental methods, followed by the results of a system validation using nitrogen as the injectant. Results for ethylene injection into ambient nitrogen are then discussed, treating flow visualization, mass flow rate measurements, and thermodynamic path analysis during injection. Finally, the differences between the injection processes of a supercritical fuel and an ideal gas are discussed.

## Experimental Methods

### Apparatus

The test fluid was injected vertically downward into a large injection chamber filled with an inert gas (nitrogen) to study the effects of fuel temperature and ambient back pressure on jet structure and mass flow rate for a fuel near its critical temperature. The apparatus consists of a fuel tank, a solenoid valve, a fuel temperature control unit, a nozzle, and the injection chamber (Fig. 2).

The fuel tank assembly was designed to allow preset initial fuel pressures and temperatures and to provide a steady fuel supply during injection. The fuel tank was a commercial ethylene bottle with an internal volume of 43.5 l. The large volume was necessary to minimize variations of injectant pressure during injection. Injection pressures were controlled to within  $\pm 1\%$  of the preset values for all present test conditions. The ethylene bottle and fuel tank were wrapped with copper tubes through which water at 313 K was circulated to prevent fuel condensation and to provide a constant initial fuel temperature. A solenoid valve with a response time of 150 ms was installed in the fuel delivery line to control the injection duration. Injection times were limited to 5–8 s to minimize fuel consumption and to maximize the number of test runs before a significant fuel vapor partial pressure was reached in the injection chamber.

Supercritical fuel temperatures were monitored with thermocouples and controlled by flowing ethylene glycol outside the fuel pipe along the fuel delivery line for a distance of over 6 m upstream of the nozzle. Through the use of a heat exchanger, the temperature of the ethylene glycol was maintained between 293–422 K, with an uncertainty of  $\pm 1$  K. Tests

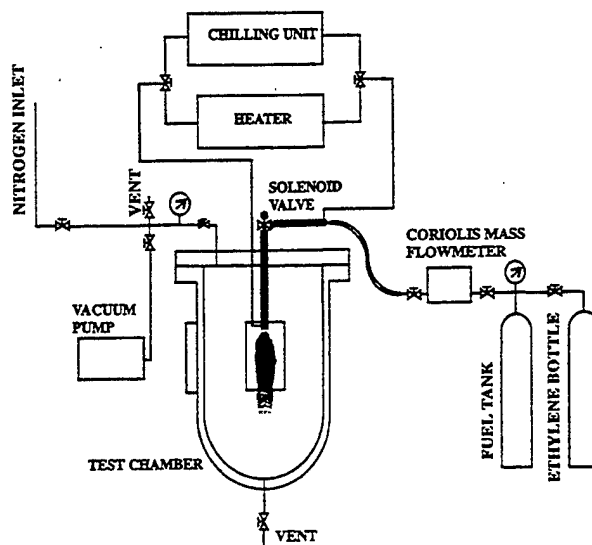


Fig. 2 Sketch of supercritical fuel injection apparatus.

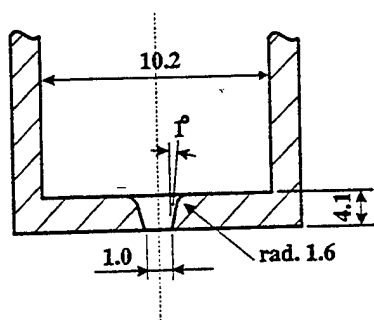


Fig. 3 Sketch of the nozzle passage; lengths are in mm.

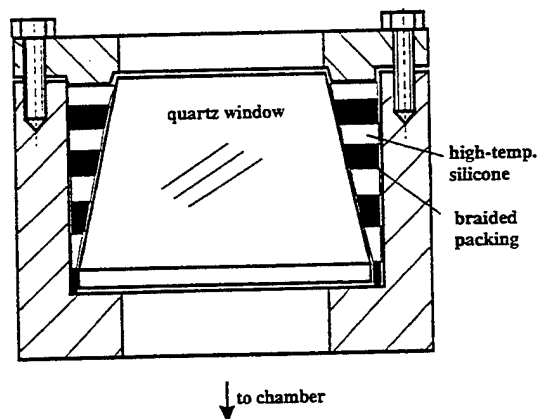


Fig. 4 Schematic diagram of the injection chamber window design.

showed that the final fuel temperature was within 2 K of the coolant temperature for moderate temperatures; the fuel temperatures reported in this study are the coolant temperatures. For higher temperatures, larger uncertainties would be expected (4 K), because of the limited heating capacity of the current heater arrangement. The fuel static pressure was measured upstream of the nozzle passage with a bridge-type pressure transducer having an uncertainty within  $\pm 7$  kPa. The measured fuel static pressure was used as the fuel stagnation pressure (injection pressure) in the following discussion, since the fluid velocities in the fuel delivery line were negligible. The measured pressure and temperature were then used to quantify the fuel properties before injection.

The nozzle passage consisted of a rounded entry and a converging section, as shown in Fig. 3. The entry, with a radius of 1.6 mm, was followed by a 1-deg converging passage to ensure that a choked point could occur only at the nozzle exit. The nozzle exit diameter was 1 mm, and the ratio of passage length to exit diameter was selected to be 4. This arrangement yielded a cross-sectional area ratio of the fuel delivery line to the nozzle exit passage of 104; this design minimizes the effect of upstream flow disturbances.<sup>12</sup>

To study the effects of ambient back pressure on the injection process, the fuel jet was enclosed in a large injection chamber. This chamber was designed to provide a high-pressure and temperature environment for the simulation of scramjet and gas turbine combustor conditions and industrial injector atomization processes. The chamber diameter is 0.42 m and its height is 0.94 m, resulting in an internal volume of 0.12 m<sup>3</sup>. Four optical ports are provided for flow diagnostics. Two 63.5-mm-thick rectangular quartz windows, each having a clear aperture of 89 × 127 mm, were installed on opposite sides of the chamber. These windows were supported from the back by layers of high-temperature silicone and graphite braided packing to ensure sealing at high chamber pressures and temperatures (Fig. 4). A rupture disc set for 9.4 MPa and a relief valve set for 6.8 MPa were attached to the chamber

for safety purposes. The chamber pressure was monitored by a second bridge-type pressure transducer, also having an uncertainty within  $\pm 7$  kPa. The chamber, with the windows installed, was hydrostatically tested to 7 MPa at room temperature.

Before measurements were made, the chamber was flushed with nitrogen to remove oxygen. The fuel pressure and temperature were set by charging the fuel tank to a specified pressure and adjusting the temperature controller of the fuel heat exchanger. Measurements were begun by activating the solenoid valve; fuel and chamber pressures and temperatures were then recorded by a high-speed data-acquisition board linked to a 486 personal computer. During each run, the rise in chamber pressure was typically less than 34 kPa. After each run, the chamber was vented and reset to the desired pressure.

#### Instrumentation

Long-exposure shadowgraphs were used to identify the thermodynamic phase (i.e., gas or liquid) of the injectant. A 35-mm Nikon camera with a shutter speed of 1/30 s and an  $f$ -number of 4.5 was used to capture the shadowgraphs. The magnification selected was about 1.63 to permit visualization of the entire jet field. Schlieren photographs were employed to resolve shock patterns and jet boundaries. The schlieren system used a Speed Graphic camera, loaded with a Polaroid type 57, 100 × 125 mm black and white film with a shutter speed of 1/125 s. Two 300-mm-diam parabolic mirrors, with focal lengths of 1220 mm, collimated and focused the light from a mercury lamp. The arrangement provided an image magnification of 4.15 and a 22 mm<sup>2</sup> field of view (FOV).

The fuel mass flow rate was measured by a Coriolis-type mass flow meter (Fig. 2). This flow meter is designed for direct measurement of the mass flow rate of any fluid at a stable thermodynamic state, with an uncertainty of less than  $\pm 1\%$ . However, the time response for this device is slow (approximately 4 s). During the present study, an injection duration of 8 s was normally employed, and mass flow rates were averaged for the last 4 s to obtain the mean mass flow rate for each run. Mass flow rates were averaged over five runs, yielding standard deviations of less than  $\pm 1\%$ .

#### Test Conditions

The fuel temperature and pressure were set to be slightly above the critical point to study the effect of near-critical-point thermophysical properties on the injection process. Ethylene was chosen as a test fuel because its critical temperature is near room temperature, which reduces system safety requirements. Nitrogen was used as the ambient gas because it is inert and has properties similar to air. The test conditions are summarized in Table 1. Fuel pressures and temperatures are expressed as reduced values (i.e., relative to the critical point values of 5.04 MPa and 283 K). The fuel injection pressure was set between 5.7–5.8 MPa,  $\pm 1\%$ , yielding reduced injection pressures from 1.13 to 1.15. Fuel temperatures were varied from 293 to 365 K, resulting in reduced temperatures from 1.04 to 1.29. Chamber pressures of 0.10–3.4 MPa provided ratios to the injection pressure ( $P_{\text{chm}}/P_{\text{inj}}$ ) of 0.018–0.59, which results in sonic and subsonic flows when nitrogen is the injectant. Jet Reynolds numbers at the nozzle exit were estimated to be between  $1.03\text{--}1.38 \times 10^6$  (see Table 2), based on the thermophysical properties of Younglove,<sup>4</sup> fluid viscosities from

Table 1 Summary of test conditions

Parameters	Ranges
$P_{\text{inj}}/P_c^*$	1.13–1.15
$T_{\text{inj}}/T_c^b$	1.04–1.29
$P_{\text{chm}}/P_{\text{inj}}$	0.018–0.59
$T_{\text{chm}}/T_c$	1.04

\* $P_c = 5.04$  MPa. <sup>b</sup> $T_c = 283$  K.

Holland et al.,<sup>3</sup> and the isentropic approximation (discussed next).

## Results and Discussion

### Injection of Nitrogen

Nitrogen was injected into nitrogen to validate the experimental system. Because nitrogen is an ideal gas under the test conditions, its injection process is well understood.<sup>8,13</sup> These tests, therefore, provided a means of assessing the overall system accuracy as well as estimating the discharge coefficient of the nozzle passage. Assuming the process to be one dimensional and isentropic and the fluid to be an ideal gas with constant specific heats, the mass flow rate  $\dot{m}$  through a circular cross-sectional nozzle (with an exit area  $A_e$ ) can be expressed as follows:

$$\dot{m} = \sqrt{2\gamma(\gamma-1)} \sqrt{(P_{\text{chm}}/P_{\text{inj}})^{(\gamma+1)/\gamma} [(P_{\text{chm}}/P_{\text{inj}})^{-(\gamma-1)/\gamma} - 1]} \times P_{\text{inj}} A_e / \sqrt{RT_{\text{inj}}/M} \quad (1)$$

When an ideal gas undergoes an isentropic process with constant  $\gamma$ , the ratio of injection pressure to nozzle exit pressure is a function of  $M$ :

$$P_{\text{inj}}/P_e = [1 + (\gamma - 1)M^2/2]^{(\gamma-1)} \quad (2)$$

The maximum value of  $(P_{\text{inj}}/P_e)$  for a convergent nozzle occurs when a sonic speed is reached at the nozzle exit ( $M = 1$ ). Further decreases of the chamber pressure do not alter the nozzle exit condition; i.e.,  $(P_{\text{inj}}/P_e)$  is a constant, but the nozzle exit pressure no longer equals the chamber pressure. For nitrogen,  $\gamma$  is equal to 1.50 under the injection conditions, and the choking pressure ratio  $(P_{\text{chm}}/P_{\text{inj}})^*$  is 0.512 from Eq. (2). The  $\dot{m}^*$  can be calculated by substituting  $(P_{\text{chm}}/P_{\text{inj}})^*$  into Eq. (1). The mass flow rate of a subsonic jet relative to that of a choked jet can then be written as

$$\dot{m}/\dot{m}^* = \sqrt{(P_{\text{chm}}/P_{\text{inj}})^{(\gamma+1)/\gamma} [(P_{\text{chm}}/P_{\text{inj}})^{-(\gamma-1)/\gamma} - 1]} / \sqrt{[(\gamma + 1)/2]^{-(\gamma+1)/(\gamma-1)} (\gamma - 1)/2} \quad (3)$$

For a sonic jet,  $\dot{m}/\dot{m}^*$  should be unity. The measured mass flow rates for nitrogen jets at different  $P_{\text{chm}}/P_{\text{inj}}$  were normalized by  $\dot{m}^*$ , using  $\gamma = 1.50$ . The normalized mass flow rates are plotted in Fig. 5, together with the calculated results from Eq. (3). A discharge coefficient of 0.97 for choked conditions and 1.03 for unchoked conditions is indicated. The agreement between experimental results and predictions is reasonable, considering the mass flow rate measurement uncertainty (1%) and the uncertainty of mass flow rate predictions from Eq. (3) (3.8%), because of uncertainties of pressure measurements and specific heat ratios. Therefore, the discharge coefficients differ from unity within experimental uncertainties. A near-unity discharge coefficient is expected based on values reported for nozzles with similar geometries.<sup>14,15</sup>

Figure 6 shows a schlieren photograph of nitrogen injected at 5.8 MPa and 293 K into nitrogen at atmospheric pressure and 293 K. The jet is highly underexpanded and produces a Mach disk at a distance of about 4.3 nozzle diameters downstream of the nozzle exit, in agreement with the prediction of 4.26 from the empirical correlation of Crist et al.<sup>8</sup> The shock structure, Mach disk, intercepting shock, and reflected shock appear clearly in the photograph. These structures will be used as a basis for comparison with the injection patterns of supercritical fuel in the following discussion.

### Flow Visualization of Ethylene Jets

#### Shadowgraphy

Typical shadowgraphs of ethylene jets injected at 5.7 MPa and 293 K into nitrogen at chamber pressures of 0.14, 0.41,

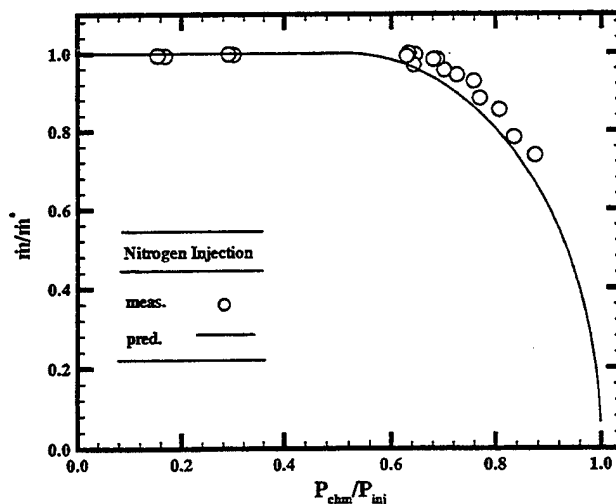


Fig. 5 Mass flow rates of nitrogen jets;  $\dot{m}^*$  is based on  $\gamma = 1.50$ .



$P_{\text{inj}} = 5.8 \text{ MPa}$   
 $P_{\text{chm}} = 0.14 \text{ MPa}$   
 $T_{\text{inj}} = 293 \text{ K}$

Fig. 6 Schlieren photograph of an underexpanded nitrogen jet.

1.36, and 3.4 MPa (resulting in  $P_{\text{chm}}/P_{\text{inj}}$  of 0.024–0.59) are illustrated in Fig. 7. Each jet undergoes a sudden expansion and produces a dome-shaped jet boundary at the nozzle exit to accommodate the large pressure drop. This dome-shaped jet boundary becomes less significant when the chamber pressure is increased, and the jet exhibits a straight surface at the nozzle exit when the chamber pressure is 3.40 MPa ( $P_{\text{chm}}/P_{\text{inj}} = 0.59$ ). These phenomena agree qualitatively with the transition of an ideal gas from an underexpanded sonic jet to a subsonic jet. The dome-shaped jet boundary near the nozzle exit suggests the presence of shock structures similar to those in a highly underexpanded ideal-gas jet. However, further evidence is needed to confirm this behavior and to resolve the shock structures.

The ethylene jets studied here produce strong fuel condensation and exhibit an opaque region. The opaque region exists even when the fuel injection pressure is below the critical pressure. This region gradually disappears when the condensed fuel absorbs sufficient heat from the ambient nitrogen and returns to the gas state. At the lowest  $P_{\text{chm}}$ , 0.14 MPa, the expansion is dramatic and fuel condensation is moderate. As the chamber pressure is increased to 0.41 MPa, the jet expansion is substantially less than that with  $P_{\text{chm}} = 0.14 \text{ MPa}$ ; however, the jet exhibits a much darker and longer opaque region that extends beyond the FOV, about 43 nozzle diameters. Fuel condensation on this scale can potentially absorb a large amount of heat, and, therefore, delay chemical reactions and reduce the performance of a supersonic combustor. As the chamber pressure is increased further, however, the opaque region be-

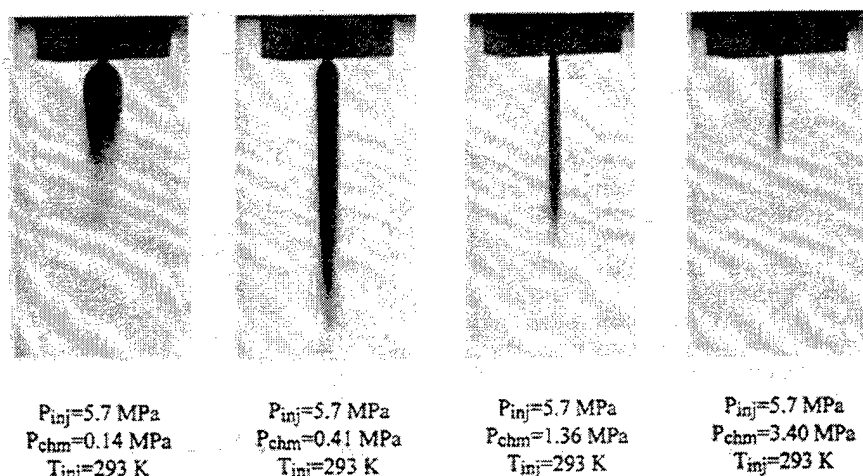


Fig. 7 Shadowgraphs of ethylene jets injected at 293 K into various chamber pressures.

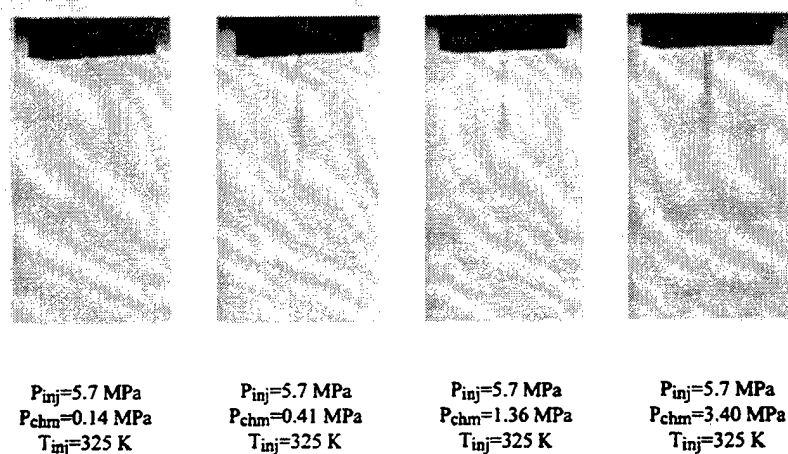


Fig. 8 Shadowgraphs of ethylene jets injected at 325 K into various chamber pressures.

comes shorter. Further studies are needed to characterize the fuel condensation phenomenon.

At higher injection temperatures, fuel condensation becomes less significant. Figure 8 shows shadowgraphs of typical ethylene jets injected at 5.7 MPa and 325 K into nitrogen at various chamber pressures. Note that only  $T_{inj}$  has been changed from the configuration discussed previously;  $P_{inj}$  remains the same. The ethylene jets still show condensation at this injection temperature, although the opaque region is smaller and not as dark as with  $T_{inj} = 293$  K. The qualitative trend of fuel condensation with respect to chamber pressures remains similar, and as at the lower  $T_{inj}$ , the dome-shaped expansion is still visible at lower  $P_{chm}$ . Shock structures can now be identified at the nozzle exit, indicating that the jet is sonic exiting the nozzle. Mach disk locations were found to be 4.3 and 2.5 nozzle diameters downstream of the nozzle exit for chamber pressures of 0.14 and 0.41 MPa, respectively. The correlation of Crist et al.<sup>8</sup> predicts 4.1 and 2.4 nozzle diameters downstream as the location of Mach disks under these conditions. The correlation of Crist et al.<sup>8</sup> describes the injection process of a nondiffusing homogeneous substance (e.g., nitrogen injection into nitrogen). However, effects of nonhomogeneity (ethylene and nitrogen) are expected to be negligible for the conditions of the present study because of the small flow residence times for supersonic flows in the shock plume and much lower chamber pressures than the ethylene critical pressure; this argument is supported by the good agreement between the predictions of Crist et al.<sup>8</sup> and the present experimental observations. Furthermore, the agreement suggests that the injection of supercritical fuel under the test conditions listed in Fig. 8 produces results that are similar, at least in

some respects, to those of an ideal gas. No measurement of Mach disk locations can be made at lower injection temperatures because of excessive fuel condensation. At higher injection temperatures, on the other hand, fuel condensation is so weak that shadowgraphy fails to record the jet image. Therefore, schlieren photography was employed to resolve the shock structures near the nozzle exit.

#### Schlieren Photography

Figure 9 shows schlieren photographs of ethylene injected at various temperatures (293, 325, 338, and 365 K) into nitrogen at 0.14 MPa and 293 K. The jets undergo a sudden expansion after leaving the nozzle. At lower temperatures, the ethylene jet exhibits an opaque region near the nozzle exit. As the injection temperature increases, the opaque region becomes lighter, and at  $T_{inj} = 338$  K the Mach disk and intercepting and reflected shocks become evident. This indicates that increases in temperature shift the thermodynamic path and, as a consequence, the fuel does not pass through the liquid-gas mixture regime.

As mentioned in reference to Fig. 8, ethylene jets at conditions of higher  $T_{inj}$  are similar in appearance to nitrogen jets. It can, therefore, be argued that an ethylene jet at higher  $T_{inj}$  is thermodynamically farther away from its critical point than a jet at lower  $T_{inj}$  and should behave more like an ideal gas. The Mach disk locations for jets at  $T_{inj} = 338$  and 365 K are about 4.1 and 3.9 mm, respectively, in close agreement to the value of 4.2 mm predicted by Crist et al.<sup>8</sup> Furthermore, Crist et al. found that the Mach disk location was a function of  $P_{chm}/P_{inj}$  alone, which agrees with the present observation.

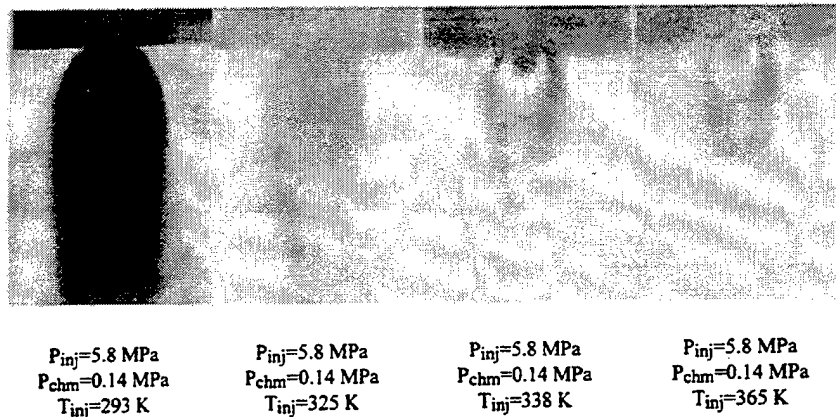


Fig. 9 Schlieren photographs of ethylene jets injected at various injection temperatures.

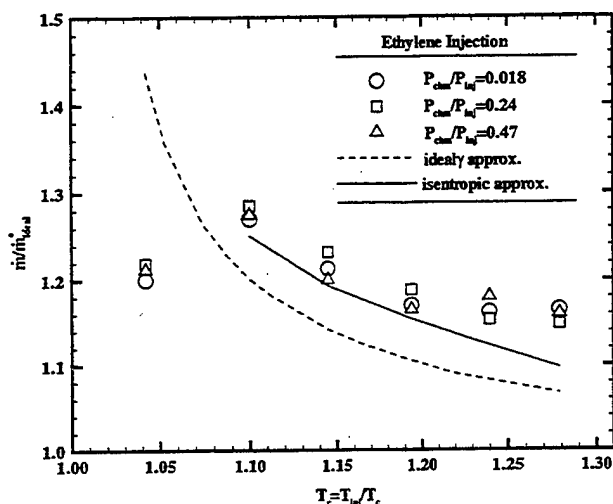


Fig. 10 Measured and calculated mass flow rates of ethylene jets under various injection conditions;  $\dot{m}_{ideal}$  is the rate using  $\gamma = 1.22$ . The idealy approximation is calculated from Eq. (3) using  $\gamma$  under fuel injection conditions, while the isentropic approximation considers the near-critical-point thermodynamic properties.

#### Mass Flow Rate Measurements

Nozzle mass flow rates were measured using a Coriolis-type mass flow meter to characterize 1) the injection processes of supercritical ethylene and 2) the effects of near-critical-point thermodynamic properties on nozzle choking. Measured mass flow rates were normalized by a choked mass flow rate calculated assuming ideal-gas behavior and isentropic flow. The calculated results, referred to as ideal choked mass flow rates, were obtained by substituting a widely used mean specific heat ratio of 1.22 for ethylene at room temperature and atmospheric pressure<sup>16</sup> into Eqs. (1) and (2). The normalized choked mass flow rates would not be temperature dependent if the ethylene were an ideal gas with constant specific heats. Therefore, the normalization demonstrates the effects of near-critical-point thermodynamic properties on the ethylene injection process.

Figure 10 shows the normalized mass flow rates vs reduced injection temperatures of the fuel at  $P_{chm}/P_{inj}$  of 0.018, 0.24, and 0.47. Mass flow rates are constant and are insensitive to increases in chamber pressure when the flow is choked. This phenomenon was observed for the present case: the mass flow rates varied less than  $\pm 2\%$  when  $P_{chm}/P_{inj}$  was increased from 0.018 to 0.47.

Ratios of measured and calculated ideal choking mass flow rates first increase as the thermodynamic critical temperature is approached and then decrease slightly at  $T_c = 1.04$ . The predicted mass flow rates are 10% lower at  $T_c = 1.28$ , and

more than 25% lower at  $T_c = 1.10$ , indicating that the ideal-gas isentropic-flow approximation with a specific heat ratio of 1.22 can lead to significant error if it is applied to supercritical fuels. Smaller  $\dot{m}/\dot{m}_{ideal}^*$  at higher temperatures indicates that supercritical fuel behaves more like an ideal gas as its thermodynamic state moves farther away from the critical point. This finding supports the conclusions drawn from the schlieren photographs (Fig. 9) for conditions of  $T_{inj} = 338$  and 365 K.

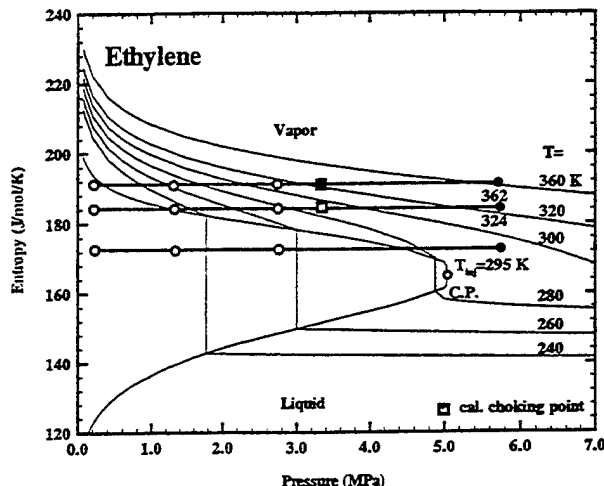
Another approach to the ideal-gas isentropic-flow approximation was developed using the specific heat ratio under fuel injection conditions.<sup>4</sup> Results from this approximation are plotted as a dashed line in Fig. 8 and referred to as the idealy approximation. This approximation underpredicts the measured values by about 7% when  $T_c \geq 1.10$ , and overpredicts significantly at  $T_c = 1.04$ . The good agreement for  $T_c \geq 1.10$ , however, is fortuitous. Based on the assumption of an ideal gas, the increase in specific heat ratio leads to overprediction of the speed of sound, which compensates for the underprediction of fluid density, and yields the observed trend. This idealy approximation has two other major failures. First of all, it fails to predict the mass flow rate at  $T_c = 1.04$ , where different injection processes are involved. One possible explanation, which will be discussed later in the consideration of thermodynamic injection paths, is that liquid and gas phases coexist at the nozzle exit. Secondly, the idealy approximation predicts incorrect ratios of nozzle exit to injection choking pressures and temperatures. As  $T_c$  decreases from 1.29 to 1.04, the approximation yields choked ratios of fluid pressure at the nozzle exit to injection pressure  $(P_c/P_{inj})^*$  from 0.517 to 0.290, and choked ratios of fluid temperature at nozzle exit to injection temperature  $(T_c/T_{inj})^*$  from 0.810 to 0.393. These results imply that flow at the nozzle exit is subsonic for  $T_c = 1.04$  and 1.10 when  $P_{chm}/P_{inj} = 0.47$ . This argument, however, contradicts the present observations because the mass flow rates with  $P_{chm}/P_{inj} = 0.018, 0.24,$  and 0.47 are the same within experimental uncertainties, indicating a choked and sonic condition.

To elucidate the injection process of supercritical ethylene, an isentropic-flow approximation considering near-critical-point thermodynamic properties was developed. This approximation does not require assumptions of constant specific heat ratios and ideal-gas state relations. The thermodynamic properties were calculated based on data from Younglove,<sup>4</sup> and an iterative procedure was used to calculate the choking mass flow rate. The entropy and enthalpy of the injection state were obtained, and an exit pressure was estimated. The fluid thermodynamic state at the nozzle exit was then determined based on the estimated pressure and the injection entropy; the fluid enthalpy and speed of sound at this state were then calculated. The exit velocity was derived from the one-dimensional energy equation, assuming negligible upstream velocity:

$$h_{inj} = h_c + u_c^2/2 \quad (4)$$

Table 2 Nozzle exit properties for choking conditions<sup>3,4</sup>

$T_{inj}/T_c$	$(P_e/P_{inj})^*$	$(T_e/T_{inj})^*$	$\rho_e$ , kg/m <sup>3</sup>	$\mu_e$ , 10 <sup>-7</sup> Pa·s	$a_e$ , m/s	$Re \times 10^{-6}$
1.100	0.572	0.878	61.1	113	253	1.38
1.145	0.572	0.876	53.2	109	271	1.33
1.194	0.572	0.880	47.6	116	287	1.18
1.240	0.570	0.884	43.6	119	299	1.11
1.279	0.569	0.892	40.5	122	310	1.03

Fig. 11 Thermodynamic paths of injection processes within the nozzle at  $T_{inj}$  of 295, 324, and 362 K.

If the calculated exit velocity is lower than the speed of sound at the estimated pressure (as given by Younglove<sup>16</sup>), a subsonic jet should result. A lower pressure was then estimated, and the procedure was repeated. If the calculated exit velocity is larger than the speed of sound, a larger exit pressure was used to repeat the procedure. Linear interpolation was used for simplicity, and the iteration stopped when the exit velocity was within 0.5 m/s of the speed of sound. Calculated choking conditions are listed in Table 2. These mass flow rates were normalized with the values from the ideal-gas isentropic-flow approximation and plotted as a solid line in Fig. 10.

The isentropic-flow approximation, which considers the near-critical-point thermodynamic properties, yielded mass flow rate values that are very close to the measured values: about 2% less than the measured values at  $T_r = 1.10$ – $1.20$  and about 6% less at  $T_r = 1.28$ . The larger discrepancy at  $T_r = 1.28$  may be attributed to the greater uncertainties in the injectant temperature at high temperatures because of the limitations of the heat exchanger. The calculated and measured values have the same trend;  $m/m_{ideal}$  increases as  $T_r$  decreases. Isentropic analysis may explain this phenomenon. The fluid density increases from 40.5 to 61.1 kg/m<sup>3</sup> as  $T_{inj}$  decreases from 362 to 311 K. The fluid speed of sound, however, decreases from 310 to 253 m/s. Since the nozzle exit cross section was the same in each case, the increase in choked mass flow rate is attributed to the large increase in fluid density. With  $T_r = 1.04$  and the assumption of an isentropic process, the final state is within the liquid–gas mixture regime. No calculation was made for this case.

Predicted choked pressure ratios  $(P_e/P_{inj})^*$  and choked temperature ratios  $(T_e/T_{inj})^*$  are also given in Table 2.  $(P_e/P_{inj})^*$  decreases from 0.572 to 0.569, and  $(T_e/T_{inj})^*$  increases from 0.878 to 0.892 as  $T_r$  increases from 1.100 to 1.279. These ratios approach the values of  $(P_e/P_{inj})^* = 0.561$  and  $(T_e/T_{inj})^* = 0.901$ , which are predicted by the ideal-gas isentropic-flow approximation with a specific heat ratio of 1.22. The increase in  $(P_e/P_{inj})^*$  and the decrease in  $(T_e/T_{inj})^*$  as the critical temperature is approached are apparently because of the unusual near-critical-point thermodynamic properties of the injectant

fluid; these ratios approach the ideal-gas values as the temperature is increased beyond the critical temperature.

#### Thermodynamic Paths of the Injection Processes Within the Nozzle

The injection processes of supercritical ethylene within the nozzle passage are illustrated on a thermodynamic chart of entropy vs pressure in Fig. 11. Selected isotherms corresponding to the present test conditions are identified, along with saturated liquid and vapor boundaries; C.P. denotes the critical point. Injection processes are assumed to be isentropic within the nozzle passage as indicated in the isentropic approximation, and to avoid confusion only three injection temperatures, 295, 325, and 362 K, were selected. Solid circles represent the initial injectant thermodynamic state, while open circles represent chamber pressures. Chamber pressures are the final pressures if the nozzle is not choked. If the nozzle is choked, the isentropic approximation is not valid outside the nozzle because of the underexpansion process and the normal shock wave (Mach disk). The square symbols denote the calculated onset choking pressure from the isentropic-flow approximation for the given injection pressure (see Table 2). Pressures lower than the onset pressures of the corresponding process indicate a choked condition.

At an injection temperature of 295 K, the constant-entropy line extends into the two-phase liquid–gas region; therefore, as indicated previously, the fluid may exist in two phases at the nozzle exit. The speed of sound of a water–air mixture in the dispersed phase varies with the void fraction and can be reduced to less than one-third of that of air at room temperature.<sup>17</sup> This may explain the observed lower mass flow rate at  $T_r = 1.04$  (Fig. 8). As the injection temperature increases, fluid at the nozzle exit, as predicted assuming an isentropic process, is gaseous. The predicted choking pressure, about 3.3 MPa, indicates that the exiting flows are, in fact, choked. Additionally, the calculated choking points are in the gas state and away from the critical temperature. Therefore, the ethylene jets should exhibit shock structures similar to those of nitrogen jets, in agreement with the observations made with schlieren photography.

#### Conclusions

The injection of supercritical ethylene at conditions near the thermodynamic critical point was studied. The experimental apparatus was validated with nitrogen injection, and the results were used as a basis for comparison with supercritical ethylene injection. The major conclusions are as follows:

- 1) Near the nozzle exit, supercritical ethylene jets exhibited an opaque region which, in the most extreme case, persisted for a distance of more than 40 nozzle diameters. This opaque region, which is believed to be caused by fuel condensation, disappears as injection temperature increases. The length of the opaque region increases when the ambient pressure increases from atmospheric pressure to about 0.41 MPa, and then decreases if the ambient pressure is increased further.
- 2) At higher injection temperatures, the supercritical ethylene jets exhibited shock structures similar to those of a highly underexpanded ideal-gas jet. The supercritical ethylene jets generated a Mach disk, intercepting shock, and reflected shock at the nozzle exit. Locations of Mach disks were compared to values predicted for ideal gases. Good agreement was ob-

tained, which indicates that the Mach disk location is insensitive to fuel type. However, the shock structure of ethylene jets at lower injection temperatures is obscured by fuel condensation, and no definite conclusion can be drawn under these conditions.

3) Jet mass flow rates were found to increase as the injection temperature approached the thermodynamic critical value. For the present test conditions, mass flow rates were about 10–25% higher than the mass flow rates calculated with the ideal-gas isentropic-flow approximation using a specific heat ratio of 1.22. A second ideal-gas isentropic-flow approximation was developed using the specific heat ratio at the injection conditions. The approximation underpredicts the measured values slightly (about 7%) for most conditions, because of the large specific heat ratios near the critical point. This approximation, however, predicts incorrect ratios of nozzle exit to injection choking pressures and temperatures.

4) An isentropic-flow approximation, which takes into account the near-critical-point thermodynamic properties, was developed for ethylene, and the resulting predicted mass flow rates agree reasonably well with the measured values. This approximation produced the same trend of mass flow rates vs reduced temperature, indicating that the increased mass flow rate (at lower reduced temperatures) is caused by the large density increase (characteristic of fluid near its critical point).

5) Thermodynamic path analyses revealed that ethylene may pass through a liquid–gas regime at lower injection temperature. This suggests the possible coexistence of liquid and gas phases at the nozzle exit. At higher injection temperatures, calculated choking pressures were greater than the maximum ambient chamber pressure, in agreement with the observation that mass flow rates are insensitive to chamber pressures since the present injection conditions are choked.

#### Acknowledgments

This work was supported by and performed at U.S. Air Force Wright Laboratory, Wright–Patterson Air Force Base, OH under Air Force Contracts F33615-93-C-2300 and F33615-92-C-2022. The assistance of K. Kirkendall, G. Haines, D. Schommer, and C. Smith of Taitech, Inc., for apparatus development, and of A. E. S. Creese for editorial comments concerning this article are appreciated.

#### References

<sup>1</sup>Edwards, T., "USAF Supercritical Hydrocarbon Fuels Interests," AIAA Aerospace Sciences Meeting, AIAA Paper 93-0807, Reno, NV, Jan. 1993.

<sup>2</sup>Nieto de Castro, C. A., "Thermal Conductivity and Thermal Diffusivity in Supercritical Fluids," *Supercritical Fluid Technology: Reviews in Modern Theory and Applications*, edited by T. J. Bruno and J. F. Ely, CRC Press, Boca Raton, FL, 1991, Chap. 9.

<sup>3</sup>Holland, P. M., Eaton, B. E., and Hanley, H. J. M., "A Correlation of the Viscosity and Thermal Conductivity Data of Gaseous and Liquid Ethylene," *Journal of Physical and Chemical Reference Data*, Vol. 12, No. 4, 1983, pp. 917–932.

<sup>4</sup>Younglove, B. A., "Thermophysical Properties of Fluids: I. Argon, Ethylene, Parahydrogen, Nitrogen, Nitrogen Trifluoride, and Oxygen," *Journal of Physical and Chemical Reference Data*, Vol. 11, Suppl. 1, 1982, pp. 58–96.

<sup>5</sup>Faeth, G. M., "Structure and Atomization Properties of Dense Sprays," *22nd Symposium (International) on Combustion*, The Combustion Inst., Pittsburg, PA., 1990, pp. 1345–1352.

<sup>6</sup>Wu, P.-K., Tseng, L.-K., and Faeth, G. M., "Primary Breakup in Gas/Liquid Mixing Layers for Turbulent Liquids," *Atomization and Sprays*, Vol. 2, No. 3, 1992, pp. 295–317.

<sup>7</sup>Adamson, T. C., and Nicholls, J. A., "On the Structure of Jets from Highly Underexpanded Nozzles into Still Air," *Journal of Aerospace Sciences*, Vol. 26, No. 1, 1959, pp. 16–24.

<sup>8</sup>Crist, S., Sherman, P. M., and Glass, D. R., "Study of the Highly Underexpanded Sonic Jet," *AIAA Journal*, Vol. 4, No. 1, 1966, pp. 68–71.

<sup>9</sup>Chen, L. D., "Heat Transfer, Fouling, and Combustion of Supercritical Fuels," Univ. of Iowa, F49620-92-J-0462, Iowa City, IA, 1994, pp. 6–25.

<sup>10</sup>Hermanson, T. C., Papas, P., and Kay, I. W., "Structure and Penetration of a Transverse Fluid Jet Injected at Supercritical Pressure into Supersonic Flow," AIAA Paper 92-3652, July 1992.

<sup>11</sup>Yang, V., Hsieh, K. C., and Shuen, J. S., "Supercritical Droplet Combustion and Related Transport Phenomena," AIAA Paper 93-0812, Jan. 1993.

<sup>12</sup>Ramjee, V., and Hussain, A. K. M. F., "Influence of the Axisymmetric Contraction Ratio on Free-Stream Turbulence," *Journal of Fluids Engineering*, Vol. 108, Ser. I, No. 3, 1976, pp. 506–515.

<sup>13</sup>Shapiro, A. H., *The Dynamics and Thermodynamics of Compressible Fluid Flow*, Vol. I, Wiley, New York, 1953, pp. 73–105.

<sup>14</sup>Arnberg, B. T., "Review of Critical Flowmeters for Gas Flow Measurements," *Journal of Basic Engineering*, Vol. 84, Ser. D, No. 4, 1962, pp. 447–460.

<sup>15</sup>Szanişzlo, A. J., "Experimental and Analytical Sonic Nozzle Discharge Coefficients for Reynolds Numbers Up to  $8 \times 10^6$ ," *Journal of Engineering for Power*, Vol. 97, Ser. A, No. 4, 1975, pp. 521–526.

<sup>16</sup>Baumeister, T., Avallone, E. A., and Baumeister, T., III, *Mark's Standard Handbook for Mechanical Engineers*, 8th ed., McGraw–Hill, New York, 1978, pp. 4–17.

<sup>17</sup>Wallis, G. B., *One-Dimensional Two-Phase Flow*, McGraw–Hill, New York, 1969.

**FEDSM97-3097**

## **THREE-DIMENSIONAL MIXING STUDY OF REACTING AND ISOTHERMAL FLOW BEHIND A BLUFF BODY FLAMEHOLDER WITH NORMAL FUEL JET INJECTION**

**Richard D. Gould**  
Dept. of Mechanical and Aerospace Engineering  
North Carolina State University  
Raleigh, North Carolina 27695, USA

**Campbell D. Carter**  
Innovative Scientific Solutions, Inc.  
3845 Woodhurst Ct.  
Beavercreek, Ohio 45430, USA

**Jeffery M. Donbar and Abdollah S. Nejad**  
Experimental Research Branch  
Aero Propulsion and Power Directorate  
Wright-Patterson AFB, Ohio 45433, USA

### **ABSTRACT**

Planar images of acetone and OH laser-induced fluorescence were made at 8 to 13 spanwise locations in the flow downstream of a bluff body flameholder with normal fuel jet injection. This study was initiated with the goals of obtaining a better understanding the jet mixing and penetration process, the size of the recirculation zone, the shear layer oscillation amplitude and frequency, and the three-dimensional flame structure behind a bluff body flameholder. A good semi-quantitative understanding of the complex time-dependent three-dimensional flow field was obtained using these scalars as flow tracers.

### **INTRODUCTION**

A recent interest in building flight vehicles with Mach 4 to 6 flight capability has put new demands on the fuel injection and flame stabilizing hardware. At these high speeds the inlet air is at such a high temperature that it can no longer be used to cool the fuel injectors and flameholder. Injection of the fuel upstream of the flameholder also presents a problem as the fuel would auto-ignite and the high temperature combustion gases would destroy the flameholder. One proposed approach is to use an integrated fuel-injector flameholder (IFF), as proposed by Hautman et al. (1990). This device uses the fuel flowing through the flameholder as a heat sink, thus allowing the flameholder to survive in the high temperature environment.

The objective of this study was three fold: 1.) design and fabricate a well characterized an easily controlled experimental

facility to study the three-dimensional flow structure behind a model bluff body flameholder with normal fuel jet injection, 2.) develop experience in applying optical diagnostics (laser Doppler velocimetry and planar laser-induced acetone/OH fluorescence) in this flow field, and 3.) make preliminary measurements of the flow structure behind a model bluff body flameholder with normal jet fuel injection using propane (with combustion) and CO<sub>2</sub> (without combustion). It is envisioned that these preliminary measurements, some of which are presented here, will be used as a guide to help design future bluff body geometries and to select operating conditions. It should be pointed out, however, that rather low fuel jet to cross-stream momentum ratios were required here since the inlet air was nearly room temperature (far lower than the auto-ignition temperature) and the cross-stream velocity was much higher than the flame speed at this temperature. Large jet momentum ratios typical of the normal jet in cross-stream studies, which produce large penetration depths, were not possible for these inlet conditions as the unburned fuel would simply travel downstream without being entrained in the recirculation zone behind the bluff body. This would not be the case with the inlet air above the auto-ignition temperature.

In particular, planar images of acetone and OH laser-induced fluorescence were made at 8 to 13 spanwise locations in the flow downstream of a bluff body flameholder with normal fuel jet injection. The fuel jet (propane or CO<sub>2</sub>) was seeded with acetone vapor, which fluoresces in the band between 350 - 550 nm when excited with UV laser light, so

that its trajectory and mixing could be studied. Three different fuel jet velocities were used and the flow behind the bluff body was studied both with and without combustion. Three-dimensional contour plots of acetone and/or OH species concentration were constructed using the 8 to 13 two-dimensional planar images.

A number of studies have been conducted in an effort to better understand the mixing process behind flameholders. Bluff body, as opposed to streamlined body, flameholders are typically used in combustion systems as they are of smaller mass for the same recirculation zone size behind the bodies. Spring et al. (1992) studied whether improved mixing behind the bluff body could be enhanced by adding vortex generators attached to the base of the bluff body. Simple two and three-dimensional bluff bodies, without combustion, have been the subject of experimental investigations for a number of years. A brief list of these include: Fuji et al. (1978), Perry and Steiner (1987), Durao et al. (1988), Williamson (1989) Muansingh and Oosthuizen (1990) and Raffoul et al. (1995a,b). The isothermal flow behind V-gutter shaped flameholders, of various geometries, were studied by Hosokawa et al. (1993). Some pertinent studies of flows behind bluff bodies with combustion, but without swirl, include those by: Fuji and Eguchi (1981), Sjunnesson et al. (1991) and Hosokawa et al. (1996). Classical studies of normal jets in a cross-stream include: Keffer and Baines (1963), Kamotani and Greber (1972), Chassing et al. (1974) and Fearn and Weston (1974).

## TEST FACILITY

Experiments were conducted in test cell 18 at the Aero Propulsion and Power Directorate at Wright Laboratory. The test facility is supplied by air compressors which are controlled using a bypass valve to provide a nearly constant 1.5 MPa (220 psia) supply pressure upstream of the test facility flow control

valve. A manifold downstream of the control valve is used to connect three high pressure 50.8 mm (2 in.) diameter hoses to the test facility feed pipe. Figure 1 shows a schematic of the flow system components. A 101.6 mm (4 in.) diameter calibrated vortex flow meter is used to determine the volumetric flow rate of air. Pressure and temperature measurements downstream of the flow meter allow the density to be determined, and thus, the mass flow rate. An orifice plate with a 31.75 mm (1.25 in.) diameter hole is used to choke the flow so that test section and supply system disturbances are isolated from one another and also to increase the pressure and thus density at the flow meter, extending its flow range capability. The flow then travels through a 152.4 mm (6 in.) diameter pipe into a settling chamber having an inside diameter of 482.6 mm (19 in.) and an overall length of 1.32 m (52 in.). A core buster, constructed out of perf-plate formed into a cone with an apex angle of 90°, is used to diffuse the high velocity air exiting the pipe at the inlet to the settling chamber. Four 482.6 mm (19 in.) diameter sheets of perf-plate, separated by 76.2 mm (3 in.) are located downstream of the core-buster and are used to equalize the pressure across the settling chamber. These are followed by a flow straightener constructed out of 76.2 mm (3 in.) thick, 6.35 mm (1/4 in.) cell size honeycomb sheet. A specially designed 304.8 mm (12 in.) long nozzle was fabricated out of plastic, using a stereo lithography process, to transition the flow from 457.2 mm (18 in.) diameter round to a 152.4 × 152.4 mm dimension square cross-section.

The test section is connected to the settling chamber with a 482.6 mm (19 in.) long by 152.4 × 152.4 mm inside dimension square cross-section transition section. Round rods, 1.587 mm (1/16 in.) in diameter were epoxied to the side walls of the transition section at the upstream end in order to trip the boundary layers so that they are turbulent. Each side wall of

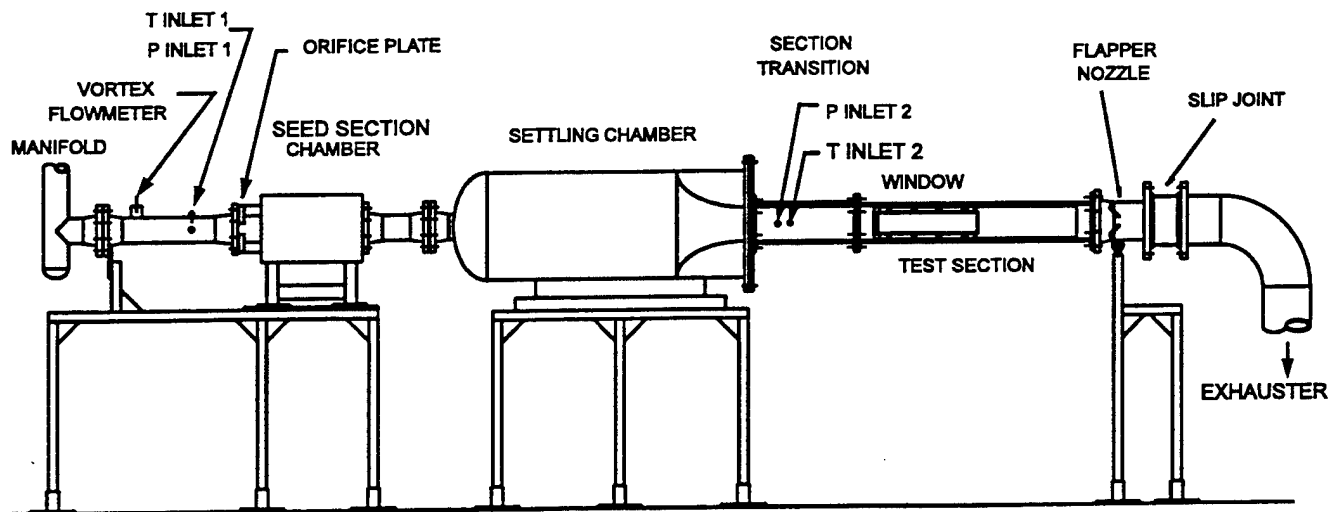


Figure 1 Flow facility in test cell 18 of the Aero Propulsion and Power Directorate at Wright Laboratory

the test section is constructed of an inside plate made of copper and an outside plate made of stainless steel. These plates are mated together using o-ring seal screws and silicon o-ring cord stock. Water passage grooves were machined in the copper plate so that the test section can be cooled. Inserts were machined in each of these walls to receive easily removable 19.05 mm (.75 in.) thick optical quality quartz windows. A window frame design was used so that all inside surfaces are flush with one another. Ports for pressure transducers and thermocouples were also included. Finally, two hinged, water cooled, user adjustable plates were located at the exit of the test section so that the flow could be choked at the exit of the test section. This feature allows the selection of test section pressure independent of flow velocity. The air facilities exhaustor in test cell 18 provided an exhaust pressure of 41.2 kPa (6 psia).

All pressure, temperature and flow devices are interfaced to a NEFF model 470 series 16 bit A/D data acquisition system interfaced to a personal computer. Air and fuel mass flow rates, pressures, temperatures, air and fuel reference velocities, fuel/air ratio and fuel jet to cross-stream flow momentum ratio are calculated and updated on the computer screen 20 times per second.

#### BLUFF BODY FUEL INJECTOR FLAMEHOLDER

The bluff body fuel injector, flameholder was fabricated out of stainless steel. Figure 2 shows the geometry of this component. The 50.8 mm long by 25.4 mm thick (height) by 151.89 mm span bluff body has a 12.7 mm hemispherical radius nose. The bluff body is oriented with its hemispherical nose facing upstream toward the incoming flow. Two fuel ports are machined into the side of this flameholder. The upstream port is used to supply fuel (propane in this study) to normal fuel jets located at the center span on the top and bottom of the bluff body while the downstream port contains a specially design propane/air torch igniter. The torch is ignited using an electrical spark prior to turning on the main fuel and is turned off once a stable flame is established behind the bluff body flameholder. One of four interchangeable main fuel jet orifice sizes can be selected. The 7.81 mm diameter top and bottom orifices were used in this study.

Gaseous propane and CO<sub>2</sub> were used as the "fuels" in this study: propane for the reacting flow studies and CO<sub>2</sub> for the isothermal flow studies. Since CO<sub>2</sub> has the same molecular weight as propane, comparisons between the flow structure downstream of the bluff body with and without combustion could be conducted where both "fuel" mass flow rate and jet to cross-stream momentum ratio could be matched simultaneously. A Tylan Model FC262HP mass flow meter, interfaced to the NEFF data acquisition system, was used to measure the total fuel flow rate through the two normal jet orifices. Using a system of valves, the propane or CO<sub>2</sub> could either be connected directly to the bluff body main fuel port or to a flow loop so that the fuel could be "bubbled" through a

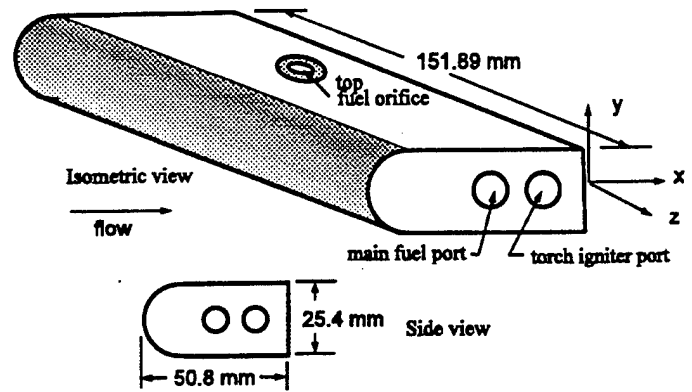


Figure 2 Bluff body fuel injector flameholder

temperature controlled reservoir containing liquid acetone. The acetone vapor was used to "seed" the fuel and thus was used as a marker for unburned fuel.

#### PLANER LASER-INDUCED FLUORESCENCE

The planer laser-induced fluorescence (PLIF) system used for this study is shown schematically in Figure 3. The laser beam for OH (Kohse-Hoinghaus, 1994) and acetone (Lozano et al., 1992) laser-induced fluorescence (LIF), produced from a Quanta-Ray Nd:YAG-pumped dye laser system, was spread into a sheet using a short focal length negative cylindrical lens and a 500-mm focal length, 100-mm diameter spherical lens; the resulting sheet dimensions (width and thickness) were ~100 mm by ~0.50 mm at the probe volume. For OH LIF, the doubled-dye output, ~10 mJ per pulse (at the probe volume) was tuned to the R<sub>1</sub>(8) transition of the A<sup>2</sup>Σ<sup>+</sup>-X<sup>2</sup>Π(1,0) band (λ=281.34 nm) (see Dieke and Crosswhite, 1961). Though the R-branch transitions are weaker than those in the P and Q branches (Dimpfl and Kinsey, 1979; Chidsey and Crosley 1980), fluorescence signals were sufficient, and absorption of the beam propagating through regions of high OH concentration is somewhat reduced by pumping a weaker transition. OH and acetone fluorescence was recorded using a Princeton Instruments 576 × 384 pixel intensified CCD camera fitted with a UV Nikkor lens. Nominal camera gain settings were varied between 9.0 and 9.5. Schott colored-glass filters, WG-295 and BG-1, rejected scattered radiation and transmitted fluorescence from the dominant (1,1)- and (0,0)-bands (λ ≈ 306-320 nm), where the (0,0)-band fluorescence is preceded by vibrational energy transfer from v'=1 to v'=0 (Paul, 1995). Of course, some of the fluorescence, principally the (0,0)-band component, is strongly absorbed as it propagates through the flame. To ensure that the doubled-dye output remained tuned to the R<sub>1</sub>(8) transition, the OH LIF signal from a laminar reference flame was continuously monitored and small adjustments to the dye-laser tuning were made as necessary. Signals were maintained to within ± 20% over the duration of the experiment. For recording the acetone



mean velocity in the core region of the flow and less than 3% of the mean velocity at the points closest to the walls in the boundary layers. Figure 4 shows vertical profiles (top to bottom) of the axial velocity at three spanwise locations while Figure 5 shows horizontal profiles (along span direction) of the axial velocity at three vertical locations. Note that the inlet velocities are nearly constant across the span of the flow as shown by the three profiles in Figure 4. Figure 5 indicates that these profiles will not start changing until one moves out toward the walls ( $> \pm 55.88$  mm (2.2 in.)) where the side wall boundary layers start having an effect. Also, Figure 5 shows the deficit velocity across the span of the flow at  $y = 0$  due to the blockage from the bluff body. The numerically integrated mass flow rate using the center span ( $z = 0$ ) velocities (Fig. 4) was found to be 1.161 kg/s (2.56 lbm/s), while that using the center height ( $y = 0$ ) velocities (Fig. 5) was found to be 1.132 kg/s (2.495 lbm/s). Considering the three-dimensional shape of these profiles, due to blockage from the bluff body and to the boundary layers, it was determined that these values are

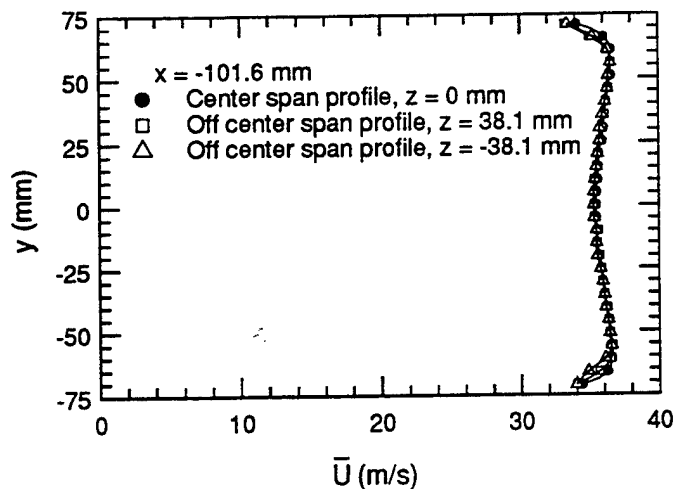


Figure 4 Inlet axial velocity profiles at three span locations

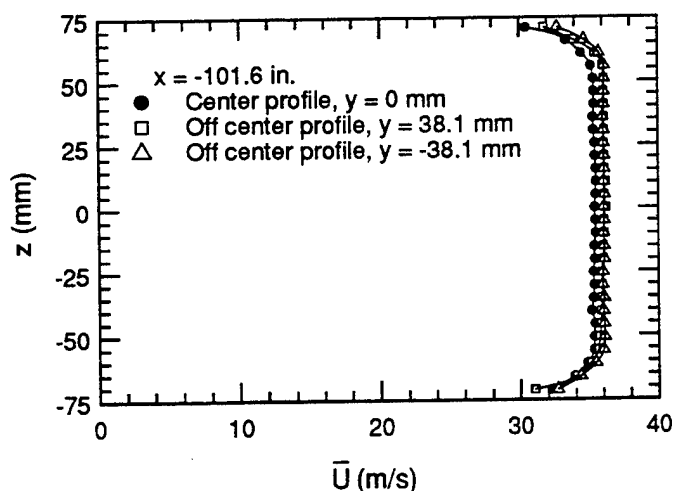


Figure 5 Inlet axial velocity profiles at three vertical locations

consistent with one another and that they are in good agreement with the vortex flow meter measurements.

Nominal air flow conditions for the PLIF studies were:  $\dot{m} = 0.578 \pm 0.011$  kg/s ( $1.275 \pm 0.025$  lbm/s),  $P_{in,2} = 111.7 \pm 1.38$  kPa ( $16.2 \pm 0.2$  psia),  $T_{in,2} = 22.2^\circ\text{C} \pm 1.1$  ( $72 \pm 2.0$  °F),  $U_{ref} = 18.90 \pm 0.31$  m/s ( $62.0 \pm 1.0$  ft/s). Note that the air velocity had to be reduced from that used for the inlet velocity profile survey so that a flame could be stabilized for a reasonable length of time behind the bluff body flameholder. Many attempts were made to light and stabilize a flame behind the bluff body at the higher flow rate without much success. Not only was lighting the flame difficult, as it required slowly increasing the fuel and air flow until the test conditions were reached, but in many cases the flame behind the bluff body extinguished shortly after the torch igniter was shut off. Based on this, it was decided to reduce the air flow rate by about a factor of two for the combustion studies.

Three fuel jet flow conditions were used in this study (Table 1). Note that the fuel mass flow rate and the fuel jet reference velocity (i.e. equivalent uniform velocity) account for fuel flowing out of the 7.81 mm diameter top and bottom orifices. Also included in Table 1 is the fuel jet to air cross-stream momentum ratio. The values in Table 1 are for both  $\text{CO}_2$  (isothermal case) and propane (reacting case) since the molecular weight is the same for both of these gases.

Table 1. Nominal fuel jet flow conditions

	Low	Medium	High
$\dot{m}$ (kg/s) (lbm/s)	$0.0263 \pm 2\%$ (0.058)	$0.0499 \pm 2\%$ (0.11)	$0.0708 \pm 2\%$ (0.156)
$U_{fuel}$ (m/s) (ft/s)	$2.286 \pm 2\%$ (7.5)	$4.572 \pm 2\%$ (15.0)	$6.096 \pm 2\%$ (20.0)
Mom. ratio	0.021	0.078	0.15

## EXPERIMENTAL RESULTS AND DISCUSSION

Although measurements were made at three fuel jet flow rates, only the results for the medium fuel flow rate will be discussed here. It should be pointed out that the general features of the flow behind the bluff body flameholder were similar at all three fuel jet flow rates. The low flow rate case tended to be more stable as indicated by high speed (200 frames/sec) video recordings. As the fuel flow rate was increased the flow structure behind the bluff body became more oscillatory. In fact, it appeared that the flame oscillated between two different flow modes at these higher fuel flows (higher heat release rates). In one mode, the flame stretched in the downstream direction and appeared to momentarily detach from the fuel jet. After this event, the flame propagated upstream towards the bluff body and reattached near the back of the bluff body. This motion was superimposed on the shear layer flapping motion and the complicated three-dimensional flow around the jet core (i.e. the horseshoe vortex structure) into the separated region immediately behind the bluff body. At the high fuel flow rate this oscillation became more severe and during some of the testing the flame blew out.

Figures 6 through 8 show PLIF images of OH and acetone (marking the fuel), acetone with combustion (i.e. OH signal filtered out) and acetone without combustion (CO<sub>2</sub> injection), respectively, across the span of the bluff body with normal fuel jet injection for the medium fuel flow rate. All dimensions given in these figures are in mm and the coordinate system corresponds to that given in Fig. 2. The  $x = 0$  location of these images is slightly upstream of the leading edge of the fuel orifices. Recall that the laser sheet propagates from the bottom to the top of the test section. As such, the bluff body blocks the laser sheet above the bluff body except when the sheet passes through the fuel jet orifice near the center span of the flow. Due to symmetry, one expects the features in this blocked region on the top to be similar to those in the corresponding region on the bottom. Comparing the images in Fig. 6 with those in Fig. 7 shows that the unburned fuel, denoted by the acetone fluorescence signal in Fig. 7, stays near the center span ( $z < 10$  mm), while the OH concentration shown in Fig. 6, denoting products of combustion, extends all the way out to the last measurement station ( $z = 34$  mm). This indicates substantial spanwise flow structure which was also confirmed with video recordings. As mentioned earlier, a flame could only be stabilized for cases with low fuel jet to cross-stream momentum ratio. These images show that the fuel has to stay very close to surface of the bluff body, perhaps in the boundary layer, in order to be entrained by the separated flow shear layer behind the bluff body. Otherwise the unburned fuel simply flows downstream at the cross-stream velocity. Thus, comparison of jet penetration and jet trajectory with classical studies, which are for relatively high jet to cross-stream momentum ratios, was not done here. Figure 8 shows the location of the CO<sub>2</sub> fuel jet without combustion. Comparison of these images with those in Fig. 7 allows one to study the effect of heat release on the fuel jet trajectory. The acetone PLIF images in Fig. 8 show that acetone spreads in the spanwise direction out to 16 mm, while the images shown in Fig. 7 indicate that there is very little fuel at  $z = 12$  mm. The reduction in acetone concentration in the reacting flow case may be due to reduced acetone number density (i.e. high temperature and nearly constant pressure), to the consumption of acetone by the flame, or a combination of these.

Figures 9 through 11 use the same data used to create Figs. 6 through 8, respectively, but are presented from an end view perspective. The fuel jet cross sections are easily identified in these views. Also, note that OH (Fig. 9) fills the entire recirculation zone behind the bluff body. It should be pointed out that the fuel jet structure shown in Figs. 10 and 11 may actually be more similar downstream of the bluff body than indicated, as no acetone vapor (marking unburned fuel) would be expected in the hot region behind the bluff body in the reacting flow case (Fig. 10). Finally, the shear layer (and thus flame front) shedding frequency was measured by propagating a HeNe laser beam across the span of the flow in the shear layer behind the bluff body flameholder. Beam bending, due to refractive index gradients, was measured using a pinhole in front of a photodetector. A shedding frequency of 50 Hz was measured corresponding to a Strouhal number of 0.067 based on bluff body height and inlet reference velocity.

This is quite different from the value of  $\approx 0.21$  found for shear layers behind bluff bodies in isothermal flows without fuel injection (Raffoul et al., 1995b).

## CONCLUSIONS

The planar laser-induced fluorescence technique was used to determine the relative OH/acetone concentration levels behind a bluff body flameholder with normal fuel jet injection in a large scale test facility. This preliminary study indicates that a series of time averaged two-dimensional images can be combined to give insight into the time averaged three-dimensional structure behind the bluff body. Fuel jet trajectory, regions of burned and unburned fuel, the effects of heat release on fuel jet trajectory, and the size and spanwise extent of the recirculation zone were determined using this technique.

## ACKNOWLEDGMENTS

The authors wish to thank the United States Air Force for their support of this research. In addition, the first author would like to express sincere gratitude to the United States Air Force Office of Scientific Research for the support of him during his one year stay at Wright Laboratory through the University Resident Research Program.

## REFERENCES

- Chassing, P., George, J., and Claria, A., (1974), "Physical Characteristics of a Subsonic Jet in a Cross-Stream," *Journal of Fluid Mechanics*, **62**, p. 41.
- Chidsey, I. L., and Crosley, D. R., (1980), "Calculated Rotational Transition Probabilities for the A-X System of OH," *JQSRT*, **23**, pp. 187-199.
- Dieke, G. H., and Crosswhite, H. M., (1961), "The Ultraviolet Bands of OH," *JQSRT*, **2**, pp. 97-199.
- Dimpfl, W. L., and Kinsey, J. L., (1979), "Radiative Lifetimes of OH(A<sup>2</sup>Σ) and Einstein Coefficients for the A-X System of OH and OD," *JQSRT*, **21**, pp. 233-241.
- Fearn, R., and Weston, R. P., (1974) "Vorticity Associated with a Jet in a Cross stream," *AIAA Journal*, **12**, p. 1666.
- Fuji, S., Gomi, M., and Eguchi, K., (1978), "Cold Flow Tests of a Bluff-Body Flame Stabilizer," *Journal of Fluids Engineering*, **100**, pp. 323-332.
- Fuji, S., and Eguchi, K., (1981), "A Comparison of Cold and Reacting Flows Around a Bluff Body Flame Stabilizer," *Journal of Fluids Engineering*, **103**, pp. 328-334.
- Hautman, D. J., Pfau, D. J., and Anderson, T. J., (1990), "Combustion Tests in a Ramjet Test Combustor," 27<sup>th</sup> JANNAF Combustion Mtg, II, pp. 421-434, Cheyenne WY.
- Hosokawa, S., Ikeda, Y., Minato, M., and Nakajima, T., (1993), "Flow Measurements Behind V-Gutter Under Non-Combusting Condition," AIAA Paper 93-0020.
- Hosokawa, S., Ikeda, Y., and Nakajima, T., (1996), "Effect of Flame Holder Shape on Vortex Shedding," AIAA Paper 96-3130.
- Keffer, J. F., and Baines, W. D., (1963), "The Round Turbulent Jet in a Cross-wind," *J. Fluid Mech.*, **15**, p. 481.
- Kohse-Hoinghaus, K., (1994), "Laser Techniques for the Quantitative Detection of Reactive Intermediates in Combustion Systems," *Prog. Energy Combust. Sci.* **20**, pp. 203-279.
- Lozano, A., Yip, B., and Hanson, R. K., (1992), "Acetone: A Tracer for Concentration Measurements in

Gaseous Flows by Planar Laser-induced Fluorescence," *Experiments in Fluids*, 13, pp. 369-376.

Mansingh, V., and Oosthuizen, P., (1990), "Effects of Splitter Plates on the Wake Flow Behind a Bluff Body," *AIAA Journal*, May, pp. 778-783.

Paul, P. H., (1995), "Vibrational Energy Transfer and Quenching of OH  $A^2\Sigma^+(v'=1)$  Measured at High Temperatures in a Shock Tube," *J. Chem. Phys.* 99, p. 8472.

Perry, A., and Steiner, T., (1987), "Large-Scale Vortex Structures in Turbulent Wakes behind Bluff Bodies: Part 1. Vortex Formation Processes," *J. Fluid Mech.*, 174, p. 233.

Raffoul, C., Nejad, A., Gould, R., and Spring, S., (1995a), "An Experimental and Numerical Study of the Isothermal Flowfield Behind a Bluff Body Flameholder," *ASME Turbo Expo '95*, Houston, TX, June 5-8, 95-GT-102, and *J. of Engr. for Gas Turbines & Power*, 119, p. 328-339, 1997.

Raffoul, C., Nejad, A., and Gould, R., (1995b), "Three-Component Velocity Measurements Downstream of a Bluff-Body Flameholder," WL-TR-95-2120.

Sjunnesson, A., Olovsson, S., and Sjoblom, B., (1991), "Validation Rig - A Tool for Flame Studies," 10<sup>th</sup> Intl. Sym. on Air Breathing Engines (ISABE), Nottingham, England.

Williamson, C. H. K., (1989), "Three-Dimensional Aspects and Transition of the Wake of a Circular Cylinder," *Turbulent Shear Flows 7*, Springer-Verlag, pp. 173-194.

Yasuhiro, K. and Greber, I., (1972), "Experiments on a Turbulent Jet in a Cross Flow," *AIAA Journal*, 10, p. 1425.

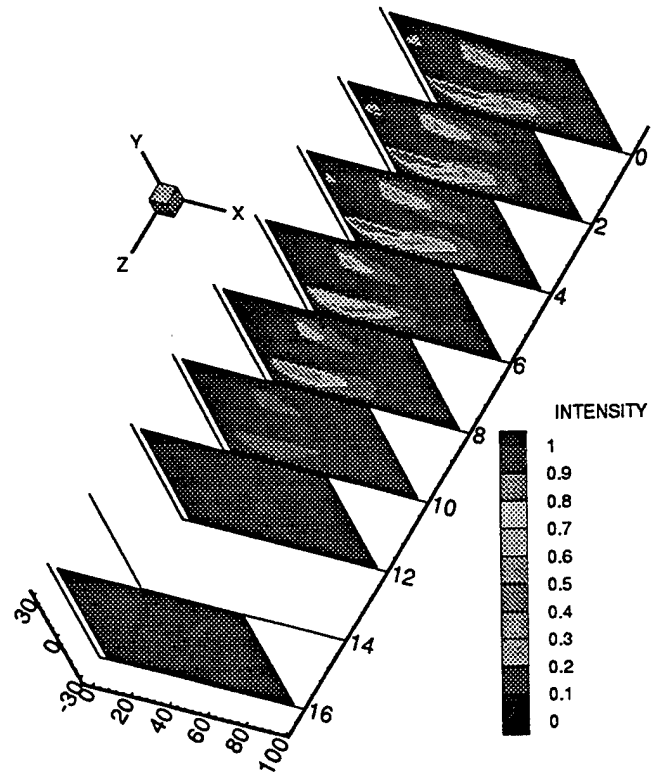


Figure 7 Acetone PLIF images across bluff body span with combustion at medium fuel flow rate

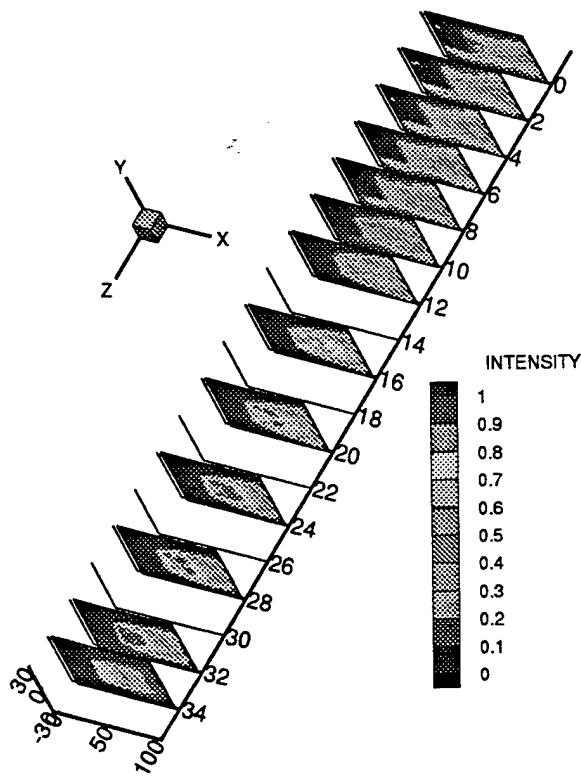


Figure 6 OH and acetone PLIF images across bluff body span with combustion at medium fuel flow rate

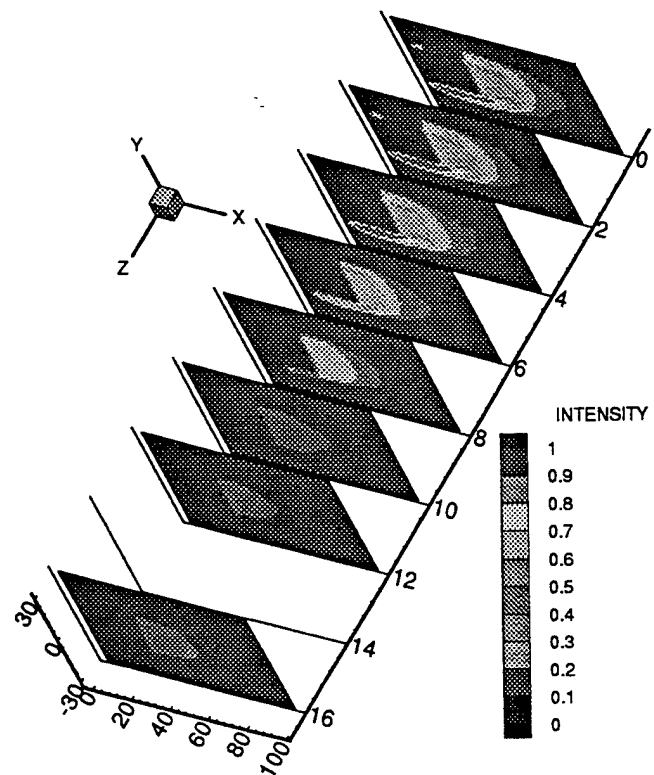


Figure 8 Acetone PLIF images across bluff body span without combustion at medium CO<sub>2</sub> flow rate

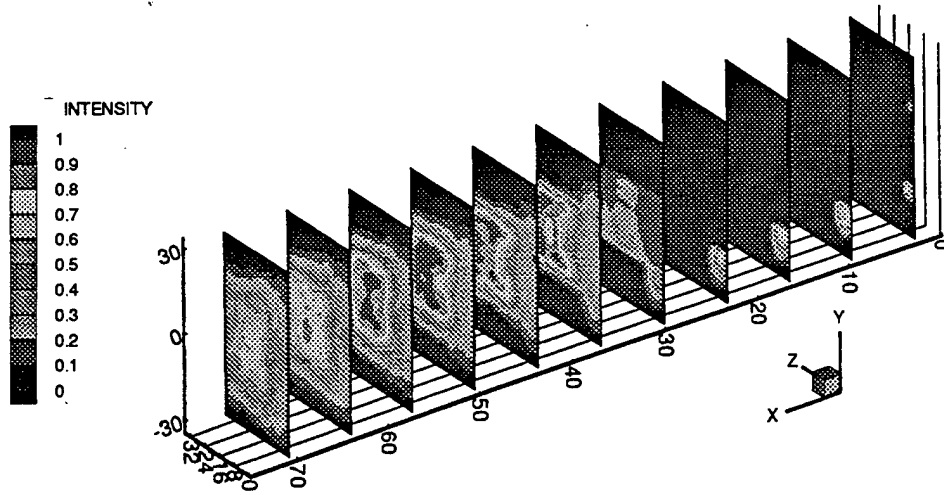


Figure 9 End view of OH and acetone PLIF images behind bluff body with combustion at medium fuel flow rate

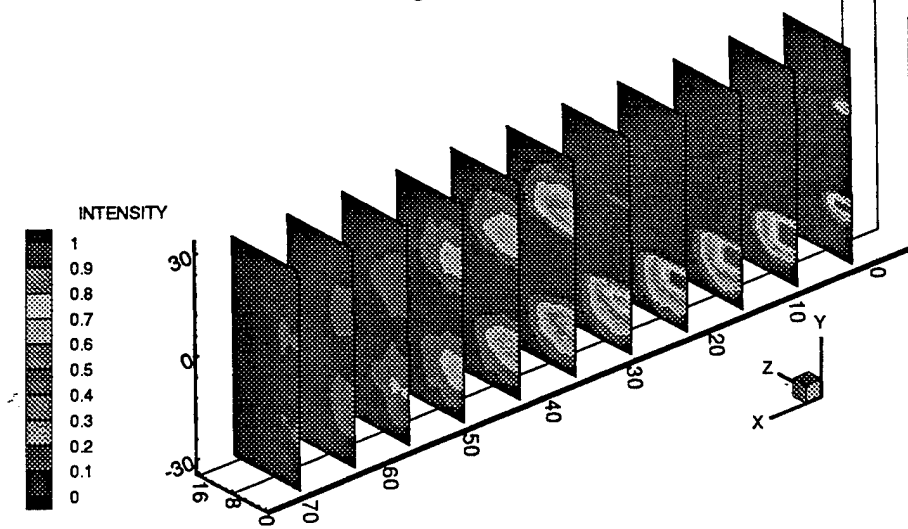


Figure 10 End view of acetone PLIF images behind bluff body with combustion at medium fuel flow rate

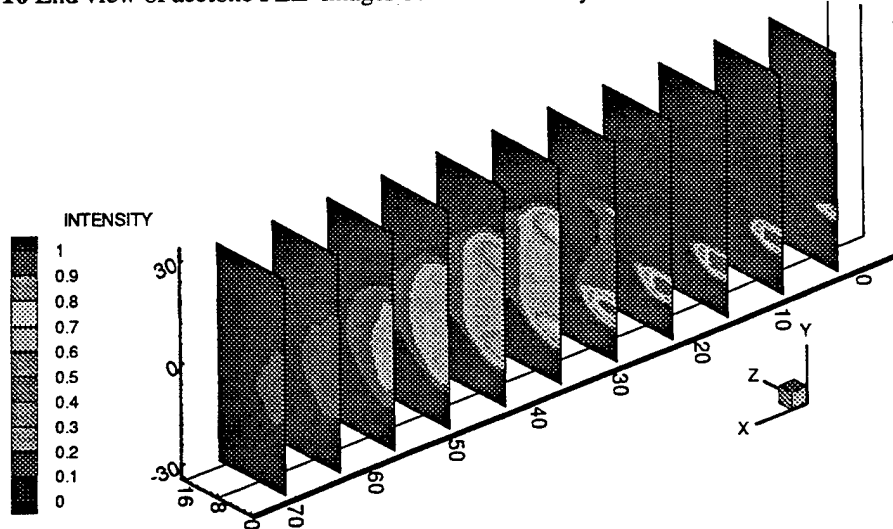


Figure 11 End view of acetone PLIF images behind bluff body without combustion at medium CO<sub>2</sub> flow rate

FEDSM97-3094

## THE MEASUREMENT OF TWO-DIMENSIONAL TEMPERATURE FIELD USING FILTERED RAYLEIGH SCATTERING

Gregory S. Elliott, Nick Glumac  
Mechanical and Aerospace Engineering  
Rutgers University  
Piscataway, NJ 08855

Campbell D. Carter  
Innovative Scientific Solutions Incorporated  
Dayton, OH 45440

Abdollah S. Nejad  
Aero Propulsion and Power Directorate  
Wright-Patterson AFB, OH 45433

### ABSTRACT

Two-dimensional temperature measurements in reacting flows have been measured using Filtered Rayleigh Scattering (FRS). In FRS iodine is contained in an optical cell. An injection seeded Nd:YAG laser is tuned to an absorption line of iodine. The iodine filter is placed in front of an intensified CCD camera recording the scattered light. Scattering from solid surfaces and particles is strongly absorbed by the iodine, while much of the Doppler broadened Rayleigh scattering is transmitted by the filter. The gas temperature can be deduced from the measured transmission of the molecular Rayleigh scattering. Two different premixed flames were investigated, a hydrogen-air flame created using a Hencken burner and a methane-air flame. The accuracy of the FRS measurements was investigated by comparing FRS-derived temperatures with calculated values and temperatures recorded with coherent anti-Stokes Raman spectroscopy. For the hydrogen-air flames, the FRS method gave temperatures within 2% of the expected value (from measurement and/or calculation). Methane-air flames were investigated to demonstrate the effectiveness of FRS to measure to obtain "large field" two-dimensional temperature information in a buoyantly driven flame. An uncertainty analysis is given to show the strengths and weaknesses of the FRS technique for temperature measurements in combustion flows.

### NOMENCLATURE

$A(v)$	Transmission profile
$f$	Property
$I(v)$	Intensity
$k$	Boltzmann constant
$k_0$	Incident unit light wave vector
$k_s$	Incident unit light wave vector
$M$	Molecular mass
$N$	Number density
$P$	Pressure
$r_i$	Scattering distribution
$S(v)$	Recorded intensity
$T$	Temperature
$\underline{V}$	Velocity
$x_i$	Mole fraction
$X$	Dimensionless frequency
$y$	y-parameter
$\Delta f_D$	Frequency Doppler shift
$\Delta u$	Uncertainty
$\theta$	Angle between incident and scattered wave vectors
$\lambda$	Laser linewidth
$\mu$	viscosity
$\nu$	Frequency
$\phi$	Equivalence ratio

## INTRODUCTION

Currently there are few optical techniques suitable for temporally resolved, two-dimensional temperature measurements in reacting flows. Two techniques that can be used for this purpose are planar laser-induced fluorescence (PLIF) and Rayleigh scattering (unfiltered). Fluorescence techniques can be classified as either multiple or single frequency methods. Multiple frequency methods in which two lasers are used simultaneously to pump different transitions using NO (McMillin et al., 1993) and OH (Seitzman et al., 1993) have been demonstrated. These methods are much more versatile and can potentially produce accurate planar temperature fields. However, the two-laser techniques are more complicated and expensive to implement. Single frequency techniques, such as two-line molecular fluorescence (TLMF) (Cattolica et al., 1983) and absolute fluorescence (ABF) (Seitzmann et al., 1985), have also been demonstrated in flames. The TLMF technique using overlapped transitions from two vibrational bands is best suited for high temperatures where significant population of the  $v = 1$  vibrational state is present. The ABS technique typically requires seeding of the reactants with a fluorescing species so that the seed species mole fraction remains constant. The required use of a nonreacting seed species is a significant limitation in practical flames.

Rayleigh scattering is a simpler approach that requires only a single laser at a fixed frequency. Fourquette et al. (1986) and Dibble et al. (1995) have used variations on this approach to obtain instantaneous two-dimensional temperature fields with accuracies better than 4% over the range of 300 to 2000 K. However, in both cases, the fuel and air were carefully filtered to insure minimal interferences from particle scattering. In practical open flames, such as the typical laboratory Bunsen flame or those found in practical devices, scattering from particles can be much greater than that from molecules, limiting the applicability of the unfiltered Rayleigh scattering technique to "ideal" environments.

Molecular filter techniques to modify the light scattered from particles or molecules in the flow field offer the possibility of measuring single or multiple properties simultaneously. The molecular filter is simply a cylindrical optical cell that contains a molecule which has absorption transitions within the frequency tuning range of the laser. The molecular filter is placed in front of the receiving optics to modify the frequency spectrum of the scattering. Miles et al. (1992) demonstrated filtered Rayleigh scattering (FRS) employing molecular iodine filters in conjunction with an injection seeded, frequency-doubled, Nd:YAG laser ( $\lambda = 532$  nm). With injection seeding the linewidth is narrow, and the laser frequency can be tuned to match the transitions of iodine. Using the FRS technique for background suppression, the laser is tuned so that unwanted scattering from walls and windows is absorbed while the Doppler shifted Rayleigh (or Mie) scattering from molecules or particles in the flow field is shifted outside the absorption well. The FRS flow visualization technique has been used for background suppression by Elliott et al. (1992), in the study of compressible

free mixing layers, and by Arnette et al. (1995) in the study of boundary layers.

Miles et al. (1992) showed that average properties of the flow at each point in the illuminated plane can be obtained with molecular scattering, when the laser frequency is tuned through the width of the absorption well of the iodine. The resulting intensity profile is then compared to a theoretical profile and the average velocity, density, temperature, and pressure are thus determined. Molecular filter-based techniques have been developed to measure the average velocity (Doppler Global Velocimetry, DGV, (Meyers and Komine, 1991)) or instantaneous velocity (Filtered Planar Velocimetry, FPV, (Elliott et al., 1994)) in a two-dimensional plane from particles in the flow field. Recently, Hoffman et al. (1995) demonstrated that FRS could be used to obtain temperature measurements in lightly sooting flames, but there is still a need for more comprehensive treatment of the uncertainty of the measurement technique.

In the present paper, FRS will be demonstrated and evaluated for measuring temperatures in combustion environments. The technique will be compared to adiabatic flame temperature calculations and measurements made using coherent anti-Stokes Raman spectroscopy (CARS). The usefulness of the technique for measurements near surfaces, in particle laden flames, and in large two-dimensional regions of the flame will be demonstrated. This will be followed by a detailed uncertainty analysis.

## EXPERIMENTAL ARRANGEMENT

The experiments were conducted at Wright Laboratory (Wright-Patterson AFB, Ohio) and at the Gas Dynamics and Laser Diagnostics Laboratory at Rutgers University. Figure 1 gives a schematic of the burner and optical arrangement for the measurements described. Two different burners were used in this study with flow conditions given in Table 1. At Wright Laboratory a hydrogen-air flame was studied using a Hencken burner. The temperatures in this flame has been measured over a wide range of conditions using CARS, and the flat temperature profile across the burner, makes it ideal for testing the FRS technique. The second burner is copper burner with an array of 64, 1 mm diameter, holes within an area of 169 mm<sup>2</sup>. Premixed methane, nitrogen, and oxygen were independently controlled and fed into the copper burner at various mixtures and flow rates (Table 1).

Using a combination of cylindrical and spherical lenses the interrogation laser beam was formed into a sheet. Two different frequency-doubled Nd:YAG lasers were used in the present experiments; a Spectra Physics GCR-150 (Hencken burner experiments at Wright Laboratories) with approximately 400 mJ per pulse and a Spectra Physics GCR-230 (copper burner experiments at Rutgers) with 650 mJ per pulse. Both lasers have an injection seeder to provide a narrow line width (~ 100 MHz) and the laser frequency can be tuned through absorption lines of iodine around 532 nm. The Nd:YAG lasers used in these experiments have a pulse duration of approximately 10 ns with a

repetition rate of 10 Hz. Photodiodes were used to monitor the laser energy and laser frequency fluctuations, using a second iodine filter. The Rayleigh scattering signal is collected using a Princeton Instruments 14-bit intensified CCD camera. The images are stored on a Pentium 100 MHz personal computer providing camera control, laser synchronization, and laser frequency tuning.

The key component of the FRS system is the iodine filter (Figure 2). The iodine filter is a glass cylinder 9 cm in diameter and 24 cm in length with flat optical windows on both ends. Similar iodine filters have been used in other molecular filter based techniques (Miles et al. 1992 and Elliott et al., 1994). Iodine vapor is formed in the cell by inserting a small amount of iodine crystals and evacuating the cell. The cell temperature ( $T_{\text{cell}}$ ) is raised above the ambient temperature with electrical heat tape so that no iodine crystallizes on the windows. The coldest point in the cell is set in the side arm ( $T_{12}$ ), which is housed in a water jacket and maintained at a constant temperature by a circulation water bath. The temperature of the side arm controls the vapor pressure (number density) of the iodine in the absorption cell. Figure 3 presents the absorption spectra; with the two optically thick absorption lines used in the present experiments at 18788.44 and 18789.28  $\text{cm}^{-1}$ . The profile was taken with the cell operated at  $T_{\text{cell}} = 358 \text{ K}$  and  $T_{12} = 318 \text{ K}$ .

## RESULTS AND DISCUSSION

Rayleigh scattering has been used to investigate reacting and nonreacting flow fields for many years, and the theoretical analysis is well known both computationally and experimentally. Using a laser to interrogate a flow field the Rayleigh scattering signal from molecules within the flow field can be collected (provided the laser has enough energy and the camera has enough sensitivity). There are several important parameters governing the scattered intensity (i.e. intensity of the illuminating light, polarization, frequency of the illuminated light, etc.). Applying the FRS technique to combustion environments, both the intensity and spectral profile of the scattering are needed to deduce the temperature. In flow fields studied at atmospheric pressure and temperature (as is the case for the conditions at the edges of the flames in the present investigation), Brillouin scattering effects should be considered. Several different models exist for calculating the Rayleigh scattering spectral profile (Yip and Nelkin, 1964 and Tenti et al., 1972), and these have been confirmed by experimental measurements (Lao et al., 1976). The scattered spectrum is typically parameterized by the dimensionless frequency  $X$  and the  $y$  parameter. The frequency is nondimensionalized by the thermal broadening and is given by

$$X = \frac{\lambda |v - v_0|}{2 \sin(\theta/2)} \sqrt{\frac{M}{2kT}} \quad (1)$$

where  $\lambda$  is the wavelength of the incident light,  $(v - v_0)$  is the frequency difference from line center,  $\theta$  is the angle between the incident and scattered wave vectors,  $k$  is the Boltzmann constant,  $T$  is the temperature of the gas, and  $M$  is the molecular mass. The  $y$  parameter, which is the ratio of the collisional frequency to the acoustic spatial frequency, characterizes the shape of the Rayleigh scattering spectrum and is given by

$$y = \frac{\lambda P}{4 \mu \sin(\theta/2)} \sqrt{\frac{M}{2kT}} \quad (2)$$

where  $P$  is the pressure and  $\mu$  is the viscosity. For  $y$  of order of unity or greater (the kinetic regime), Brillouin components become important and kinetic models must be used. For  $y \ll 1$  (low pressures or high temperatures) the scattering spectrum is Gaussian and the Brillouin components can be neglected (Pitz et al., 1976). The total spectral intensity (Pitz et al., 1976) is given by the intensity of the scattering of the  $i$ th gas species weighted with its mole fraction  $x_i$  and Rayleigh cross section  $\sigma_{Ri}$  and is given by

$$I(v) = C I_0 N \sum_i x_i \sigma_{Ri} r_i(T, P, M_i, \theta, v) \quad (3)$$

where  $C$  is the optics calibration constant,  $I_0$  is the incident laser light intensity,  $N$  is the total number density, and  $r_i$  is the scattering distribution of the  $i$ th gas species determined by the kinetic model (i.e. S6 model used by Tenti et al., 1972).

The total intensity collected (by the detection device) is a convolution of the total spectral intensity ( $I(v)$ ) and the transmission profile ( $A(v)$ ), as shown schematically in Figure 4, and is given by

$$S(v) = \int I(v') A(v - v') dv' \quad (4)$$

Scattering from particles and surfaces has a narrow linewidth and is attenuated by the iodine filter (Figure 4). Since the Rayleigh scattering from molecules is thermally broadened, part of the scattered intensity (16% to 42%) passes outside the absorption profile (as illustrated by the shaded region of Figure 4). This is a significant characteristic of FRS, since molecular Rayleigh scattering is generally weak relative to surface and particle scattering. In order to eliminate the optical calibration constant on the incident laser irradiance distribution, flame images were nondimensionalized by scattering collected from the air at ambient conditions.

For the present experiments only premixed flames are considered and the dominant species is nitrogen, therefore the scattering will be assumed to be from a single species. This is a

common assumption in Rayleigh scattering temperature measurements in combustion and will be evaluated in the uncertainty analysis. With these assumptions, and since the flames are all at atmospheric pressure, the intensity is a function only of temperature for a given optical arrangement; thus the normalized intensity is

$$\frac{S(v)}{S_{\text{air}}(v)} = \frac{N_{N_2} \int \sigma_{N_2} r(T, P, M_{N_2}, \theta, v) A(v - v') d v'}{N_{\text{air}} \int \sigma_{\text{air}} r(T_{\text{STP}}, P_{\text{STP}}, M_{\text{air}}, \theta, v) A(v - v') d v'} \quad (5)$$

by looking at the local gas temperature one can see the influence on the collected intensity through the gas number density ( $N$ ) and by influence in changing the thermal broadening, which increases the portion of the scattering transmitted by the filter. For the present experiments two different iodine lines were used (at 18788.44 and 18789.28  $\text{cm}^{-1}$ ). Therefore, if the normalized intensity ratio ( $S(v)/S_{\text{air}}(v)$ ) is known the temperature can be determined from the profiles of intensity ratio and temperature which can be calculated from the computational model of the Rayleigh scattering process.

Although not significant in the relatively low speeds of the present experiments, one should note that the profile can also be shifted in frequency relative to the illuminating laser due to the Doppler shift which is given by

$$\Delta f_D = \frac{1}{\lambda} (k_x - k_0) \cdot \underline{V} \quad (6)$$

where  $k_s$  and  $k_0$  are the observed and incident unit light wave vectors, respectively, and  $\underline{V}$  is the flow velocity vector. The error analysis will show that in the present experiments, the flow rates are relatively low and the scattering is collected normal to the primary velocity component, resulting in a negligibly small Doppler shift.

### Hydrogen-Air Flame

Figure 5 gives the two-dimensional temperature field (x-y view) for a hydrogen-air flame (equivalence ratio  $\Phi = 0.25$ ) 2 cm above the Henken burner with a plot of the temperature profile in the center of the image given below the appropriate image. No particular care was taken to physically eliminate particles in the flame or in the surroundings. Scattering from particles generally will dominate the Rayleigh scattering; however, in the present experiment particle scattering is strongly absorbed since it is not thermally broadened. The adiabatic flame temperature in this case is 1065 K. Figure 5a shows a single-shot instantaneous temperature field with the average temperature away from the edges of the flame being 1062 K. The instantaneous profile has large temperature variations in what should be a relatively flat

profile, as shown by CARS measurements. Most likely this temperature variation is due to the photon shot-noise statistics. Thus the signal-to-noise ratio can be improved by either increasing the number of photons collected (more laser energy per pulse), low pass filtering, or binning multiple pixels together. Figure 5b shows the effect of binning 3 adjacent pixels together (Fig. 5c). As expected, the random temperature fluctuations decrease, but at the cost of decreased spatial resolution (0.1  $\text{mm}^2$  to 1  $\text{mm}^2$ ). Figure 5c is the two-dimensional temperature field made by averaging 40 instantaneous images together. As expected this shows the least amount of temperature fluctuation, but of course the instantaneous information is lost.

Figure 6a and 6b gives the average temperature and standard deviation in the flat portion of the hydrogen-air flame for various equivalence ratios. The temperatures measured with FRS have excellent agreement with the adiabatic flame temperatures and the CARS measurements. The maximum deviations are at the highest temperatures with the FRS measurements always slightly lower, as expected. It should be noted that the CARS measurements use the highest temperature as a calibration and may actually have even better agreement with the FRS measurements than is shown here. The standard deviation of the temperature across the flat portion of the flame is given in Figure 6b for the instantaneous, bin-by-three, and average temperature fields for various equivalence ratios. Binning the pixels of the instantaneous image by three decreases the signal to noise ratio by approximately three for all cases which would be the case if the fluctuations were a result of photon statistics. The percent of temperature fluctuation for the average, instantaneous, and instantaneous bin-by-three temperature fields were found to be approximately 2%, 8%, and 3% respectively.

### Methane-Nitrogen-Oxygen Flame

Figure 7 shows the temperature field from the copper burner with a premixed methane-nitrogen-oxygen flames stabilized above the copper burner. Figure 7a is averaged from 120 instantaneous images for each case. Figure 7b shows temperature fields at an equivalence ratio of 0.65. The corresponding adiabatic temperature is 1664 K with an average temperature from FRS of 1594 K. The instantaneous images show temperature fluctuations within the product region due to nonuniformities in the flow through the holed-array burner. As expected, the measured temperatures are below the adiabatic flame temperatures due to the averaging process, heat losses to the burner surface, and mixing with ambient air. The temperature in the premixed region would be expected to be at a temperature of approximately 300 K, but the temperature was measured to be slightly lower (271K and 283 K) due to the presence of the methane which has a much higher Rayleigh scattering cross section.

One of the greatest advantages of FRS for two-dimensional temperature measurements is in its ability to capture instantaneous fluctuations of unsteady flames. Figure 8 shows the average

(Figure 8a) and instantaneous temperature fields (Figures 8b,c) of the premixed methane-nitrogen-oxygen flame with an equivalence ratio of 1.21 and an adiabatic flame temperature of 2510 K. Using FRS the flame temperature was measured at 2265 K. Again this lower temperature is due to unsteadiness of the flame in conjunction with the averaging process. Almost all the instantaneous images show buoyantly driven vortices rolling up on the edge of the flame and the associated temperature variation within them.

### Uncertainty Analysis

A simple uncertainty analysis has been performed to estimate the uncertainty associated with the temperature measurements using FRS. The absolute error can be calculated if the property measured can be written as a function of the independent variables. Generally, the overall uncertainty is defined as

$$\Delta u_f = \sqrt{\sum_{i=1}^n \left( \Delta u_i \frac{\partial f}{\partial u_i} \right)^2} \quad (7)$$

where  $\Delta u_f$  is the overall uncertainty and  $f(u_1, u_2, \dots, u_n)$  is the property measured as a function of the independent variables  $u_1, u_2, \dots, u_n$ , which have corresponding uncertainties of  $\Delta u_1, \Delta u_2, \dots, \Delta u_n$ . Ideally one could write a closed-form expression for the dependent variable (i.e. temperature), however, this is not possible due to the computational model which is utilized in FRS. Therefore, the partial derivatives and the total uncertainty are solved computationally using the model. The uncertainty in temperature for each independent variable and the total uncertainty is given in Table 2 for the average measurements of the hydrogen-air flame. Note that measurements were made in the reactants and products. Equilibrium concentrations of the species present in the flame were used to calculate the uncertainty due to differences of molecular weight and Rayleigh scattering cross section from that of nitrogen.

As seen in Table 2, the uncertainties for the hydrogen-air flame are approximately 8.5% on average which is high when compared with the agreement obtained between the FRS measured temperatures and the adiabatic flame temperature. This is due mainly to the fact that for these flames the uncertainty due to the molecular weight and Rayleigh scattering cross section are added when in actuality they cancel each other out (i.e. the molecular weight of the mixture is lower than nitrogen which results in more of the scattering broadened outside of the absorption filter, while that of the Rayleigh scattering cross section of the mixture is lower than nitrogen resulting in less signal). Taking this fact into consideration reduces the uncertainty to approximately 5%, which is more in line with the measurements.

The highest uncertainties were found to be within the reactant region of the methane flame given in Table 3, particularly for the flame with the equivalence ratio of 1.2. The predominance of

methane with a Rayleigh scattering cross section twice that of nitrogen causes the temperatures to be underestimated, as is seen in the Figures 7 and 8. The product region of the flame, however, shows a lower uncertainty of approximately 4%. Of course the uncertainties for the instantaneous images are higher (due to higher noise in the recorded intensity) than those given in Table 3: greater than 10% in the reactant region and 7% in the products. It should also be noted here that the values for the uncertainty of the independent variables were generally overestimated, resulting in very conservative total uncertainties in the temperature measured with FRS. Also if more information is known about the composition, the total uncertainty can be further reduced.

For future studies it may be possible that the uncertainties associated with the Rayleigh scattering cross section can be eliminated. This is done by using a second camera, with no filter, to normalize the filtered image. The uncertainty analysis shows this would greatly reduce the error, but the temperature measurement would be susceptible to scattering from particles and surfaces. Also the uncertainty could be greatly reduced by enhancing the thermodynamic stability of the molecular filter and by more accurate cameras which may be available in the future.

### CONCLUSIONS

Filtered Rayleigh Scattering (FRS) was demonstrated for two-dimensional thermometry in reacting flows. Temperatures were recorded in laboratory flames containing particles and/or near surfaces using molecular Rayleigh scattering. Hydrogen-air flames created using a Hencken burner, and premixed methane-oxygen-nitrogen flames were investigated. The accuracy of the FRS measurements was tested by comparing FRS-derived temperatures with calculated values and temperatures recorded with coherent anti-Stokes Raman spectroscopy (CARS). For these flames, the FRS method gave temperatures within 2% of the expected value (from measurement and/or calculation). Furthermore, the precision of single-shot FRS measurements in the hydrogen/air flame was within  $\pm 8\%$  for individual pixels; of course, binning signals from individual pixels significantly improved the precision (though at the cost of reducing the spatial resolution). Methane-air flames were investigated to demonstrate the usefulness of FRS to obtain "large field" two-dimensional temperature information in buoyantly driven flames.

### ACKNOWLEDGMENT

The Authors would like to thank the staff at Wright Laboratory and graduate students at Rutgers, Andrew Mosedale and Bradford Price, for their help in running these experiments. Also, Dr. Elliott would like to acknowledge the support of AFOSR for funding this work and the National Science Foundation, grant number NSF-9622108 with Dr. R. Arndt. Dr. Carter acknowledges support under Air Force Contract F33615-92-C-2202.

## REFERENCES

Arnette, S.A., Samimy, M., and Elliott, G.S. (1996). "Two-Component filtered Planar Velocimetry in the Compressible Turbulent Boundary Layer," *AIAA Paper*, AIAA-96-0305.

Cattolica, R.J., and Stephenson, D.A. (1983). "Dynamics of Flames and Reactive Systems," Bowen, J.R., Manson, N., Oppenheim, A.K., and Soloukhin, R.I. (Eds.), *Progress in Astronautics and Aeronautics*.

Dibble, R.W., Long, M.B. and Masri, A. (1985). "Dynamics of Flames and Reactive Systems," Bowen, J.R., Leyer, J.C., Soloukhin, R.I. (Eds.), *Progress in Astronautics and Aeronautics*.

Elliott, G.S., Samimy, M., and Arnette, S.A. (1992). "Study of Compressible Mixing Layers Using Filtered Rayleigh Scattering Based Visualizations," *AIAA Journal*, Vol. 30, No. 10.

Elliott, G.S., Samimy, M., and Arnette, S.A. (1994). "A Molecular Filter Based Velocimetry Technique for High Speed Flows," *Experiments in Fluids*, Vol. 18, pp. 107-118.

Fourquette, D.C., Zurn, R.M., and Long, M.B. (1986). "Two-Dimensional Rayleigh thermometry in a Turbulent Nonpremixed Methane-Hydrogen Flame," *Combustion Science Technology*, Vol. 44, No. 30.

Hoffman, D., Munch, K.U., and Leipertz, A. (1995). "Two-Dimensional Temperature Determination in Sooting Flames by Filtered Rayleigh Scattering," *Optics Letters*, Vol. 21, pp. 525-526.

Lao, Q.H. Schoen, P.E., and Chu, B. (1976). "Rayleigh-Brillouin Scattering of Gases with Internal Relaxation," *The Journal of Chemical Physics*, Vol. 64, No. 9, pp. 3547-3555.

Meyers, J.F., and Komine, H. (1991). "Doppler Global Velocimetry: A New Way to Look at Velocity," *Laser Anemometry*, Vol. 1.

Miles, R.B., Forkey, J.N., and Lempert, W.R. (1992). "Filtered Rayleigh Scattering Measurements in Supersonic/Hypersonic Facilities," *AIAA Paper*, AIAA-92-3894.

McMillin, B.K., Palmer, J.L., Seitzman, J., and Hanson, R.K. (1993). "Two Line Instantaneous Temperature Imaging of NO in a SCRAMJET model Flowfield," AIAA-93-0044.

Pitz, R.W., Cattolica, R., Robben, F., and Talbot, L. (1976). "Temperature and Density in a Hydrogen-Air Flame from Rayleigh Scattering," *Combustion and Flame*, pp. 313-320.

Seitzman, J.M., Kychakoff, G., and Hanson, R.K. (1985). "Instantaneous Temperature Field Measurements Using Planar Laser- Induced Fluorescence," *Optics Letters*, Vol. 10, p. 439.

Seitzman, J.M., Palmer, J.L., Antonio, A.L., Hanson, R.K., Debarber, P.A., and Hess, C. (1993). "Instantaneous Planar Thermometry of Shock Heated Flows Using PLIF of OH," *AIAA Paper*, AIAA-93-0802.

Tenti, G., Boley, C., and Desai, R. (1974). "On the Kinetic Model Description of Rayleigh-Brillouin Scattering from Molecular Gases," *Canadian Journal of Physics*, Vol. 52, pp. 285-290.

Yip, S. and Nelkin, M. (1964). "Application of a Kinetic Model to Time-Dependent Density Correlations in Fluids," *Physical Review*, Vol. 135, pp. A1241-A1245.

**Table 1. Flame Conditions for FRS Experiments**

Flame	Burner	Equiv. Ratio	Moles of N <sub>2</sub>	Flow Rate SLM
H <sub>2</sub> -Air	Hencken	0.13 to 1.0	0.75 to 0.56	-
CH <sub>4</sub> -A	Copper	0.65	0.76	1.6
CH <sub>4</sub> -B	Copper	1.21	0.56	2.41

**Table 2. Uncertainty in Temperature for H<sub>2</sub> Flame**

Flame $\Phi$	H <sub>2</sub> -Air 0.13	H <sub>2</sub> -Air 0.45	H <sub>2</sub> -Air 1.0
A(v) $\pm 2\%$	31 K	31 K	31 K
v $\pm 20$ MHz	14 K	14 K	14 K
M	10 K	96 K	149 K
V $\pm 1$ m/s	2 K	2 K	2 K
$\sigma_R$	42 K	65 K	87 K
Total	66 K	126 K	180 K
% Error	9.3 %	8.3 %	7.5 %

**Table 3. Uncertainty in Temperature for Methane Flame**

Flame $\Phi$	CH <sub>4</sub> -A Reactant	CH <sub>4</sub> -E Reactant	CH <sub>4</sub> -C Products	CH <sub>4</sub> -E Products
$\Phi$	0.65	1.2	0.65	1.2
A(v) $\pm 2\%$	12 K	12 K	31 K	12 K
v $\pm 20$ MHz	14 K	14 K	14 K	14 K
M	0.2 K	52 K	2.1 K	42 K
V $\pm 1$ m/s	2 K	2 K	2 K	2 K
$\sigma_R$	23 K	86 K	52 K	7 K
Total	33 K	103 K	73 K	66 K
% Error	11 %	34 %	4.4 %	2.6 %

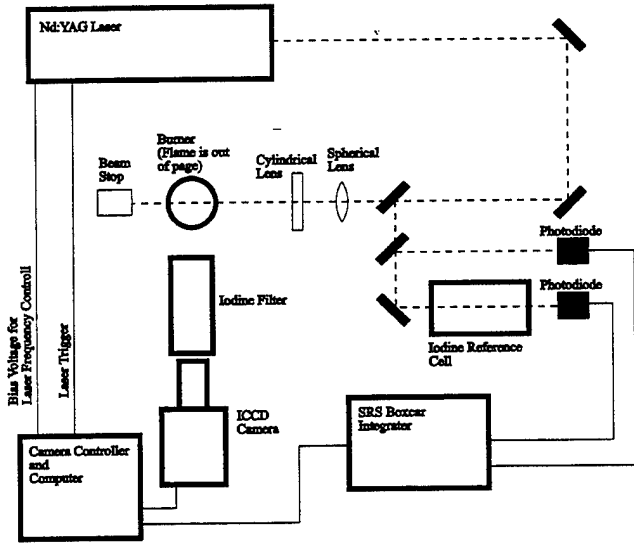


Figure 1. Schematic of laser and optical arrangement for FRS temperature measurements.

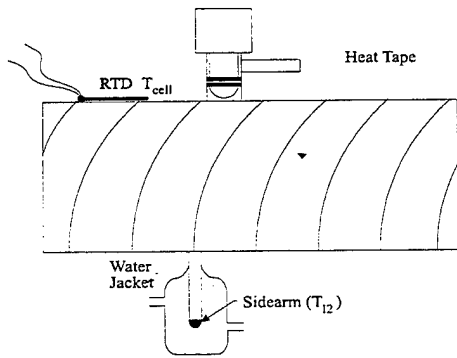


Figure 2. Schematic of Iodine Filter.

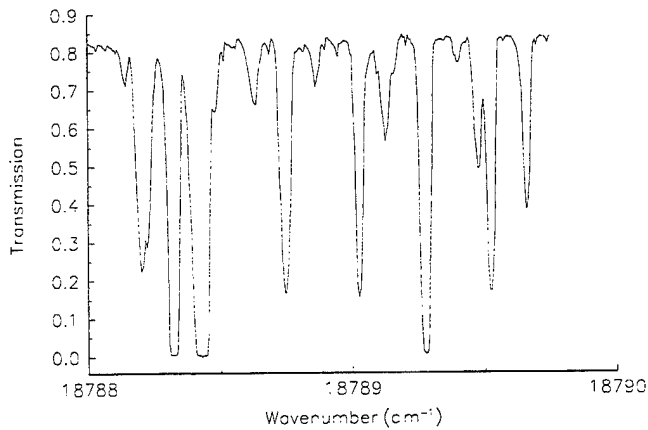


Figure 3. Absorption lines of iodine in the frequency tuning range of the Nd:YAG laser.

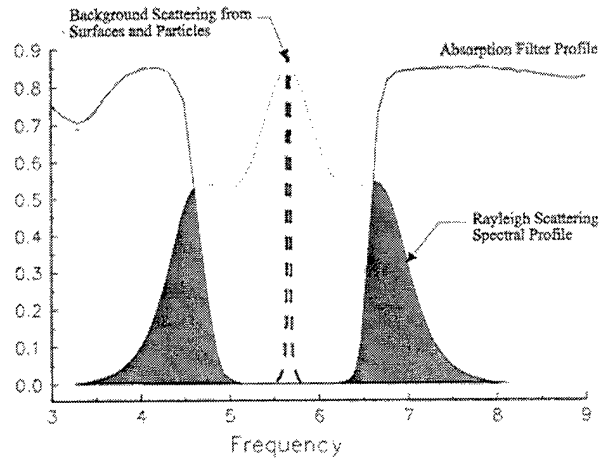


Figure 4. Schematic of absorption profile convoluted with molecular Rayleigh scattering.

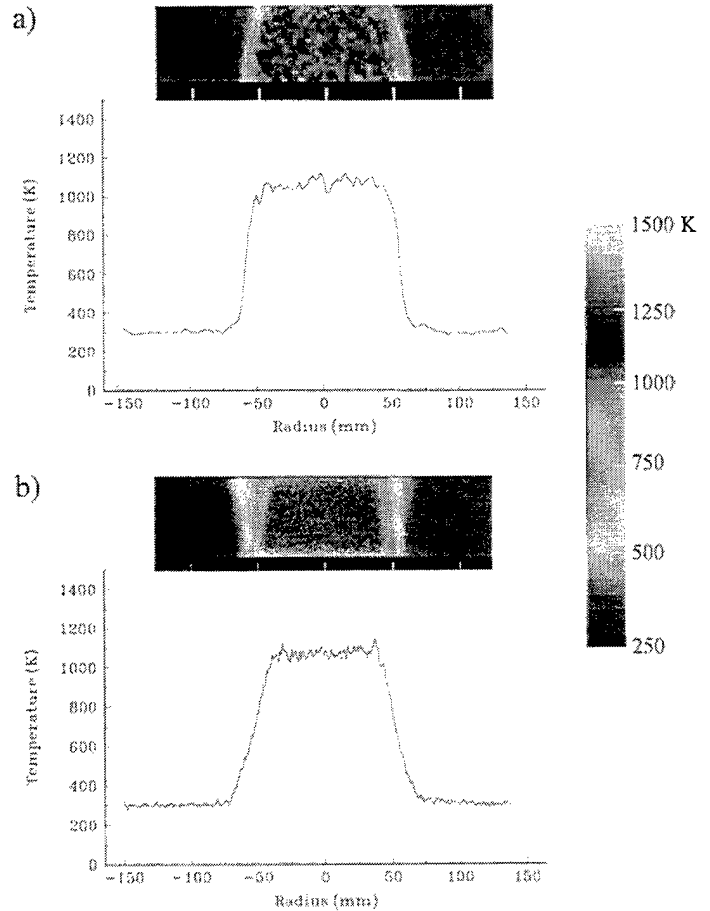


Figure 5. Instantaneous (a) and average (b) images and temperature profiles above a hydrogen-air flame.

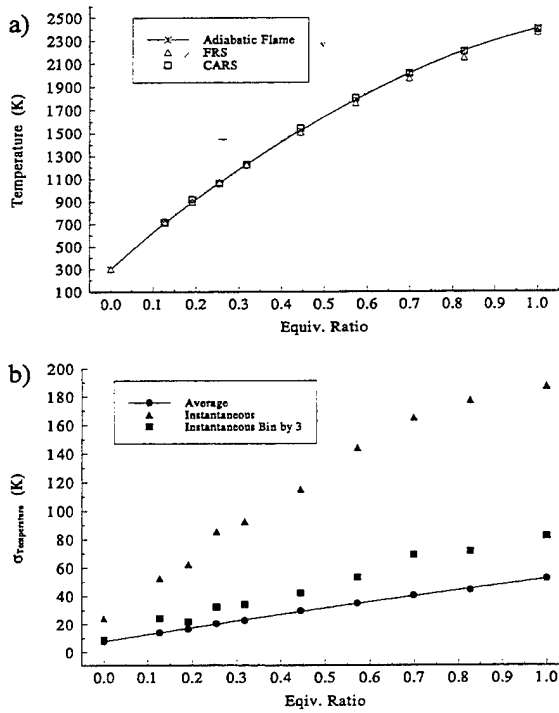


Figure 6. Average temperature (a) and standard deviation (b) of the temperatures for a hydrogen-air flame operated at various equivalence ratios.

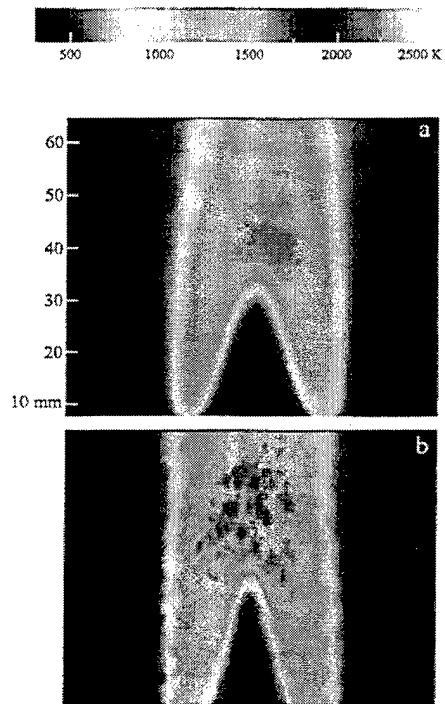


Figure 7. Average (a) and instantaneous (b) temperature fields of an unsteady premixed methane flame operated at an equivalence ratio of 0.65.

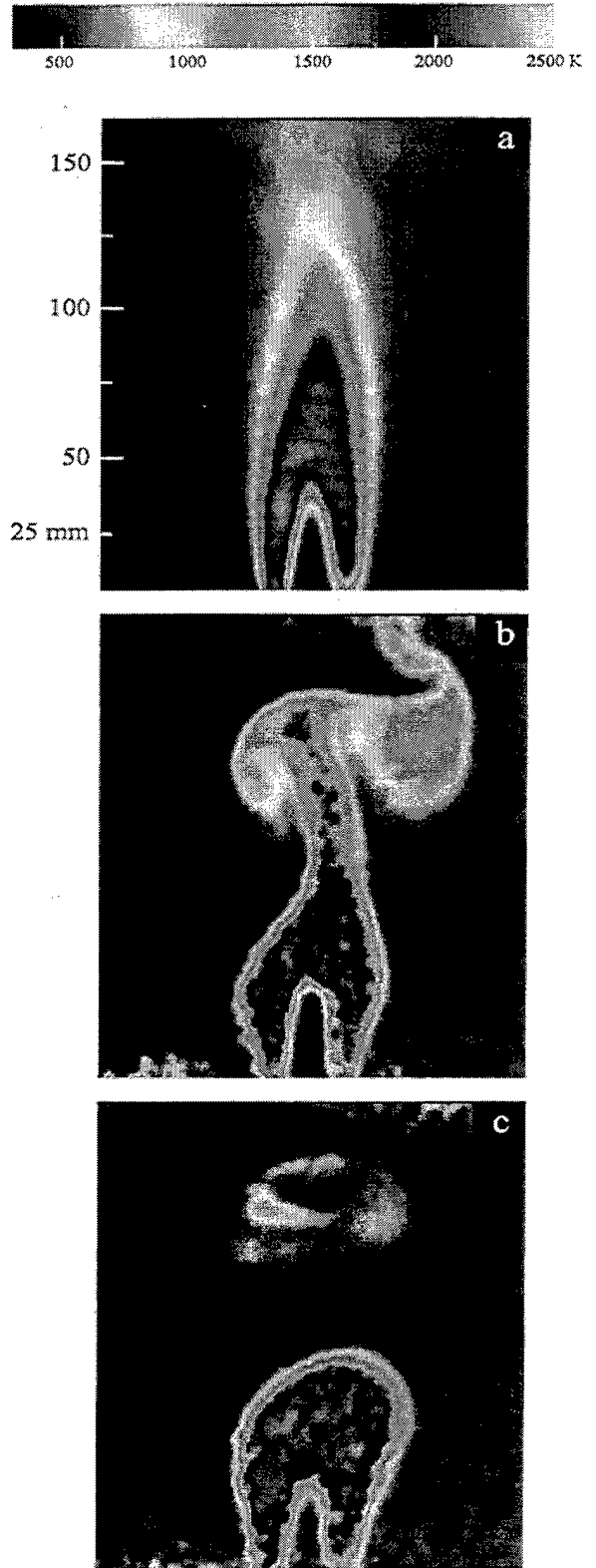


Figure 8. Average (a) and instantaneous (b,c) temperature fields of an unsteady premixed methane flame (1.12).

## Two-Dimensional Temperature Field Measurements Using a Molecular Filter Based Technique

Gregory S. Elliott<sup>†</sup>, Nick Glumac<sup>‡</sup>, Campbell D. Carter<sup>‡</sup>, and Abdollah S. Nejad<sup>\*</sup>  
*Accepted for publication in Combustion Science and Technology, January 27, 1997*

### ABSTRACT

Filtered Rayleigh Scattering (FRS) has been investigated to determine the feasibility of the technique to obtain instantaneous two-dimensional temperature measurements in reacting flows. The laser frequency, of an injection seeded Nd:YAG laser, is tuned to an absorption line of iodine which is contained in an optical cell. The iodine filter is placed in front of an intensified CCD camera recording the scattered light. Background scattering from solid surfaces and particles is strongly absorbed by the iodine, while much of the Doppler broadened Rayleigh scattering is transmitted by the filter. The gas temperature can then be deduced from the measured transmission of the molecular Rayleigh scattering. Two different premixed flames were investigated, a hydrogen-air flame created using a Hencken burner and a methane-air flame. The accuracy of the FRS measurements was investigated by comparing FRS-derived temperatures with calculated values and temperatures recorded with coherent anti-Stokes Raman spectroscopy. For the hydrogen-air flames, the FRS method gave temperatures within 2% of the expected value (from measurement and/or calculation). Methane-air flames were investigated to demonstrate the effectiveness of FRS to measure temperatures near surfaces (within 300  $\mu\text{m}$ ) and to obtain "large field" two-dimensional temperature information in a buoyantly driven flame. A detailed uncertainty analysis is provided to show the strengths and limitations of the FRS technique for temperature measurements in reacting flows.

---

<sup>†</sup> Mechanical and Aerospace Engineering, Rutgers University, Piscataway, NJ 08855

<sup>‡</sup> Innovative Scientific Solutions Incorporated, Dayton, OH 45440

<sup>\*</sup> Aero Propulsion and Power Directorate, Wright-Patterson AFB, OH 45433

## BACKGROUND

Few optical techniques are suitable for temporally resolved (resolution  $< 1 \mu\text{s}$ ), two-dimensional temperature measurements in reacting flows. Two techniques that can be used for this purpose are planar laser-induced fluorescence (PLIF) and Rayleigh scattering (unfiltered). Fluorescence techniques can be classified as either single or multiple frequency methods. Single frequency techniques, such as variants of two-line molecular fluorescence (TLMF) (Cattolica et al., 1983) and absolute fluorescence (ABF) (Seitzmann et al., 1985), have been demonstrated in flames previously. The TLMF technique using overlapped transitions from two vibrational bands is best suited for high temperatures where significant population of the  $v = 1$  vibrational state is present. The ABS technique typically requires seeding of the reactants with a fluorescing species so that the seed species mole fraction remains constant. The required use of a nonreacting seed species is a significant limitation in practical flames.

Multiple frequency methods in which two lasers are used simultaneously to pump different transitions using NO (McMillin et al., 1993) and OH (Seitzman et al., 1993) have also been demonstrated. These methods are much more versatile and can potentially produce accurate planar temperature fields. However, the two-laser techniques are more complicated and expensive to implement. Planar Rayleigh scattering represents a simpler approach that requires only a single laser at a fixed frequency. Fourquette et al. (1986) and Dibble et al. (1995) have used variations on this approach to obtain instantaneous (within a few nanoseconds) planar temperature fields with accuracies better than 4% over the range of 300 to 2000 K. However, in both cases, the fuel and air were carefully filtered to insure minimal interferences from particle scattering. In open flames, such as the typical laboratory Bunsen flame or those found in practical devices, scattering from particles can be much greater than that from molecules, limiting the applicability of the unfiltered Rayleigh scattering technique to controlled environments.

G.S. Elliott et al. 2

Techniques employing molecular filters to modify the light scattered from particles or molecules in the flow field offer the possibility of measuring single or multiple properties simultaneously. One of the first uses of molecular filters in a diagnostic technique was to eliminate large particle scattering in LIDAR temperature measurements (Shimizu et al., 1983 and 1986). The molecular filter is simply a cylindrical optical cell that contains a molecule which has absorption transitions within the frequency tuning range of the laser. The molecular filter is placed in front of the receiving optics to modify the frequency spectrum of the scattering. Miles et al. (1992) first demonstrated filtered Rayleigh scattering (FRS) employing molecular iodine filters in conjunction with an injection seeded, frequency-doubled, Nd:YAG laser ( $\lambda = 532$  nm). With injection seeding the linewidth is narrow, and the laser frequency can be tuned to match the transitions of iodine. Using the FRS technique for background suppression, the laser is tuned so that unwanted scattering from walls and windows is absorbed while the Doppler shifted Rayleigh (or Mie) scattering from molecules or particles in the flow field is shifted outside the absorption well. The FRS flow visualization technique has been used for background suppression by Elliott et al. (1992), in the study of compressible free mixing layers, and by Arnette et al. (1995) in the study of boundary layers.

In addition to qualitative flow visualizations, Miles et al. (1992) showed that average properties of the flow at each point in the illuminated plane can be obtained with molecular scattering, when the laser frequency is tuned through the width of the absorption well of the iodine. The resulting intensity profile is then compared to a theoretical profile and the average velocity, density, temperature, and pressure are thus determined. Other molecular filter-based techniques have been developed to measure the average velocity (Doppler Global Velocimetry, DGV, (Meyers and Komine, 1991)) or instantaneous velocity (Filtered Planar Velocimetry, FPV, (Elliott et al., 1994)) in a two-dimensional plane from particles in the flow field. Recently, Hoffman et al. (1995) demonstrated that FRS could be used to obtain temperature measurements in lightly sooting flames, but there is still a need for more comprehensive treatment of the uncertainty of the measurement

G.S. Elliott et al. 3

technique.

In the present paper, FRS will be demonstrated and evaluated for measuring temperatures in combustion environments. The technique will be compared to adiabatic flame temperature calculations and measurements made using coherent anti-Stokes Raman spectroscopy (CARS). The usefulness of the technique for measurements near surfaces, in particle laden flames, and in large two-dimensional regions of the flame will be demonstrated. This will be followed by a detailed uncertainty analysis.

## EXPERIMENTAL ARRANGEMENT

The experiments were conducted at Wright Laboratory (Wright-Patterson AFB, Ohio) and at the Gas Dynamics and Laser Diagnostics Laboratory at Rutgers University. Figure 1 gives a schematic of the burner and optical arrangement for the measurements described. Three different burners were used in this study with flow conditions given in Table 1. At Wright Laboratory a hydrogen-air flame was studied using a Hencken burner with a 25mm square combustion region. The temperatures in this flame has been measured over a wide range of conditions using CARS, and the flat temperature profile across the burner, makes it ideal for testing the FRS technique. The applicability of FRS for measuring temperatures near the burner surface was investigated in a methane-air flame stabilized on a sintered-bronze McKenna burner which was water cooled to 283 K. The third burner is copper burner with an array of 64, 1 mm diameter, holes within an area of 169 mm<sup>2</sup>. Premixed methane, nitrogen, and oxygen were independently controlled and fed into the copper burner at various mixtures and flow rates (Table 1).

The interrogation laser beam was formed into a sheet with a combination of cylindrical and spherical lenses. Two different frequency-doubled Nd:YAG lasers were used in the present experiments; a Spectra Physics GCR-150 (Hencken and McKenna burner experiments at Wright Laboratories) with approximately 400 mJ per pulse and a Spectra Physics GCR-230 (copper burner

experiments at Rutgers) with 650 mJ per pulse. Both lasers have an injection seeder to provide a narrow line width ( $\sim 100$  MHz) and the laser frequency can be tuned through absorption lines of iodine around 532 nm. The Nd:YAG lasers used in these experiments have a pulse duration of approximately 10 ns with a repetition rate of 10 Hz. Photodiodes were used to monitor the laser energy and laser frequency fluctuations, using a second iodine filter. The Rayleigh scattering signal is collected using a Princeton Instruments 14-bit intensified CCD camera. The images are stored on a Pentium 100 MHz personal computer providing camera control, laser synchronization, and laser frequency tuning.

A major component of the FRS system is the iodine filter. The iodine filter is simply a glass cylinder 9 cm in diameter and 24 cm in length with flat optical windows on both ends. Similar iodine filters have been used in other molecular filter based techniques (Miles et al. 1992 and Elliott et al., 1994). Iodine vapor is formed in the cell by inserting a small amount of iodine crystals and evacuating the cell. The cell temperature ( $T_{\text{cell}}$ ) is raised above the ambient temperature with electrical heat tape so that no iodine crystallizes on the windows. The coldest point in the cell is set in the side arm ( $T_{12}$ ), which is housed in a water jacket and maintained at a constant temperature by a circulation water bath. The temperature of the side arm controls the vapor pressure (number density) of the iodine in the absorption cell. Figure 2 presents the absorption spectra; with the two optically thick absorption lines used in the present experiments at 18788.44 and 18789.28  $\text{cm}^{-1}$ . The profile was taken with the cell operated at  $T_{\text{cell}} = 358$  K and  $T_{12} = 318$  K.

## THEORETICAL DESCRIPTION

Rayleigh scattering has been used to investigate reacting and nonreacting and flow fields for many years, and much of the theoretical analysis is well known. When interrogating a flow field with a laser and collecting the Rayleigh scattering signal from molecules within the flow field, there are several important parameters governing the scattered intensity (i.e. intensity of the illuminating

light, polarization, frequency of the illuminated light, etc.). In the current use of the FRS technique in combustion environments, the intensity and spectral profile of the scattering are needed to deduce the temperature. Since the flames studied here are at atmospheric pressure, Brillouin scattering effects should be considered. Several different models exist for calculating the Rayleigh scattering spectral profile (for example see Yip and Nelkin, 1964 and Tenti et al., 1972), and these have been confirmed by experimental measurements (Lao et al., 1976). The shape of the scattered spectrum is typically parameterized by the dimensionless frequency  $X$  and the  $y$  parameter. The frequency is nondimensionalized by the thermal broadening and is given by

$$X = \frac{\lambda |v - v_0|}{2 \sin(\theta/2)} \sqrt{\frac{M}{2kT}} \quad (1)$$

where  $\lambda$  is the wavelength of the incident light,  $(v - v_0)$  is the frequency difference from line center,  $\theta$  is the angle between the incident and scattered wave vectors,  $k$  is the Boltzmann constant,  $T$  is the temperature of the gas, and  $M$  is the molecular mass. The  $y$  parameter, which is the ratio of the collisional frequency to the acoustic spatial frequency, characterizes the shape of the Rayleigh scattering spectrum and is given by

$$y = \frac{\lambda P}{4 \mu \sin(\theta/2)} \sqrt{\frac{M}{2kT}} \quad (2)$$

Here,  $P$  is the pressure and  $\mu$  is the viscosity. For  $y$  of order of unity or greater (the kinetic regime), Brillouin components become important and kinetic models must be used. For  $y \ll 1$  (low pressures or high temperatures) the scattering spectrum is Gaussian and the Brillouin components can be neglected (Pitz et al., 1976). The total spectral intensity (Pitz et al., 1976) is given by the intensity

of the scattering of the  $i$ th gas species weighted with its mole fraction  $x_i$  and Rayleigh cross section  $\sigma_{Ri}$  and is given by

$$I(\nu) = C I_0 N \sum_i x_i \sigma_{Ri} r_i(T, P, M_i, \theta, \nu) \quad (3)$$

where  $C$  is the optics calibration constant,  $I_0$  is the incident laser light intensity,  $N$  is the total number density, and  $r_i$  is the scattering distribution of the  $i$ th gas species determined by the kinetic model (i.e. S6 model used by Tenti et al., 1972).

The intensity collected by the camera is a convolution of the total spectral intensity  $I(\nu)$  and the transmission profile  $A(\nu)$ , as shown schematically in Figure 3, and is given by

$$S(\nu) = \int I(\nu') A(\nu - \nu') d\nu' \quad (4)$$

The scattering from particles and surfaces has a narrow linewidth and is attenuated by the iodine filter (Fig. 3). Since the Rayleigh scattering from molecules is thermally broadened, part of the scattered intensity (16% to 42%) passes outside the absorption profile (as illustrated by the shaded region of Figure 3). This is a significant characteristic of FRS, since molecular Rayleigh scattering is generally weak relative to surface and particle scattering. In order to eliminate the optical calibration constant on the incident laser irradiance distribution, flame images were nondimensionalized by scattering collected from the air at ambient conditions.

For the present experiments only premixed flames are considered and the dominant species is nitrogen, therefore the scattering will be assumed to be from a single species. This is a common assumption in Rayleigh scattering temperature measurements in combustion and will be evaluated in the uncertainty analysis. With these assumptions, and since the flames are all at atmospheric pressure, the intensity is a function only of temperature for a given optical arrangement; thus the normalized intensity is

$$\frac{S(\nu)}{S_{\text{air}}(\nu)} = \frac{N_{N_2} \int \sigma_{N_2} \Gamma(T, P, M_{N_2}, \theta, \nu) A(\nu - \nu') d\nu'}{N_{\text{air}} \int \sigma_{\text{air}} \Gamma(T_{\text{STP}}, P_{\text{STP}}, M_{\text{air}}, \theta, \nu) A(\nu - \nu') d\nu'} \quad (5)$$

The local gas temperature influences the collected intensity through the gas number density ( $N$ ) and by changing the thermal broadening, which increases the portion of the scattering transmitted by the filter. For the present experiments two different iodine lines were used (at 18788.44 and 18789.28  $\text{cm}^{-1}$ ), resulting in two different temperature versus intensity profiles, as shown in Figure 4. Thus, if the normalized intensity ratio ( $S(\nu)/S_{\text{air}}(\nu)$ ) is known the temperature can be determined from the profiles shown in Figure 4.

It should be noted that the profile can be shifted in frequency relative to the illuminating laser due to the Doppler shift which is given by

$$\Delta f_D = \frac{1}{\lambda} (\underline{k}_s - \underline{k}_0) \cdot \underline{V} \quad (6)$$

where  $\underline{k}_s$  and  $\underline{k}_0$  are the observed and incident unit light wave vectors, respectively, and  $\underline{V}$  is the flow velocity vector. In the present experiments, however, the flow rates are relatively low and the scattering is collected normal to the primary velocity component, resulting in a negligibly small Doppler shift.

## TEMPERATURE MEASUREMENTS

### Hydrogen-Air Flame

Figure 5 gives the two-dimensional temperature field (x-y view) for a hydrogen-air flame (equivalence ratio  $\Phi = 0.25$ ) 2 cm above the Henken burner with a plot of the temperature profile

G.S. Elliott et al. 8

in the center of the image given below the appropriate image. It should be noted that no particular care was taken to physically eliminate particles in the flame or in the surroundings. Scattering from particles generally will dominate the Rayleigh scattering; however, in the present experiment particle scattering is strongly absorbed since it is not thermally broadened. The adiabatic flame temperature in this case is 1065 K. Figure 5a shows a single-shot instantaneous temperature field with the average temperature away from the edges of the flame being 1062 K. The instantaneous profile has large temperature variations in what should be a relatively flat profile, as shown by CARS measurements. Most likely this temperature variation is due to the photon shot-noise statistics. Thus the signal-to-noise ratio can be improved by either increasing the number of photons collected (more laser energy per pulse), low pass filtering, or binning multiple pixels together. Figure 5b shows the effect of binning 3 adjacent pixels together (Fig. 5c). As expected, the random temperature fluctuations decrease, but at the cost of decreased spatial resolution ( $0.1 \text{ mm}^2$  to  $1 \text{ mm}^2$ ). Figure 5c is the two-dimensional temperature field made by averaging 40 instantaneous images together. As expected this shows the least amount of temperature fluctuation, but of course the instantaneous information is lost.

Figure 6a and 6b gives the average temperature and standard deviation in the flat portion of the hydrogen-air flame for various equivalence ratios. The temperatures measured with FRS have excellent agreement with the adiabatic flame temperatures and the CARS measurements. The maximum deviations are at the highest temperatures with the FRS measurements always slightly lower, as expected. It should be noted that the CARS measurements use the highest temperature as a calibration and may actually have even better agreement with the FRS measurements than is shown here. The standard deviation of the temperature across the flat portion of the flame is given in Figure 6b for the instantaneous, bin-by-three, and average temperature fields for various equivalence ratios. Binning the pixels of the instantaneous image by three decreases the signal to noise ratio by approximately three for all cases which would be the case if the fluctuations were a result of photon

statistics. The percent of temperature fluctuation for the average, instantaneous, and instantaneous bin-by-three temperature fields were found to be approximately 2%, 8%, and 3% respectively.

### Methane-Air Flame

One advantage of FRS is that it can be used to make measurements close to surfaces without being affected strongly by surface scattering, since surface scattering like particle scattering is at the laser frequency and is not Doppler shifted or broadened outside of the absorption profile. Figure 7a and b are respective average two-dimensional temperature fields of a methane-air flame lifted and attached to the McKenna burner surface. The burner is water cooled and has a surface temperature of approximately 283 K with the edge located at  $x = 0$  slightly off the left side of the image. For the lifted flame (Fig. 7a) the temperature before the flamefront is slightly low (262 K) which, as will be seen in the uncertainty analysis, is due primarily to the fact that the Rayleigh scattering cross section of the mixture is slightly higher than that of pure nitrogen. For the attached flame (Fig. 7b) the temperature gradient can be seen on the left side of the image due to the slight lifting of the flame near the burner edge. The adiabatic flame temperature for the lifted and attached flames was 1620 K and 1690 K, respectively, while the measured temperatures were 1522 K and 1537 K, respectively. Note that the measured values are expected to be lower due to the heat transfer to the much cooler burner surface and the averaging process. Measurements were recorded within 300  $\mu\text{m}$  of the burner surface and were limited primarily by the camera lens used in these experiments.

Figure 8 shows the temperature field from the copper burner with a premixed methane-nitrogen-oxygen flames (two different equivalence ratios) stabilized above the copper burner. Figures 8a and 8d are averaged from 120 instantaneous images for each case. Figure 8a-c show temperature fields at an equivalence ratio of 0.65. The corresponding adiabatic temperature is 1664 K with an average temperature from FRS of 1594 K. Figures 8 d-f are temperature fields at an

equivalence ratio of 0.71, again the adiabatic flame temperature is 2230 K while the average temperature from FRS is 2000 K. The instantaneous images show temperature fluctuations within the product region due to nonuniformities in the flow through the holed-array burner. As expected, the measured temperatures are below the adiabatic flame temperatures due to the averaging process, heat losses to the burner surface, and mixing with ambient air. The temperature in the premixed region would be expected to be at a temperature of approximately 300 K but in both cases the temperature was measured to be lower (271K and 283 K) due to the presence of the methane which has a much higher Rayleigh scattering cross section.

One of the greatest advantages of FRS for two-dimensional temperature measurements is in its ability to capture instantaneous fluctuations of unsteady flames. Figure 9 shows the average (Figure 9a) and instantaneous temperature fields (Figs. 9b-h) of the premixed methane-nitrogen-oxygen flame with an equivalence ratio of 1.21 and an adiabatic flame temperature of 2510 K. Using FRS the flame temperature was measured at 2265 K. Again this lower temperature is due to unsteadiness of the flame in conjunction with the averaging process. Almost all the instantaneous images show buoyantly driven vortices rolling up on the edge of the flame and the associated temperature variation within them.

## UNCERTAINTY ANALYSIS

A simple uncertainty analysis has been performed to estimate the uncertainty associated with the temperature measurements using FRS. The absolute error can be calculated if the property measured can be written as a function of the independent variables. Generally, the overall uncertainty is defined as

$$\Delta u_f = \sqrt{\sum_{i=1}^n \left( \Delta u_i \frac{\partial f}{\partial u_i} \right)^2} \quad (7)$$

where  $\Delta u_f$  is the overall uncertainty and  $f(u_1, u_2, \dots, u_n)$  is the property measured as a function of the independent variables  $u_1, u_2, \dots, u_n$ , which have corresponding uncertainties of  $\Delta u_1, \Delta u_2, \dots, \Delta u_n$ . Ideally one could write a closed-form expression for the dependent variable (i.e. temperature), however, this is not possible due to the computational model which is utilized in FRS. Therefore, the partial derivatives and the total uncertainty are solved computationally using the model. The uncertainty in temperature for each independent variable and the total uncertainty is given in Table 2 for the average measurements of the flames studied. For the hydrogen-air flame, measurements were made in the reactants and products. Equilibrium concentrations of the species present in the flame were used to calculate the uncertainty due to differences of molecular weight and Rayleigh scattering cross section from that of nitrogen.

As seen in Table 2, the uncertainties for the hydrogen-air flame are approximately 8.5% on average which is high when compared with the agreement obtained between the FRS measured temperatures and the adiabatic flame temperature. This is due mainly to the fact that for these flames the uncertainty due to the molecular weight and Rayleigh scattering cross section are added when in actuality they cancel each other out (i.e. the molecular weight of the mixture is lower than nitrogen which results in more of the scattering broadened outside of the absorption filter, while that of the Rayleigh scattering cross section of the mixture is lower than nitrogen resulting in less signal). Taking this fact into consideration reduces the uncertainty to approximately 5%, which is more in line with the measurements.

The highest uncertainties were found to be within the reactant region of the methane flame, particularly for the flame with the equivalence ratio of 1.2. The predominance of methane with a Rayleigh scattering cross section twice that of nitrogen causes the temperatures to be underestimated, as is seen in the Figures 7-9. The product region of the flame, however, shows a lower uncertainty of approximately 4%. Of course the uncertainties for the instantaneous images are higher (due to higher noise in the recorded intensity) than those given in Table 2: greater than 10% in the reactant

region and 7% in the products. It should also be noted here that the values for the uncertainty of the independent variables were generally overestimated, resulting in very conservative total uncertainties in the temperature measured with FRS. Also if more information is known about the composition, the total uncertainty can be further reduced.

It should be noted that it is possible that the uncertainties associated with the Rayleigh scattering cross section can be eliminated. This is done by using a second camera, with no filter, to normalize the filtered image. The uncertainty analysis shows this would greatly reduce the error, but the temperature measurement would be susceptible to scattering from particles and surfaces. Also the uncertainty could be greatly reduced by enhancing the thermodynamic stability of the molecular filter and by more accurate cameras which may be available in the future.

## CONCLUSIONS

Filtered Rayleigh Scattering (FRS) was demonstrated for two-dimensional thermometry in reacting flows. Temperatures were recorded in laboratory flames containing particles and/or near surfaces using molecular Rayleigh scattering. Hydrogen-air flames created using a Hencken burner, and premixed methane-oxygen-nitrogen flames were investigated. The accuracy of the FRS measurements was tested by comparing FRS-derived temperatures with calculated values and temperatures recorded with coherent anti-Stokes Raman spectroscopy (CARS). For these flames, the FRS method gave temperatures within 2% of the expected value (from measurement and/or calculation). Furthermore, the precision of single-shot FRS measurements in the hydrogen/air flame was within  $\pm 8\%$  for individual pixels; of course, binning signals from individual pixels significantly improved the precision (though at the cost of reducing the spatial resolution). Methane-air flames were investigated to demonstrate the usefulness of FRS for measurements near surfaces (within 300  $\mu\text{m}$ ) and to obtain "large field" two-dimensional temperature information in buoyantly driven flames.

G.S. Elliott et al. 13

## ACKNOWLEDGMENT

The Authors would like to thank the staff at Wright Laboratory and graduate students at Rutgers, Andrew Mosedale and Bradford Price, for their help in running these experiments. Also, Dr. Elliott would like to acknowledge the support of AFOSR for funding this work and the National Science Foundation, grant number NSF-9622108 with Dr. R. Arndt. Dr. Carter acknowledges support under Air Force Contract F33615-92-C-2202.

## REFERENCES

- Arnette, S.A., Samimy, M., and Elliott, G.S. (1996). "Two-Component filtered Planar Velocimetry in the Compressible Turbulent Boundary Layer," *AIAA Paper*, AIAA-96-0305.
- Cattolica, R.J., and Stephenson, D.A. (1983). "Dynamics of Flames and Reactive Systems," Bowen, J.R., Manson, N., Oppenheim, A.K., and Soloukhin, R.I. (Eds.), *Progress in Astronautics and Aeronautics*.
- Dibble, R.W., Long, M.B. and Masri, A. (1985). "Dynamics of Flames and Reactive Systems," Bowen, J.R., Leyer, J.C., Soloukhin, R.I. (Eds.), *Progress in Astronautics and Aeronautics*.
- Elliott, G.S., Samimy, M., and Arnette, S.A. (1992). "Study of Compressible Mixing Layers Using Filtered Rayleigh Scattering Based Visualizations," *AIAA Journal*, Vol. 30, No. 10.
- Elliott, G.S., Samimy, M., and Arnette, S.A. (1994). "A Molecular Filter Based Velocimetry Technique for High Speed Flows," *Experiments in Fluids*, Vol. 18, pp. 107-118.
- Fourquette, D.C., Zurn, R.M., and Long, M.B. (1986). "Two-Dimensional Rayleigh thermometry in a Turbulent Nonpremixed Methane-Hydrogen Flame," *Combustion Science Technology*, Vol. 44, No. 30.
- Hoffman, D., Munch, K.U., and Leipertz, A. (1995). "Two-Dimensional Temperature Determination in Sooting Flames by Filtered Rayleigh Scattering," *Optics Letters*, Vol. 21, pp. 525-526.

G.S. Elliott et al. 14

- Lao, Q.H. Schoen, P.E., and Chu, B. (1976). "Rayleigh-Brillouin Scattering of Gases with Internal Relaxation," *The Journal of Chemical Physics*, Vol. 64, No. 9, pp. 3547-3555.
- Meyers, J.F., and Komine, H. (1991). "Doppler Global Velocimetry: A New Way to Look at Velocity," *Laser Anemometry*, Vol. 1.
- Miles, R.B., Forkey, J.N., and Lempert, W.R. (1992). "Filtered Rayleigh Scattering Measurements in Supersonic/Hypersonic Facilities," *AIAA Paper*, AIAA-92-3894.
- McMillin, B.K., Palmer, J.L., Seitzman, J., and Hanson, R.K. (1993). "Two Line Instantaneous Temperature Imaging of NO in a SCRAMJET model Flowfield," AIAA-93-0044.
- Pitz, R.W., Cattolica, R., Robben, F., and Talbot, L. (1976). "Temperature and Density in a Hydrogen-Air Flame from Rayleigh Scattering," *Combustion and Flame*, pp. 313-320.
- Seitzman, J.M., Kychakoff, G., and Hanson, R.K. (1985). "Instantaneous Temperature Field Measurements Using Planar Laser- Induced Fluorescence," *Optics Letters*, Vol. 10, p. 439.
- Seitzman, J.M., Palmer, J.L., Antonio, A.L., Hanson, R.K., Debarber, P.A., and Hess, C. (1993). "Instantaneous Planar Thermometry of Shock Heated Flows Using PLIF of OH," *AIAA Paper*, AIAA-93-0802.
- Shimizu, H., Lee, S.A., and She, C.Y. (1983) "High Spectral Resolution LIDAR System with Atomic Blocking Filters for Measureing Atmospheric Parameters," *Applied Optics*, Vol. 22, pp. 1373.
- Shimizu, H., Noguchi, K., and She, C.Y. (1986) "Atmospheric Temperature Measurement by High Spectral Resolution LIDAR," *Applied Optics*, Vol. 25, pp. 1460.
- Tenti, G., Boley, C., and Desai, R. (1974). "On the Kinetic Model Description of Rayleigh-Brillouin Scattering from Molecular Gases," *Canadian Journal of Physics*, Vol. 52, pp. 285-290.
- Yip, S. and Nelkin, M. (1964). "Application of a Kinetic Model to Time-Dependent Density Correlations in Fluids," *Physical Review*, Vol. 135, pp. A1241-A1245.

**Table 1. Flame Conditions for FRS Experiments**

Flame	Burner	Equivalence Ratio	Mole Fraction of N <sub>2</sub>	Total Flow Rate SLM
H <sub>2</sub> -Air	Hencken	0.13 to 1.0	0.75 to 0.56	-
CH <sub>4</sub> -A	McKenna	0.58	0.75	19.1
CH <sub>4</sub> -B	McKenna	0.62	0.74	19.1
CH <sub>4</sub> -C	Copper - holed array	0.65	0.76	1.6
CH <sub>4</sub> -D	Copper - holed array	0.71	0.64	0.93
CH <sub>4</sub> -E	Copper - holed array	1.21	0.56	2.41

Table 2. Uncertainty in Temperature Due to Various Experimental Properties

Flame	H <sub>2</sub> -Air Products 0.13	H <sub>2</sub> -Air Products 0.45	H <sub>2</sub> -Air Products 1.0	CH <sub>4</sub> -C Reactants 0.65	CH <sub>4</sub> -D Reactants 0.71	CH <sub>4</sub> -E Reactants 1.2	CH <sub>4</sub> -C Products 0.65	CH <sub>4</sub> -D Products 0.71	CH <sub>4</sub> -E Products 1.2
$\Phi$	31 K	31 K	31 K	12 K	12 K	12 K	31 K	31 K	12 K
A(v) ±2%	14 K	14 K	14 K	14 K	14 K	14 K	14 K	14 K	14 K
v ±20MHz	10 K	96 K	149 K	0.2 K	4.3 K	52 K	2.1 K	5.3 K	42 K
M	2 K	2 K	2 K	2 K	2 K	2 K	2 K	2 K	2 K
V ±1 m/s	42 K	65 K	87 K	23 K	42 K	86 K	52 K	75 K	7 K
$\sigma_R$	37 K	37 K	37 K	15 K	15 K	15 K	37 K	37 K	37 K
S(v) ± 2.5%	66 K	126 K	180 K	33 K	48 K	103 K	73 K	91 K	66 K
Total Uncert.	9.3 %	8.3 %	7.5 %	11 %	16 %	34 %	4.4 %	4.1 %	2.6 %
% Error									

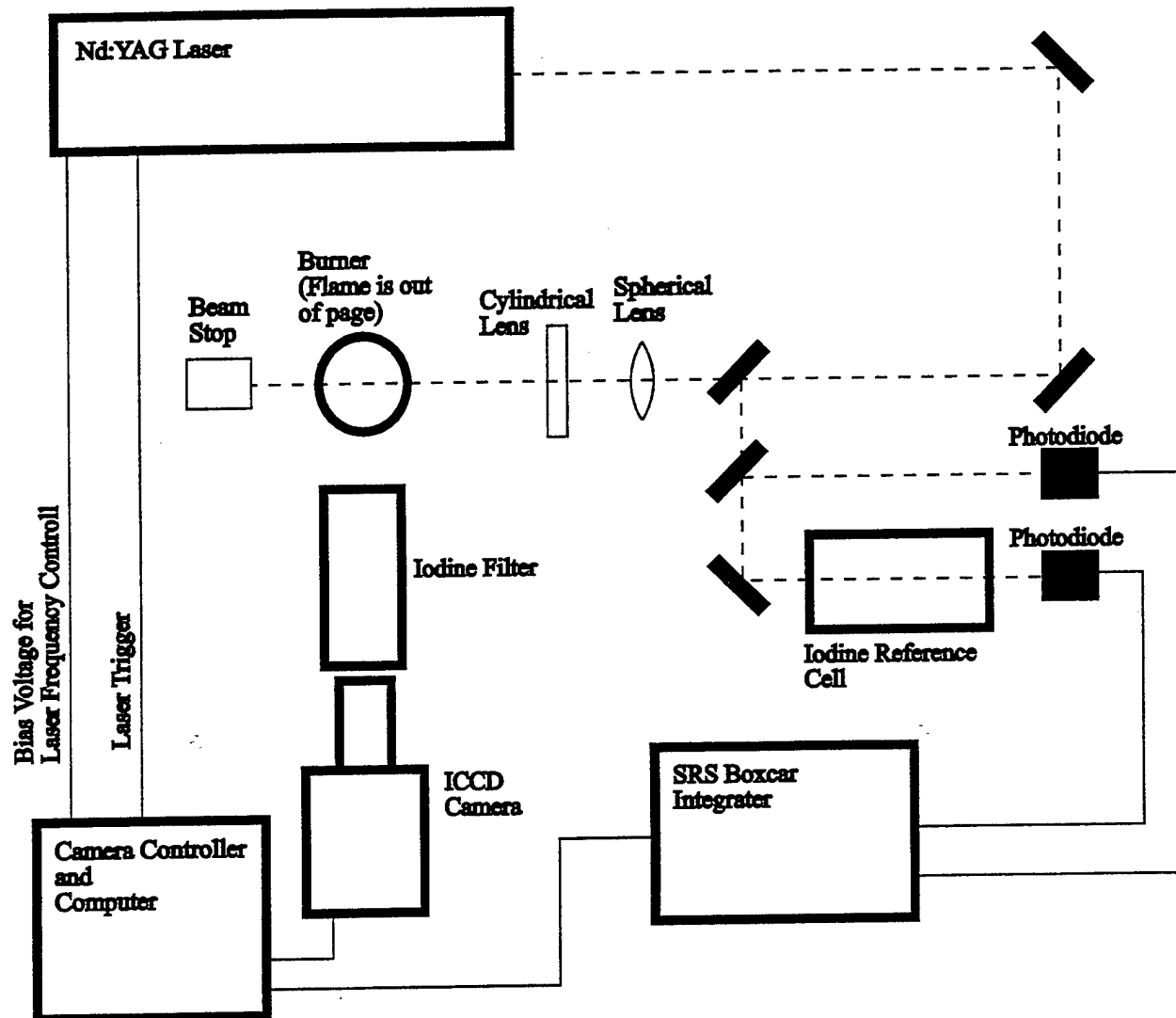


Figure 1. Schematic of laser and optical arrangement for FRS temperature measurements.

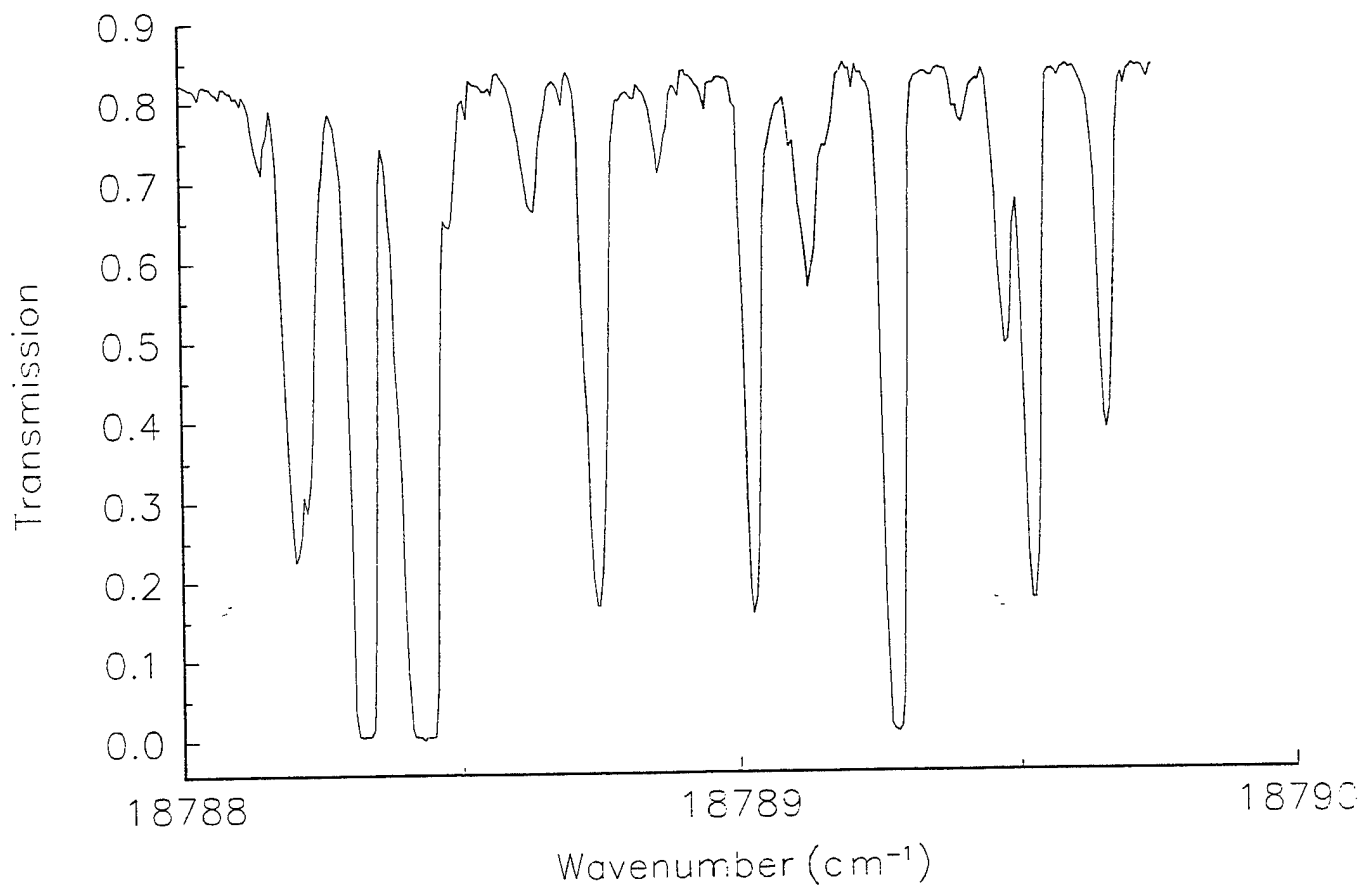


Figure 2. Absorption lines of iodine in the frequency tuning range of the Nd:YAG laser.

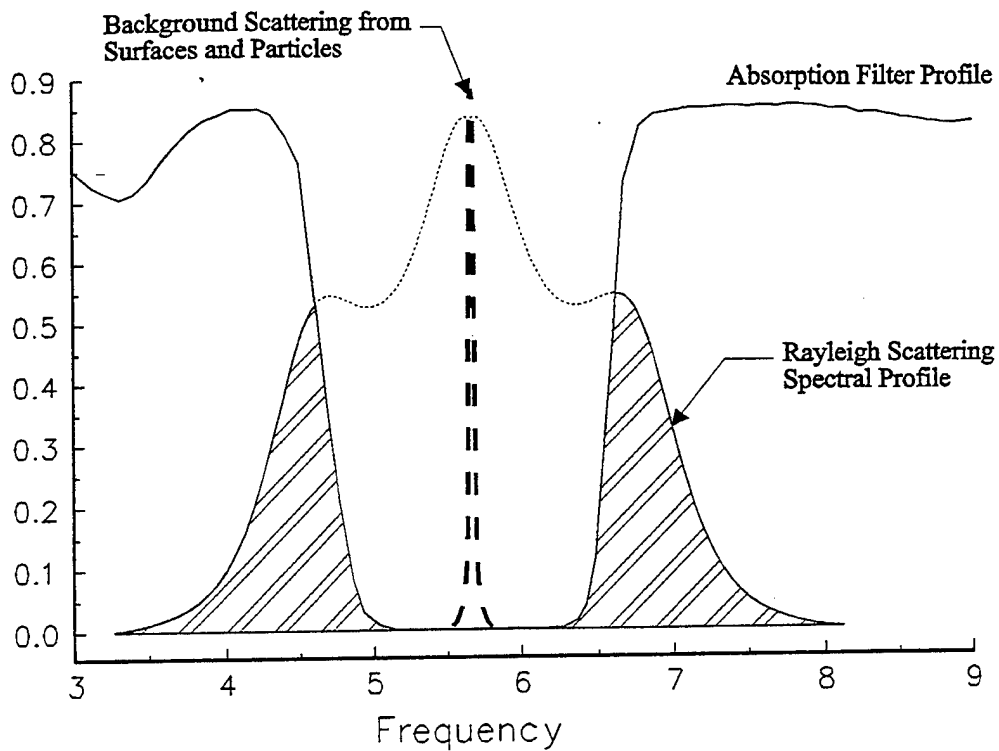


Figure 3. Schematic of absorption profile convoluted with molecular Rayleigh scattering.

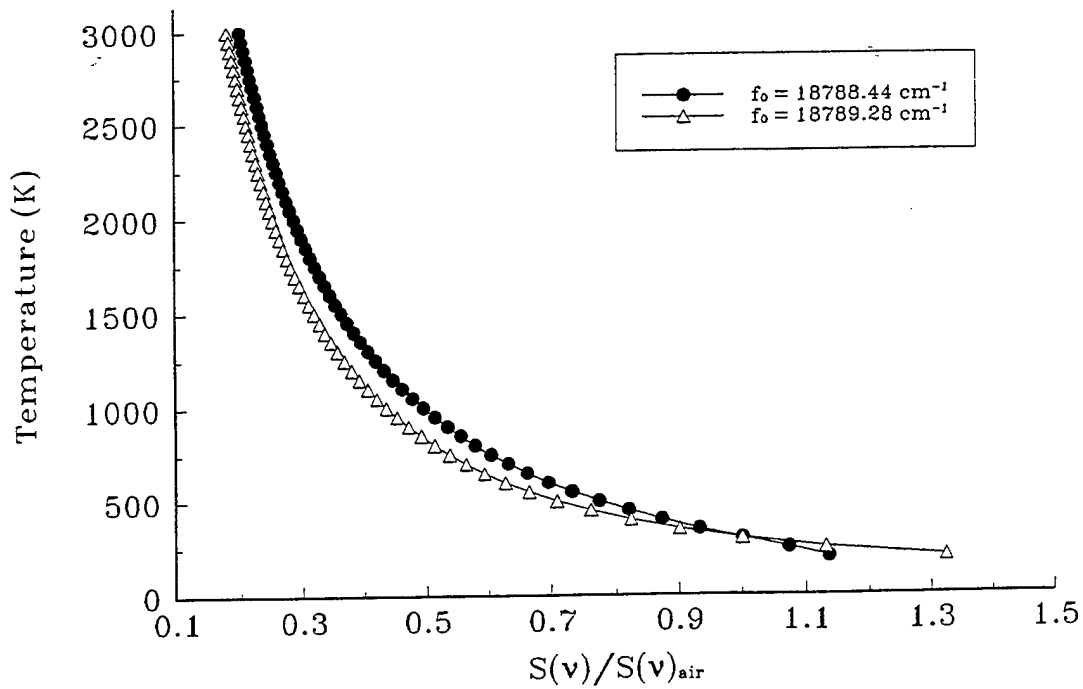


Figure 4. Intensity ratio for temperatures measured using FRS in reacting flows.

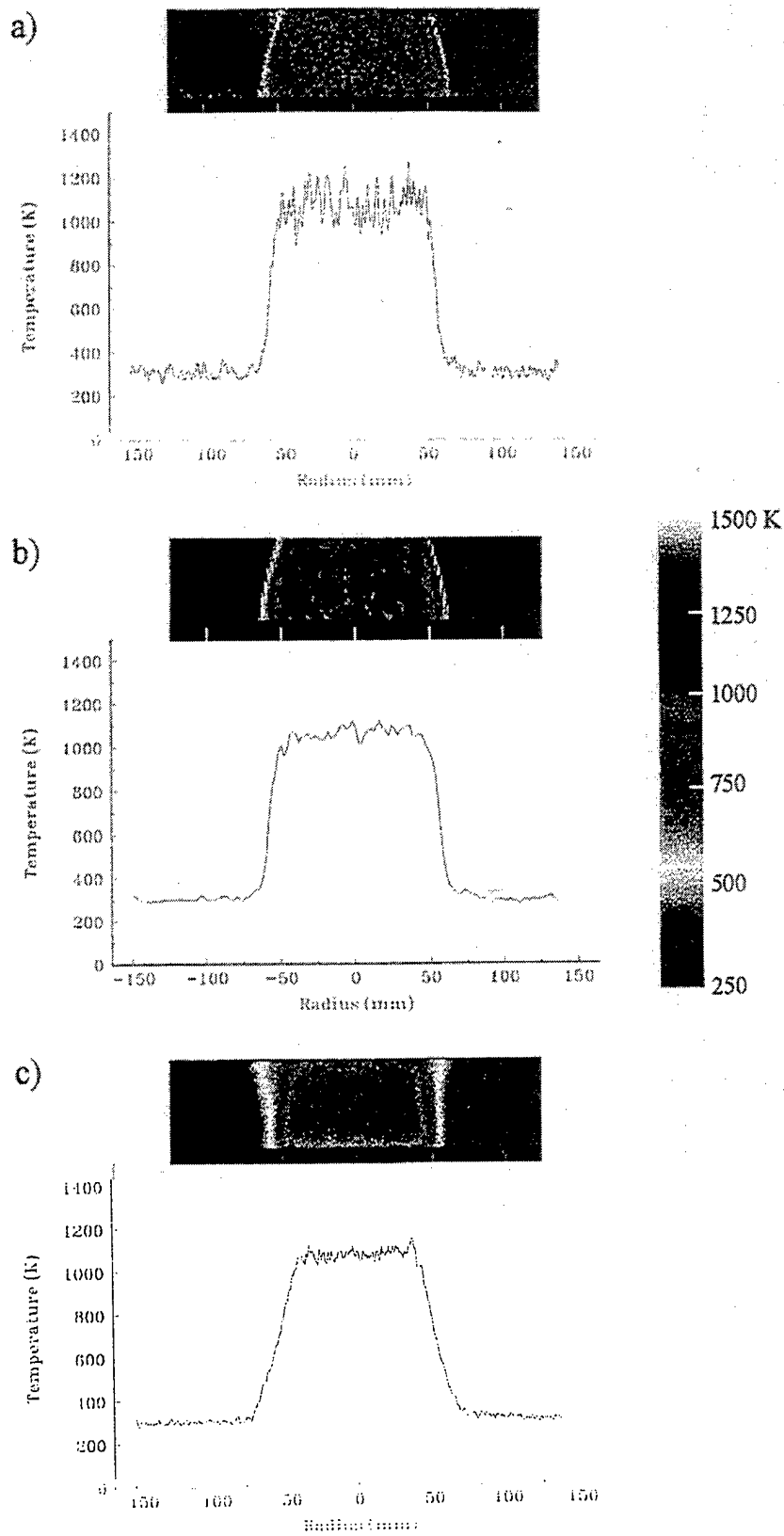


Figure 5. Instantaneous (a) bin by 3 (b) and average (c) images and temperature profiles taken using FRS above a hydrogen-air flame.

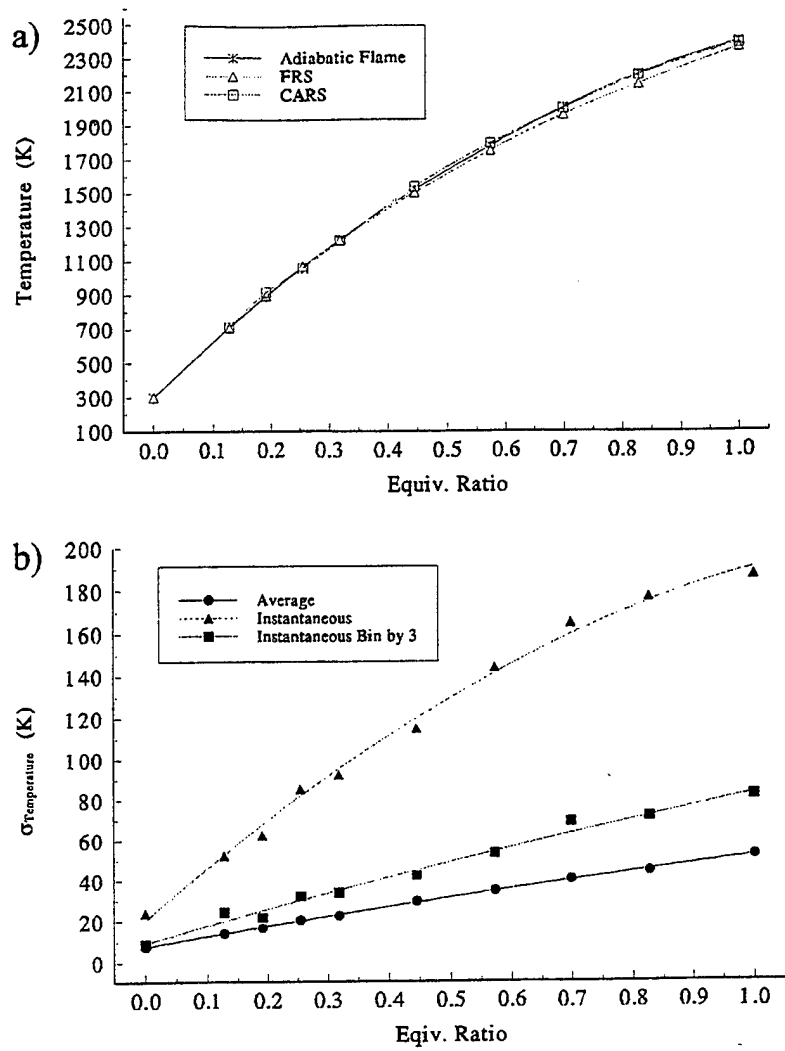


Figure 6. Average temperature (a) and standard deviation (b) of the temperatures for a hydrogen-air flame operated at various equivalence ratios.

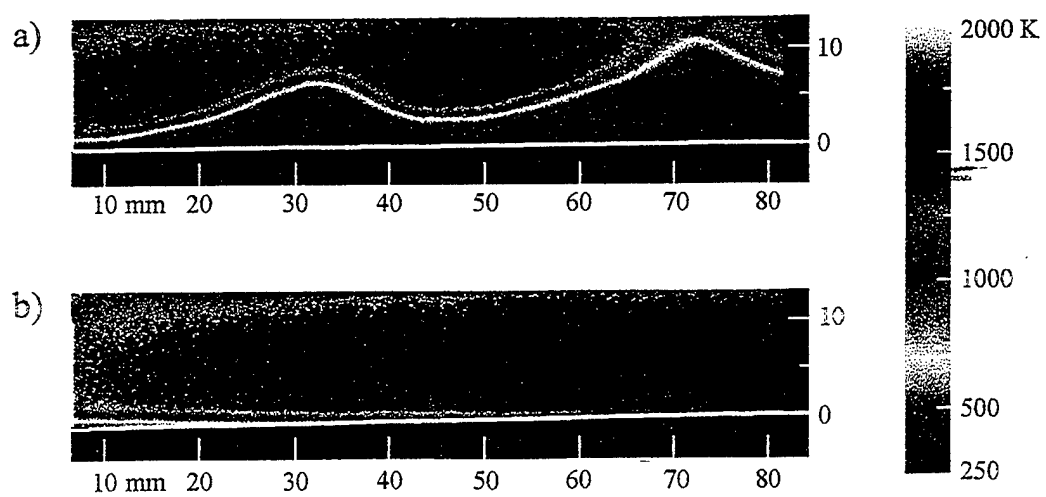


Figure 7. Average two-dimensional temperature fields of a methane-air flame lifted (a) and attached (b) to the burner surface.

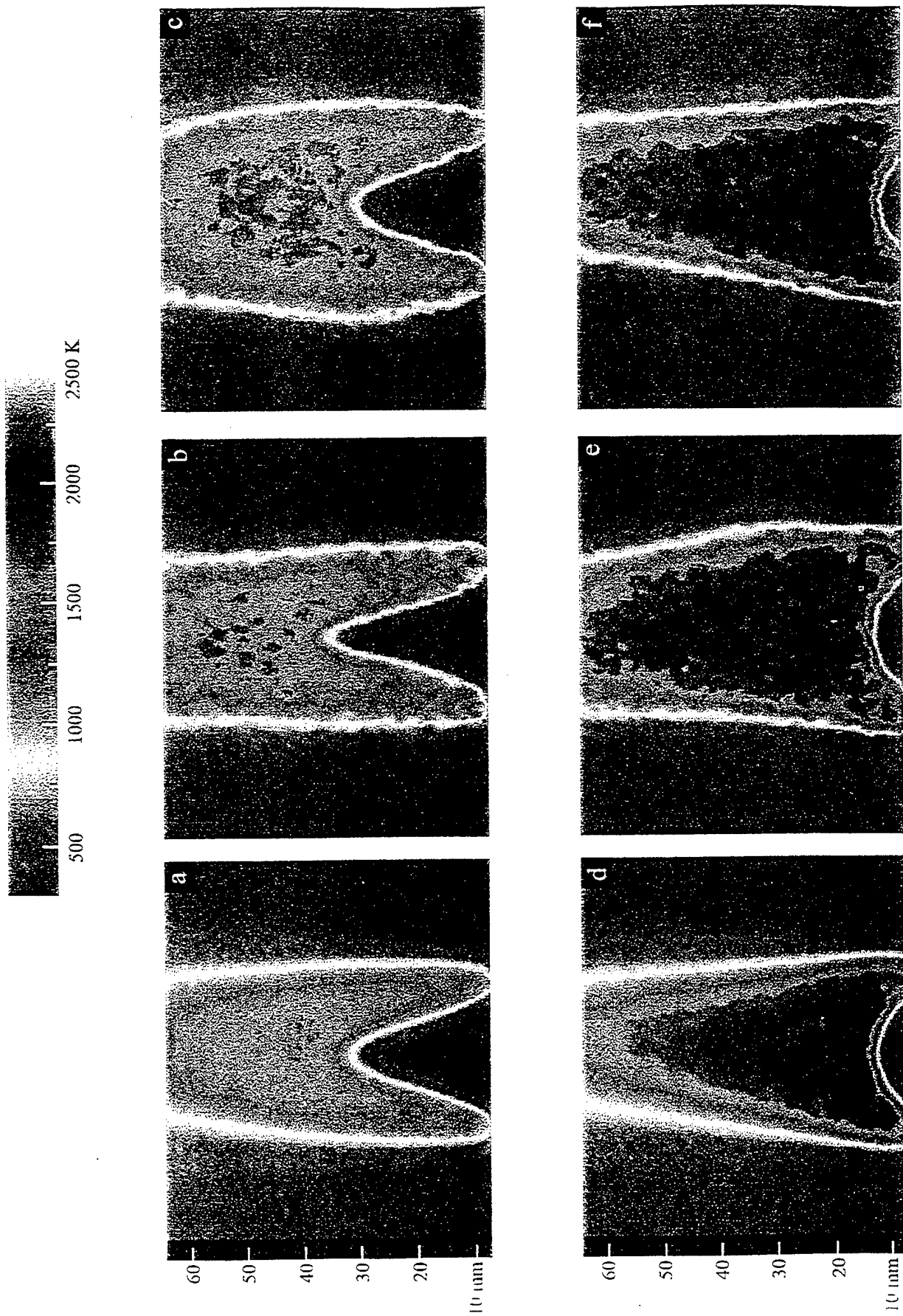


Figure 8. Average (a and d) and instantaneous (b, c, e, and f) temperature fields of an unsteady premixed methane flame operated at equivalence ratios of 0.65 (a - c) and 0.71 (d - f) taken using FRS.

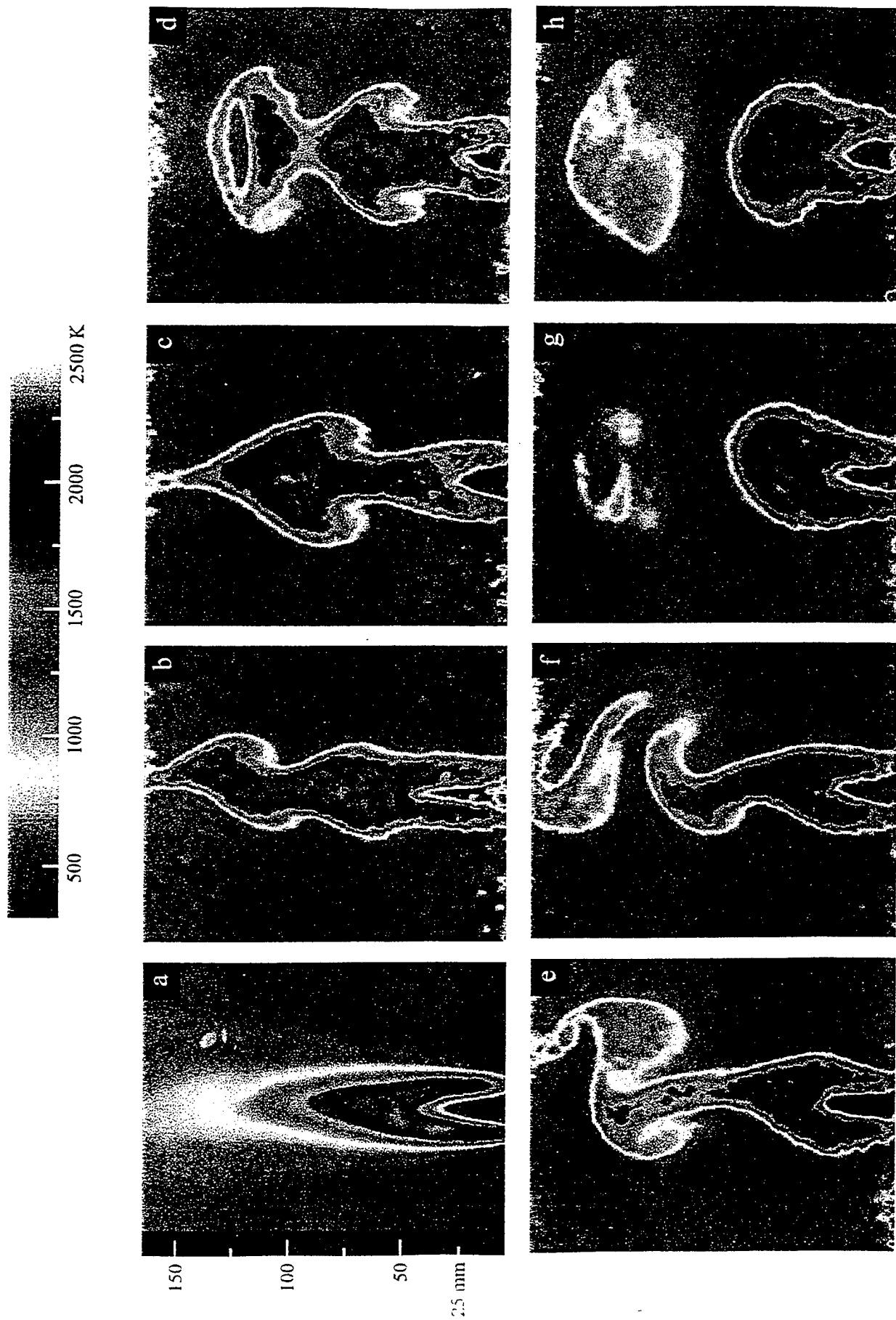


Figure 9. Average and instantaneous temperature fields of an unsteady premixed methane flame taken using FRS.

## The Structure of a Dynamic Nonpremixed H<sub>2</sub>-Air Flame

C. D. Carter, L. P. Goss, K. Y. Hsu, V. R. Katta, and D. D. Trump

Systems Research Laboratories, Inc.  
A Division of Space Industries International, Inc.  
2800 Indian Ripple Rd.  
Dayton, OH 45440-3696

### INTRODUCTION

Studies of simple vertically oriented nonpremixed jet flames have shown that when the co-flow velocity is sufficiently low, buoyancy-induced, periodic toroidal vortices form outside the flame surface. These vortices wrinkle the flame surface and produce stretched and compressed flamelets, thereby providing a relatively simple means of studying flame-vortex interactions. Recent calculations by Katta et al. [1,2] suggest that preferential diffusion due to nonunity Lewis number in these H<sub>2</sub>-air flames influences the gas temperature along the flame surface. In particular, Katta et al. [1,2] find that the flame temperature increases in the compressed regions of the flame and decreases in the stretched regions. That the flame temperature varies in this manner has been confirmed in part by previous experimental studies [3,4].

To characterize the structure of a dynamic nonpremixed H<sub>2</sub>-air flame, we have made sequential point measurements of temperature using thin-filament-pyrometry (TFP) and concentrations of hydroxyl (OH) and nitric oxide (NO) using laser-induced fluorescence (LIF). We have chosen three downstream locations of 135 mm, 85 mm, and 50 mm from the jet exit; for each of these positions, we have recorded the radial and temporal variation of these scalars. For this paper, we will focus on measurements recorded at 135 mm.

### EXPERIMENTAL METHODS

#### Facilities and Techniques

Shown in Fig. 1 is a schematic of the experimental facility. The burner consists of a tapered fuel tube (1-cm ID) surrounded by a co-annular air section (15-cm ID); both the burner and the co-annular section are mounted to an *x-y-z* translation system employing stepper motors. Assuming a uniform velocity profile, the

flow velocities for the fuel and air were 4.62 m/s and 0.40 m/s, respectively. These flow rates resulted in a buoyant frequency of 15.2 Hz. Although a range of frequencies (10 to 20 Hz) can be obtained by varying the gas flow rates, the 15-Hz frequency is optimum for the available laser system (a 30-Hz Nd:YAG pump laser), insofar as the laser is triggered at twice the frequency of the buoyant fluctuations. The laser and detection electronics were phase locked to the 15.2-Hz buoyant frequency using the passage of these structures through a cw laser beam; the beam steering induced by the passage of the flame bulge moved the laser beam on and off a photodiode at the frequency of 15.2 Hz; with the flame isolated from disturbances, the variation in the trigger frequency was only  $\pm 0.2$  Hz. To maintain the trigger signal, we mounted both the cw laser and the photodiode detector to the burner/co-flow housing. Thus, the detection electronics were triggered from the same flame structure, regardless of the burner position. Finally, to reduce the maximum temperatures and, thereby, extend the lifetimes of the filaments, we

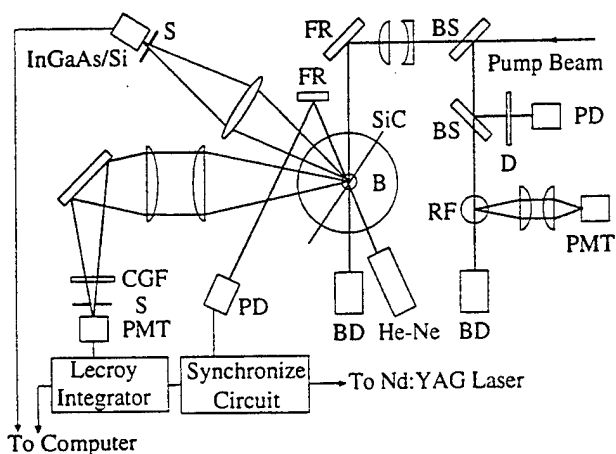


Fig. 1. Schematic of experimental setup

employed a diluted fuel mixture in the ratio of 2.22 parts  $H_2$  to 1 part  $N_2$ .

Originally the filament emission and NO fluorescence were recorded simultaneously. However, the flame proved to be reproducible, and subsequent to our initial simultaneous measurements, each (NO fluorescence, OH fluorescence, and temperature) was recorded sequentially. The  $\beta$ -SiC filaments, due to their small diameter (14  $\mu\text{m}$ ) and low thermal conductivity (10 kcal/m-hr-K or about 40 times lower than that of a type S or R thermocouple) exhibit excellent temporal response and spatial resolution. The filament acts as a graybody with an emissivity of 0.88. The detection limit for the filament corresponds to  $\sim 900$  K; the high-temperature limit,  $\sim 2300$  K in practice, is determined by the sublimation point of the  $\beta$ -SiC material.

We overlapped the filament and LIF probe volumes using a 500- $\mu\text{m}$  pinhole--which was mounted on a kinematic magnetic base assembly--in combination with a He-Ne alignment laser; the pinhole defined the spatial resolution of both the LIF and the TFP measurements. The light from the He-Ne laser was split into two beams, which were made to pass through the alignment pinhole. The intersection of the two beams was then used as a marker for the probe volume, and the filament was properly aligned when scattering from both He-Ne beams was observable. With all three measurements, we translated the burner to the axial and radial position of interest. The signals were then recorded as a function of delay relative to the trigger signal; the 2-D maps (signal vs. time and radius) were then constructed from the individual signal vs. time traces. With temperature we recorded the signals in real time; that is, we sampled the filament emission at a frequency of  $\sim 1$  kHz. Typically, we averaged the filament emission over 45 cycles for each spatial location. Strong emission from  $H_2O$  was also present in the hottest regions of the flame; consequently, recording the background flame emission was necessary. Thus, subsequent to recording the filament emission map (i.e., in time and space), the filament was broken and the background was recorded for the same phases and radial positions. With the LIF measurements, we were limited by the 30-Hz pulse repetition frequency of the laser; thus, we obtained measurements on successive cycles of the buoyant structures. Typically, we averaged the fluorescence from 45 laser pulses--corresponding to 45 successive buoyant cycles--for each temporal and spatial location.

The filament emission was collected with a conventional camera lens and focused onto a dual photodiode detector. This dual photodiode is composed of sandwiched InGaAs and Si diodes having respective spectral ranges of about 0.9 to 1.8  $\mu\text{m}$  and 0.45 to 1.0  $\mu\text{m}$ . Because the temperature is derived from a ratio of the photodiode signals, the measurement is less sensitive to possible variation in the filament emissivity (due to long exposure at high temperatures, for example) and to small variations in the optical alignment. The frequency response of the filament is better than 1 kHz for flame conditions. Therefore, we expect that the filament will accurately reflect the temporal variations in gas temperature.

The laser-beam diameters for OH and NO excitation were adjusted to allow  $\sim 90\%$  of the beam energy through the alignment pinhole. The probe-volume beam energies for OH and NO were kept below the 10- $\mu\text{J}$  level to ensure that the fluorescence would remain within the linear regime. We collected the fluorescence with two 100-mm-diameter fused-silica lenses--a 250-mm focal length collection lens and a 500-mm focal length focusing lens--which resulted in a system magnification of  $\sim 2$ . A slit-and-photomultiplier-tube housing was positioned at the focus of the fluorescence beam. For both NO and OH fluorescence collection, the slit width was set to  $\sim 1.0$  mm, resulting in a resolution of  $\sim 0.5$  mm along the axis of the LIF laser beams.

For NO and OH fluorescence excitation, we employed a Nd:YAG-pumped dye laser system with a 30-Hz pulse repetition frequency. To generate the wavelength for NO excitation, the frequency-doubled output of the dye laser was mixed with the residual IR radiation from the Nd:YAG. We tuned this system to the  $Q_1(28)$  transition of the  $A^2\Sigma^+-X^2\Pi(0,0)$  band ( $\lambda = 225.20$  nm). A Schott UG-5 colored-glass filter, a KrF excimer-laser turning mirror, and the spectral response of a solar-blind PMT photocathode were used to isolate the NO fluorescence from the ( $v'=0$ ,  $v''=1-5$ ) bands and reject background radiation. Although interfering fluorescence from vibrationally hot  $O_2$  is present, the level of interference in this flame is small relative to the NO fluorescence [5]. For OH excitation, we tuned the same laser system (using the frequency-doubled dye laser beam) to the  $S_{21}(8)$  line of the  $A^2\Sigma^+-X^2\Pi(1,0)$  band ( $\lambda = 278.91$  nm). By pumping a satellite transition, we greatly reduced absorption of the laser beam propagating through the flame [6]. Schott colored-glass filters, WG-295 and UG-11, blocked

scattered radiation and transmitted fluorescence from the dominant (1,1) and (0,0) bands, where the (0,0) band fluorescence is preceded by vibrational energy transfer from  $v'=1$  to  $v'=0$  [7]. Some of the fluorescence, principally the (0,0)-band component, is strongly absorbed as it propagates through the flame. For this reason, we collected fluorescence from the *near* half of the flame. For both LIF measurements, we recorded the laser energy in addition to the OH or NO fluorescence from a laminar, near-adiabatic reference flame (Fig. 1). The reference flame served two purposes: first, the LIF signal allowed easy tuning of the laser wavelength to the desired transition; second, the recorded fluorescence allowed correction of the LIF signal in the  $H_2$ -air flame for minor wavelength drift of the dye laser.

### Calibrations and Corrections

The filament was calibrated using a near-stoichiometric  $H_2$ -air flame produced by a Hencken burner [8]. This 25-mm-square burner consists of an array of small fuel tubes surrounded by a Hastelloy honeycomb matrix which provides for the flow of air. The uncooled burner thus produces an array of nonpremixed flames; with sufficiently high flow rates of  $H_2$  and air (total cold-gas flow rates of  $\sim 50$  slpm for this 25-mm-square burner), the heat loss to the burner is negligible and the temperature is near the adiabatic value [8]. The hot-gas velocity--which is necessary for calculation of the radiation correction--can easily be calculated due to the 1-D nature of the flow field; additionally, the gas properties can be obtained from equilibrium calculations. Because of the nonpremixed nature of the burner, one can obtain a wide range of temperatures (from below 1000 K to greater than 2300 K) simply through variation of the  $H_2$  flow rate [8]. A comparison of the derived filament temperature (calibrating the filament at one Hencken flame condition) and the adiabatic equilibrium temperature showed excellent agreement between the calculated temperatures and those obtained from the filament.

To convert the emission measurement into gas temperature, the measured filament temperature must be corrected for radiative losses [4]. A numerical simulation of the flame (described below) shows that the velocity field is relatively uniform--i.e., a factor of two variation--in the region of interest; thus, we have simply used a constant velocity of 3.6 m/s for all the radiation corrections. However, to assess the sensitivity of the derived temperature to the time-

varying velocity and temperature fields, we have used the calculated fields and gas properties as inputs into the radiation correction algorithm. The difference in temperatures derived by means of the two approaches, one using uniform velocity and gas properties and the other using the time-varying calculated values, is small due to the relatively high velocity of the gas.

To calibrate the OH fluorescence, we used the same burner. At heights greater than  $\sim 2$  cm above the burner, the OH fluorescence is constant, indicating that the OH has equilibrated. We used the measured [OH] reported by Barlow and Carter [8] for a lean ( $\phi = 0.94$ )  $H_2$ -air flame. This concentration,  $[OH] = 2.16 \times 10^{16} \text{ cm}^{-3}$ , compares well with the adiabatic equilibrium value of  $2.31 \times 10^{16} \text{ cm}^{-3}$ . Unlike the concentrations of OH, those of NO are too small for reliable absorption measurements and are typically far below equilibrium at reasonable distances above the burner. Consequently, the approach taken was to dope a lean laminar flame with a small, known concentration of NO (from a bottle with  $\sim 200$  ppm of NO in  $N_2$ ). The calibration procedure consists of measuring NO fluorescence signals in a doped flame and in an undoped flame, where a portion of the pure  $N_2$  is substituted for the NO-doped  $N_2$ . Thus, except for the NO levels, the flames are identical; by subtracting the signal from the undoped flame from that of the doped flame, we obtain the signal corresponding to the doped NO.

Using quantities obtained from the calibration flame (those quantities denoted with the subscript *cal*), we have converted the linear fluorescence signals  $S_f$  to mole fraction with the following equation:

$$X_i = \frac{S_f}{N_T} \left[ \frac{N_i}{S_f} \right]_{cal} \left( \frac{[F_B]_{cal}}{F_B} \right) \left( \frac{[E_L/Q]_{cal}}{E_L/Q} \right).$$

Here,  $N_T$  is the total number density;  $[N_i/S_f]_{cal}$  is the fluorescence calibration factor (species number density divided by fluorescence signal);  $F_B$  is the Boltzmann fraction;  $E_L$  is the laser energy; and  $Q$  is the net quenching rate. For the NO fluorescence, we also took into account the effect of line broadening; however, its effect on the derived concentrations is small for the range of temperatures recorded with the filament. Of course, for both OH and NO LIF the transitions were chosen to minimize the temperature sensitivity of the respective ground-state populations over the temperature range appropriate for the filament (i.e., 900 to 2300 K).

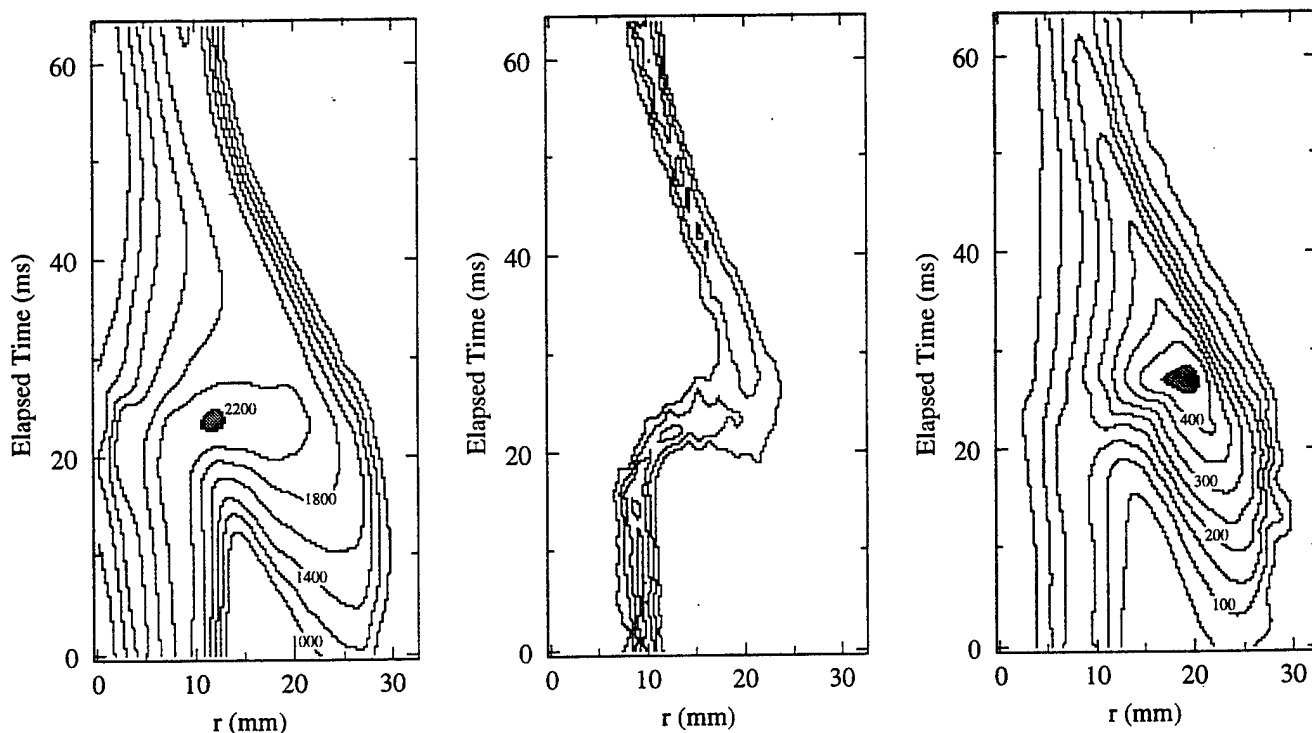


Fig. 2. Contour plots of measured temperature (left), OH concentration (middle), and NO concentration (right) in space (radius) and time. For temperatures and NO concentrations, contour levels are shown (temperature increments of 200 K with a maximum level of 2200 K; NO mole fraction increments of 50 ppm with a maximum level of 450 ppm). For OH mole fraction, contours are in increments of 0.2 percent with a maximum contour of 0.8 percent (fourth-level contour).

Currently we can only approximate the quenching variation using the recorded temperatures. Because one can distinguish fuel-rich from fuel-lean regions, the mix of species necessary to produce the measured temperatures can be estimated from equilibrium calculations. Because OH exists over only a limited range of conditions, its fluorescence is minimally affected by this estimate; for NO fluorescence, however, the quenching rate can vary by a factor of two over the range 1000 K to 2200 K. Consequently, to correct the fluorescence for the quenching variation across the flame, we constructed a *look-up* table of the quenching rate vs. temperature, which was based on an adiabatic temperature and the corresponding equilibrium mixture of species. The corrections differ for rich and lean conditions; thus, the correction algorithm distinguishes between the fuel-rich (inner) and fuel-lean (outer) regions of the flame. The models for OH and NO quenching include the quenching cross sections recently described by Paul et al. [Refs. 9 and 10 for NO; Refs. 11 and 12 for OH quenching].

## RESULTS AND DISCUSSION

Shown in Fig. 2 are the measurements of temperature and mole fraction of OH and NO (again, at the

downstream location of 135 mm) versus radial position and time, relative to the photodiode trigger signal. The temperature and mole fractions are represented with contour plots. Smooth curves have been drawn through the NO and temperature data for ease of interpretation; the same was not done for the OH plot, due to the coarse mapping resulting from 1-mm radial steps. The maximum observed temperature,  $\sim 2250$  K, occurs at the location of the flame bulge, i.e., the compressed region of the flame. In the stretched regions of the flame, the maximum temperatures across the flame drop to  $\sim 1900$  to 2000 K. Currently, we are investigating this drop in temperature below the adiabatic value of  $\sim 2200$  K.

As expected, OH exists only over a relatively narrow region of space. This region matches well that bracketed by the  $T > 1800$  K contour; consequently, the OH marks the high-temperature regions where we expect NO to be produced. For OH we find that the maximum concentrations of 0.8 to 0.9 percent by volume are in the thin stretched regions; at the bulge, the peak concentrations are lower. Katta et al. [4] attribute this behavior to flame curvature effects. Unfortunately, the flame stability was somewhat worse on the day when the OH was recorded (0.4 Hz vs. 0.2

Hz); as a consequence, the sharpest features of the OH map have probably been lost and the contour plot appears *noisy*. For NO the higher temperatures within the bulge result in concentrations in excess of 400 ppm. As expected, away from the bulge, even along the flame surface, the NO concentration is lower. Of course, once the NO is produced, it is transported as a relatively stable product; thus, we observe considerable concentrations of NO even in fuel-rich regions.

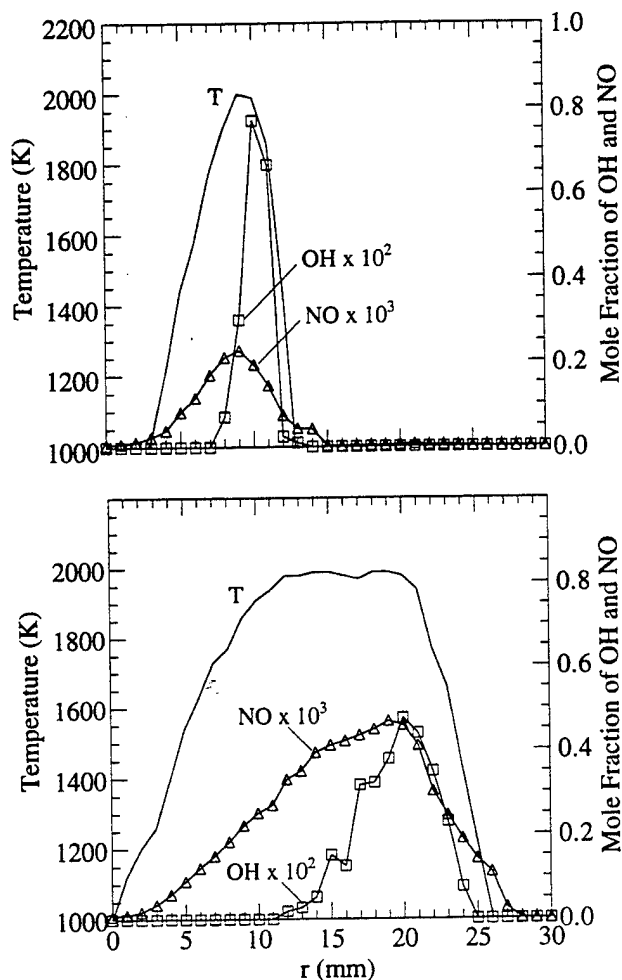


Fig. 3. Line plots of temperature,  $X_{OH}$ , and  $X_{NO}$  vs. radius at two times (top plot, 59 ms; bottom plot, 28 ms) relative to the trigger signal.

In Fig. 3 we show radial profiles at two times (i.e., phases), 28 and 59 ms, corresponding respectively to profiles across the compressed and stretched portions of the flame. The profiles from the stretched regions show narrow distributions of temperature, of  $X_{NO}$ , and especially of  $X_{OH}$ . The OH peaks slightly to the lean side--based on the temperature profile--of stoichiometric at  $\sim 0.8$  mole fraction; the peak  $X_{NO}$  ( $\sim 220$  ppm) corre-

lates well with the peak temperature ( $\sim 2000$  K). In the compressed region, the profiles of temperature,  $X_{NO}$ , and  $X_{OH}$  are broad. The NO peaks at about the same radial location (20 mm) as the OH. As mentioned above, the NO concentration is at its maximum value at this location; on the other hand, the peak OH concentrations are somewhat less than in the stretched regions.

Finally, in Fig. 4 we show results from the aforementioned numerical simulation, which has been described in detail by Katta et al. [1,2]. Briefly, the time-dependent Navier-Stokes equations, along with the species- and energy-conservation equations, are integrated on a nonuniform staggered-grid system. The detailed chemistry model includes 13 species and 52 elementary reactions. The effective binary-diffusion coefficient of the individual species in the local mixture is calculated using molecular dynamics and Lennard-Jones potentials. Across the compressed region, we find the maximum concentrations in the range of 420 to 480 ppm, in good agreement with the measured values. The maximum OH concentrations, occurring along the stretched regions, are between 0.8 and 1.0 percent mole fraction. Again, this matches well the experimental maximum of about 0.8 to 0.9 percent mole fraction. However, across the bulge, the calculated  $X_{OH}$  are somewhat larger than the measured values. Perhaps a more significant area of disagreement, however, is in the temperature field: while the measured temperatures drop 200 to 300 K in the stretched regions of the flame, the drop in the calculated values is less than 100 K.

## CONCLUSIONS

We have investigated the structure of a dynamic nonpremixed  $H_2$ -air flame. In particular, we have mapped in space and time through sequential point measurements the temperature through thin filament pyrometry and the concentrations of OH and NO through laser-induced fluorescence. The measurements show that OH is confined to relatively narrow regions, especially in the stretched portion of the flame. The peak values across the stretched regions of the flame are  $X_{OH} \cong 0.8$  to 0.9 percent mole fraction. The OH distribution across the compressed region is significantly broader (10 mm vs. 4 mm) and the peak concentrations are reduced.

NO is distributed over a wide region of the flame (from lean to rich, whereas the OH is found primarily in fuel-lean mixtures), with peak concentrations of  $\sim 450$  ppm in the compressed (bulge) region; in contrast, peak  $X_{NO}$  across the stretched region are as

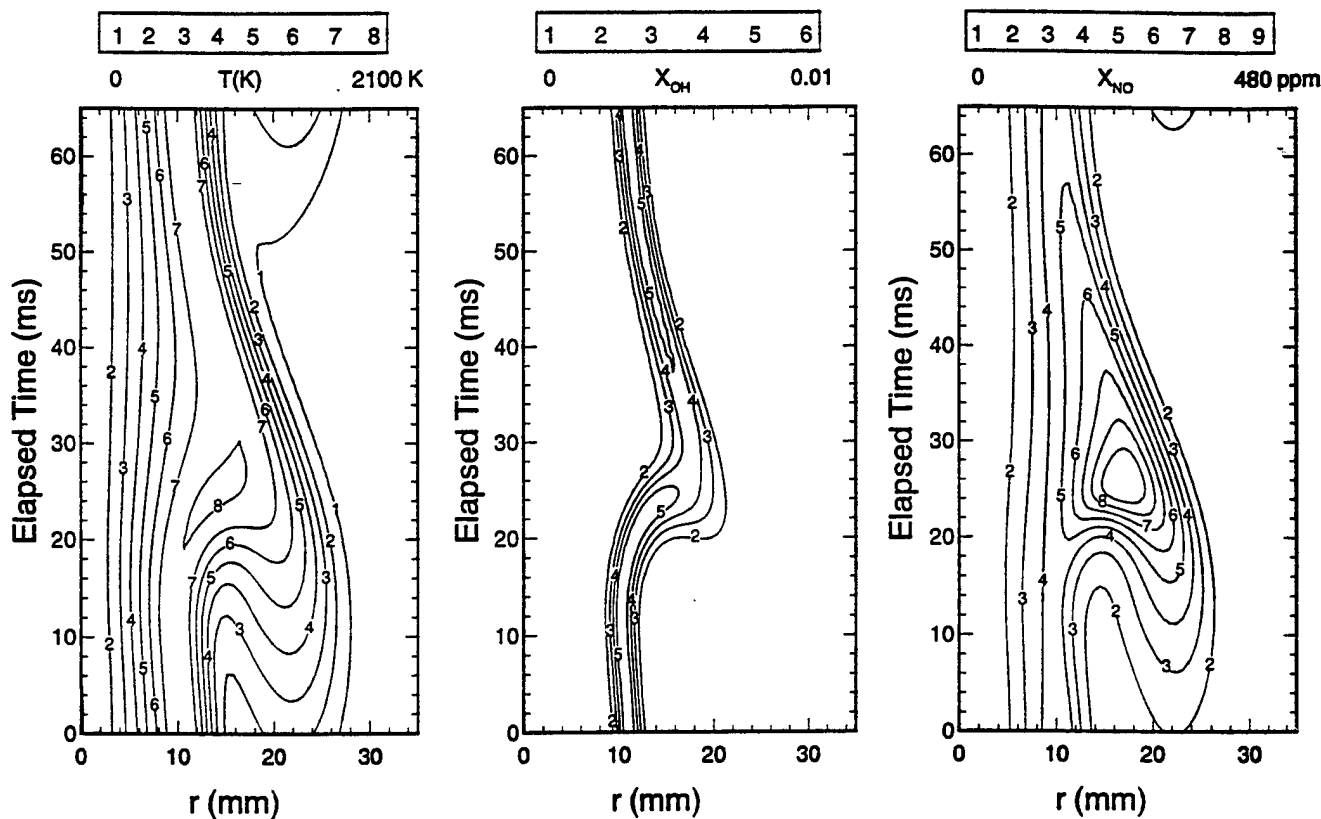


Fig. 4. Contour plots of calculated temperature (left), OH concentration (middle), and NO concentration (right) in space (radius) and time. Contour levels are indicated above each plot.

low as  $\sim 180$  ppm. A numerical simulation of the flame produced good agreement with the measured NO concentrations. Both calculations and measurements show peak NO concentrations of 450 to 480 ppm in the bulge and significantly reduced concentrations in the stretched regions. Currently, the most significant area of disagreement between simulation and experiment is the temperature field. We expect that future measurements and calculations will resolve this discrepancy.

#### ACKNOWLEDGMENTS

This work was supported by Wright Laboratory, Wright-Patterson Air Force Base, OH, under Contract No. F 33615-90-C-2033.

#### REFERENCES

- Katta, V. R., Goss, L. P., and Roquemore, W. M., *Combust. Flame* **96**: 60-74 (1994).
- Katta, V. R. and Roquemore, W. M., *Combust. Flame* **100**: 61-70 (1995).
- Vilimpoc, V. and Goss, L. P., *Twenty-Second Symposium (International) on Combustion*. The Combustion Institute, Pittsburgh, 1988, pp. 1907-1914.
- Goss, L. P., Vilimpoc, V., Sarka, B., and Lynn, W. F., *ASME Trans.* **111**: 46-52 (1989).
- Carter, C. D. and Barlow, R. S., *Opt. Lett.* **19**: 299-301 (1994).
- Chidsey, I. L. and Crosley, D. R., *J. Quant. Spectrosc. Radiat. Transfer* **23**: 187-199 (1980).
- Smith, G. P. and Crosley, D. R., *Appl. Opt.* **22**: 1428-1430 (1983).
- Barlow, R. S. and Carter, C. D., *Combust. Flame* **97**: 261-280 (1994).
- Paul, P. H., Carter, C. D., Gray, J. A., Durant Jr., J. L., and Furlanetto, M. R., *Correlations for the NO A<sup>2</sup> $\Sigma$  + (v'=0) Electronic Quenching Cross-section*, Sandia Report SAND94-8237, Sandia National Laboratories, Livermore, CA 94551 (1995).
- Paul, P. H., Gray, J. A., Durant Jr., J. L., and Thoman Jr., J. W., *AIAA J.* **32**: 1670 (1994).
- Paul, P. H., Carter, C. D., Gray, J. A., Durant Jr., J. L., Thoman, J. W., and Furlanetto, M. R., *Correlations for the OH A<sup>2</sup> $\Sigma$  + (v'=0) Electronic Quenching Cross-section*, Sandia Report SAND94-8244, Sandia National Laboratories, Livermore, CA 94551 (1994).
- Paul, P. H., *J. Quant. Spectrosc. Radiat. Transfer* **51**: 511 (1994).

## The Structure of a Dynamic Nonpremixed H<sub>2</sub>-Air Flame

C. D. Carter  
Systems Research Laboratories, Inc.  
2800 Indian Ripple Rd.  
Dayton, OH 45440-3696  
E-mail: cartercd@possum.appl.wpafb.af.mil

R. D. Gould  
Mechanical and Aerospace Engineering Department  
North Carolina State University  
Raleigh, NC 27695

L. P. Goss, V. R. Katta, and K.-Y. Hsu  
Innovative Scientific Solutions, Inc  
3845 Woodhurst Ct.  
Dayton, OH 45430

Presented at the Western States Section/The Combustion Institute  
1995 Fall Meeting, Stanford, California  
October 30-31, 1995

# The Structure of a Dynamic Nonpremixed H<sub>2</sub>-Air Flame

C. D. Carter  
Systems Research Laboratories, Inc.  
2800 Indian Ripple Rd.  
Dayton, OH 45440-3696  
E-mail: cartercd@possum.appl.wpafb.af.mil

R. D. Gould  
Mechanical and Aerospace Engineering Department  
North Carolina State University  
Raleigh, NC 27695

L. P. Goss, V. R. Katta, and K.-Y. Hsu  
Innovative Scientific Solutions, Inc  
3845 Woodhurst Ct.  
Dayton, OH 45430

## INTRODUCTION

Studies of simple, vertically oriented, nonpremixed jet flames have shown that when the co-flow velocity is sufficiently low, buoyancy-induced, periodic toroidal vortices form outside the flame surface [1-4]. These vortices wrinkle the flame surface and produce stretched and compressed flamelets, thereby providing a relatively simple means of studying flame-vortex interactions. Recent direct numerical simulations of these unsteady laminar flames (with H<sub>2</sub> as the fuel) suggest that preferential diffusion—due to nonunity Lewis number (*Le*, the ratio of rates of heat and species diffusion)—acting in concert with flame curvature influences the gas temperature along the flame surface [1,2,5]. In particular, Katta *et al.* [1,2] find that the flame temperature increases in the compressed regions of the flame and decreases in the stretched regions. That the flame temperature varies in this manner has been confirmed, in part, by previous experimental studies showing increased temperature within the compressed regions [3-4,6-7].

To characterize the structure of a dynamic nonpremixed H<sub>2</sub>-air flame, we have made sequential point measurements of temperature using thin-filament pyrometry (TFP) and of concentrations of hydroxyl (OH) and nitric oxide (NO) using laser-induced fluorescence (LIF). Because the NO production rate is strongly temperature sensitive (e.g., at flame temperatures the production rate for thermal NO increases by a factor of ~2 for increases in temperature of 100 K), NO is a good marker for the higher temperature zones. We have chosen three downstream locations, 50, 85, and 135 mm from the jet exit, that illustrate the downstream development of the buoyant flame structure. For each of these positions, we have recorded the radial *and* temporal variation of these scalars.

## EXPERIMENTAL METHODS

### Facilities and Techniques

Shown in Fig. 1 is a schematic of the experimental facility. The burner consists of a tapered fuel tube (1.0-cm ID) surrounded by a co-annular air section (15.0-cm ID); both the burner and the co-annular section are mounted to an *x-y-z* translation system employing stepper motors. The area-averaged flow velocities for the fuel and air were 4.6 and 0.42 m/s, respectively. Recent velocity measurements (employing LDV) across the co-annular region show that the air velocity is reasonably uniform (at ~0.44 m/s) away from the fuel nozzle; however, a significant lower-speed region (due to the boundary layer and the taper of the fuel nozzle) exists adjacent to the fuel tube. The selected air and fuel flow rates result in a buoyant frequency of 15.2 Hz. Although a range of frequencies (10 to 20 Hz) can be obtained by varying

the gas flow rates, the 15-Hz frequency is optimum for the available laser system, a 30-Hz Nd:YAG pump laser, insofar as the laser is triggered at twice the frequency of the buoyant fluctuations. The laser and detection electronics were phase locked to the 15.2-Hz buoyant frequency using the passage of these structures through a cw laser beam; the beam steering induced by the passage of the flame bulge moved the laser beam on and off a photodiode at the 15.2-Hz frequency. With the flame isolated from disturbances, the variation in the trigger frequency was within  $\pm 0.2$  Hz. To maintain a consistent trigger-flame phase relationship while probing different regions of the flow, we mounted both the cw laser and the photodiode detector to the burner/co-flow housing. Thus, the detection electronics were triggered from the same flame structure, regardless of the burner position. Finally, to reduce the maximum temperatures and, thereby, extend the lifetimes of the filaments, we employed a diluted fuel mixture in the ratio of 2.22 parts  $H_2$  to 1 part  $N_2$ ; the corresponding maximum adiabatic equilibrium temperature is  $\sim 2220$  K.

Originally the filament emission and NO fluorescence were recorded simultaneously. However, the flame proved to be reproducible, and subsequent to our initial simultaneous measurements, each (NO fluorescence, OH fluorescence, and temperature) was recorded sequentially. The  $\beta$ -SiC filaments, due to their small diameter (14  $\mu m$ ) and low thermal conductivity (10 kcal/m-hr-K or about 40 times lower than that of a Type-S or -R thermocouple), exhibit excellent temporal response and spatial resolution. The filament acts as a graybody with an emissivity of 0.88. The detection limit for the filament is detector dependent and was  $\sim 900$  K for the sandwiched Si and InGaAs photodiodes employed in this experiment; the high-temperature limit,  $\sim 2350$  K in practice (depending on the tension on the filament), is determined by the sublimation point of the  $\beta$ -SiC material. The InGaAs and Si photodiodes have respective spectral ranges of about 0.9 to 1.8  $\mu m$  and 0.45 to 1.0  $\mu m$ ; and because the temperature is derived from a ratio of the photodiode signals, the measurement is less sensitive to any variation in the filament emissivity and to small variations in the optical alignment. The frequency response of the filament is better than 1 kHz for flame conditions. Therefore, we expect that the filament will accurately reflect the temporal variations in gas temperature.

We overlapped the filament and LIF probe volumes using a 500- $\mu m$  pinhole—which was mounted on a kinematic magnetic base assembly—in combination with a He-Ne alignment laser; the pinhole defined the spatial resolution of both the LIF and the TFP measurements. The light from the He-Ne laser was split into two beams which were directed through the alignment pinhole. The intersection of the two beams was then used as a marker for the probe volume, and the filament was properly aligned when scattering from both He-Ne beams was observable. With all three measurements, we translated the burner to the axial and radial position of interest. The signals were then recorded as a function of delay relative to the trigger signal; the 2-D maps (signal versus time and radius) were then constructed from the individual signal-versus-time traces. With temperature we recorded the signals in real time; that is, we sampled the filament emission at a frequency of 1 kHz. Typically, we averaged the filament emission over 30 cycles for each spatial location. Strong emission originates from  $H_2O$  within the hottest regions of the flame; consequently, we simultaneously recorded the background flame emission and the filament emission. The emission was collected and focused by a concave spherical mirror (to eliminate chromatic aberration present with the available transmissive-lens systems) and then directed onto two optical fibers (one fiber specifically for filament emission and the other for flame emission), which routed the radiation to *two* dual-photodiode detectors. The spatial resolution of the temperature measurement, which was determined by the magnification of the mirror system (0.5) and the fiber core diameter (0.55 mm), was  $\sim 1.1$  mm. The effective separation of the background and filament fibers was  $\sim 3$  mm. To account for differences in optical efficiencies and detector gain, the recorded signals for the two detectors were *matched* with the filament well away from the flame, to ensure that both detectors recorded only background flame emission. Unfortunately, we did observe the effects of movement of the filament (due to gas velocity variations), not only within the unsteady flame but also in the transition from the unsteady flame to the calibration flame; of course movement of the filament can bias the temperature measurements.



measurements, we recorded the laser energy in addition to the OH or NO fluorescence from a laminar, near-adiabatic reference flame (Fig. 1). The reference flame served two purposes: first, the LIF signal allowed easy tuning of the laser wavelength to the desired transition; second, the recorded fluorescence allowed correction of the LIF signal from the unsteady flame for minor wavelength drift of the dye laser.

### Calibrations and Corrections

The filament was calibrated using a near-adiabatic H<sub>2</sub>-air flame produced by a Hencken burner [11]. This 25-mm-square burner consists of an array of small fuel tubes within a Hastelloy honeycomb matrix which provides for the flow of air. The uncooled burner thus produces an array of nonpremixed flames; with sufficiently high flow rates of H<sub>2</sub> and air (total cold-gas flow rates of ~50 slpm for this 25-mm-square burner), the heat loss to the burner is negligible and the temperature is near the adiabatic value [11]. The hot-gas velocity—which is necessary for calculation of the radiation correction—can easily be calculated because of the approximate 1-D nature of the flow field; additionally, the gas properties can be obtained from equilibrium calculations. Because of the nonpremixed nature of the burner, one can obtain a wide range of temperatures (from < 900 K to > 2300 K) simply through variation of the H<sub>2</sub> flow rate [11]. In Fig. 2, we show a comparison between the derived filament temperatures (calibrating the filament at one Hencken flame condition) and the calculated adiabatic equilibrium temperatures.

To convert the emission measurement into gas temperature, the measured filament temperature must be corrected for radiative losses [7]. The numerical simulation of the flame (described below) shows that the velocity field is relatively uniform (i.e., a factor of two variation) in the region of interest; thus, we have simply used a constant velocity of 3.6 m/s for all the radiation corrections. However, to assess the sensitivity of the derived temperature to the time-varying velocity and temperature fields, we have used the calculated fields and gas properties as inputs for the radiation-correction algorithm. The difference in temperatures derived by the two approaches—one using uniform velocity and gas properties and the other using the time-varying values—is small because of the relatively high velocity of the gas. This effect is illustrated in Fig. 2 where the temperatures derived using 1) a velocity of 6 m/s (for all the TFP measurements) and 2) the calculated burnt-gas velocity—which varies from 4 to 12 m/s—are virtually identical.

To calibrate the OH fluorescence, we used the same burner. At heights  $\geq 3$  cm above the burner, the OH fluorescence is constant, indicating that the OH has equilibrated. We recorded OH absorption spectra in a lean ( $\phi = 0.94$ ) H<sub>2</sub>-air flame by scanning the dye laser over several transitions in the (0,0) band. We derived the absorption pathlength (about 28 mm) from a measurement of the OH LIF across the burner. The resulting concentration,  $[\text{OH}] = 2.18 \times 10^{16} \text{ cm}^{-3}$ , compares well with the adiabatic equilibrium value of  $2.37 \times 10^{16} \text{ cm}^{-3}$  (with  $T_{ad,eq} = 2340 \text{ K}$ ) and is consistent with a temperature only ~25 K below the adiabatic value. A comparison of the OH LIF data (calibrated using this absorption measurement) and the adiabatic equilibrium value is also shown in Fig. 2. The OH fluorescence signal has been corrected for variations in Boltzmann fraction and quenching (see the equation below), although both of these corrections are relatively small. This figure demonstrates that OH concentrations are indeed close to the adiabatic equilibrium values. Note that in correcting the fluorescence, we have not taken into account fluorescence trapping, either in the calibration flame or in the unsteady flame (although we expect that this correction is relatively small).

Unlike the concentrations of OH, those of NO are too small for reliable absorption measurements and are typically far below equilibrium at reasonable distances above the burner. Consequently, the approach we took was to dope a lean laminar flame with a small, known concentration of NO (from a bottle with ~200 ppm of NO in N<sub>2</sub>). The calibration procedure consists of measuring NO fluorescence signals in a doped flame and in an undoped flame, where a portion of the pure N<sub>2</sub> is substituted for the NO-doped N<sub>2</sub>.

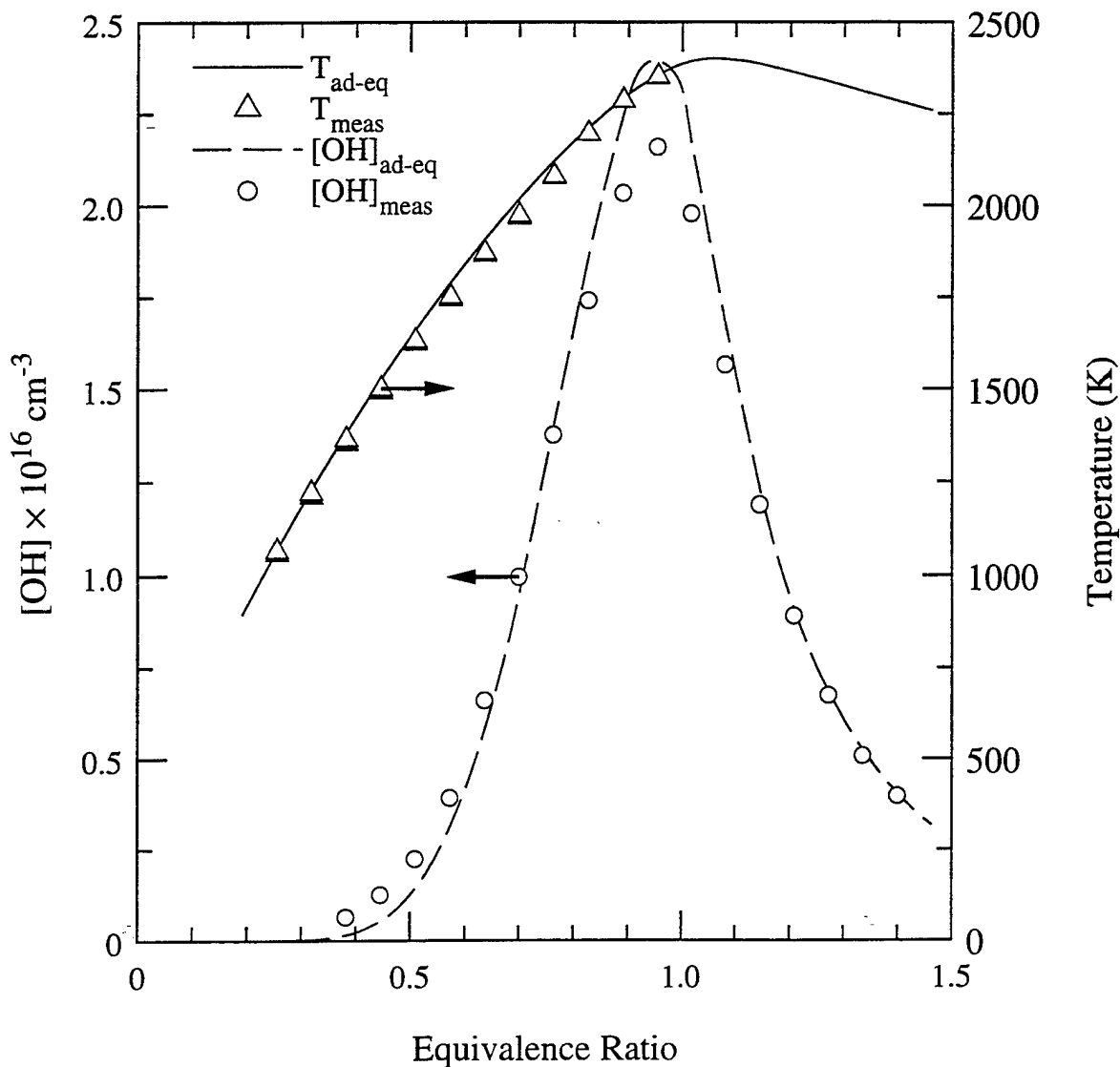


Fig. 2. Temperature and OH concentration over a near-adiabatic H<sub>2</sub>-air Hencken flame. The experimental temperatures and OH concentrations were recorded with TFP and LIF, respectively. The filament emission was calibrated using the adiabatic equilibrium temperature at  $\phi = 0.95$ , while the OH was calibrated with an independent absorption measurement. The TFP temperatures derived using the burnt-gas velocity are represented by open triangles, while those derived using a single velocity are represented by closed triangles.

Thus, except for the NO levels, the flames are identical; by subtracting the signal from the undoped flame from that of the doped flame, we obtain the signal corresponding to the doped NO.

Using quantities obtained from the calibration flame (denoted with the subscript *cal*), we convert the linear fluorescence signals  $S_f$  to mole fraction with the following equation:

$$X_i = \frac{S_f}{N_T} \left[ \frac{N_i}{S_f} \right]_{cal} \left( \frac{[F_B]_{cal}}{F_B} \right) \left( \frac{[E_L/Q]_{cal}}{E_L/Q} \right).$$

Here,  $N_T$  is the total number density,  $[N_i/S_f]_{cal}$  the fluorescence calibration factor (species number density divided by fluorescence signal),  $F_B$  the Boltzmann fraction,  $E_L$  the laser energy, and  $Q$  the net quenching rate. For the NO fluorescence, we also took into account the effect of line broadening; however, its effect on the derived concentrations is small for the range of temperatures recorded with the filament. Of course, for both OH and NO LIF, we chose transitions to minimize the temperature sensitivity of the respective ground-state populations over the temperature range appropriate for the filament (i.e., 900 - 2300 K).

Currently we can only approximate the quenching variation using the recorded temperatures. Because one can distinguish fuel-rich from fuel-lean regions, the mix of species necessary to produce the measured temperatures can be estimated from equilibrium calculations. Because OH exists over only a limited range of conditions, its fluorescence is minimally affected by the accuracy of this estimate; for NO fluorescence, however, the quenching rate can vary by a factor of two over the range 900 - 2300 K. Consequently, to correct the fluorescence for the quenching variation across the flame, we constructed a *look-up* table of the quenching rate as a function of temperature, which was based on an adiabatic equilibrium temperature and the corresponding mixture of species. The corrections differ for rich and lean conditions; thus, the correction algorithm must distinguish between the fuel-rich (inner) and fuel-lean (outer) regions of the flame. The models for OH and NO quenching include the quenching cross sections recently described by Paul *et al.* [12, 13 for NO; 14, 15 for OH].

## RESULTS AND DISCUSSION

The numerical model that we employ has been described in detail by Katta *et al.* [1,2], although we note the following: 1) the time-dependent Navier-Stokes equations, along with the species- and energy-conservation equations, are integrated on a nonuniform staggered-grid system; 2) the detailed chemistry model includes 13 species and 52 elementary reactions; and 3) the effective binary-diffusion coefficient of the individual species in the local mixture is calculated using molecular dynamics and Lennard-Jones potentials. The numerical results presented herein are for a uniform air co-flow velocity of 0.3 m/s rather than the area-averaged value of 0.42 m/s. Use of the area-averaged value, though, results in a flow development that does not match the experimental observations. Recently, we have attempted to remedy this discrepancy by recording an inlet co-flow velocity profile with laser-Doppler velocimetry; however, updated calculations were not available for this paper. Nevertheless, we show Figs. 3, 4, and 5 the experimental and numerical values (using the 0.3-m/s co-flow velocity) of temperature and mole fraction of OH and NO at the three downstream locations of 50, 85, and 135 mm, respectively, versus radial position and time (relative to the photodiode trigger signal). These figures show the development of the flame bulge as the observation point moves downstream. The NO and temperature data were acquired in 1-mm radial steps, while the OH was recorded in 0.5-mm (at 50 and 85 mm downstream) and 0.75-mm (at 135 mm downstream) radial increments; however, linear interpolation has been used to *smooth* the images. Note that for purposes of comparison, we have displayed the measured (left-hand side) and calculated (right-hand side) values in a *mirror-image* format; in addition, we have shown only the computed and measured contours above 1000 K, since we were limited to measuring temperatures above 900 K with our TFP apparatus.

At 50 mm (Fig. 3), the flame resembles a steady flame, though we note some temporal variation in the position of the flame surface; furthermore, the measurements and calculations show a small variation (temporal) in temperature along the flame surface and a concomitant variation in  $X_{NO}$ . Maximum concentrations of NO in the measurements and calculations are similar at about ~300 ppm. Consistently (at the three downstream locations), we obtain slightly greater measured  $X_{OH}$  (~1.1 percent by volume) than calculated  $X_{OH}$  (~0.9 to 1.0); however, fluorescence trapping in the *calibration flame* presumably results in a small error (perhaps +10%) in the calibration factor. As expected, OH exists only over a relatively narrow region of space. This region matches well that bracketed by the  $T > 1800$  K contour; consequently, the OH marks the high-temperature regions where we expect NO to be produced. In addition, we

consistently observed somewhat greater experimental flame temperatures, 2350 K measured versus ~2200 K calculated, at each downstream position; this, however, may be the result of movement of the filament in the calibration process (due to the high burnt-gas velocity in the Hencken flame).

At 85 mm downstream of the jet exit (Fig. 4), the development of the flame bulge continues. The effect of the nonunity  $Le$  is now clearly seen in the NO image; within the bulge the NO concentration peaks at greater than 400 ppm (with the calculated values being slightly higher than the measured ones). Away from the bulge, however, the NO concentration across the flame is much reduced (i.e.,  $X_{NO} \cong 200$  ppm from the measurements and calculations at about 28 ms). The width of the OH zone is maximum within the bulge, but the peak concentration across the flame drops slightly ( $X_{OH} \cong 0.008$  near the bulge vs.  $X_{OH} \cong 0.009$  away from the bulge). Again, the maximum measured temperature is ~2350 K, while the maximum calculated value is ~2200 K. In general, however, the agreement between the measurements and calculations is good, not only in terms of peak concentrations and temperatures, but also in terms of the shapes of the concentration and temperature maps (although there are some differences, particularly with the  $X_{NO}$  and temperature at ~40 ms).

At 135 mm downstream of the jet exit (Fig. 5), the flame bulge is fully developed. The maximum observed temperature, ~2350 K from the measurements and ~2200 K from the calculations, occurs at the location of the flame bulge, i.e., the compressed region of the flame; in the stretched regions of the flame, the maximum temperatures across the flame drop to ~2100 K. The discrepancy between the measured and calculated temperature aside, there is reasonably good agreement between the calculated and measured temperature. We also observe good agreement between the measured and computed values of  $X_{OH}$  and  $X_{NO}$ . Of course, flame disturbances from room drafts are more evident at this position than at 50 and 85 mm; thus, the  $X_{OH}$  map in particular (due to the small region over which OH exists) appears somewhat *noisy*. The maximum measured  $X_{OH}$  are somewhat higher than the calculated ones; however, across the flame bulge, the measured  $X_{OH}$  are somewhat lower than the calculated values. The  $X_{NO}$  peaks in the compressed regions (at  $X_{NO} \cong 490$  ppm from the measurements and  $X_{NO} \cong 550$  ppm from the calculations), as expected based on the high temperatures within the bulge. In the stretched regions, the  $X_{NO}$  decreases significantly; for example at ~25 ms, the measurements show that  $X_{NO} \cong 180$  ppm (the calculated value is somewhat higher, however). Of course, once the NO is produced, it is transported as a relatively stable product, and thus we observe considerable concentrations of NO even in fuel-rich regions

## CONCLUSIONS

We have investigated the structure of a dynamic nonpremixed  $H_2$ -air flame through experiments and a direct numerical simulation. In particular, we have recorded in space and time through sequential phase-locked point measurements the temperature using TFP and the concentrations of OH and NO using LIF. The measurements and calculations show the evolution of the flame with increasing distance from the jet exit. Near the jet exit the flame resembles its steady counterpart; however, even at 50 mm downstream, we observe some temporal structure that includes small broadening and narrowing of the high-temperature and high- $X_{NO}$  zones; this effect is less pronounced with the thin OH region. Accompanying the broadening of the temperature/ $X_{NO}$  zones is a modest increase in the NO concentration. The comparison between measurements and computations is good, especially for OH and NO concentrations. Consistently, the temperature recorded with TFP was 100 to 150 K higher than expected; this may result from movement of the filament. With increasing downstream distance, the dynamic character of the flame continues to develop. At 85 mm above the jet, the compressed and stretched regions are now clearly visible, as are the effects of the flame curvature and nonunity  $Le$  on the  $X_{NO}$  and  $X_{OH}$ ; whereas the NO concentrations are maximum within the compressed region, the OH concentrations across the flame zone are at their minimum values. Again, the comparison between modelling and experimental results is good, not only in terms of the magnitudes of the concentrations and temperatures but also in terms of the shapes of the concentration and

temperature maps. Finally, at 135 mm downstream, we find the bulge to be fully developed, and the combined effects of flame curvature and nonunity  $Le$  are most evident from the NO map, due to the temperature sensitivity of the thermal-NO mechanism. With both measurements and calculations, the  $X_{NO}$  within the bulge is in excess of 450 ppm. Within the stretched regions of the flame, the  $X_{NO}$  is greatly reduced. Again, the measured temperatures are somewhat high across the reaction zone, and our future work will focus on improving the accuracy of the recorded temperatures. In addition, for the numerical simulation, we selected a co-flow velocity (one somewhat less than the area-averaged value) such that the simulation matched the general observations of the flame development; of course, future calculations will incorporate the measured velocity profile.

## ACKNOWLEDGMENTS

This work was supported by Wright Laboratory, Aero Propulsion and Power Directorate, Wright-Patterson Air Force Base, OH, under Contract Nos. F33615-90-C-2033 and F33615-95-C-2507.

## REFERENCES

1. Katta, V. R., Goss, L. P., and Roquemore, W. M., *Combust. Flame* **96**: 60-74 (1994).
2. Katta, V. R. and Roquemore, W. M., *Combust. Flame* **100**: 61-70 (1995).
3. Katta, V. R., Grisch, F., Attal-Tretout, B., Bouchardy, P., and Roquemore, W. M. "Vortex-Flame Interactions in a Hydrogen Jet Diffusion Flame," Presented at 1995 Joint Technical Meeting (Central and Western States and Mexican National Sections) of the Combustion Institute, April 23-26, 1995, San Antonio, TX.
4. Carter, C. D., Goss, L. P., Hsu, K.-Y., Katta, V. R., and Trump, D. D., "The Structure of a Dynamic Nonpremixed  $H_2$ -air Flame," Presented at 1995 Joint Technical Meeting (Central and Western States and Mexican National Sections) of the Combustion Institute, April 23-26, 1995, San Antonio, TX.
5. Law, C. K. and Chung, S. H., *Combust. Sci. Technol.* **29**: 129-145 (1982).
6. Vilimpcoc, V. and Goss, L. P., *Twenty-Second Symposium (International) on Combustion*. The Combustion Institute, Pittsburgh, 1988, pp. 1907-1914.
7. Goss, L. P., Vilimpcoc, V., Sarka, B., and Lynn, W. F., *ASME Trans.* **111**: 46-52 (1989).
8. Carter, C. D. and Barlow, R. S., *Opt. Lett.* **19**: 299-301 (1994).
9. Chidsey, I. L. and Crosley, D. R., *J. Quant. Spectrosc. Radiat. Transfer* **23**: 187-199 (1980).
10. Smith, G. P. and Crosley, D. R., *Appl. Opt.* **22**: 1428-1430 (1983).
11. Barlow, R. S. and Carter, C. D., *Combust. Flame* **97**: 261-280 (1994).
12. Paul, P. H., Carter, C. D., Gray, J. A., Durant Jr., J. L., and Furlanetto, M. R., *Correlations for the  $NO A^2\Sigma^+(v'=0)$  Electronic Quenching Cross-section*, Sandia Report SAND94-8237, Sandia National Laboratories, Livermore, CA, 1995.
13. Paul, P. H., Gray, J. A., Durant Jr., J. L., and Thoman Jr., J. W., *AIAA J.* **32**: 1670 (1994).
14. Paul, P. H., Carter, C. D., Gray, J. A., Durant Jr., J. L., Thoman, J. W., and Furlanetto, M. R., *Correlations for the  $OH A^2\Sigma^+(v'=0)$  Electronic Quenching Cross-section*, Sandia Report SAND94-8244, Sandia National Laboratories, Livermore, CA, 1994.
15. Paul, P. H., *J. Quant. Spectrosc. Radiat. Transfer* **51**: 511 (1994).

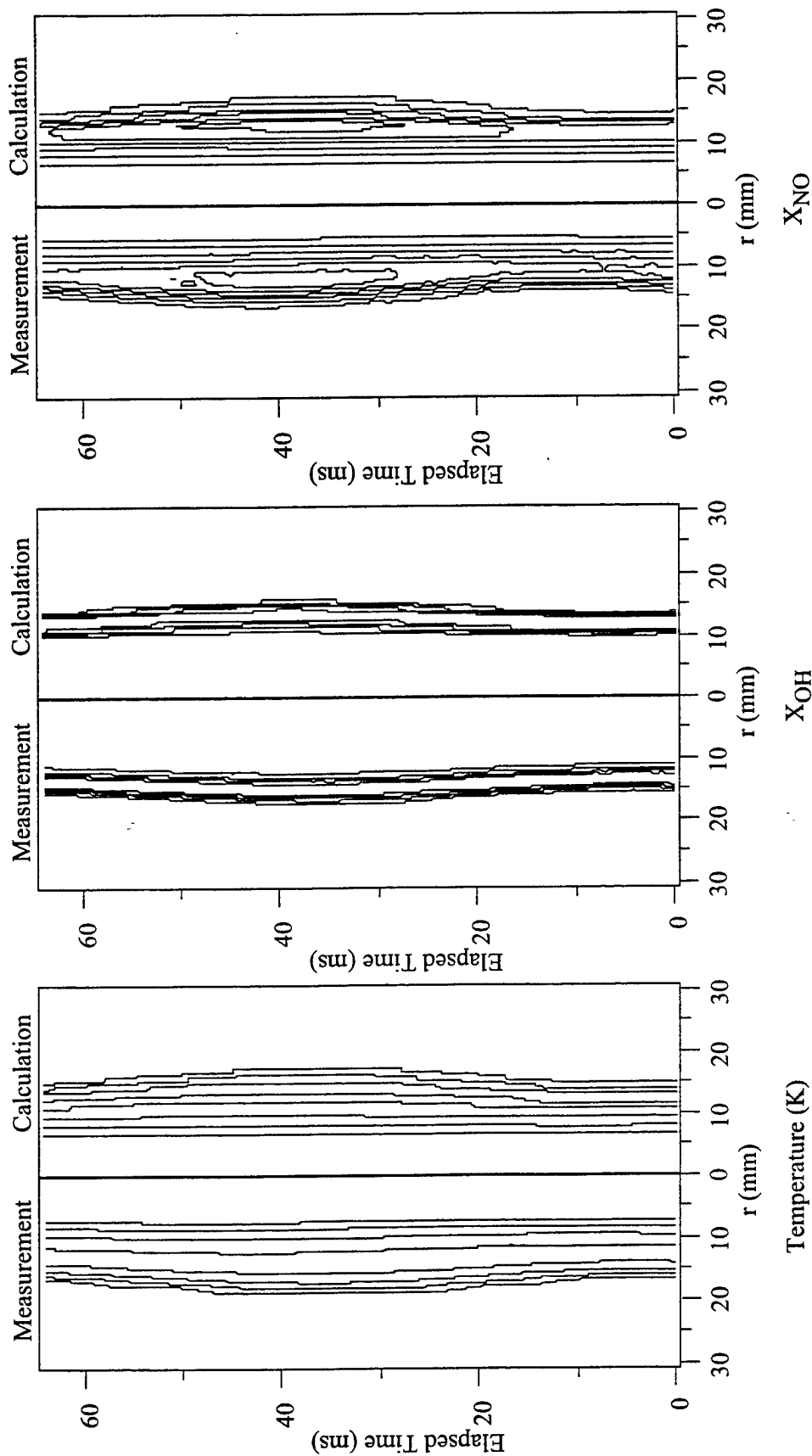


Fig. 3. Contour plots of measured (left-hand side) and calculated (right-hand side) (1) temperature (middle), and (3) NO concentration (right) in space (radius) and time at 50 mm downstream of the jet exit. The description of the contours is as follows: (1) temperature, from 1000 to 2200 K with 400 K intervals; (2) OH mole fraction,  $X_{OH}$ , from 0.002 to 0.008 with 0.002 intervals; (3) NO mole fraction,  $X_{NO}$ , from 50 to 300 ppm with 50 ppm intervals.

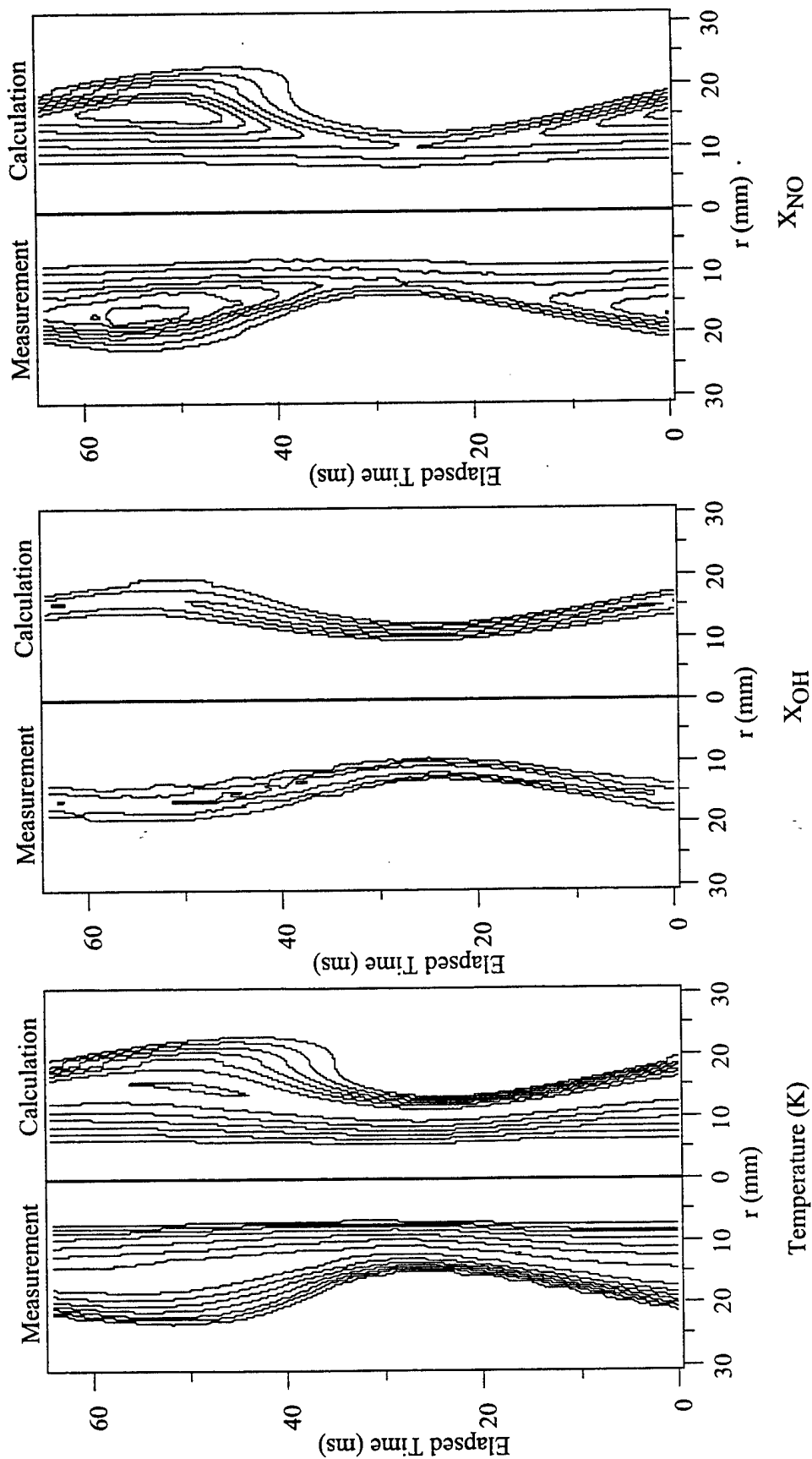


Fig. 4. Contour plots of measured (left-hand side) and calculated (right-hand side) (1) temperature (middle), (2) OH concentration (middle), and (3) NO concentration (right) in space (radius) and time at 85 mm downstream of the jet exit. The description of the contours is as follows: (1) temperature, from 1000 to 2000 K with 200 K intervals; (2) OH mole fraction,  $X_{OH}$ , from 0.003 to 0.009 with 0.003 intervals; (3) NO mole fraction,  $X_{NO}$ , from 100 to 400 ppm with 50 ppm intervals.

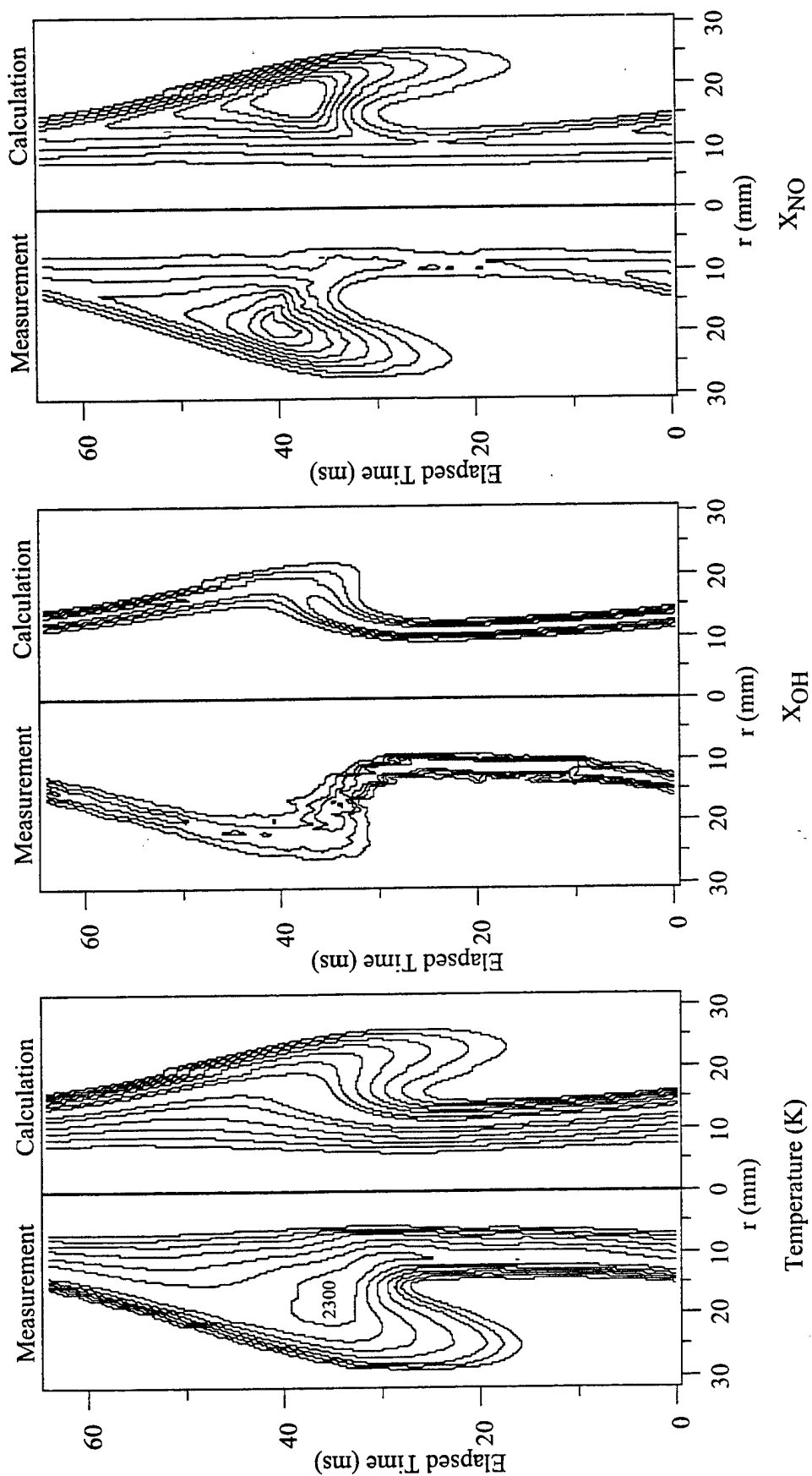


Fig. 5. Contour plots of measured (left-hand side) and calculated (right-hand side) (1) temperature (left), (2) OH concentration (middle), and (3) NO concentration (right) in space (radius) and time at 135 mm downstream of the jet exit. The description of the contours is as follows: (1) temperature, from 1000 to 2000 K with 200 K intervals (the measured temperatures > 2300 K are also shown); (2) OH mole fraction,  $X_{OH}$ , from 0.002 to 0.008 with 0.002 intervals; (3) NO mole fraction,  $X_{NO}$ , from 100 to 450 ppm with 50 ppm intervals.